

Development of new ferritic 14 Cr ODS steels with
four oxides formers (Y, Ti, Zr, Al) for nuclear
applications

by

Eric Macía Rodríguez

A dissertation submitted by in partial fulfillment of the requirements
for the degree of Doctor of Philosophy in

Materials Science and Engineering

Universidad Carlos III de Madrid

Advisor(s):

Mónica Campos Gómez

Tutor:

Mónica Campos Gómez

October 2019

This thesis is distributed under license “Creative Commons **Attribution – Non Commercial – Non Derivatives**”.



A Eduardo
Pilar
Cristina
María
Manolo
Manuela
Stefano
Alba

PREFACE

The PhD thesis here presented has been carried out at the Department of Materials Science and Engineering and Chemical Engineering of the Carlos III University of Madrid.

This work have been developed in the frame of two coordinated projects awarded by the Spanish Ministry of Economy and Competitiveness **MAT2013-47460-C5-5-P** (PROCESADO PULVIMETALÚRGICO DE NUEVAS ALEACIONES FERRÍTICAS ODS (FEAL (CRZR) PARA CONDICIONES SEVERAS DE UTILIZACIÓN) and **MAT2016-80875-C3-3-R** (ESTABILIDAD MICROSTRUCTURAL DE ACEROS FERRÍTICOS ODS PARA FUTUROS SISTEMAS DE ENERGÍA) and thanks to the financial support of the competitive grant FPI BES-2014-070836.

This doctoral thesis has been recognized with the mention of International PhD that have been established in article 15 of the Royal Decree 99/2011 establishing the Ordination of Official University Education (B.O.E No.35 of January 28, 2011, p. 13909-13926) as is described in the *Rules and Regulations* for Ph.D. studies at Universidad Carlos III de Madrid.

In order to utilize the best available equipment, part of the research work –mainly SPS consolidation and part of microstructural characterization- has been carried out at different Institutions: at the Oxford under the supervision of Prof. S. Lozano-Perez during 1 month, at Kongyu National University (South Korea) under the supervision of Prof S.J. Hong during 4 months and at the Fraunhofer IFAM of Dresden (Germany) under the supervision of Prof Dr.Ing Thomas Weissgärber for 3 months. Moreover, two international experts have reviewed the present manuscript.

Part of the results obtained during the course of this thesis have been published in Journal of Nuclear Materials (top international journals in the field of nuclear materials), and are currently submitted to Journal of Materials Science and Technology. Additionally, this research has been well accepted at international conferences on the field of materials for special applications.

AGRADECIMIENTOS

Me gustaría empezar a agradecer este trabajo al departamento de materiales de la Universidad Carlos III de Madrid, desde los jefes a los técnicos y en especial al grupo de investigación de tecnología de polvos (GTP), Elena, Elisa, Toñi, Maru, Sofía, Juan, Sandra, Eva, Susana, Christian, María, por su enorme cariño en estos años que hemos compartido, ha sido un enorme placer! A mis compañeros del GTP, Betty, Eduardo, Paula y a los que ya no están Alicia, Carol, Rafa, Julia, Miguel gracias por los momentos vividos y por las risas pasadas. A José Manuel que junto a Mónica empezó esta tesis conmigo y por el cual también estoy aquí. Muchas gracias por tus palabras amables siempre que hemos coincidido. A Elena Bernardo y en especial a Paula Alvaredo y por ser mis primeras tutoras en esta universidad y por los conocimientos compartidos. ¡Muchas gracias!

A los centros de investigación que cordialmente han apoyado mi investigación, IMDEA Materials, que de la mano de Andrea García Junceda nos ha permitido el uso de un gran número de equipos, incluido el EBSD. ¡Gracias por las charlas sobre los ODS y las diferentes discusiones varias!

Al CIEMAT inmejorable equipo formado por Marta, Daniel, Rebeca, por sus lecciones sobre small punch y por el trato buenísimo cada vez que he trabajado con vosotros. ¡Os quiero dar las gracias en especial! A Mercedes y Manuel ha sido genial poder hacer los ensayos de In-situ TEM annealing con vosotros y aprender más cosas sobre el complejo TEM. ¡Muchas gracias por haberme enseñado, no todo el mundo lo hace, gracias!

A los centros de investigación donde he realizado las estancias, por su disponibilidad tanto en equipos como personal y por el buen trato. Oxford University de la mano de Sergio Lozano, Kongju University de la mano de Soon-jik Hong y finalmente al IFAM de la mano de Thomas Weissgärber.

A mi directora de tesis Mónica ¡Qué decir que no hayamos dicho ya! Gracias por convertirme en el profesional que soy, por enseñarme esa pasión llamada Ciencia de Materiales, por enseñarme a presentar y a escribir una tesis, por sorprenderme cada vez que nos reunimos, por los momentos malos y buenos pasados juntos tanto en lo personal como en la tesis, muchas gracias por guiarme en estos 4 años ¡No tengo palabras, esta investigación es fruto de un grandísimo esfuerzo y lo estamos viendo reflejado ahora! ¡Muchísimas gracias!

¡A mis compañeros de lucha de investigación y de profesión ¡qué puedo decir de estos cuatro años! Me llevo un trocito de todos y todas. Sois unos profesionales gigantes solo puedo daros las gracias. A Javi por tus bromas y tus risas por tus consejos en determinados momentos, por formar parte del eje del mal, por las tardes de cervezas, ¡qué grande científico se ha perdido la UC3M! suerte en tu nueva etapa y gracias por todo. A Lucía por ese carácter indomable, por tus palabras y por ser una química buenísima, te va a ir genial en todo lo que hagas. A María por su forma de decirte todo con una sonrisa, a Sara por su enorme positividad, a Nieves ¡olé tú olé! por el enorme apoyo en los últimos meses de tesis y porque nunca dices nada malo de nadie! ¡Gracias! A Andrés por su magia incomprensible, por sus grandísimas letras y por sus canciones sin ritmo, gracias, ¡suerte también! A Borja roquero donde los haya la sinfonía de la fiesta, la batuta en las risas en el zulo, gracias por todo. ¡A Gelydis por los ritmos caribeños y las risas pasadas desde el máster, gracias! A Olivier très bon ami,

gracias por esos tres años juntos por las tardes de conversaciones sobre fútbol baloncesto, ¡por lo bien que lo pasamos en la Summer School gracias por todo! A Andrea, por haber sido grandes compañeros de tesis, por darnos una mano siempre que lo hemos necesitado. ¡Muchas gracias por escucharme siempre! ¡A Pedro por haber empezado juntos la etapa profesional, por ser mi compañero de pádel de despacho y de risas en el último año, gracias! ¡¡A Rachel esa canarionaa!! ¡Por tus hellouss matutinos y tu constante lucha en este doctorado! ¡Mucho ánimo y muchas gracias! A Morena, el clan italiano, grazie mille per questi anni di amicizia , per il tuo sorriso e la tua forza! ¡A Carla por la sal de la tierra o el azúcar de la mar y tu forma de tomarte todo siempre con alegría y humildad, muchas gracias! A Guille por nuestros partidos de futbol por nuestras conversaciones y risas, a las cenas románticas, por las bromas con tu mochila, por todo gracias, me llevo un gran amigo. A Andrea (Phh) gran compañera de despacho y risas confía en ti vas a llegar muy lejos. ¡Pequeños cambios por un mundo mejor! Muchas gracias ¡A mi Carmela por tus ideas alocadas, por tus bailes y tus músicas, porque necesitamos acabar la tesis, por ser una gran amiga! ¡Más que grupos de investigación formamos un gran departamento de materiales gracias a todas y a todos!

A mi bro, gracias, Koke por lo que hemos creado juntos, por haber fundado prácticamente este club de montaña Cara sur UC3M, ¡por haber guiado juntos a tanta gente y por habernos divertido de la manera en lo que lo hemos hecho! ¡Por ser Zipi y yo Zape o a la inversa! Compañero de todo, de batallas, de tesis, ¡de risas y de viajes!! ¡Nos queda mucho por andar juntos, solo puedo decir gracias! A mis compañeros de expedición Pelu, grandísimo montañero y mejor persona y amigo ,gracias por enseñarme por cuidarme por transmitirme el arte del barranquismo y por inculcarme esos valores locos de la montaña por todo esto gracias , a David por formar parte del big three de las rutas locas largas y de cuanto más desnivel mejor, por la enorme confianza adquirida en tan poco tiempo por todas aventuras que nos quedan por vivir gracias por todo , a Carlos por ser un cabezón ,casi tanto como yo, por querer aprender, por transmitir un enorme entusiasmo, por las canciones haciendo de Paulina Rubio en los viajes gracias! , a todo el club cara sur UC3M nos queda mucho por subir y descender. ¡Gracias!

A mi Natalia y Amaya que suerte haberos conocido. ¡Vaya dos compañeras! Nat, aunque ahora estés en Polonia y estemos un poco lejos, nunca dudo cuando tengo que acudir a ti por algún consejo. ¡Qué hubiese sido de mi sin ti!! No sé como darte las gracias por todo lo que me has aportado. ¡Gracias por tus lecciones de vida y feminismo!! Eres una grandísima persona, amiga y tremenda profesional. Amaya, la mejor investigadora que ha tenido el GTP (sin faltar al respecto a todos y todas las profesionales que han pasado por este grupo). Tú fuerza está en la persona que eres. ¡No cambies nunca! Gracias por ser como dijiste tú en su momento, mi compañera indudable de lucha en la UC3M por enseñarme tantas cosas. No puedo pedir mejor amiga. ¡Os valoro un montón queda mucho camino!!

A mi Estela y a Marta porque sin duda son las que más habéis sufrido a mi lado, tremendas tesis las que estáis o habéis hecho y tremendo trabajo. ¡Sois muy top! Como personas hay mucho que decir y pocas líneas, luchadoras con una enorme energía, duras por fuera pero un trocito de pan por dentro. Me llevo unas grandes amigas. Gracias por todo. Marta sin ti esta tesis hubiese sido más dura. ¡Gracias por escucharme siempre!!

¡A mi Edu Alberto y Caterina que decir de vosotros, una sonrisa perenne cada vez que estamos juntos! A mi canario favorito ¡qué gran fichaje de verano! Cuanto nos queda por hacer, impresión 3D, chiringuitos con música (Merenguito a ser posible), en definitiva, ¡gran amigo! A mi sucesor en esta aventura llamados los ODS gracias por ser tan buen compañero de investigación por ayudarme por apoyarme por dejarte ayudar y guiar. ¡Eres muy top meu! Sigue así. No puedo pedir mejor pupilo y amigo. ¡ODS! Caterina el terror caraqueño que gran persona y que gran luchadora y siempre con una sonrisa, espero haberte ayudado en todo lo que has necesitado. ¡¡Gracias por todo!!

¡¡A mis amigos de aeronáutica Raúl y Jaime, cuanto tiempo os debo después de estos dos años enfocados a la tesis!! Grandísimas personas y grandes profesionales. Nunca me habéis fallado y siempre habéis estado para apoyarme en todo momento. ¡Tengo unos grandísimos amigos y siempre formaréis parte de esta familia madrileña que hemos creado! ¡Gracias a los dos de corazón!! Tenemos muchos viajes que recuperar a partir de ya.

A miña xente galega graciñas a todos todas , Ana , Luca , Marta ; Javi , Odilo , Iago , Paula , gracias por acollerme cada vez que volvo a terriña levome un trociño de todos vos!! Hector , Castao que dicirvos xa son moitos anos de risas ,de festas, de vida en definitiva !! Gracias por todo, por acollerme cando vin de Suiza e por darme o que buscaba una amistad como a que temos !!

A mis Macía: Abuela, Salesa, Daniel, Inés, Jaime, Olga, Delfín, Eva, Rubén, Angelines, Gabi, Vanesa, Alex, Marina, Nardo, Marinita, Adrián, Alfonso, Pili, José, David y Sara gracias por todo por inculcarme muchas cosas y por recordarme que en esta vida no hay nada más importante que la familia, ¡todo se olvida!! Bryan, Alba, Aitor, mis amigos y confidentes ¡no perdamos nunca esta relación que tenemos!

A mis Rodríguez: Olga, Chamaco, Marisol, Melín, Sami, Estiban, Ismael ¡gracias!

Grazie alla mia famiglia svizzera , a te Migu un fratello in tutti questi anni! Le nostre avventure sono sempre bellissime quasi tanto come le nostre conversazioni sul sistema!!! Grazie per essere la mia forza nel cambio!! Insieme faremo di questo mondo un posto migliore! Grazie a tutta la famiglia Rudel-Filesi, Roman, Ginevra, María Romana, Giovanna, Emanuele, Benedetta, Francesca. Grandissime persone!! Per le cene, per le pizze, per i giochi, per le ciambelle!! Tanti ricordi assieme a voi, da piccolo e adesso da grande ! Come dico io siete la mia vita in Svizzera, grazie per farmi sentire sempre a casa!! Grazie mille, Elisa per volermi così bene! Il cambio succede basta crederci!! Che presidenta si è persa l'Italia!

A mi familia, mis segundos padres, Manolo y Manuela, por educarme, quererme cuidarme y enseñarme. Parte de la persona que soy es por vosotros ¡gracias! A mis primitos, Stefano por querer imitarme siempre que has tenido la oportunidad y por tenerme en un pedestal sin merecerlo, ¡por ser el final de mis juegos de la infancia! El mejor hermanito que podía pedir. A alba mi peque, por ser una persona fantástica, ¡por tu sonrisa preciosa y contagiosa!

A mi padre Eduardo por ser mi ejemplo de vida, mi enseñante número uno, mi creador favorito de chapuzas, mi principal consejero y apoyo y ¡mi principal foco de discusiones!! Por crear mi camino y acompañarme en él, ¡Por ser mi juego favorito y llevarme al futbol, a esquiar, a escalar! ¡Gracias Papá! ¡Qué sería de Eric sin Eduardo!!

A mi madre Pilar por trasmitirme su bondad su forma de tomarse la vida con humildad y buenas maneras, por llevarme parte de tu carácter por llamarme todos los días. Por darme todo por mí, por aguantar mi mal humor con una sonrisa, ¡Porque eres una luchadora y porque nadie como tú nos enseña que mediante esfuerzo se llega a todas partes! ¡Gracias Mamá! ¡Qué sería de Eric sin Pilar!

A mi hermana Cristina, no puedo pedir mejor hermana, por aconsejarme, por guiarme en todos los aspectos, por cuidarme y protegerme, por estar siempre presente cuando lo necesito, por ser una crack como médica y como persona, sin duda por aguantar todos mis berrinches, ¡TODOS!! Por seguirme a todas partes, por ser la hermana responsable. Por todo esto muchas gracias. Gracias Dani por cuidarla y por estar a su lado ¡Gracias!

A mi compañera de vida, mi sol y mi luna a ti María te dedico estas palabras, por aguantarme en mis malos momentos, por ser la fiesta, la burla y la sonrisa en los buenos, por apoyarme cuando ni yo creía en mí mismo, ¡por tus hipérbolos hacia mis habilidades! Por las tardes en Galapagar, los viajes a Dresden, Corea, Asturias, Bruselas, ¡Por formar parte de este equipo tan genial que hemos creado, por todo lo que nos queda por vivir! ¡Gracias!

¡¡Me haría falta otra tesis para expresar todo lo que siento por los 8!! ¡¡Muchas gracias!! ¡Esta tesis es tan vuestra como mía!

A la familia de Nicolás-Morillas y en especial a José Miguel, María José e Irene por acogerme como un hijo más por vuestro inmenso buen trato y apoyo, ¡¡muchísimas gracias!!

A Maria, teacher, thank you so much for your big support during these years! And thank you so much for teaching me this beautiful language!!

A mis compañeras y compañeros de piso, María, Alba, Raúl, Rachel, David por compartir el día a día, por ser buenos amigos, ¡muchísimas gracias!

Además, quisiera agradecer este trabajo a aquellas personas que me han acompañado en mi camino y cuyas enseñanzas no puedo olvidar: A mis abuelos maternos a la enseñanza de que en esta vida hay que luchar hasta el final. ¡Nuestros recuerdos son los que nos hacen personas! GRACIAS por vuestra sonrisa y vuestro cariño. A mi hermano de montaña, mi mentor y amigo Raúl. Nunca olvidaré tu forma de vivir y de actuar con los demás, tu manera de divertirme con cada rayo de luz. Fuiste y serás un ejemplo de vida para mí. Ha sido un enorme placer caminar a tu lado y celebrar nuestros picos de las maneras en las que lo hacíamos (Picos Maciarg). ¡Lo he logrado hermano! ¡Esta ha sido una de mis cimas más duras, gracias por haberme traído hasta aquí! Esta tesis te la dedico especialmente. Te echo de menos.

Por último, agradecer también a aquellas personas con las cuales no he coincidido en muchos aspectos de la vida, ni profesional ni personal, a todo ese grupo quiero darle las gracias también, ya que me habéis indicado el camino a no seguir. ¡GRAZIE A TUTTI!

Todo lo que somos es el resultado de lo que hemos pensado

Siddharta

Publications

1. ***“Effect of the heating rate on the microstructure of a ferritic ODS steel group four (Y-Ti-Al-Zr) consolidated by Spark Plasma Sintering (SPS)”*** E.Macia, A.García-Junceda, M.Serrano, M.Hernandez-Mayoral, L.A.Diaz, M.Campos
doi.org/10.1016/j.jnucmat.2019.02.043

Part of the information compiled on this paper was reported in Chapter 4 and 5. I participate in all the experimental part as well as the writing of the paper itself.

2. ***“Effect of the mechanical alloying step on the final consolidation and microstructure of a ferritic ODS steel with (Y-Ti-Al-Zr) consolidated by Spark Plasma Sintering (SPS)”***
E.Macia, A-García-Junceda, M. Serrano, S.J. Hong, M. Campos. ***To be submitted.***

The information of this paper is reported in Chapter 4. I participate in all the experimental part as well as the writing of the paper itself.

3. ***“14Cr-ODS steel produced by SPS from mechanical milled powders with high efficiency oxide precursors incorporation”*** E. Macía, A. Meza, ME Rabanal, A. García-Junceda, M. Serrano, C. Recknagel, Gaizt.U ,T. Weißgärber , M. Campos.***To be submitted.***

The information of this paper is reported in Chapter 7. I participate in all the experimental part as well as the writing of the paper itself.

4. ***Evaluation of microstructural and oxide stability of a ferritic ODS steel group four (Y-Ti-Al-Zr) by using TEM insitu annealing.*** E. Macía, M. Hernández-Mayoral A-García-Junceda, M. Cartón, M. Campos. ***To be submitted.***

The information of this paper is reported in Chapter 6. I participate in all the experimental part as well as the writing of the paper itself.

National and International Conferences related to the doctoral thesis:

1.	Authors: (P.O) <u>Eric Macía Rodríguez</u> , Andrea García Junceda, Mónica Campos Gómez <u>Title: Efecto de la adición del Zr en los precipitados de un acero ferrítico (14Cr-3W-5Al)</u> XIV Congreso Nacional de materiales. Communication type: Oral. Gijón, Asturias (Spain), June 2016.
2.	Authors: (P.O) <u>Eric Macía Rodríguez</u> , Juan Cornide, Marta Cartón, Andrea García Junceda, Mónica Campos Gómez. <u>Title: Influence of Zr addition on the different precipitates of ODS ferritic Steel.</u> World Pm 2016. Communication type: Oral. Hamburgo (Germany), October 2016.

- Authors: (P.O) Eric Macía Rodríguez, Juan Cornide, Marta Cartón, Andrea García Junceda, Mónica Campos Gómez.
3. **Title: Effect of Zr source on oxide dispersion in ferritic ODS steel with addition of four group Elements (Y-Al-Ti-Zr-O)**
AMPT 2016. Communication type: **Oral**.
Kuala Lumpur (Malaysia), November 2016.
- Authors: (P.O) Eric Macía Rodríguez, Juan Cornide, Andrea García Junceda, Mónica Campos Gómez.
4. **Title: Estudio de la evolución microestructural de un acero ferrítico de grupo 4 (Y-Al-Ti-Zr-O) consolidado por Spark Plasma Sintering (SPS)**
VI Congreso Nacional de pulvimetalurgia 2017. Communication type: **Oral**.
Ciudad Real (Spain), June 2017.
- Authors: (P.O) Eric Macía Rodríguez, Andrea García Junceda, Marta Serrano, Mónica Campos Gómez.
5. **Title: Effect of the heating rate on the microstructural and mechanical properties of a four group element 14Cr-ODS steel (Y-Al-Ti-Zr) consolidated by SPS**
XV Congreso Nacional de materiales 2018. Communication type: **Oral**.
Salamanca (Spain), July 2018.
- Authors: (P.O) Alberto Meza, Eric Macía Rodríguez, Andrea García Junceda, M Erugenia Rabanal, Marta Serrano, Mónica Campos Gómez.
6. **Title: Grain size control by B addition on a sintered 14Cr ODS ferritic steel.**
XV Congreso Nacional de materiales 2018. Communication type: **Oral**.
Salamanca (Spain), July 2018.
- Authors: (P.O) Eric Macía Rodríguez, Alberto Meza, Andrea García Junceda, M.Eugenia Rabanal, Marta Serrano, C.Recknagel, T.Weissgarber, Mónica Campos Gómez.
7. **Title: 14Cr-ODS steel produced by SPS from mechanical milled powders with high efficiency oxide precursors incorporation**
EUROP 2018. Communication type: **Oral**.
Bilbao (Spain), October 2018.
- Authors: (P.O) Eric Macía Rodríguez, Andrea García Junceda, Marta Serrano, Luis Antonio Diaz, Mónica Campos Gómez.
8. **Title: Effect of the heating rate on the microstructural and mechanical properties of a four group element 14Cr-ODS ferritic Steel (Y-Al-Ti-Zr) consolidated by SPS**
EUROP 2018. Communication type: **Oral**.
Bilbao (Spain), October 2018.

9. Authors: (P.O) Alberto Meza, Eric Macía Rodríguez, Andrea García Junceda, ,M.Eugenia Rabana, Marta Serrano, Mónica Campos Gómez.
Title: Effects of the Boron addition on the microstructural evolution and mechanical properties of a 14Cr ODS ferritic steel. Communication type: **Oral.**
 EUROPM,
 Bilbao (Spain), October 2018.
10. Authors: (P.O) Alberto Meza, Eric Macía Rodríguez, Andrea García Junceda, M Erugenia Rabanal, Marta Serrano, Mónica Campos Gómez.
Title: Synthesis of Y-Ti-Zr-O complex system nanoparticles by an experimental method at room temperatures and its evaluation on the mechanical properties of ODS steels VI
 International conference of interphases, ICCL, Communication type: **Poster.**
 (Japan), October 2018.
11. Authors: (P.O) Alberto Meza, Eric Macía Rodríguez, Andrea García Junceda, M Erugenia Rabanal, Mónica Campos Gómez, E.Altstadt.
Title: The role of composition and microstructure on creep strength in a Ferritic ODS steel
 EUROPM 2019, Communication type: **Oral.**
 Maastricht (Netherlands), October 2019.
12. Authors: (P.O) Eric Macía Rodríguez, Alberto Meza, Andrea García Junceda, Marta Serrano, Mónica Campos Gómez.
Title: On the influence of processing conditions on the microstructure of a 14Cr ferritic ODS steel with Y-Ti-Zr-Al addition.
 Congreso Nacional de pulvimetalurgia, Communication type: **Oral.**
 Madrid (Spain), June 2019.
13. Authors: (P.O), Alberto Meza, Eric Macía Rodríguez, Andrea García Junceda, M.E. Rabanal ,Mónica Campos Gómez, E.Altstadt, P.Chekhonin.
Title: The role of composition and microstructure on creep strength in a Ferritic ODS steel
 Congreso Nacional de pulvimetalurgia, Communication type: **Oral.**
 Madrid (Spain), June 2019.
13. Authors: (P.O), Alberto Meza, Eric Macía Rodríguez, Andrea García Junceda, M.E. Rabanal, Mónica Campos Gómez, E.Altstadt, P.Chekhonin.
Title: The role of composition and microstructure on creep strength in a Ferritic ODS steel
 EUROMAT 2019, Communication type: **Oral.**
 Stockolm (Sweden), September 2019.

Authors: (P.O) Eric Macía Rodríguez, Mercedes Hernández, Alberto Meza, Andrea García Junceda, Mónica Campos Gómez.

14. Title: **In Situ Thermal Annealing Transmission Electron Microscopy (TEM) Investigation of an Oxide Dispersion Strengthened ferritic stainless steels (ODS FS)**

EUROMAT 2019, Communication type: **Oral**.

Stockolm (Sweden), September 2019.

OTHER RESEARCH MERITS

National and international collaborative conferences:

1.	<p>Authors : (P.O) Paula Alvaredo Olmos, <u>Eric Macía Rodríguez</u>, Elena Gordo Oderiz</p> <p><u>Title: Estudio de la intercara en materiales compuestos tipo cermet para el diseño de matrices metálicas alternativas</u></p> <p>V Congreso nacional de pulvimetalurgia. Communication type: Oral.</p> <p style="text-align: center;">Girona (Spain), July 2015</p> <p style="text-align: center;">ISBN:978-84-606-9427-4,pag 418-425.</p>
2.	<p>Authors : (P.O) Paula Alvaredo Olmos,<u>Eric Macía Rodríguez</u>,Elena Gordo Oderiz</p> <p><u>Title: Estudio de la intercara en materiales compuestos tipo cermet para el diseño de matrices metálicas alternativas</u></p> <p>XI Congreso nacional de materiales compuestos. Communication type: Oral.</p> <p style="text-align: center;">Móstoles (Spain), July 2015</p>
3.	<p>Authors : (P.O) Marta Carton Cordero, Monica Campos Gómez, <u>Eric Macía Rodríguez</u>, Luis Antonio Diaz, Jesus Cano, Andrea García Junceda, José Manuel Torralba Castelló.</p> <p><u>Title: Estudio microestructural de aleaciones de Co-9Al-9W producidas por SPS con Ti, Ta como aleantes.</u></p> <p>VI Congreso Nacional de pulvimetalurgia 2017. Communication type: Oral.</p> <p style="text-align: center;">Ciudad Real (Spain), June 2017.</p>
4.	<p>Authors : (P.O) Laura Cordoba, <u>Eric Macía Rodríguez</u>, Mónica Campos Gómez, Tiedo Tinga.</p> <p><u>Title: Mechanical properties of aluminum alloys produced by Metal Additive Manufacturing</u></p> <p>EUROPAM 2018, Communication type: Oral.</p> <p style="text-align: center;">Bilbao (Spain), October 2018.</p>
5.	<p>Authors: (P.O) Estela María Prieto, Jesus Gonzalez Julian, Manja Kruger, <u>Eric Macía Rodríguez</u>, Paula Alvaredo.</p> <p><u>Title: FeCrAlTiMoNi multicomponent alloys produced by SPS from gas atomization powders</u></p> <p>VII Congreso Nacional de pulvimetalurgia 2019, Communication type: Oral.</p> <p style="text-align: center;">Madrid (Spain), July 2019</p>

Contents

Abstract	1
Resumen	3
Chapter 1: Background and literature review	5
1.1. Introduction to nuclear energy demands	9
1.1.1. Effect of irradiation on the materials used in nuclear reactors	10
1.1.2. Effect of the temperature on the materials used in nuclear reactors	11
1.2. Steels for nuclear materials	14
1.2.1. Austenitic steels.....	15
1.2.2. Ferritic Martensitic steels	15
1.2.3. Oxide dispersion strengthened steels: from F/M to Ferritic ODS steels.....	16
1.3. Mechanical properties: Strengthening mechanisms	19
1.3.1. Oxide dispersion strengthened	19
1.3.2. Dislocation density strengthening	21
1.3.3. Grain size strengthening.....	21
1.3.4. Solid solution strengthening.....	22
1.4. Processing of ODS steels	23
1.4.1. Powder production: Mechanical alloying.....	23
1.4.2. Consolidation: Diffusive processes	24
1.4.3. Consolidation by FAST techniques: Spark Plasma Sintering.....	25
1.4.4. Main features of SPS on ODS steels	27
Bibliography	29
Chapter 2: Motivation and objectives	43
2.1. Motivation	45
2.2. Objectives	46
Bibliography	48
Chapter 3: Materials and experimental procedure	49
3.1. Methodology	53
3.2. Materials	54
3.2.1. Nano-oxides synthesis by co-precipitation	54
3.3. Processing of the powdered ferritic ODS steel by MA	55
3.3.1. Milling parameters optimization	55
3.4. MA powder consolidation	57
3.4.1. Field assisted hot pressing (FAHP).....	57
3.4.2. Spark Plasma Sintering (SPS)	58
3.5. Characterization of sintered samples	59
3.5.1. Density measurement	59
3.5.2. Microstructural characterization.....	59
3.6. Mechanical properties	61
3.6.1. Microhardness.....	62
3.6.2. Tensile tests	62
3.6.3. Small punch test	62
Bibliography	64

Chapter 4: Processing ODS ferritic steels: Preliminary results	67
4. Preamble to this chapter	71
4.1. Validation of MA as powder processing technique	72
4.1.1. Sinterability studies through FAHP	73
4.2. MA Optimization for Ferritic-ODS-I	76
4.3. Consolidation by SPS of Ferritic-ODS-I: Temperature effect	78
4.4. Evaluation of mechanical response	83
4.4.1. Room temperature behaviour	83
4.4.2. High temperature behaviour	83
4.5. Partial discussion of dual size evolution: M_{std} vs M_{act}	85
4.6. Partial remarks	86
Bibliography	87
Chapter 5: Processing ODS ferritic steels: Promoting bimodal grain size with Zr addition	91
5. Preamble to this chapter	95
5.1. Characterization of consolidated samples: Effect of heating rate on the microstructure	96
5.2. Nano-structured ferritic alloy microstructure: Study of the oxide dispersion	98
5.2.1. Analysis of precipitates on the ultrafine grain area.....	99
5.2.2. Analysis of precipitates on the micrometric grain.....	101
5.2.3. SPS Heating rate effect: Low HR vs high HR	102
5.2.4. Effect of Zr addition on the precipitates size distribution	104
5.3. Evaluation of the mechanical behaviour	105
5.3.1. Room temperature behaviour	105
5.3.2. High temperature behaviour by SP test	107
5.4. Partial discussion	108
5.4.1. Influence of processing conditions	108
5.4.2. Effect of Zr addition on the nature of the nano-precipitates	108
5.4.3. Effect of Zr addition on the nano-precipitates size and density.....	110
5.4.4. Strengthened mechanisms	111
5.4.5. Evaluation of the material under high temperature	113
5.5. Partial remarks	114
Bibliography	115
Chapter 6: Microstructural evaluation under high temperature conditions: In-situ TEM annealing	121
6. Preamble to this chapter	125
6.1. Introduction to in-situ TEM annealing test	126
6.2. Ultrafine grain evaluation: Tracking the nano-oxides size and location	127
6.3. Micrometric area analysis: Tracking precipitates and grain size	134
6.4. Microstructural features after the annealing	135
6.5. Partial discussion	137
6.5.1. Effect of temperature on microstructure	137
6.5.2. Effect of temperature on mechanical properties	139
6.6. Partial remarks	140
Bibliography	141
Chapter 7: Processing ODS ferritic steels: New nano-oxides precursors for 14 Cr ODS steels	145
7. Preamble to this chapter	149

7.1. Synthetized nano-precipitates	150
7.2. Characterization of F-ODS-II mechanically alloyed powders	152
7.3. F-ODS-II: Optimization of SPS consolidation	153
7.3.1. Distribution of precipitates in the F-ODS-II	156
7.4. Mechanical response on F-ODS-II materials	160
7.4.1. Room temperature behaviour	160
7.4.2. High temperature evaluation	162
7.5. Partial discussion	163
7.5.1. Influence of complex oxide addition on the composition of nano-precipitates	163
7.5.2. Heating rate effect on the final consolidation of material	164
7.5.3. Bimodal grain size microstructure	164
7.5.4. F-ODS-II mechanical behaviour: Room temperature conditions	165
7.5.5. F-ODS-II mechanical behaviour: High temperature conditions	167
7.6. Partial Remarks	167
Bibliography	169
Chapter 8: Final Remarks	173
Chapter 9: Future research lines	177

Abstract

Throughout the last decades, the population is globally growing, demanding more energy to persevere the required lifestyle. Investigations are focused on several sources of energy (renewable, thermal...), nevertheless, nuclear power plants are postulated as an important alternative due to their huge electrical productivity. Contemporary ideas lead the energetic industry to low emission highly efficient design systems. Therefore, raising the service operated temperature leads to higher energetic productions. However, safety and durability are the main conditioning and limitation factors on the development of nuclear materials. On this complex scenery, the new GEN IV reactors project has emerged.

As it is well known, regarding nuclear reactors, phenomena such as irradiation, corrosion or high temperature environments are faced. Consequently, designing the structural material has to be prioritized to ensure safe and productive power plants.

Along with, oxide dispersion strengthened (ODS) ferritic steels are one of the main candidates for nuclear cladding and tubes. During the last years, researchers were especially focused on the evolution of the alloy design. Therefore, the high potential resistance under extreme temperature and neutron exposure environments is provided by BCC crystal structure together with an explicit material composition. In this work, Cr and W allow to improve the final service temperature, thanks to their solid solution strengthening. Besides, Cr and Al are selected to improve the corrosion properties. Developing stable nano-oxides dispersed into the ferritic matrix is provided by Y_2O_3 , Ti, and Zr addition. These nano-precipitates block the movement of dislocations, improving the mechanical behaviour under high temperatures conditions.

Traditionally, Y_2O_3 was the main compound used to produce nano-oxides. However, during the last years, Ti was employed to provide a particle size refinement, developing non-stoichiometric Y-Ti-O nanoclusters whose nature and size increased the performance of the ODS alloy.

The objective of this Thesis is to develop an ODS ferritic steel alloyed with Al, whose microstructure has greater mechanical properties stability than current microstructures. To achieve this, the Zr addition has been considered as an element that would refine the dispersion and prevent the incorporation of Al into the nano-oxides.

Therefore, Zr will improve the creep behaviour thanks to the formation of high thermal stable Y-Zr-O. However, facing Al, the precipitates composition varies forming: Y-Al-O, Y-Ti-O, Y-Zr-Al-O, Y-Zr-Al-Ti-O, Y-Zr-Ti-O, W-Ti-Zr, Zr-Ti.

Trying to avoid the competition established between the different oxide formers and to control the oxides species formation, a unique nano-oxide (YTiZrO), synthesized by co-precipitation, is used.

Indeed, the processed steels developed in this Thesis are divided in F-ODS-I, in which the different oxides formers are inserted as Y_2O_3 , Zr and Ti and in F-ODS-II where the oxides formers are added as a complex nano-oxide YTiZrO.

Traditionally, ODS steels are manufactured by mechanical alloying following by hot isostatic pressing (HIP) or hot extrusion (HE) whose thermal activation could lead to a noticeable grain growth. Therefore, the use of field assisted sintering techniques (FAST), including spark plasma sintering (SPS) is postulated as an alternative on the densification of ferritic ODS steel. In this research, it has been demonstrated how the use of faster heating rate together with short sintering times, allows to achieve accurate density values without losing some microstructure features reached during the milling step.

Moreover, the nano-precipitate nature was studied by transmission electron microscopy (TEM). The nano-precipitates thermal stability was evaluated by In-situ TEM annealing. This study allows to assess the microstructure stability under high temperature conditions.

The mechanical behaviour at room temperature was analysed by microhardness and microtensile tests, comparing the response with the same material without Zr. To analyse the material response at high temperature, small punch tests were carried out. Eventually, the different strengthening mechanisms were studied through a mathematical model, to estimate a theoretical value of the Yield strength (YS).

The produced materials (F-ODS-I and F-ODS-II) presented an interesting stability at high temperature along with highlighted mechanical properties, being consequently an interesting candidate for its final application on GENIV reactors.

Resumen

El crecimiento mundial de la población durante las últimas décadas ha provocado un fuerte aumento en la demanda energética. Las energías renovables han ocupado un lugar destacado en la investigación, sin embargo, las centrales nucleares mantienen un gran protagonismo en la producción energética y se postulan como principales candidatas para sufragar la elevada demanda de electricidad. De entre los principales retos, la industria energética se mueve hacia un incremento de la eficiencia. Por ende, se pretende alcanzar una mayor temperatura de operación acrecentando la productividad eléctrica y reduciendo las emisiones. Sin embargo, seguridad y durabilidad son los principales condicionantes y limitantes en el desarrollo de materiales nucleares. Precisamente, en este escenario, surge un nuevo proyecto mundial enfocado a la nueva generación de reactores nucleares (GENIV).

Como es bien sabido, los reactores nucleares se enfrentan a fenómenos como la irradiación, la corrosión o a entornos de alta temperatura. En consecuencia, para garantizar plantas de energía seguras y productivas el diseño del material estructural debe priorizarse.

En las últimas décadas los aceros ferríticos ODS, debido a su extraordinario comportamiento a alta temperatura y bajo irradiación, han sido considerados uno de los principales candidatos para el revestimiento y los tubos nucleares. Todo ello es fruto de años de investigación en los cuales se puso especial énfasis en el diseño de la aleación. Para empezar, se desarrolló el acero con una estructura de tipo BCC para aprovechar su buen comportamiento frente a la irradiación. Por otro lado, el Cr y W fueron elegidos para incrementar la temperatura de servicio del material (endurecimiento por solución sólida). Además, el Cr y el Al fueron seleccionados para mejorar el comportamiento bajo corrosión. Por último, el comportamiento mecánico se alcanzó gracias a una distribución de óxidos de tamaño nanométrico promovido por la introducción de Zr, Y_2O_3 y Ti en la aleación. Dichos óxidos se encargan de anclar el movimiento de las dislocaciones dando lugar a un óptimo comportamiento bajo fluencia.

Tradicionalmente, la Y_2O_3 era el óxido usado para generar la distribución homogénea de los mismos. Sin embargo, durante los últimos años se han llevado a cabo distintas evoluciones con la idea de reducir su tamaño e incrementar la densidad de precipitados obtenida. En consecuencia, se añadió primero Ti, cuyo precipitado Y-Ti-O permitió incrementar la capacidad de anclaje y mejorar el comportamiento mecánico.

El objetivo de esta tesis se centra en desarrollar aceros ferríticos aleados con Al y endurecidos mediante dispersión de óxidos, cuyas microestructuras posean una mayor estabilidad en las propiedades mecánicas que las microestructuras de los aceros actuales. Para lograr esto, se ha considerado la adición de Zr como elemento que refine la dispersión y evite la incorporación del Al en los nano-óxidos.

Esto se debe a que el Zr produce óxidos del tipo Y-Zr-O cuya naturaleza proporciona una alta estabilidad a alta temperatura. Con la presencia de Aluminio la naturaleza de los distintos tipos de precipitados es muy variable formando muchas especies: Y-Al-O, Y-Ti-O, Y-Zr-Al-O, Y-Zr-Al-Ti-O, Y-Zr-Ti-O, W-Ti-Zr, Zr-Ti.

Para evitar la competitividad entre los formadores de óxidos y establecer un control en la naturaleza de los precipitados en esta tesis, se ha desarrollado un nano-óxido estable por medio de co-precipitación del compuesto Y-Ti-Zr-O.


De esta forma, se ha procesado la familia "F-ODS-I" incorporando en la molienda la Y_2O_3 , el Zr y el Ti como elementos puros formadores de óxidos y por otro lado a través del óxido complejo Y-Ti-Zr-O, (familia "F-ODS-II").

Convencionalmente, estos materiales se fabrican partiendo de molienda mecánica y consolidándolo mediante HIP o HE cuya elevada activación térmica puede dar lugar a un crecimiento excesivo del grano final. En este trabajo se hizo uso de una técnica novedosa basada en el pulso eléctrico y la presión conocida como SPS (Spark Plasma Sintering). Se ha comprobado en esta investigación como las altas velocidades de calentamiento unidas a los tiempos cortos de sinterización permite alcanzar altos grados de densificación sin perder parte de las características de la microestructura lograda durante la molienda mecánica.

La naturaleza de los precipitados se estudió mediante microscopía electrónica de transmisión TEM, incluyendo también el estudio de la estabilidad térmica realizando recocidos simultáneos a la observación con TEM, In-situ. Este estudio ha permitido corroborar la estabilidad microestructural de los aceros desarrollados.

Además, el comportamiento del material a temperatura ambiente se evaluó con ensayos de microdureza y micro-tracción, comparando la respuesta con el mismo acero ferrítico sin adición de Zr. Para analizar su comportamiento a alta temperatura se ha recurrido al ensayo Small Punch Test. Finalmente, se explican a través de un modelo matemático teórico, los distintos sistemas de endurecimiento y su aporte al límite elástico.

Los materiales desarrollados en esta tesis (F-ODS-I y F-ODS-II) presentan un gran comportamiento, así como una alta estabilidad térmica. Son por lo tanto interesantes candidatos de cara a su uso en futuros reactores de GEN IV.



1



*Background and literature
review*

Contents

1.1. Introduction to nuclear energy demands	9
1.1.1. Effect of irradiation on the materials used in nuclear reactors	10
1.1.2. Effect of the temperature on the materials used in nuclear reactors	11
1.2. Steels for nuclear materials	14
1.2.1. Austenitic steels.....	15
1.2.2. Ferritic /Martensitic steels	15
1.2.3. Oxide dispersion strengthened steels: from F/M to Ferritic ODS steels.....	16
1.3. Mechanical properties: Strengthening mechanisms	19
1.3.1. Oxide dispersion strengthened	19
1.3.2. Dislocation density strengthening.....	21
1.3.3. Grain size strengthening.....	21
1.3.4. Solid solution strengthening.....	22
1.4. Processing of ODS steels	23
1.4.1. Powder production: Mechanical alloying.....	23
1.4.2. Consolidation: Diffusive processes.....	24
1.4.3. Consolidation by FAST techniques: Spark Plasma Sintering.....	25
1.4.4. Main features of SPS on ODS steels	27
Bibliography	29

1.1. Introduction to nuclear energy demands

Nowadays, population is growing every year, demanding energy to sustain the required lifestyle. This claim has supposed one of the biggest challenges of the new era. Hence, different sources of electrical potential have been proposed (renewable or thermal energies) nevertheless, nuclear power plants are postulated as the main candidates to defray this demand due to their high efficiency and low emissions [1].

Nuclear power plants base their operation on hot steam water heated by the energy released by a fission or fusion reaction. The generated steam passes through a large turbine, whose rotation produces electricity.

Along the last century, the nuclear reactor evolution favoured a methodological classification, divided into four different groups which in turn presents other new specific ratings [2]. The first reactors used were the Gen I especially in the 50's. Gen I were the first commercial prototypes. Thereafter, the Gen II were operated in 70's. They were composed by commercial reactors, included light water reactors (LWR) which were reliable and competitive within the energetic industry. Finally, the Gen III based their development, in a clear bet on safety, by improving chiefly the efficiency of LWR reactors. Nowadays, GEN III are the reactors in service.

On this scenery, GIF project (Generation -IV forum) founded in 2001, was developed to coordinate and focus the research and development of six types of new generation reactors which can be englobed in Generation IV types: gas cooled fast reactors (GFR), lead cooled fast reactors (LFR), molten salt reactors (MSR) , super critical water cooled reactor (SCRW) , sodium cooled fast reactor (SFR), very high temperature reactor (VHTR) [3].

The founders of this macro research based their goals on four big pillars, namely: sustainability, safety and reliability, economics, proliferation resistance and physical protection [4].

Furthermore, it is necessary to consider that these fission reactors for GEN IV will demand similar operation conditions as a fusion reactor: working temperatures over 300 to 1000 °C, high neutrons carrying ≈ 200 dpa and a working lifetime of at least 60 years. Therefore, the materials development in conceptual design of GenIV fusion reactors require the same characteristic [5–8]:

- High strength at high temperature.
- Good creep properties.
- Neutron irradiation tolerance.
- Microstructural and chemical stability.
- Corrosion and oxidation resistance

Materials development is a slow procedure which starts from the experimental tests until the optimization of the productive process and finally, the granting of license for its use on nuclear field. Table 1.1 sums up some of the most important materials studied by GIF project to develop the different components of the new GEN IV reactors.

Table 1.1. Materials for new GEN IV reactors R&D stage: [a] Experimental phase [b] Optimization of productive process [c] Licensing for nuclear sector, [d] Ready [e] Industrialization phase [3,9–11].

<i>Class</i>	<i>Material</i>	<i>Concerned project</i>	<i>Main reference</i>	<i>R & D stage</i>
Advanced nickel alloys	Hastalloy XR	GTHTR300C	Asayama and Tachibana (2007)[12]	[d]
	800 H	PB-ATHR VHTR	Corwin (2008) [13]	[d]
	Inconel 617	VHTR GFR	Corwin (2009) [14]	[c]
	Haynes 230	VHTR GFR	Murty and Charit (2008) [15]	[a]
	Super alloy (IN740)	VHTR GFR	Bai et al (2011)[16]	[a]
Ceramic Materials	Ni-Cr-W	MSR VHTR		
	Ceramic Cladding	VHTR GFR	Corwin et al (2008)[13]	[c]
	SiC/SiC composites	VHTR GFR	Kohyama et al (2011) [17]	[e]
Refractory metals alloys	C/C composites	VHTR GFR	Avezedo (2011) [18]	
	ZrC	VHTR GFR		
Refractory metals alloys	Molybdenum and tungsten alloys	LFR for hydrogen production	Murty and Charit (2008) [15]	[a]
	T91	LFR SFR	Fazio et al (2011) [19]	[c]
Ferritic/Martensitic steels	9Cr1MoV	VHTR GFR	Corwin (2009)[14]	[b]
	A5533B	NGNP SCWR	Corwin et al (2009)[14]	[b]
	A508			
ODS steels	9Cr	SFR	Ukai et al (2004) [20]	[b]
	12 Cr			
	Aluminium addition	SCWR LFR	Kimura et al (2011) [21]	[a]
	Austenitic	SFR SCWR LFR	Xu et al (2011) [22]	[a]
Coated steels	High Chromium ferritic		De Carlan et al (2009) [23]	[a]
	Coated steels	LFR MSR SCWR	Kurata et al (2011) [24]	[a]

This research is especially focused on the development of aluminium containing 14 Cr ODS steels in which the next paragraphs will be gathered their attention.

1.1.1. Effect of irradiation on the materials used in nuclear reactors

Materials working on nuclear field have the mandatory feature to be resistant under irradiation conditions. Fusion reactors create energy as a result of the union between deuterium and tritium nuclei. On the other hand, fission reactors provide its energy through the fragmentation of uranium -235 nuclei into three neutrons, two nuclei lighter than U-235 and, finally, gamma rays. Consequently, the neutrons generated, independently on the type of reaction used, are absorbed by the structural material. This absorption induces atoms displacement, whose cascade effect, promotes transmutation reactions (radioactive material). This damage will determine directly the microstructural features and the mechanical properties of the selected material.

Atomic displacements induce structural defects (vacancies and interstitial together with the formation of impurities such as He or H) changing the dimensional stability of the material. The induced defects on the microstructure, such as clusters defects, dislocations loops, precipitates voids, He bubbles and so on, could compromise the dimensional stability of the material. This phenomenon is called swelling [25].

Measuring the ability of the material to resist to irradiation it is necessary to evaluate its capability to reduce the number of displacements produced by the neutrons in the microstructures. This unit is defined as dpa or number of atoms displaced. The unit dpa is a representation of the irradiation effect for a given neutron fluence. For instance, 1 dpa means that on an average, the atoms have been moved from their lattice site at least once [26]. The reactor operating temperatures is higher enough to promote diffusion and consequently recombination of the induced radiation defects. Therefore one of the strategies used for designing nuclear materials is to promote materials with self-recovery to defects [26].

Low activated materials do not become radioactive during the whole service life time or the induced radioactivity decreases to low levels after being irradiated [27]. Using low activated materials allows to develop safety and durable structural components which lower the reactors accidents risk and reduces the high level of irradiated nuclear waste, that leads directly into a reduction on the substantial costs [28].

1.1.2. Effect of the temperature on the materials used in nuclear reactors

Creep conditions are obtained when the selected service temperature is around 0.3 or 0.4 T_m (where T_m is the melting point of the material). Creep flow takes place when a structural component undergoes a slow and continuous deformation when the applied load is not enough to cause the fracture of the material (the load is constant and under the structural material YS). Creep flow induces a progressive and catastrophic loose on mechanical properties of the structural component. Normally, these phenomena are studied considering the strain evolution with the loading time (Fig 1.1).

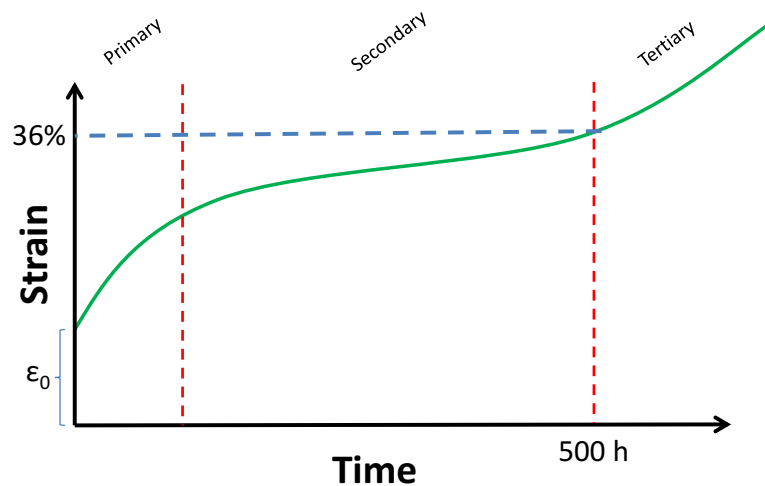


Fig 1.1. Theoretical creep behaviour for ODS steels, $\sigma=90\text{MPa}$, $900\text{ }^\circ\text{C}$ [6].

One of the most important parameters in Fig 1.1 is presented as the slope of the secondary stage ($\Delta\varepsilon/\Delta t$), the deformation rate. For long life applications, such as the one required in nuclear industry, a structural material must operate on the secondary part of the creep curve. As the slope is maintained constant, the creep rate is stable, which can ensure several operating years without components replacement [29].

During the period of time in which the material is submitted through creep conditions, defects may be located at points (vacancies), lines (dislocations) or planes (grain boundaries).

Creep mechanisms are studied by the deformation mechanisms' maps as a function of the temperature and stress, such as the one showed in Fig 1.2.

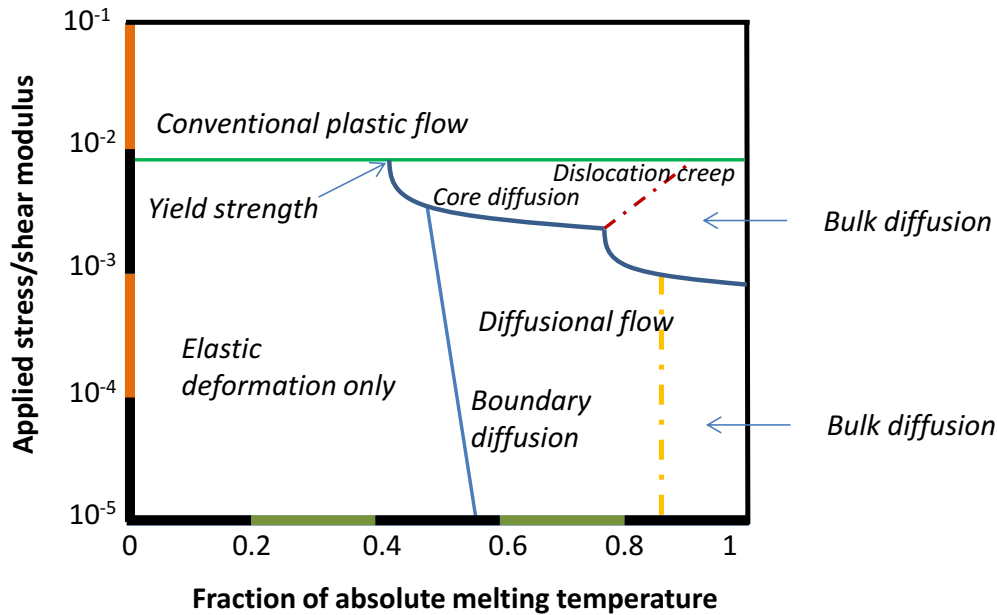


Fig 1.2. Generic deformation mechanisms map under different temperatures [30].

When a material suffers high temperature but low stresses, two main diffusive processes control the diffusion [31,32]:

- Nabarro-Herring: the diffusion of vacancies takes place through the grains [33]. It is intrinsically a very slow process but at relatively high temperatures where the diffusion is fast enough, it can produce a measurable creep rate:

$$\dot{\epsilon} = K' \frac{\sigma^n}{d^2} e^{-\left(\frac{Q}{RT}\right)} \quad (\text{eq 1.1})$$

- Coble: the diffusion of vacancies takes place along the grain boundaries. Since the activation energy for grain boundary diffusion is considerably less than that for bulk diffusion, at low T, Coble mechanism controls the creep rate [33]:

$$\dot{\epsilon} = K'' \frac{\sigma^n}{d^3} e^{-\left(\frac{Q}{RT}\right)} \quad (\text{eq 1.2})$$

In both equations (Eq 1.1 and Eq 1.2) Q represents the activation energy, K and n are constant which are independent on the applied load in which n is the Norton exponent and R is the universal constant for all gases.

Moreover, grain boundary sliding appears as a consequence of Coble mechanisms (GBS). The basic mechanism of GBS lays on the movement of dislocations through the boundary. Dislocations generate a stress concentration on the triple junction and on the grain ledge. This stress concentration is mitigated through the movement of dislocations into bordering grains or through the production of new nucleation sites [31].

For an important range of higher stress and at temperatures in excess of 0.5 T_m the strain rate is related to the stress by an equation of the form of the power law creep:

$$\dot{\epsilon} = K \sigma^n e^{-\left(\frac{Q}{RT}\right)} \quad (\text{eq 1.3})$$

Essentially it describes the deformation produced by the movement (glide) of dislocations which is limited itself by the climb of those same dislocations around enough substantial obstacles to prevent plastic flow. The obstacles are precipitates or dislocation blocks.

Creep resistant alloys should have precipitates or dispersion of coherent or incoherent particles to prevent dislocation glide. At temperatures in excess of $0.5 T_m$, the dislocations can escape from the obstacles by climbing out through a slip plane and thus continue to glide. The rate determining the step is the climb process, but strain is produced during the glide to next obstacle. The rate of creep is thus determined by the rate at which the dislocations move that also depend on the density of dislocations.

The creep rate defines the moment in which the material fails which is the main factor on creep tests. Grain size (d) is inversely proportional to creep rate (d^2 for Nabarro-Herring and d^3 for Coble theories) [34]. Increasing the grain size reduces the creep rate and, therefore, raises the transition between secondary and tertiary creep stage. Materials design, according to this specification, is crucial, highlighting the importance of controlling the grain size microstructure.

However, it was noticed that the creep rate in ODS steels is not highly influenced by grain size, which leaves on nano-particles distribution the great creep behaviour [34–36].

The creep behavior is also determined by the irradiation. This can be seen in the following example where the deformation maps of three components (AISI 316 steel) working in a sodium-cooled reactor are shown. In these maps the normalized shear stress versus temperature is represented reporting which is the deformation mechanism predominates according to the conditions in service. This map shows the deformation mechanisms that prevail in the steady state for the reactor components (Fig 1.3). It is noticeable the change in the deformation mechanism for the reactor skirt that moves from elastic deformation to diffusional flow (Nabarro-Herring creep).

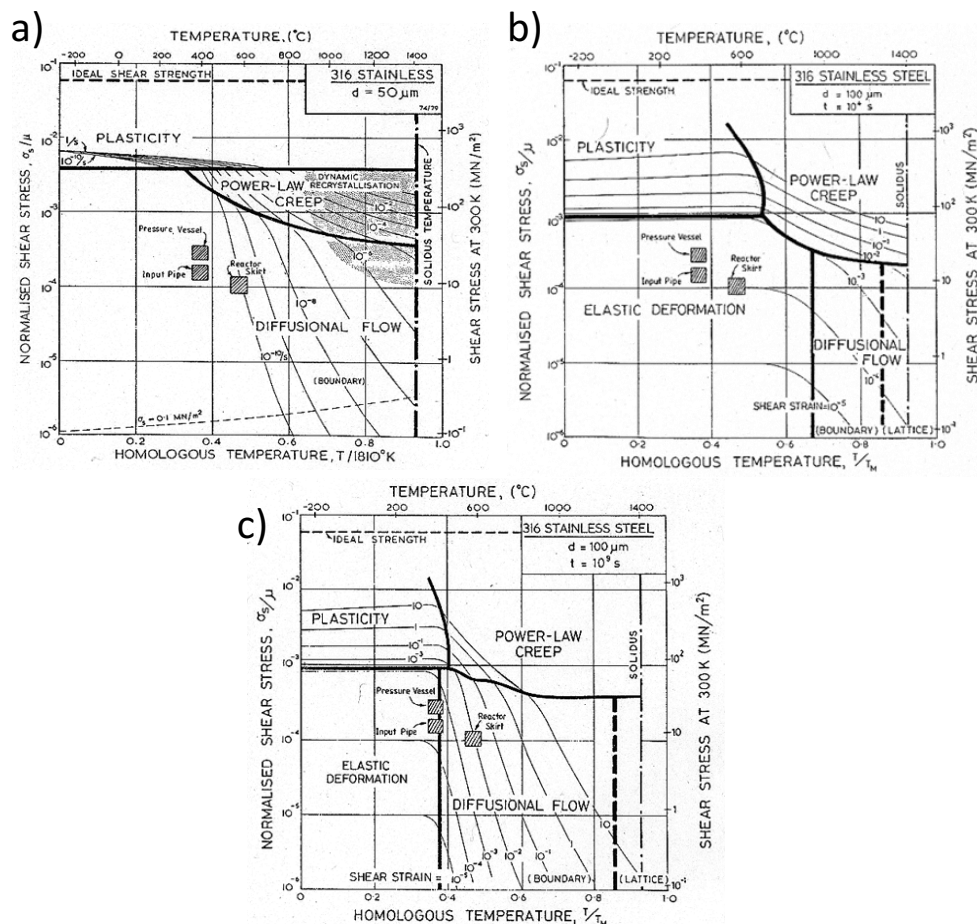


Fig 1.3. Creep maps for an AISI 316: 12Cr18Ni10Ti as exposure time to neutron irradiation evolves, a) starting point, b) after 10^3 s, c) after 10^9 s. See three components from the sodium-cooled reactor: *sodium input pipes, pressure vessel, reactor skirt*. [30].

Moreover, neutron irradiation can produce important hardening at low and intermediate temperature due to the formation of a high scale of clusters defects provided by He bubbles or dislocations loops which forms an obstacle to dislocation. Consequently, the tensile elongation and fracture toughness are quite reduced. These effects appears on a low dpa value (around 0.1) and in range of temperature of $0.35 T_m$ [26].

On intermediated temperatures many are the microstructural features which must be taken into the account. The most important radiation phenomena are: radiation induced solute degradation, void swelling, irradiation creep and anisotropic growth [26]. The first phenomenon which appears between $0.3-0.6 T_m$, could lead to localized corrosion or grain embrittlement reducing the mechanical properties. The second one, also on the same range of temperature, should lead to volumetric expansion. Finally the third one, between 0.2 and $0.6 T_m$, can produce dimensional expansion along the stress direction or in some specific crystallographic orientation.

At higher temperatures ($0.5-0.6 T_m$) the annealing promotes the recovery of most of the irradiation damage, expect for He. He embrittlement occurs when diffuses to the grain boundaries forming bubbles and decreasing the ductility of the material (provokes intergranular fracture). This circumstance should appear on He concentration around 10-100 ppm and a damage between 0.1 and 100 dpa (depending on the material, temperature and applied stress). Together with thermal creep material resistance, this phenomenon should be taken into account to establish the final service temperature attained [1,26].

Consequently, only few materials are chosen to fulfil the nuclear demand and steels are one of them.

1.2. Steels for nuclear materials

The extreme environmental conditions limit the options that can be chosen. Besides the service temperature (up to $500\text{ }^{\circ}\text{C}$), irradiation doses (up to 200 dpa) and corrosive environments, composition must be selected depending on the activation behaviour. Only few elements evolves to low activated isotopes; they can be listed as : Fe, Cr, Mn, Ta, Ti, V, W, P, C and O [37]. Accordingly, Fe based alloys with Cr, V, Ti can be considered as structural material for this application. During the last decades, three categories of steels have been specially highlighted(Fig 1.4.) [38].

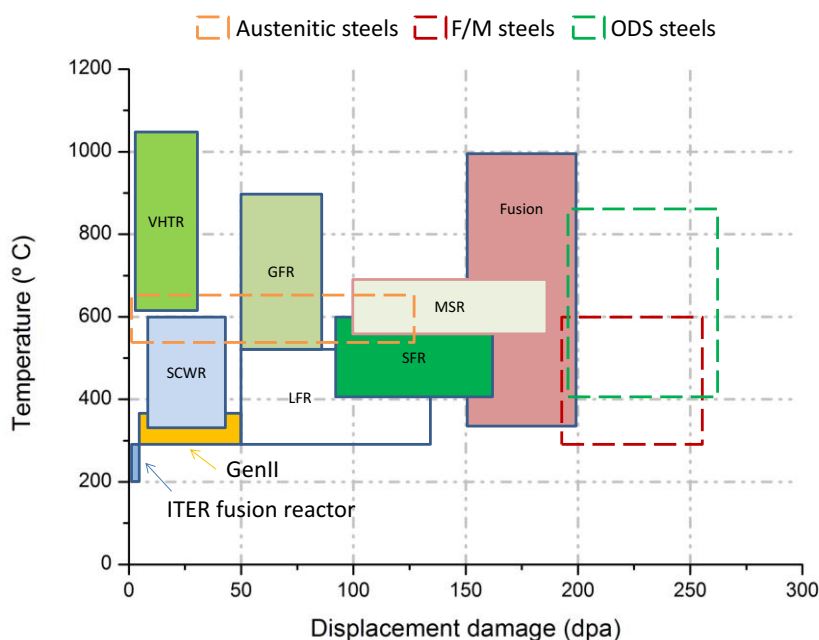


Fig 1.4. Materials requirements in the future Gen IV reactors [8,32,39].

1.2.1. Austenitic steels

Austenitic steels have been widely studied to be used as a structural material on the first wall and blanket structure on nuclear fusion reactors. Their outstanding properties under high temperature conditions make these alloys an optimum candidate to operate under extreme conditions.

However, their limited resistance under irradiation restricts their applicability on nuclear field [40]. Their main alloying elements produce long life irradiated isotopes which lead to radioactive waste, difficult to be managed. Besides, their crystal structure type FCC, leads to less stable steels under irradiation damage due to swelling effect and He embrittlement [41]. This phenomenon is explained through He and its condition of noble gas. In the FCC matrix, the solubility of He is limited. In this crystal lattice, the minimum configuration energy for the vacancies agglomeration is flat meanwhile He is spherical [25]. As a consequence, He bubbles are stored in the crystal structure promoting the structural material swelling. F. Ganer et al [42] reported this behaviour observing voids when austenitic steels were irradiated under low dosis of neutrons.

In order to improve the neutron resistance of these steels, studies are focus on the use of low activated elements such Mn to replace Ni [27] or W to replace Mo [43] or even through high dispersion of different nano-oxides [44].

1.2.2. Ferritic /Martensitic steels

Ferritic martensitic (F/M steels) steels own a distinguished interest on nuclear applications, based on their BCC crystal structure. On the contrary to FCC crystal structure, BCC materials present the advantage of having a spherical minimum energy configuration for vacancies agglomerations having consequently a special good resistance to swelling and to dimensional changes.

However, their limited operation temperatures restrict the range of use, and their applicability on new GENIV. Indeed, $M_{23}Cr_6$ precipitates loose the effect on the grain pinning as soon as the temperature is raised leading into low creep resistance [45,46]. Trying to improve their properties up to 600 °C, two methods have been widely managed: On one side, oxide dispersion strengthening was find as a solution [46–49]. On the other side, the use of complex thermomechanical treatments and new chemical compositions were investigated [50–56].

Comparing different F/M steels of the literature S. J. Zinkle et al [50] examine, the effect of different thermomechanical treatments on the final creep properties. Results are plotted on Fig 1.5.

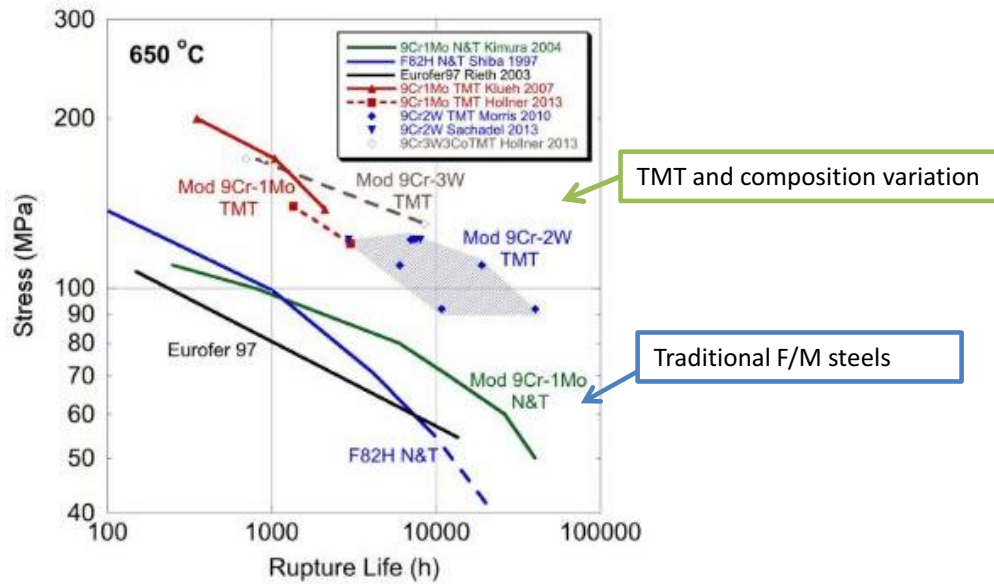


Fig 1.5. F/M creep behaviour after TMT (thermomechanical treatment and composition variations [50,57–61].

Undoubtedly, as soon as the optimized thermomechanical treatments are applied the resistance of the material to creep is extraordinarily improved.

1.2.3. Oxide dispersion strengthened steels: from F/M to Ferritic ODS steels

In nuclear application the versatility of a structural material is determined by its capability to resist high irradiation doses together with high temperature conditions resistance. In fact, during the last ten years oxide dispersion strengthened (ODS) steels have taken different path to fulfil the common goals.

Regularly, ODS steels are developed to be used as cladding, tubes and structural components in fission or fusion reactors. ODS steels base their properties on a wide dispersion of oxides (nanoxides and nanoclusters) almost homogeneously distributed along the whole material [62]. These precipitates tends to be stable under high temperature conditions (around 900 °C) and practically chemical inert, providing a high performance material for high temperature applications [63,64].

Besides, the amount of Cr sets up the maximum service temperature. Usually, steels whose Cr amount is restricted to 8-9 wt% are working under 600 °C. Moreover, higher Cr contents materials (higher than 12 wt%) usually operate on temperature around 800 °C. T. Muroga et al [56] showed how by increasing the Cr content (from 9 to 12%) it is possible to cut down the precipitated carbides which improves the creep behaviour of the material.

Ordinarily, on high Cr steels, the Cr content chosen is defined on 14 to 16%, owing to the thermal aging embrittlement. Higher than 16 %, the formation of Cr- α [65–69] due to the miscibility gap between Fe and Cr, together with the formation of σ phase because of the material aging at temperatures over 500 °C, induces embrittlement and subsequent material failure [70–72]. Nowadays Cr amounts higher than 16 wt% are rejected for nuclear applications. On the other side corrosion behaviour is also determined by Cr amount. Up to 12 wt% the material presents an extraordinary behaviour under corrosion requirements[73–76].

As ODS steels, the F/M and ferritic steels are the most important families. Even if ferritic ODS steels (with Cr content higher than 12 %) present the higher service temperature, F/M steels are providing isotropic properties and favourable fracture toughness after the corresponding TMT

[73]. S. J. Zinkle et al [50] have done a complete review comparing the most important ODS steels reporting an outstanding improvement on the creep behaviour (Fig 1.6).

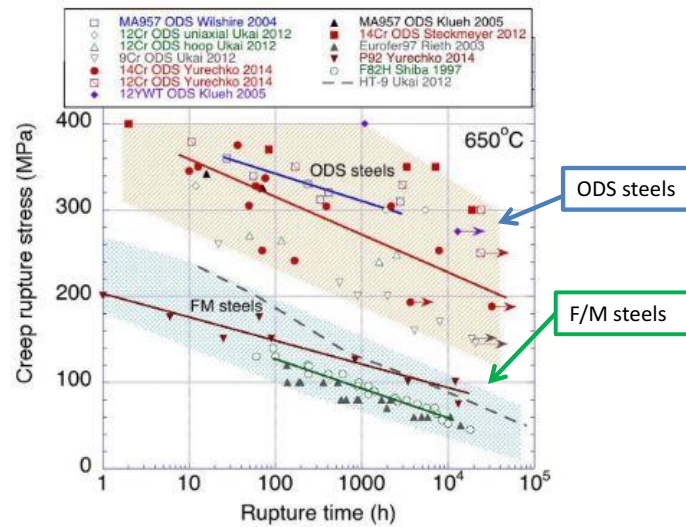


Fig 1.6. Comparison between ODS steels and F/M steels on creep behaviour [50,77–79].

Besides Cr, different alloying elements have been selected to fulfil the requirements or increase some specific properties. W additions are used to stabilize the ferritic phase and to strengthen the material by solid solution [80]. The increase of W, from 1 to 3% [55,81] increases the creep behaviour and consequently, the final service temperature [64]. Besides, W is used instead of Mo due to the provided activation properties [23,82].

Al is added seeking for an increase on corrosion resistance (Fig 1.7). After long thermal aging exposition, the Al forms a protective layer of Al₂O₃ for high temperatures and corrosive environments [83–85]. Normally, the Al content could vary from 2 to 5% as a compromise between the Al required for the corrosion protection and a reduction on tensile test and on creep properties due to formation of large Y-Al-O nano-oxides, which, as it will be, has to be avoided [21,84,86–89].

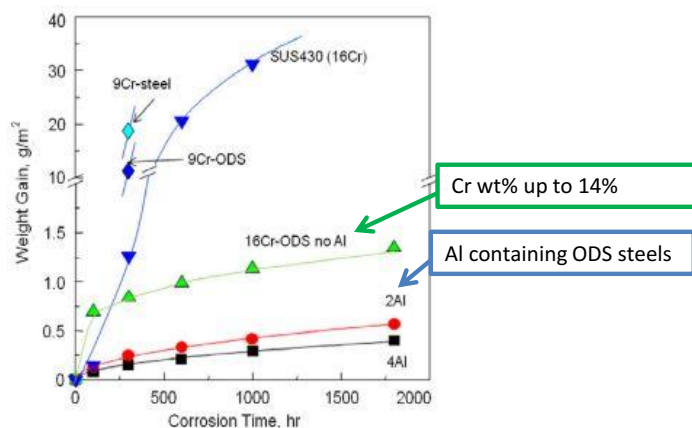


Fig 1.7. Corrosion test on ODS steels materials [21].

Besides, apart from the BCC microstructure in ODS steels the nanoclusters provides high irradiation resistance thanks to their extraordinary resistance to swelling induced by voids [76,90,91]. ODS steels present an extraordinary resistance to neutron irradiation thanks to their high point defects sink strength related to the nanoclusters and the nano-oxide dispersed (Fig 1.8). Traditionally, Y₂O₃ was added in order to favour the oxide dispersion [62]. However, Fe and Y are difficult to be mixed by traditional ways of melting. Besides, even if Y could be dissolved in the Fe matrix, Y₂O₃ would be difficult to be formed due to the presence of Cr and Al whose reactive behaviour absorb part of the oxygen offered. Consequently, an option to introduce Y into the alloy is by using mechanical alloying process of powdered materials, i.e., following a PM route for consolidation [92].

To explain how Y_2O_3 forms nano-oxides, many theories have been supposed during the last years [93]: starting with the mechanical alloying and fragmentation of oxides [94], amorphisation of Y_2O_3 and further dissolution [95] and finally fragmentation, dissociation and dissolution of the Yttria nano powder into the ferritic matrix [92].

However, the real mechanisms are still not clear and a combination of the three processes could be happening at the same time. Normally, the amount of added Y_2O_3 varies from in 0.25 to 0.35 % which is enough to promote a high dispersion of nanoparticles or even nanoclusters formations [96]. Nanocluster is the name given to nano-oxides whose stoichiometry is not well defined.

Refining the size of the different precipitates is mandatory to increase the mechanical properties. Ti was added to refine the Y_2O_3 precipitates. S. Ukai et al have been the first observing this behaviour [97–99]. Ti addition increases the driving force for nucleation of Y-Ti-O instead of Y_2O_3 leading into this refinement [100–106]. During consolidation (around 900-1000 °C), the high temperature allows the combination between Ti, Y and O reprecipitating as Y-Ti-O. Normally, Ti is added from 0.1 to 0.4 % in order to control the type of nano-precipitates formed through the atomic ratio (Y/Ti content) [107,108]. Atom probe tomography demonstrated that low atomic ratio (Y/Ti < 1) produces Y-Ti-O nanoclusters whose size is around 15 nm. Besides, bigger oxides (15-35 nm) are formed when high atomic ratio is achieved (Y/Ti \approx 1.4) such as $Y_2Ti_2O_7$ or Y_2TiO_5 [105]. Usually materials with Ti and Y_2O_3 achieve a precipitation density (N_p) of about 10^{23} oxd/m³ with mean sizes from 1-5 nm [109]. However, the addition of Al changes the results.

The problem appears in ODS alloys with Al additions. During sintering large Y-Al-O nano-oxides (>100nm) such as $Y_4Al_2O_9$ (YAM) or $YAlO_3$ (YAP) and $Y_2Al_5O_{12}$ (YAG) can be precipitated [110–113]. Although Ti would be added, its effect for promoting smaller nano-oxides (below 20 nm) disappear in Al presence [88]. The precipitation density (N_p) is reduced to 10^{20} - 10^{21} oxd/m³ and the precipitates mean size could vary from 10-30 nm [109,114,115]. In this case, the strength of Al containing ODS alloys can be clearly reduced, including a worst behaviour under high temperature conditions. This behaviour is induced as a consequence of the less thermal stability provided by Y-Al-O which is going to lose its stability as soon as the temperature is increased, losing its capability to strengthen the material [116].

In Al containing ODS steels, elements such as Hf or Zr are selected to increase the creep behaviour, by reducing and increasing the size and number density of oxides respectively in Al containing ODS steels. Usually the amount of Zr introduced could vary from 0.3 to 0.6 wt% in Al ODS steels [21,117–120] to even 1.5 wt% in those steels without Al [121,122]. This phenomenon is specially related to the bonding energy of Zr-Y-O which can be assumed to be far superior to that of Y-Al-O when those compounds are formed in an Fe matrix. That means that initially, Y-Zr-O should form more easily than Y-Al-O or Y-Ti-O [119]. Moreover, the presence of Zr could lead to a refinement of the nano-oxides when Al is present, which leads to an increase in the high temperature behaviour, while the corrosion resistance is not modified. Besides, of the newly promoted oxides have superior thermal stability and irradiation tolerance [117][123–125]. In Al containing ODS steels, Zr addition promotes precipitates with mean size around 4 to 10 nm and a precipitation density (N_p) of 10^{22} to 10^{23} oxd/m³ [118,123,126].

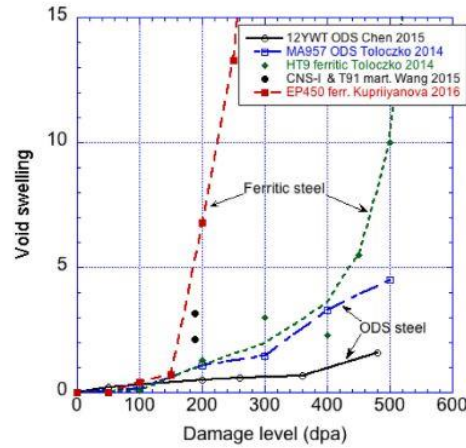


Fig 1.8. Void swelling on ODS steels [50].

1.3. Mechanical properties: Strengthening mechanisms

1.3.1. Oxide dispersion strengthened

The main objective of dispersing particles on the ferritic matrix or ferritic/martensitic steel, is to produce an obstacle to dislocation movement (Fig 1.9.).

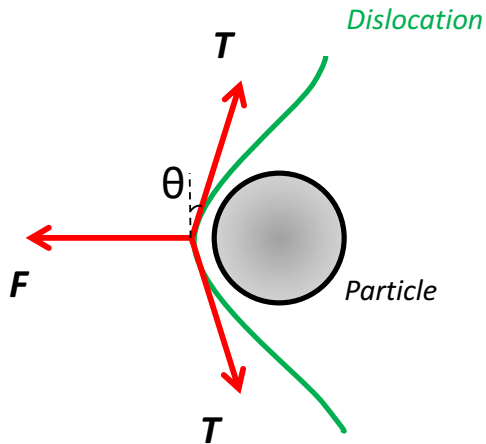


Fig 1.9. Balance of forces during the interaction between particles and dislocations [127].

Dislocations, during the material deformation or warming, try to move when they interact with an oxide. T. Gladman [127] defines the forces balance between the line tension of dislocation (T) and the resistance force of the precipitate particle (F) as:

$$F = 2T \sin \theta \quad (\text{eq 1.4})$$

F increases when θ rises, conducting on an increase of the bow of the dislocation. It is supposed that the maximum force (F_{\max}) achieves a plateau when θ is equal to 90° which means that $\sin \theta$ is equal to 1 [127]. The particles hardness determines directly the way in which the particle interacts with the dislocation. When F

is higher than $2T$ (Orowan theory) the interparticle spacing determines the strengthening of the material, and the dislocation bows around the particle to continue with its movement. If the maximum resistance is attained before $\sin \theta$ is equal to 1, the particle is sliced and the dislocation passes through the particle.

Consequently, dislocations should bow around the particles or cut the particles given as a result two types of shear stress (τ_c and τ_B). The final contribution in yield strength depends on the slip mechanisms dominant in each moment. Besides, the provided final strength depends basically on: size, shape and volumetric particle fraction and the nature of the boundary between matrix and particles [128].

The nature of the interphase boundary depends on many factors: size and the used method to introduce the different particles are some of them. Usually particles that come from supersaturated solid solutions present coherency with the matrix. On other side particles introduced by powder metallurgy (mechanical alloying) techniques follow incoherent pattern. Coherency between particles and matrix has a direct effect on the strengthening. On coherent particles, distortion can appear on the interphase boundary, given as a result a coherency strain (Fig 1.10.). Namely misfit, it produces a relative strain (Eq 1.5) [129].

$$\varepsilon = \frac{a_\alpha - a_\beta}{a_\alpha} \quad (\text{eq 1.5})$$

The lattice distortion produced by particles has the same effect on dislocations as the one presented by an element in solid solution. Smaller particles inserted in the lattice matrix produce tensile stresses meanwhile larger particles cause compression stresses. Consequently, depending on the sign of the dislocations, there will be an attraction or repulsion. When coherent particles are faced usually ε is around 1, particles are semi coherent when ε is lower than 25, and finally particles are incoherent when it achieves values higher than 50 is.

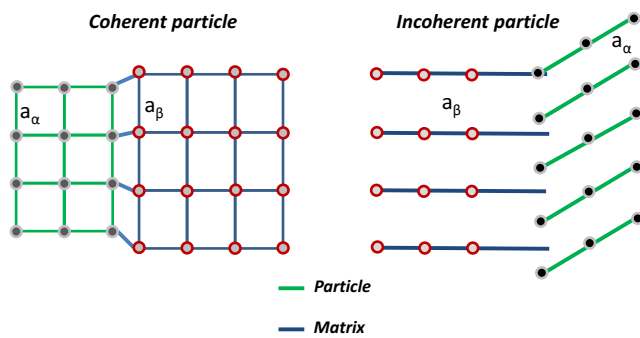


Fig 1.10. Coherency of particles [129].

through or cut by the dislocation. Whereas, dislocations bow when incoherent or larger particles are faced [129].

Usually, when dislocations interact with particles, different hardening systems are sharing. Selecting the transition between the moment when the particle strengthens the material by cutting shear stress or true bow shear stress, determines when the particle contributes with the maximum strengthening. Fig 1.11 shows clearly how particles volume fraction (f), particles size and hardness are determining this parameter[129].

If the hardness of particles is fixed, the critical radius is determined by r_2 . This represents the maximum size available to strengthen the material by using the maximum force. Increasing the hardness of particles has a strong influence on the cutting shear stress; reducing the size for which the maximum strengthening is attained (r_1). Hardness do not determine the bow shear stress since this parameter is only influenced by the distance between particles. Finally, if the volume fraction is changed (increasing it) the final radius obtained increases too (r_3).

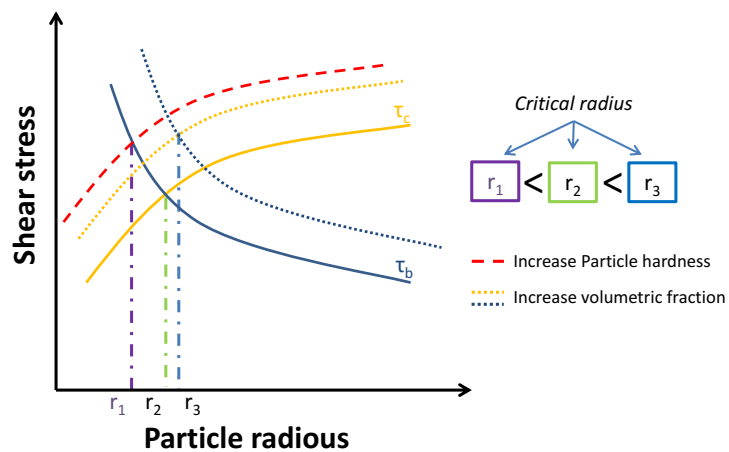


Fig 1.11. Interaction between particle and dislocation depending on volume fraction , hardness and particle size [129].

However, Fig 1.11 represents the critical radius for a constant temperature. Changing temperature could vary the results expressed. Temperature should change the way in which the precipitate modified the yield strength. Consequently, the nature of the particle is also important. The final composition attained should determine the stability of the particles when temperature changes. Coherent particles used to be more stable than incoherent particles when temperature is faced since the interphase energy is lowered respect the incoherent ones. The coherency is size dependant, consequently small size coherent oxides will be stable at high temperature (explaining the reason for selecting Zr in this research). Particles coarsening have to be avoided to keep the strengthening mechanisms mentioned before.

The oxide contribution can be estimated by the Orowan bypassing mechanism when non coherent oxides are made up or strong obstacles are dispersed. This theory supposed that the

Coherency is lost when the particles attained some specific critical size. Therefore, a disordered (incoherent boundary) interface is produced. Especially on ODS materials intermediates boundary should also be located, receiving the name of semicoherent particles.

Furthermore, coherent boundaries and small particle tends generally to be passed

oxides particles are impenetrable. Besides, Ashby took into the account the interparticle spacing [127]. As a consequence, the contribution of particles to the strengthened material (σ_p) is expressed by the Ashby-Orowan equation (1.6) [130]:

$$\sigma_p = \frac{0.8MGb}{2\pi L\sqrt{1-\nu}} \ln\left(\frac{x}{2b}\right) \quad (\text{eq 1.6})$$

where M is the Taylor factor, G is the shear modulus of iron, b is the burger vector and ν is the Poisson's ratio, L is the average inter-particle spacing that can be calculated by

$$L = \sqrt{\frac{2}{3} \left(\sqrt{\frac{\pi}{4f}} - 1 \right)} \cdot d_p \quad (\text{eq 1.7})$$

And f is the volume fraction of precipitates; x is the average diameter of oxides particles on the slip planes and d_p is the average diameter of oxides particles that is calculated as:

$$x = \sqrt{\frac{2}{3}} d_p \quad (\text{eq 1.8})$$

However, this model does not take into account the coherency of the particle with matrix. For this reason, nowadays, there are other expressions for (σ_p) considering this feature:

$$\sigma_p = \alpha_p M G b \sqrt{N_p d_p} \quad (\text{eq 1.9})$$

Where α_p is the obstacle strength for oxide nanoparticles which could vary from 0.1 to 0.5 (depending on the particle type and the degree of coherency) and N_p is the density of the nano-oxides in the material [131].

1.3.2. Dislocation density strengthening

Mechanical alloying is the most common method to disperse oxides and alloy steels as it was described in the previous paragraphs. As a result, as soon as the milling time is increased, the powder suffers deformation and consequently the dislocation density increases. After consolidation, part of this deformation is maintained on the material contributing to the final hardening of the material. The dislocation density contributes to the strengthening of the material through the such as called work hardening system [129]. The following equation defines this phenomenon:

$$\sigma_{\text{disl}} = \alpha_d M G b \sqrt{\rho_{\text{dis}}} \quad (\text{eq 1.10})$$

Where M is the Taylor factor, α_d is a constant which represents an obstacle strenght to dislocations by dislocations and ρ_{dis} is the dislocation density [132,133].

1.3.3. Grain size strengthening

Grain size and consequently grain boundaries, also promote obstacles to dislocations movement (Hall-Pecht effect). The grain boundary impede the movement of dislocation through the entire slip plane and, therefore, strengthens the material [129]. Equation 1.11 reported this strengthening mechanism:

$$\sigma_{\text{gb}} = f_{\text{area}} \cdot \left(\frac{1}{5} G \sqrt{\frac{b}{d_g}}\right) \quad (\text{eq 1.11})$$

Where f_{area} is the area fraction fulfil by the different grain size attained (ultrafine and micrometric regions for ODS steels) [131].

In particular, oxides dispersion has also a strong influence on the grain growth. The pressure that drives the grain dimensional change can be overcome by the particle pinning force at the

grain boundary. Zener was the first to express this behaviour on particles reinforced materials. Consequently, defines a critical particle radius which marks the maximum grain size (R_c) attained by an equiaxial grain when a particles distribution (with some specific volume fraction, f) are dispersed. Equation 1.12 defines this behaviour [127]:

$$R_c = \frac{4r_p}{3f_p} \quad (\text{eq 1.12})$$

Where r_p is radius of the particle and f_p is the volume fraction.

Thus, smaller particles and higher volume fraction reduce the grain growth directly. This equation explains why recent ODS strategies are dealing with refinement of nano sized oxides through the addition of other oxide formers such as Zr, Hf or Ti [21,97–99,117–120]. During the ODS steels consolidation, the high temperature of the consolidation process causes the primary recrystallization of the steel, but also the nano sized oxides will precipitate between 600 and 900 °C. Therefore, even the evolution of recrystallization and grain size growth will depend on that precipitates formation [134–136]. Since normally ODS ferritic steels are working under high temperature conditions, the commitment between smaller submicron and micro grain size has to be achieved.

Choosing new consolidation methods, such as FAST techniques, can regulate and control the grain growth [137–141].

1.3.4. Solid solution strengthening

When solid solution strengthening is considered, W and Cr are the most important elements that meet that demands. Basically, if an element is in solid solution, it produces a lattice distortion which interacts directly with dislocations. For this reason, the material strengthening is increased. Usually this contribution is estimated by the next equation [131]:

$$\sigma_{ss} = 0.0069KX^n \quad (\text{eq 1.13})$$

Where X is the equilibrium concentration of substitutional elements in atomic percentage and n is a constant; K is a value which determines directly the strengthening promoted. This parameter change from one element to the other as it is reported in Table 1.2 [131].

Table 1.2 Strengthening from substitutional alloying elements dissolved in the matrix [131].

Element	K
Cr	1400
W	11000
Si	11000
Mn	7000
Ni	6100

Using different elements modify the input to the final strengthening. Normally the contribution provided by minor alloying elements such as Y, Zr or Ti should be considered negligible due to the low content.

1.4. Processing of ODS steels

1.4.1. Powder production: Mechanical alloying

J.S. Benjamin et al [142] were the first authors on using the mechanical alloying (MA) as a method to obtain oxide dispersion strengthened materials on Ni superalloys. Their main motivation was to increase the service temperature range.

This technique induces kinetic energy in the balls inside the mill, whose impact with powder and vessel, promotes fine alloyed powders. Generally, three steps are followed: deformation, fracture and welding [143]. When the equilibrium between deformation, welding and fracture is attained, a stationary state is reached, representing the final milling step. Besides a narrow particle size distribution is accomplished [144].

The main objective of using MA to process ODS powders is to disperse the oxides formers (Y_2O_3 , Ti, Zr) and to produce nanostructured materials. During MA, the high number of energetic collisions promote a highly deformed powder whose effect during consolidation is determining directly the final microstructure [145].

Additionally different parameters could affect the achieved microstructure after consolidation: first of all the energy milling [146]. This parameter is controlled through the potential and kinetic energy induced through the rotation speed of the mill (rpm). Moreover, the ball to powder ratio determines the time and the attained dislocation density. More than the energy, the type of used mill influences itself, the milling process.

Milled powders heavily deformed can be monitored by X-ray diffraction. The most important feature to describe permanent deformed materials are the mean size of coherency diffracting domains (crystallite size) and the microstrain level within these domains as an indication of the reticular changes of the structure. Both parameters are determined by the plastic deformation fracture and welding of MA and by the incorporation of alloying elements (in this thesis Y_2O_3 , Ti, Zr).

The formation of the nano grain size passes through three basic stages [148]: During the first stage of MA, deformation is localized in shear bands where high dislocation densities can be located. The crystal size during this step is reduced until it achieves a critical value. When deformation continues, the annihilation and recombination of dislocations will form small grain boundaries composed by low angle misorientations (around 20-30 nm). In the end, the orientation of the new developed subgrains becomes totally random [149].

Therefore, the formation of the nanostructure is related to crystallite size and microstrain value. During MA these two parameters tend to follow the behaviour explained in Fig 1.12. During the first stage of MA, the powder impact between balls, grinding media and powders increases the dislocation density inside the grains.

Microstrain tends to increase rapidly during the first stage of MA, following high slopes respect the time, leading on a reduction of crystallite size with a similar trend (with a different sign). If the milling time increases (second stage) both microstrain and crystallite size start to be stabilised, increasing and decreasing smoothly as soon as the time rises. Finally, crystallite size

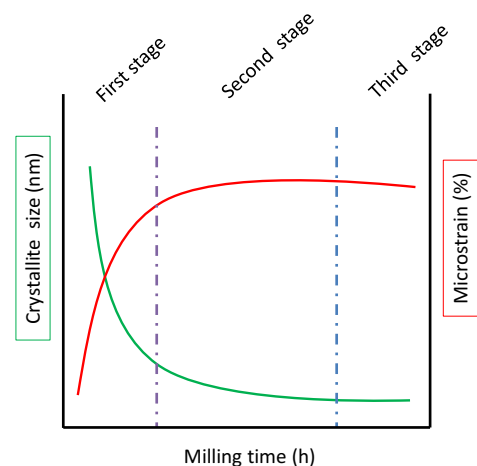


Fig 1.12. Theoretical evolution of crystallite size and microstrain during the MA process [32,147].

achieved a plateau and microstrain could decrease as dislocation recombined (the third stage) (Fig 1.12).

1.4.2. Consolidation: Diffusive processes

Typically, the most common compositions of ferritic ODS steels with Ti and Y_2O_3 additions are produced by hot extrusion (HE) or hot isostatic pressing (HIP) [150,151]. Depending on the processing route, the difference of the stored energy will affect the final grain size distribution. Moreover, high temperatures and/or high activation energies determine the final grain size. For this reason, one of the main objectives on this thesis is based on reducing the grain growth by low activated sintering technology.

When a material is submitted to high temperature (such as the one necessary to consolidate the final components) most of the stored energy expended in plastic deformation is released. Hence, to describe the final microstructure it is necessary to take into the account three steps [152]: Recovery, recrystallization, grain growth.

During the recovery step, the material produces a rearrangement of dislocations, forming subgrains with smaller misorientation (low angle boundaries). In this step no change on orientation or grain shape is produced.

During the recrystallization, high deformed grains are substituted by new ones with much lower dislocation densities. Precisely, it is this reduction in energy which drives the recrystallization process. Recrystallization temperature is influenced by purity, the amount of cold work, prior grain size and size of precipitates. Solid solution elements, such as Cr or W in ODS steels, can raise the temperature in which the material recrystallizes.

Grain growing starts when the material is fully recrystallized. The free Gibb's energy reduction produced as a consequence of the reduction of the total amount of grain frontiers, leads into this rise in the grain size. The extensive growing of some grains at expenses of others, known as abnormal grain growing (typics in ODS steels), is directly affected by the pinning produce by the nano-particles dispersed into the matrix and by the uneven plastic deformation stored in the different particles. Abnormal grain growth induces a clearly bimodal grain size distribution, with ultrafine grain size and micro grain size. This features provide the material with a good behaviour at room and at high temperature [153].

On ODS steels many are the factor that should influence the recrystallization process. First, the powders coming from mechanical alloying, lead into lower recrystallization temperature, due to the high level of plastic deformation. Besides, it increases the nucleation rate and the growing of new grains. Furthermore, the grain size before cold working affects the number of sites for nucleation, consequently the finer grains are (such the one obtained in MA) the lower recrystallization temperature will be achieved.

N. Sallez et al [134] have a completed study of the effect of the temperature on MA ODS steel powders obtained, sum up in Fig 1.13.

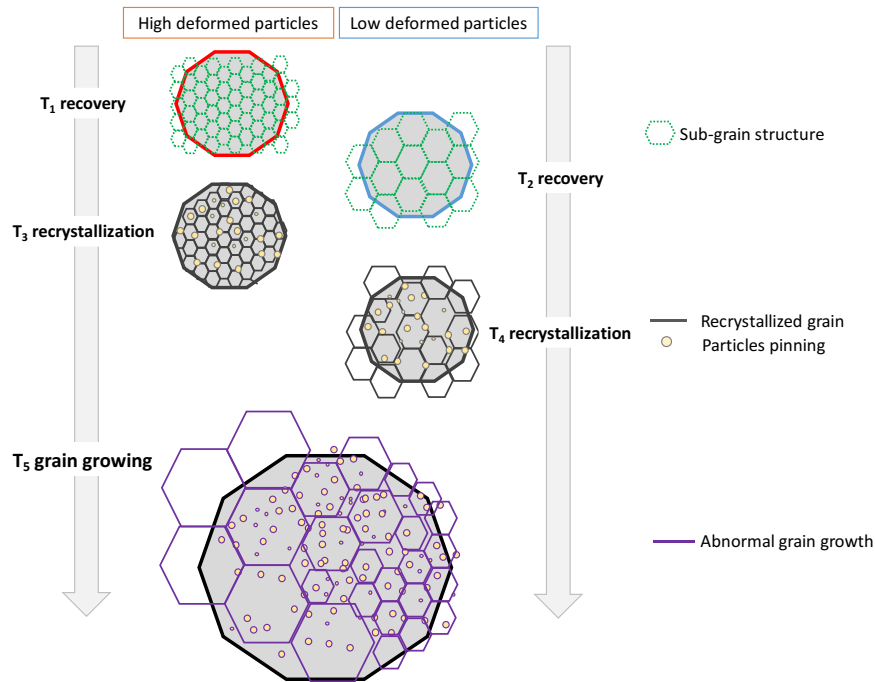


Fig 1.13. Recovery, recrystallization and grain growth on ODS steel.

Consequently, the driving pressure for recrystallization is still higher enough.

At higher consolidation temperature, such (850-900 °C) crystallite size grows rapidly leading into a steady reduction of the dislocation density. From 800 to 1100 °C, the microstructure is no longer stopped on the recovery. Dislocation density accomplishes a maximum meanwhile the crystallite size increases continuously. Recrystallization occurs in ODS steels around 800 °C and heterogeneous grain growth appears around 900 °C. This is the moment in which ultrafine grain size appears whose regions are not affected by the abnormal grain growing [134]. This abnormal growing appears in the micrometric regions whose behaviour is controlled by the heterogeneous energy and the pinning pressure exerted by particles [135,136,139,154,155].

Time is also a parameter which is determining the grain growth. The diffusion processes are directly related to the time. Therefore, as an alternative to consolidate the ferritic ODS steel, the use of field assisted sintering techniques (FAST), including Spark plasma sintering (SPS), have been also considered where the powder placed in a graphite die is simultaneously uniaxially pressed and heated by the Joule effect provided by pulses of high intensity current [141,156,157]. The fast generation of internal heat increases the sintering kinetics giving a minimal grain growth and a rapid densification if a proper final temperature is selected.

1.4.3. Consolidation by FAST techniques: Spark Plasma Sintering

To overcome the grain growth problem and giving a shorter alternative processing route, unconventional sintering and densification techniques have been proposed. FAST techniques (field assisted sintering technology) englobe those consolidations that simultaneously applied pressure and temperature heating the component based on the Joule effect.

During the last decade, spark plasma sintering (SPS) is a method widely used to consolidate metallic and ceramics powders. Its main operation is based on hot pressing, where the powder is placed in a die (normally graphite die) and uniaxially pressed meanwhile the powder is heated. The biggest difference between both methods relies on the electrical field used to rise the temperature inside the die, which represent the main advantage and characteristic of this new method.

During the first stage of consolidation, around 600 °C ferritic ODS steels undergo a homogeneous recovery without having a strong effect on the final grain growth. Besides, the energy accumulated during the mechanical alloying start to be released, producing a small reduction of the dislocation density stored during MA.

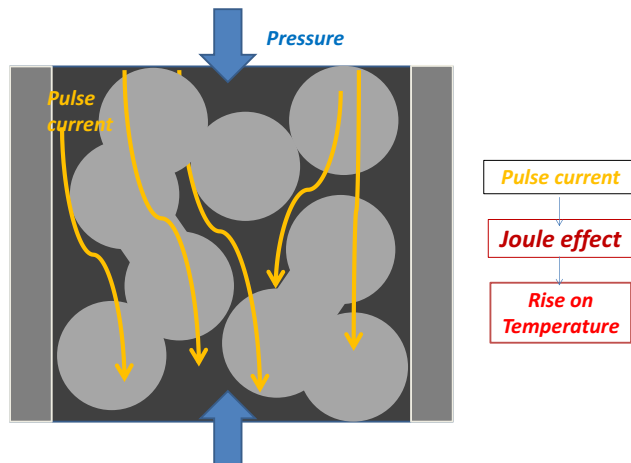


Fig 1.14. Scheme of Spark plasma sintering consolidation.

Depending on the current type inserted, FAST can be classified as stated in the literature [158]: Direct current (DC), alternative current (AC), pulse current, single pulse. Spark plasma sintering is a technique englobed on pulse DC current techniques. Besides, depending on the type and model the SPS can handle with frequencies of 10^2 - 10^8 Hz, voltage of 1-50V and current densities under 1 kA/cm^2 .

In general, four parameters are normally defining the final densification of the sample processed by SPS: The maximum

temperature, the achieved the pressure, the electrical current used and the initial properties of the material.

During the last decades, besides producing the Joule effect, one of the most interesting discussions about SPS deals with the effect that the currents has on the sample. In fact, the role played by the different currents (ac and dc) are still not clear. Many physical phenomena could appear because of the current (electro-migration, electromagnetic effect, electroplasticity...), nevertheless, the common goal is to simplify the system and explain one single mechanism that lead the sample to a final densification: the Joule effect. U. Unselmi-Tamburini et al reported these phenomena on many of their researches [158–161]. First, it is necessary to understand that most of the current used in the process does not pass through the sample since the die is extremely better conductor than the sample itself. Consequently most of the current flows through the die [158,162]. Metallic powders, usually present high resistivity to current, especially on the first stage of densification.

Some theories states about the macroscopic inhomogeneity produced in SPS such as hot spots (due to the percolation path). Those located hot points on the contact between particles could be overestimated since the highest amount of the current will pass through the die [158,159].

Besides, many are the theories that suppose that SPS bases are established on the sintering through a spark and plasma generated due to the used pulsed current, that causes to the Joule effect producing a local melting on the particles surface. This phenomenon joined to the surface cleaning role of the plasma leads to the successful sintering of the metal/ceramic powder [163]. However as it is stated before, there is no a clear theory which can probe this phenomenon and it could be unlikely [164].

Based on Joule effect, the heat generated inside the matrix is dependent on the resistance provided by the material. The equilibrium has to be achieved between the intensity and the material conductivity. Simplifying the system taking into the account only the Joule effect, the temperature between two particles is stated as [165]:

$$\dot{Q} = R \cdot I^2 \quad (\text{eq 1.14})$$

Where \dot{Q} is the released heating as a function of time, R is the resistance promoted by the particle and finally I is the intensity of current introduce in the equipment. Consequently, temperature and time are not independent parameters since the thermal effect promoted by current is highly influenced by the type or the pulse [161], or intensity inserted in the equipment [159].

Another important aspect that must be taken into the account is the temperature distributions. In SPS process, measuring the real temperature of the powder inside the die is always difficult.

Temperature differences inside the matrix can be obtained dependently on the SPS used [166,167]. This factor is quite important when it is necessary to deal with scaling samples. An homogenous temperature distribution will condition the homogeneity of the samples and the final microstructure and mechanical properties reproducibility [162]. Usually it is normal to detect hot spots in the middle of the sample. Besides, both thermal and electrical properties changes with temperature and densification, making difficult to control this kind of in-homogeneities. The nature of the material and consequently their conductivity will determine directly the temperature distribution. Regularly, on conductive samples the maximum temperature is attained in the centre of the sample, meanwhile in non-conductive samples as the current flow through the die, the highest temperatures are detected on the edges of the specimen. These phenomena, nevertheless, are normally related to the dimension of the sample, being negligible for these samples whose diameter varies from (10-15mm), such as the one presented in this work [158].

During the consolidation of SPS, the achieved temperature is far from the liquid phase, consequently, SPS involves only phenomena related to solid solution sintering. The current has a strong influence on the mass transport as it was reported by Z. A. Munir et al [159,168]. During the heating rate the thermal activated powders promote the formation of necks around particles. X.Song et al [163] reported how in conductive powders such as Cu, inhomogeneous distribution in temperature increases in those regions in which the particles are in contact. The temperature on the surface may achieve the boiling temperature of the powder, leading into the formation of necking networks. The neck growth will be determined by the local current distribution, which depends on the cross section area of the particle contacting part and the electrical resistivity which increase as soon as the temperature rises. S. Diouf et al [169] reported also how a reduction in particle size could increase the mass transport phenomena.

The applied pressure plays a secondary role on the final densification and its effect depends directly on the particles size to be consolidated. Smaller particle size does not seem to be affected by pressure meanwhile larger particles do [159]. The moment in which the pressure is applied could also have some effect over the final densification [169]. Commonly, on ODS steels a lower pressure is applied to rearrange particles (around 5 MPa) and to ensure the contact between particles at lower temperatures, applying the maximum pressure up to 600 °C.

Moreover, one of the most important characteristic of SPS relies on the high heating rates promoted. In fact, using FAST techniques, consolidation takes place in a matter of minutes meanwhile HP (Hot Pressing) could take few hours. This is possible thanks to the fast heating rate which allows, in some equipment, to achieve 1000 °C/min [36,159,164,170]. The studies about heating rate are quite limited [171], being one important parameter taken into the account on this research.

1.4.4. Main features of SPS on ODS steels

The influence of different parameters such as pressure, holding time, final temperature and heating rate used, promote a long series of works in ODS steels. Some authors such as X. Boulnat et al [138–141] have performed long studies about the influence of the different parameters on the final consolidation of the material. These contribution have shown how under low temperature, the pressure is used only to rearrange the particles inside the matrix. Normally, pressure between 50 and 80 MPa are used to consolidate ODS steels, even if the best values of densities are achieved when the maximum pressure achieved is around 70 MPa [172–174]. Under this pressure authors have checked that a plateau in density is achieved around 96%, independently on the temperature used.

The temperature was varied by different author from 850 to 1200 °C and it is clear that the temperature required to consolidate ODS steels is between 1100 and 1200 °C, especially in powders that are mechanical alloyed [157,172,175–180]. Temperature plays an important role

in the diffusion process, consequently if the powder is not activated adequately the final consolidation is not achieved [138,156,157].

The holding time does not seem to have a clear effect on the final consolidation of the material since normally it is maintained between few seconds to higher minutes [138,181].

The heating rate effect on the final densification of the material has not been completely studied. An increase of the heating rate can change the electrical current that passes through the sample, leading into a higher densification. Heating rates between 100 to 500 °C/min has been typically explored [140,182–184].

Bibliography

- [1] S.J. Zinkle, J.T. Busby, Structural materials for fission & fusion energy, *Mater. Today*. 12 (2009) 12–19. doi:10.1016/S1369-7021(09)70294-9.
- [2] J.G. Marques, Evolution of nuclear fission reactors: Third generation and beyond, *Energy Convers. Manag.* 51 (2010) 1774–1780. doi:10.1016/j.enconman.2009.12.043.
- [3] G. Locatelli, M. Mancini, N. Todeschini, Generation IV nuclear reactors: Current status and future prospects, *Energy Policy*. 61 (2013) 1503–1520. doi:10.1016/j.enpol.2013.06.101.
- [4] J.E. Kelly, Generation IV International Forum: A decade of progress through international cooperation, *Prog. Nucl. Energy*. 77 (2014) 240–245. doi:10.1016/j.pnucene.2014.02.010.
- [5] B. Corwin, J. Nichols, R. Stoller, S. Zinkle, Workshop on Advanced Computational Materials Science: Application to Fusion and Generation IV Fission Reactors, (2004). internal-pdf://2004_corwin_compmatsci-fusion-fission-3714483968/2004_Corwin_CompMatSci-Fusion-Fission.pdf.
- [6] D.K. Mukhopadhyay, F.H. Froes, D.S. Gelles, Development of oxide dispersion strengthened ferritic steels for fusion, *J. Nucl. Mater.* 258–263 (1998) 1209–1215. doi:10.1016/S0022-3115(98)00188-3.
- [7] D.L. Smith, M.C. Billone, S. Majumdar, R.F. Mattas, D.K. Sze, Materials integration issues for high performance fusion power systems, *J. Nucl. Mater.* 258–263 (1998) 65–73. doi:10.1016/S0022-3115(98)00355-9.
- [8] A.A.F. Tavassoli, Present limits and improvements of structural materials for fusion reactors - A review, *J. Nucl. Mater.* 302 (2002) 73–88. doi:10.1016/S0022-3115(02)00794-8.
- [9] E.E. Bloom, The challenge of developing structural materials for fusion power systems, *J. Nucl. Mater.* 258–263 (1998) 7–17. doi:10.1016/S0022-3115(98)00352-3.
- [10] S.J. Zinkle, Advanced materials for fusion technology, *Fusion Eng. Des.* 74 (2005) 31–40. doi:10.1016/j.fusengdes.2005.08.008.
- [11] K. Ehrlich, E.E. Bloom, T. Kondo, International strategy for fusion materials development, *J. Nucl. Mater.* 283 (2000) 79–88. doi:10.1016/S0022-3115(00)00102-1.
- [12] T. Asayama, Y. Tachibana, Collect Available Creep-Fatigue Data and Study Existing Creep-Fatigue Evaluation Procedures for Grade 91 and Hastelloy XR Revision 3—Final Report. JAEA., 2007.
- [13] W.R. Corwin, Generation IV Reactors Integrated Materials Technology Program Plan: Focus on Very High Temperature Reactor Materials. ORNL/TM-2008/129. Oak Ridge National Laboratory., 2008.
- [14] W.R. Corwin, Status of ongoing research. Within the GIF VHTR Materials Project, in: GIF Symp. Parigi, Paris, Fr. 9 10 Sept., 2009.
- [15] K.L. Murty, I. Charit, Structural materials for Gen-IV nuclear reactors: Challenges and opportunities, *J. Nucl. Mater.* 383 (2008) 189–195. doi:10.1016/j.jnucmat.2008.08.044.
- [16] G. Bai, J. Li, R. Hu, Z. Tang, X. Xue, H. Fu, Effect of temperature on tensile behavior of Ni-Cr-W based superalloy, *Mater. Sci. Eng. A*. 528 (2011) 1974–1978. doi:10.1016/j.msea.2010.11.053.
- [17] A. Kohyama, J.S. Park, H.C. Jung, Advanced SiC fibers and SiC/SiC composites toward

- industrialization, *J. Nucl. Mater.* 417 (2011) 340–343. doi:10.1016/j.jnucmat.2010.12.086.
- [18] C.R.F. Azevedo, Selection of fuel cladding material for nuclear fission reactors, *Eng. Fail. Anal.* 18 (2011) 1943–1962. doi:10.1016/j.engfailanal.2011.06.010.
- [19] C. Fazio, D.G. Briceno, M. Rieth, A. Gessi, J. Henry, L. Malerba, Innovative materials for Gen IV systems and transmutation facilities: The cross-cutting research project GETMAT, *Nucl. Eng. Des.* 241 (2011) 3514–3520. doi:10.1016/j.nucengdes.2011.03.009.
- [20] S. Ukai, T. Narita, A. Alamo, P. Parmentier, Tube manufacturing trials by different routes in 9CrW-ODS martensitic steels, *J. Nucl. Mater.* 329–333 (2004) 356–361. doi:10.1016/j.jnucmat.2004.04.082.
- [21] A. Kimura, R. Kasada, N. Iwata, H. Kishimoto, C.H. Zhang, J. Isselin, P. Dou, J.H. Lee, N. Muthukumar, T. Okuda, M. Inoue, S. Ukai, S. Ohnuki, T. Fujisawa, T.F. Abe, Development of Al added high-Cr ODS steels for fuel cladding of next generation nuclear systems, *J. Nucl. Mater.* 417 (2011) 176–179. doi:10.1016/j.jnucmat.2010.12.300.
- [22] Y. Xu, Z. Zhou, M. Li, P. He, Fabrication and characterization of ODS austenitic steels, *J. Nucl. Mater.* 417 (2011) 283–285. doi:10.1016/j.jnucmat.2010.12.155.
- [23] Y. de Carlan, J.-L. Bechade, P. Dubuisson, J.-L. Seran, P. Billot, A. Bougault, T. Cozzika, S. Doriot, D. Hamon, J. Henry, M. Ratti, N. Lochet, D. Nunes, P. Olier, T. Leblond, M.H. Mathon, CEA developments of new ferritic ODS alloys for nuclear applications, *J. Nucl. Mater.* 386–388 (2009) 430–432. doi:10.1016/j.jnucmat.2008.12.156.
- [24] Y. Kurata, H. Yokota, T. Suzuki, Development of aluminum alloy coating for advanced nuclear, in: *Proc. ASME 2011 Small Modul. React. Symp.* Washingt., 2011.
- [25] L.K. Mansur, Theory and experimental background on dimensional changes in irradiated alloys, *J. Nucl. Mater.* 216 (1994) 97–123. doi:10.1016/0022-3115(94)90009-4.
- [26] S.J. Zinkle, G.S. Was, Materials challenges in nuclear energy, *Acta Mater.* 61 (2013) 735–758. doi:10.1016/j.actamat.2012.11.004.
- [27] R.L. Klueh, D.S. Gelles, M. Okada, N.H. Packan, *Reduced activation materials for fusion reactors*, 1990.
- [28] R.H. Jones, H.L. Heinisch, K.A. McCarthy, Low activation materials, *J. Nucl. Mater.* 271–272 (1999) 518–525. doi:10.1016/S0022-3115(98)00864-2.
- [29] P.J. Ennis, A. Czyrska-Filemonowicz, Recent advances in creep-resistant steels for power plant applications, *Sadhana - Acad. Proc. Eng. Sci.* 28 (2003) 709–730. doi:10.1007/BF02706455.
- [30] H.J. Frost, F. Ashby, *Deformation-mechanism maps: the plasticity and creep of metals and ceramics*, 1982.
- [31] T.G. Langdon, An Analysis of Flow Mechanisms in High Temperature Creep and Superplasticity, *Mater. Trans.* 46 (2005) 1951–1956. doi:org/10.2320/matertrans.46.1951.
- [32] N. Garcia, M. Campos, J.M. Torralba, *Desarrollo de Nuevos Aceros Ferríticos ODS para Aplicaciones Nucleares*, 2014.
- [33] D.M. Owen, T.G. Langdon, Low stress creep behavior: an examination of Nabarro-Herring and Harper-Dorn creep, *Mater. Sci. Eng.* 216 (1996) 20–29. doi:10.1016/0921-5093(96)10382-8.
- [34] P. Susila, D. Sturm, M. Heilmaier, B.S. Murty, V. Subramanya Sarma, Effect of yttria

- particle size on the microstructure and compression creep properties of nanostructured oxide dispersion strengthened ferritic (Fe-12Cr-2W-0.5Y₂O₃) alloy, *Mater. Sci. Eng. A*. 528 (2011) 4579–4584. doi:10.1016/j.msea.2011.02.078.
- [35] T. Hayashi, P.M. Sarosi, J.H. Schneibel, M.J. Mills, Creep response and deformation processes in nanocluster-strengthened ferritic steels, *Acta Mater.* 56 (2008) 1407–1416. doi:10.1016/j.actamat.2007.11.038.
- [36] X. Boulnat, A. Deschamps, M. Perez, FAST high-temperature consolidation of Oxide-Dispersion Strengthened (ODS) steels: process, microstructure, precipitation, properties., 2014.
- [37] E.E. Bloom, R.W. Conn, J.W. Davis, R.E. Gold, R. Little, K.R. Schultz, D.L. Smith, F.W. Wiffen, Low activation materials for fusion applications, *J. Nucl. Mater.* 123 (1984) 17–26. doi:10.1016/0022-3115(84)90570-1.
- [38] P. Schiller, Review of materials selection for fusion reactors, *J. Nucl. Mater.* 206 (1993) 113–120. doi:10.1016/0022-3115(93)90118-1.
- [39] IAEA, IAEA Nuclear Energy Series Publications, (2010) 35–37. doi:http://dx.doi.org/10.1016/S0167-8140(05)81513-0.
- [40] C.M. Parish, K.A. Unocic, L. Tan, S.J. Zinkle, S. Kondo, L.L. Snead, D.T. Hoelzer, Y. Katoh, Helium sequestration at nanoparticle-matrix interfaces in helium + heavy ion irradiated nanostructured ferritic alloys, *J. Nucl. Mater.* 483 (2017) 21–34. doi:10.1016/j.jnucmat.2016.10.038.
- [41] M.J. Caturla, T. Diaz de la Rubia, M. Fluss, Modeling microstructure evolution of f.c.c. metals under irradiation in the presence of He, *J. Nucl. Mater.* 323 (2003) 163–168. doi:10.1016/j.jnucmat.2003.08.003.
- [42] F.A. Garner, M.B. Toloczko, Irradiation creep and void swelling of austenitic stainless steels at low displacement rates in light water energy systems, *J. Nucl. Mater.* 251 (1997) 252–261. doi:10.1016/S0022-3115(97)00260-2.
- [43] E. Salama, M.M. Eissa, A.S. Tageldin, Distinct properties of tungsten austenitic stainless alloy as a potential nuclear engineering material, *Nucl. Eng. Technol.* 51 (2019) 784–791. doi:10.1016/j.net.2018.12.021.
- [44] A. Yabuuchi, M. Maekawa, A. Kawasuso, Influence of oversized elements (Hf, Zr, Ti and Nb) on the thermal stability of vacancies in type 316L stainless steels, *J. Nucl. Mater.* 430 (2012) 190–193. doi:10.1016/j.jnucmat.2012.07.005.
- [45] L. Tan, L.L. Snead, Y. Katoh, Development of new generation reduced activation ferritic-martensitic steels for advanced fusion reactors, *J. Nucl. Mater.* 478 (2016) 42–49. doi:10.1016/J.JNUCMAT.2016.05.037.
- [46] R.J. Kurtz, A. Alamo, E. Lucon, Q. Huang, S. Jitsukawa, A. Kimura, R.L. Klueh, G.R. Odette, C. Petersen, M.A. Sokolov, P. Spätig, J.-W. Rensman, Recent progress toward development of reduced activation ferritic/martensitic steels for fusion structural applications, *J. Nucl. Mater.* 386–388 (2009) 411–417. doi:10.1016/j.jnucmat.2008.12.323.
- [47] R. Schäublin, A. Ramar, N. Baluc, V. de Castro, M.A. Monge, T. Leguey, N. Schmid, C. Bonjour, Microstructural development under irradiation in European ODS ferritic/martensitic steels, *J. Nucl. Mater.* 351 (2006) 247–260. doi:10.1016/j.jnucmat.2006.02.005.
- [48] K. Mo, Z. Zhou, Y. Miao, D. Yun, H.M. Tung, G. Zhang, W. Chen, J. Almer, J.F. Stubbins,

- Synchrotron study on load partitioning between ferrite/martensite and nanoparticles of a 9Cr ODS steel, *J. Nucl. Mater.* 455 (2014) 376–381. doi:10.1016/j.jnucmat.2014.06.060.
- [49] Y. Li, T. Nagasaka, T. Muroga, A. Kimura, S. Ukai, High-temperature mechanical properties and microstructure of 9Cr oxide dispersion strengthened steel compared with RAFMs, *Fusion Eng. Des.* 86 (2011) 2495–2499. doi:10.1016/j.fusengdes.2011.03.004.
- [50] S.J. Zinkle, A. Möslang, T. Muroga, J.L. Boutard, D.T. Hoelzer, A. Kimura, R. Lindau, G.R. Odette, M. Rieth, L. Tan, H. Tanigawa, Development of next generation tempered and ODS reduced activation ferritic/martensitic steels for fusion energy applications, *Nucl. Fusion.* 57 (2017) 17. doi:10.1088/1741-4326/57/9/092005.
- [51] P. Prakash, J. Vanaja, N. Srinivasan, P. Parameswaran, G.V.S. Nageswara Rao, K. Laha, Effect of thermo-mechanical treatment on tensile properties of reduced activation ferritic-martensitic steel, *Mater. Sci. Eng. A.* 724 (2018) 171–180. doi:10.1016/j.msea.2018.03.080.
- [52] P. Prakash, J. Vanaja, G. V. Prasad Reddy, K. Laha, G.V.S. Nageswara Rao, On the effect of thermo-mechanical treatment on creep deformation and rupture behaviour of a reduced activation ferritic-martensitic steel, *J. Nucl. Mater.* 520 (2019) 65–77. doi:10.1016/j.jnucmat.2019.04.014.
- [53] J. Vivas, C. Capdevila, E. Altstadt, M. Houska, D. San-Martín, Importance of austenitization temperature and ausforming on creep strength in 9Cr ferritic/martensitic steel, *Scr. Mater.* 153 (2018) 14–18. doi:10.1016/j.scriptamat.2018.04.038.
- [54] K. Tippey, P. Jablonski, Ö. Doğan, J. Almer, R. Hackenberg, J. Speer, A. Stebner, K. Clarke, A. Clarke, K. Findley, Effects of alloying and processing modifications on precipitation behavior and elevated temperature strength in 9% Cr ferritic/martensitic steels, *Mater. Sci. Eng. A.* 756 (2019) 172–183. doi:10.1016/j.msea.2018.11.133.
- [55] T. Narita, S. Ukai, S. Ohtsuka, M. Inoue, Effect of tungsten addition on microstructure and high temperature strength of 9CrODS ferritic steel, *J. Nucl. Mater.* 417 (2011) 158–161. doi:10.1016/j.jnucmat.2011.01.060.
- [56] T. Muroga, T. Nagasaka, Y. Li, H. Abe, S. Ukai, A. Kimura, T. Okuda, Fabrication and characterization of reference 9Cr and 12Cr-ODS low activation ferritic/martensitic steels, *Fusion Eng. Des.* 89 (2014) 1717–1722. doi:10.1016/j.fusengdes.2014.01.010.
- [57] R.L. Klueh, N. Hashimoto, P.J. Maziasz, New nano-particle-strengthened ferritic/martensitic steels by conventional thermo-mechanical treatment, *J. Nucl. Mater.* 367-370 A (2007) 48–53. doi:10.1016/j.jnucmat.2007.03.001.
- [58] S. Hollner, E. Piozin, P. Mayr, C. Caës, I. Tournié, A. Pineau, B. Fournier, Characterization of a boron alloyed 9Cr3W3CoVNbBN steel and further improvement of its high-temperature mechanical properties by thermomechanical treatments, *J. Nucl. Mater.* 441 (2013) 15–23. doi:10.1016/j.jnucmat.2013.05.018.
- [59] U.A. Sachadel, P.F. Morris, P.D. Clarke, Design of 10%Cr martensitic steels for improved creep resistance in power plant applications, *Mater. Sci. Technol.* 29 (2012) 767–774. doi:10.1179/0267083612z.000000000218.
- [60] S. Hollner, B. Fournier, J. Le Pendu, T. Cozzika, I. Tournié, J.C. Brachet, A. Pineau, High-temperature mechanical properties improvement on modified 9Cr-1Mo martensitic steel through thermomechanical treatments, *J. Nucl. Mater.* 405 (2010) 101–108. doi:10.1016/j.jnucmat.2010.07.034.
- [61] L. Tan, Y. Yang, J.T. Busby, Effects of alloying elements and thermomechanical treatment on 9Cr Reduced Activation Ferritic-Martensitic (RAFM) steels, *J. Nucl. Mater.* 442 (2013)

- S13–S17. doi:10.1016/j.jnucmat.2012.10.015.
- [62] S. Ukai, M. Fujiwara, Perspective of ODS alloys application in nuclear environments, *J. Nucl. Mater.* 307–311 (2002) 749–757. doi:10.1016/S0022-3115(02)01043-7.
- [63] N. Cunningham, Y. Wu, D. Klingensmith, G.R. Odette, On the remarkable thermal stability of nanostructured ferritic alloys, *Mater. Sci. Eng. A.* 613 (2014) 296–305. doi:10.1016/j.msea.2014.06.097.
- [64] M.K. Miller, D.T. Hoelzer, E. a. Kenik, K.F. Russell, Stability of ferritic MA/ODS alloys at high temperatures, *Intermetallics.* 13 (2005) 387–392. doi:10.1016/j.intermet.2004.07.036.
- [65] C. Capdevila, M.K. Miller, K.F. Russell, Aluminum partitioning during phase separation in Fe-20%Cr-6%Al ODS alloy, *J. Mater. Sci.* 43 (2008) 3889–3893. doi:10.1007/s10853-007-2228-z.
- [66] C. Capdevila, M.K. Miller, I. Toda, J. Chao, Influence of the α - α' phase separation on the tensile properties of Fe-base ODS PM 2000 alloy, *Mater. Sci. Eng. A.* 527 (2010) 7931–7938. doi:10.1016/j.msea.2010.08.083.
- [67] C. Capdevila, M.K. Miller, K.F. Russell, J. Chao, J.L. González-Carrasco, Phase separation in PM 2000™ Fe-base ODS alloy: Experimental study at the atomic level, *Mater. Sci. Eng. A.* 490 (2008) 277–288. doi:10.1016/j.msea.2008.01.029.
- [68] C. Capdevila, M.K. Miller, J. Chao, Phase separation kinetics in a Fe-Cr-Al alloy, *Acta Mater.* 60 (2012) 4673–4684. doi:10.1016/j.actamat.2012.05.022.
- [69] C. Capdevila, M.K. Miller, G. Pimentel, J. Chao, Influence of recrystallization on phase separation kinetics of oxide dispersion strengthened Fe-Cr-Al alloy, *Scr. Mater.* 66 (2012) 254–257. doi:10.1016/j.scriptamat.2011.11.003.
- [70] S. Li, Z. Zhou, J. Jang, M. Wang, H. Hu, H. Sun, L. Zou, G. Zhang, L. Zhang, The influence of Cr content on the mechanical properties of ODS ferritic steels, *J. Nucl. Mater.* 455 (2014) 194–200. doi:10.1016/j.jnucmat.2014.05.061.
- [71] M. Terada, M.F. Hupalo, I. Costa, A.F. Padilha, Effect of alpha prime due to 475 °c aging on fracture behavior and corrosion resistance of DIN 1.4575 and MA 956 high performance ferritic stainless steels, *J. Mater. Sci.* 43 (2008) 425–433. doi:10.1007/s10853-007-1929-7.
- [72] G. Bonny, D. Terentyev, L. Malerba, On the α - α' miscibility gap of Fe-Cr alloys, *Scr. Mater.* 59 (2008) 1193–1196. doi:10.1016/j.scriptamat.2008.08.008.
- [73] H. Sakasegaw, H. Tanigaw, M. Ando, Corrosion-resistant coating technique for oxide-dispersion-strengthened ferritic/martensitic steel, *J. Nucl. Sci. Technol.* 51 (2014) 737–743. doi:10.1080/00223131.2014.894950.
- [74] W. Krauss, S.E. Wulf, J. Konys, Long-term corrosion behavior of ODS-Eurofer in flowing Pb-15.7Li at 550 °C, *Nucl. Mater. Energy.* 9 (2016) 512–518. doi:10.1016/j.nme.2016.04.011.
- [75] M. Terada, A.J. De Oliveira Zimmermann, H.R.Z. Sandim, I. Costa, A.F. Padilha, Corrosion behavior of Eurofer 97 and ODS-Eurofer alloys compared to traditional stainless steels, *J. Appl. Electrochem.* 41 (2011) 951–959. doi:10.1007/s10800-011-0320-1.
- [76] T. Kaito, T. Narita, S. Ukai, Y. Matsuda, High temperature oxidation behavior of ODS steels, *J. Nucl. Mater.* 329–333 (2004) 1388–1392. doi:10.1016/j.jnucmat.2004.04.203.
- [77] R.L. Klueh, J.P. Shingledecker, R.W. Swindeman, D.T. Hoelzer, Oxide dispersion-

- strengthened steels: A comparison of some commercial and experimental alloys, *J. Nucl. Mater.* 341 (2005) 103–114. doi:10.1016/j.jnucmat.2005.01.017.
- [78] M. Yurechko, C. Schroer, O. Wedemeyer, A. Skrypnik, J. Konys, Creep-rupture tests on chromium-containing conventional and ODS steels in oxygen-controlled Pb and air at 650 °C, *Nucl. Eng. Des.* 280 (2015) 686–696. doi:10.1016/j.nucengdes.2014.06.003.
- [79] A. Steckmeyer, V.H. Rodrigo, J.M. Gentzittel, V. Rabeau, B. Fournier, Tensile anisotropy and creep properties of a Fe-14CrWTi ODS ferritic steel, *J. Nucl. Mater.* 426 (2012) 182–188. doi:10.1016/j.jnucmat.2012.03.016.
- [80] R.L. Klueh, D.S. Gelles, S. Jitsukawa, A. Kimura, G.R. Odette, B. van der Schaaf, M. Victoria, Ferritic/martensitic steels – overview of recent results, *J. Nucl. Mater.* 307–311 (2002) 455–465. doi:10.1016/S0022-3115(02)01082-6.
- [81] J. Froitzheim, G.H. Meier, L. Niewolak, P.J. Ennis, H. Hattendorf, L. Singheiser, W.J. Quadackers, Development of high strength ferritic steel for interconnect application in SOFCs, *J. Power Sources.* 178 (2008) 163–173. doi:10.1016/j.jpowsour.2007.12.028.
- [82] N. Baluc, D.S. Gelles, S. Jitsukawa, A. Kimura, R.L. Klueh, G.R. Odette, B. van der Schaaf, J. Yu, Status of reduced activation ferritic/martensitic steel development, *J. Nucl. Mater.* 367–370 (2007) 33–41. doi:10.1016/j.jnucmat.2007.03.036.
- [83] S. Takaya, T. Furukawa, G. Müller, A. Heinzl, A. Jianu, A. Weisenburger, K. Aoto, M. Inoue, T. Okuda, F. Abe, S. Ohnuki, T. Fujisawa, A. Kimura, Al-containing ODS steels with improved corrosion resistance to liquid lead–bismuth, *J. Nucl. Mater.* 428 (2012) 125–130. doi:10.1016/j.jnucmat.2011.06.046.
- [84] T. Liu, C. Wang, H. Shen, W. Chou, N.Y. Iwata, A. Kimura, The effects of Cr and Al concentrations on the oxidation behavior of oxide dispersion strengthened ferritic alloys, *Corros. Sci.* 76 (2013) 310–316. doi:10.1016/j.corosci.2013.07.004.
- [85] S. Ohtsuka, T. Kaito, M. Inoue, T. Asayama, S.W. Kim, S. Ukai, T. Narita, H. Sakasegawa, Effects of aluminum on high-temperature strength of 9Cr-ODS steel, *J. Nucl. Mater.* 386–388 (2009) 479–482. doi:10.1016/j.jnucmat.2008.12.147.
- [86] M.K. Miller, C.M. Parish, Role of alloying elements in nanostructured ferritic steels, *Mater. Sci. Technol.* 27 (2011) 729–734. doi:10.1179/1743284710Y.0000000039.
- [87] P. Dou, A. Kimura, T. Okuda, M. Inoue, S. Ukai, S. Ohnuki, T. Fujisawa, F. Abe, Effects of extrusion temperature on the nano-mesoscopic structure and mechanical properties of an Al-alloyed high-Cr ODS ferritic steel, *J. Nucl. Mater.* 417 (2011) 166–170. doi:10.1016/j.jnucmat.2011.01.061.
- [88] C.H. Zhang, A. Kimura, R. Kasada, J. Jang, H. Kishimoto, Y.T. Yang, Characterization of the oxide particles in Al-added high-Cr ODS ferritic steels, *J. Nucl. Mater.* 417 (2011) 221–224. doi:10.1016/j.jnucmat.2010.12.063.
- [89] H.S. Cho, A. Kimura, S. Ukai, M. Fujiwara, Corrosion properties of oxide dispersion strengthened steels in super-critical water environment, *J. Nucl. Mater.* 329–333 (2004) 387–391. doi:10.1016/j.jnucmat.2004.04.040.
- [90] S. Yamashita, K. Oka, S. Ohnuki, N. Akasaka, S. Ukai, Phase stability of oxide dispersion-strengthened ferritic steels in neutron irradiation, *J. Nucl. Mater.* 307–311 (2002) 283–288. doi:10.1016/S0022-3115(02)01077-2.
- [91] P. Song, K. Yabuuchi, A. Kimura, Cavity evolution and hardness changes in a 15Cr-ODS ferritic steel by post He-implantation annealing, *Nucl. Mater. Energy.* 15 (2018) 115–121. doi:10.1016/j.nme.2018.03.006.

- [92] M.J. Alinger, G.R. Odette, D.T. Hoelzer, On the role of alloy composition and processing parameters in nanocluster formation and dispersion strengthening in nanostructured ferritic alloys, *Acta Mater.* 57 (2009) 392–406. doi:10.1016/j.actamat.2008.09.025.
- [93] M. Nagini, R. Vijay, M. Ramakrishna, a. V. Reddy, G. Sundararajan, Influence of the duration of high energy ball milling on the microstructure and mechanical properties of a 9Cr oxide dispersion strengthened ferritic–martensitic steel, *Mater. Sci. Eng. A.* 620 (2015) 490–499. doi:10.1016/j.msea.2014.10.050.
- [94] M. Klimiankou, R. Lindau, A. Möslang, HRTEM study of yttrium oxide particles in ODS steels for fusion reactor application, *J. Cryst. Growth.* 249 (2003) 381–387. doi:10.1016/S0022-0248(02)02134-6.
- [95] S.-W. Kim, T. Shobu, S. Ohtsuka, T. Kaito, M. Inoue, M. Ohnuma, Kinetic Approach for Growth and Coalescence of Nano-Size Oxide Particles in 9Cr-ODS Steel Using High-Energy Synchrotron Radiation X-rays in SPring-8, *Mater. Trans.* 50 (2009) 917–921. doi:10.2320/matertrans.MER2008439.
- [96] S. Yamashita, T. Yoshitake, N. Akasaka, S. Ukai, A. Kimura, Mechanical Behavior of Oxide Dispersion Strengthened Steels Irradiated in JOYO, *Mater. Trans.* 46 (2005) 493–497. doi:10.2320/matertrans.46.493.
- [97] S. Ohtsuka, S. Ukai, M. Fujiwara, T. Kaito, T. Narita, Improvement of 9Cr-ODS martensitic steel properties by controlling excess oxygen and titanium contents, *J. Nucl. Mater.* 329–333 (2004) 372–376. doi:10.1016/j.jnucmat.2004.04.043.
- [98] S. Ukai, S. Mizuta, M. Fujiwara, T. Okuda, T. Kobayashi, Development of 9cr-ods martensitic steel claddings for fuel pins by means of ferrite to austenite phase transformation, *J. Nucl. Sci. Technol.* 39 (2002) 778–788. doi:10.1080/18811248.2002.9715260.
- [99] S. Ohtsuka, S. Ukai, M. Fujiwara, T. Kaito, T. Narita, Nano-structure control in ODS martensitic steels by means of selecting titanium and oxygen contents, *J. Phys. Chem. Solids.* 66 (2005) 571–575. doi:10.1016/j.jpcs.2004.06.033.
- [100] L. Barnard, N. Cunningham, G.R. Odette, I. Szlufarska, D. Morgan, Thermodynamic and kinetic modeling of oxide precipitation in nanostructured ferritic alloys, *Acta Mater.* 91 (2015) 340–354. doi:10.1016/j.actamat.2015.03.014.
- [101] Z. Oksiuta, N. Baluc, Role of Cr and Ti contents on the microstructure and mechanical properties of ODS ferritic steels, *Adv. Mater. Res.* 59 (2009) 308–312. doi:10.4028/www.scientific.net/AMR.59.308.
- [102] S. Ukai, T. Okuda, M. Fujiwara, T. Kobayashi, S. Mizuta, H. Nakashima, Characterization of high temperature creep properties in recrystallized 12cr-ods ferritic steel claddings, *J. Nucl. Sci. Technol.* 39 (2002) 872–879. doi:10.1080/18811248.2002.9715271.
- [103] M. Klimiankou, R. Lindau, A. Möslang, TEM characterization of structure and composition of nanosized ODS particles in reduced activation ferritic-martensitic steels, *J. Nucl. Mater.* 329–333 (2004) 347–351. doi:10.1016/j.jnucmat.2004.04.083.
- [104] A.J. London, S. Santra, S. Amirthapandian, B.K. Panigrahi, R.M. Sarguna, S. Balaji, R. Vijay, C.S. Sundar, S. Lozano-Perez, C.R.M. Grovenor, Effect of Ti and Cr on dispersion, structure and composition of oxide nano-particles in model ODS alloys, *Acta Mater.* 97 (2015) 223–233. doi:10.1016/J.ACTAMAT.2015.06.032.
- [105] C. Lu, Z. Lu, R. Xie, Z. Li, C. Liu, L. Wang, Effect of Y/Ti atomic ratio on microstructure of oxide dispersion strengthened alloys, *Mater. Charact.* 134 (2017) 35–40. doi:10.1016/J.MATCHAR.2017.10.004.

- [106] S. Yamashita, S. Ohtsuka, N. Akasaka, S. Ukai, S. Ohnuki, Formation of nanoscale complex oxide particles in mechanically alloyed ferritic steel, *Philos. Mag. Lett.* 84 (2004) 525–529. doi:10.1080/09500830412331303609.
- [107] G.R. Odette, D.T. Hoelzer, Irradiation-tolerant Nanostructured Ferritic Alloys: Transforming Helium from a Liability to an Asset, (n.d.) 84–92. doi:10.1007/s11837-010-0144-1.
- [108] S. Ukai, S. Mizuta, T. Yoshitake, T. Okuda, M. Fujiwara, S. Hagi, T. Kobayashi, Tube manufacturing and characterization of oxide dispersion strengthened ferritic steels, *J. Nucl. Mater.* 283–287 (2000) 702–706. doi:10.1016/S0022-3115(00)00114-8.
- [109] K. Dawson, S.J. Haigh, G.J. Tatlock, A.R. Jones, Nano-particle precipitation in mechanically alloyed and annealed precursor powders of legacy PM2000 ODS alloy, *J. Nucl. Mater.* 464 (2015) 200–209. doi:10.1016/j.jnucmat.2015.04.039.
- [110] L.L. Hsiung, M.J. Fluss, S.J. Tumej, B.W. Choi, Y. Serruys, F. Willaime, A. Kimura, Formation mechanism and the role of nanoparticles in Fe-Cr ODS steels developed for radiation tolerance, *Phys. Rev. B - Condens. Matter Mater. Phys.* 82 (2010) 1–13. doi:10.1103/PhysRevB.82.184103.
- [111] R. Kasada, N. Toda, K. Yutani, H.S. Cho, H. Kishimoto, A. Kimura, Pre- and post-deformation microstructures of oxide dispersion strengthened ferritic steels, *J. Nucl. Mater.* 367–370 (2007) 222–228. doi:10.1016/j.jnucmat.2007.03.141.
- [112] L. Hsiung, M. Fluss, S. Tumej, J. Kuntz, B. El-Dasher, M. Wall, B. Choi, A. Kimura, F. Willaime, Y. Serruys, HRTEM study of oxide nanoparticles in K3-ODS ferritic steel developed for radiation tolerance, *J. Nucl. Mater.* 409 (2011) 72–79. doi:10.1016/j.jnucmat.2010.09.014.
- [113] L.L. Hsiung, M.J. Fluss, A. Kimura, Structure of oxide nanoparticles in Fe–16Cr MA/ODS ferritic steel, *Mater. Lett.* 64 (2010) 1782–1785. doi:10.1016/j.matlet.2010.05.039.
- [114] A. Wasilkowska, M. Bartsch, U. Messerschmidt, R. Herzog, A. Czyrska-Filemonowicz, Creep mechanisms of ferritic oxide dispersion strengthened alloys, *J. Mater. Process. Technol.* 133 (2003) 218–224. doi:10.1016/S0924-0136(02)00237-6.
- [115] J.H. Schneibel, M. Heilmaier, W. Blum, G. Hasemann, T. Shanmugasundaram, Temperature dependence of the strength of fine- and ultrafine-grained materials, *Acta Mater.* 59 (2011) 1300–1308. doi:10.1016/j.actamat.2010.10.062.
- [116] P. Dou, A. Kimura, T. Okuda, M. Inoue, S. Ukai, S. Ohnuki, T. Fujisawa, F. Abe, Polymorphic and coherency transition of Y–Al complex oxide particles with extrusion temperature in an Al-alloyed high-Cr oxide dispersion strengthened ferritic steel, *Acta Mater.* 59 (2011) 992–1002. doi:10.1016/j.actamat.2010.10.026.
- [117] P. Dou, A. Kimura, R. Kasada, T. Okuda, M. Inoue, S. Ukai, S. Ohnuki, T. Fujisawa, F. Abe, TEM and HRTEM study of oxide particles in an Al-alloyed high-Cr oxide dispersion strengthened steel with Zr addition, *J. Nucl. Mater.* 444 (2014) 441–453. doi:10.1016/j.jnucmat.2013.10.028.
- [118] R. Gao, T. Zhang, X.P. Wang, Q.F. Fang, C.S. Liu, Effect of zirconium addition on the microstructure and mechanical properties of ODS ferritic steels containing aluminum, *J. Nucl. Mater.* 444 (2014) 462–468. doi:10.1016/j.jnucmat.2013.10.038.
- [119] J. Isselin, R. Kasada, A. Kimura, T. Okuda, M. Inoue, S. Ukai, S. Ohnuki, T. Fujisawa, F. Abe, Effects of Zr Addition on the Microstructure of 14%Cr4%Al ODS Ferritic Steels, *Mater. Trans.* 51 (2010) 1011–1015. doi:10.2320/matertrans.MBW200923.

- [120] A. García-Junceda, N. García-Rodríguez, M. Campos, M. Cartón-Cordero, J.M. Torralba, Effect of Zirconium on the Microstructure and Mechanical Properties of an Al-Alloyed ODS Steel Consolidated by FAHP, *J. Am. Ceram. Soc.* 98 (2015) 3582–3587. doi:10.1111/jace.13691.
- [121] W. Li, H. Xu, X. Sha, J. Meng, W. Wang, C. Kang, X. Zhang, Z. Wang, Microstructural characterization and strengthening mechanisms of a 15Cr-ODS steel produced by mechanical alloying and Spark Plasma Sintering, *Fusion Eng. Des.* 137 (2018) 71–78. doi:10.1016/j.fusengdes.2018.08.020.
- [122] R. Rahmanifard, H. Farhangi, A.J. Novinrooz, Effect of zirconium and tantalum on the microstructural characteristics of 12YWT ODS steel nanocomposite, *J. Alloys Compd.* 622 (2015) 948–952. doi:10.1016/j.jallcom.2014.11.018.
- [123] C.Z. Yu, H. Oka, N. Hashimoto, S. Ohnuki, Development of damage structure in 16Cr–4Al ODS steels during electron-irradiation, *J. Nucl. Mater.* 417 (2011) 286–288. doi:10.1016/j.jnucmat.2011.02.037.
- [124] H. Kishimoto, R. Kasada, A. Kimura, M. Inoue, T. Okuda, F. Abe, S. Ohnuki, T. Fujisawa, No Title, in: *Proc. ICAPP 2009*, 2009.
- [125] S. Ohnuki, N. Hashimoto, S. Ukai, A. Kimura, M. Inoue, T. Kaito, T. Fujisawa, T. Okuda, F. Abe, A. Kimura, No Title, in: *Proceeding of the ICAPP*, 2009.
- [126] H. Dong, L. Yu, Y. Liu, C. Liu, H. Li, J. Wu, Enhancement of tensile properties due to microstructure optimization in ODS steels by zirconium addition, *Fusion Eng. Des.* 125 (2017) 402–406. doi:10.1016/J.FUSENGDES.2017.03.170.
- [127] T. Gladman, Precipitation hardening in metals, 0836 (1999). doi:10.1179/026708399773002782.
- [128] R.E. Smallman, A.H.W. Ngan, *Physical metallurgy*, 2014.
- [129] T.H. Courtney, *Mechanical Behavior of Materials*, 1990.
- [130] J. Shen, Y. Li, F. Li, H. Yang, Z. Zhao, S. Kano, Y. Matsukawa, Y. Satoh, H. Abe, Microstructural characterization and strengthening mechanisms of a 12Cr-ODS steel, *Mater. Sci. Eng. A.* 673 (2016) 624–632. doi:10.1016/j.msea.2016.07.030.
- [131] A. Chauhan, F. Bergner, A. Etienne, J. Aktaa, Y. De Carlan, C. Heintze, D. Litvinov, M. Hernandez-Mayoral, E. Oñorbe, B. Radiguet, A. Ulbricht, Microstructure characterization and strengthening mechanisms of oxide dispersion strengthened (ODS) Fe-9 % Cr and Fe-14 % Cr extruded bars, *J. Nucl. Mater.* 495 (2017) 6–19. doi:10.1016/j.jnucmat.2017.07.060.
- [132] R.E. Stoller, S.J. Zinkle, On the relationship between uniaxial yield strength and resolved shear stress in polycrystalline materials, *J. Nucl. Mater.* 283–287 (2000) 349–352. doi:10.1016/S0022-3115(00)00378-0.
- [133] M. Praud, F. Momprou, J. Malaplate, D. Caillard, J. Garnier, A. Steckmeyer, B. Fournier, Study of the deformation mechanisms in a Fe-14% Cr ODS alloy, *J. Nucl. Mater.* 428 (2012) 90–97. doi:10.1016/j.jnucmat.2011.10.046.
- [134] N. Sallel, X. Boulnat, A. Borbély, J.L. Béchade, D. Fabregue, M. Perez, Y. De Carlan, L. Hennet, C. Mocuta, D. Thiaudiere, Y. Brechet, In situ characterization of microstructural instabilities : Recovery , recrystallization and abnormal growth in nanoreinforced steel powder, 87 (2015) 377–389. doi:10.1016/j.actamat.2014.11.051.
- [135] N. Sallel, C. Hatzoglou, F. Delabrouille, D. Sornin, L. Chaffron, M. Blat-Yrieix, B. Radiguet, P. Pareige, P. Donnadieu, Y. Bréchet, Precipitates and boundaries interaction in ferritic

- ODS steels, *J. Nucl. Mater.* 472 (2016) 118–126. doi:10.1016/j.jnucmat.2016.01.021.
- [136] X. Boulnat, N. Sallez, M. Dadé, A. Borbély, J. Béchade, Y. De Carlan, J. Malaplate, Y. Brechet, F. de Geuser, A. Deschamps, P. Donnadiou, D. Fabregue, M. Perez, Influence of oxide volume fraction on abnormal growth of nanostructured ferritic steels during non-isothermal treatments: An in situ study, *Acta Mater.* 97 (2015) 124–130. doi:10.1016/j.actamat.2015.07.005.
- [137] E. Macía, A. García-Junceda, M. Serrano, M. Hernández-Mayoral, L.A. Diaz, M. Campos, Effect of the heating rate on the microstructure of a ferritic ODS steel with four oxide formers (Y-Ti-Al-Zr) consolidated by spark plasma sintering (SPS), *J. Nucl. Mater.* 518 (2019) 190–201. doi:10.1016/j.jnucmat.2019.02.043.
- [138] X. Boulnat, D. Fabrègue, M. Perez, S. Urvoy, D. Hamon, Y. de Carlan, Assessment of consolidation of oxide dispersion strengthened ferritic steels by spark plasma sintering: from laboratory scale to industrial products, *Powder Metall.* 57 (2014) 204–211. doi:10.1179/1743290114Y.0000000091.
- [139] I. Hilger, X. Boulnat, J. Hoffmann, C. Testani, F. Bergner, Y. De Carlan, F. Ferraro, A. Ulbricht, Fabrication and characterization of oxide dispersion strengthened (ODS) 14Cr steels consolidated by means of hot isostatic pressing, hot extrusion and spark plasma sintering, *J. Nucl. Mater.* 472 (2015) 206–214. doi:10.1016/j.jnucmat.2015.09.036.
- [140] X. Boulnat, D. Fabregue, M. Perez, M.H. Mathon, Y. De Carlan, High-temperature tensile properties of nano-oxide dispersion strengthened ferritic steels produced by mechanical alloying and spark plasma sintering, *Metall. Mater. Trans. A Phys. Metall. Mater. Sci.* 44 (2013) 2461–2465. doi:10.1007/s11661-013-1719-6.
- [141] X. Boulnat, M. Perez, D. Fabregue, T. Douillard, M.H. Mathon, Y. De Carlan, Microstructure evolution in nano-reinforced ferritic steel processed by mechanical alloying and spark plasma sintering, *Metall. Mater. Trans. A Phys. Metall. Mater. Sci.* 45 (2014) 1485–1497. doi:10.1007/s11661-013-2107-y.
- [142] J.S. Benjamin, T.E. Volin, The Mechanism of Mechanical Alloying, *Metall. Mater. Trans. A.* 5 (1974) 1929–1934. doi:10.1007/BF02644161.
- [143] W. Schatt, K.P. Wieters, *Powder metallurgy*, 1997.
- [144] C. Suryanarayana, Mechanical alloying and milling, *Prog. Mater. Sci.* 46 (2001) 1–184. doi:10.1016/S0079-6425(99)00010-9.
- [145] N.Y. Iwata, R. Kasada, A. Kimura, T. Okuda, M. Inoue, F. Abe, S. Ukai, S. Ohnuki, T. Fujisawa, Characterization of Mechanically Alloyed Powders for High-Cr Oxide Dispersion Strengthened Ferritic Steel, *ISIJ Int.* 49 (2009) 1914–1919. doi:10.2355/isijinternational.49.1914.
- [146] C.C. Koch, Synthesis of nanostructured materials by mechanical milling: Problems and opportunities, *Nanostructured Mater.* 9 (1997) 13–22. doi:10.1016/S0965-9773(97)00014-7.
- [147] J.M. Torralba, L. Fuentes-Pacheco, N. García-Rodríguez, M. Campos, Development of high performance powder metallurgy steels by high-energy milling, *Adv. Powder Technol.* 24 (2013) 813–817. doi:10.1016/j.apt.2012.11.015.
- [148] P. Matteazzi, G. Le Caër, A. Mocellin, Synthesis of Nanostructured Materials by Mechanical Alloying, *Ceram. Int.* 23 (1997) 39–44. doi:doi.org/10.1016/0272-8842(95)00138-7.
- [149] F.A. Mohamed, Y. Xun, Correlations between the minimum grain size produced by

- milling and material parameters, *Mater. Sci. Eng. A.* 354 (2003) 133–139. doi:10.1016/S0921-5093(02)00936-X.
- [150] Z. Oksiuta, N. Baluc, Effect of mechanical alloying atmosphere on the microstructure and Charpy impact properties of an ODS ferritic steel, *J. Nucl. Mater.* 386–388 (2009) 426–429. doi:10.1016/j.jnucmat.2008.12.148.
- [151] Z. Oksiuta, P. Hosemann, S.C. Vogel, N. Baluc, Microstructure examination of Fe-14Cr ODS ferritic steels produced through different processing routes, *J. Nucl. Mater.* 451 (2014) 320–327. doi:10.1016/j.jnucmat.2014.04.004.
- [152] G.P. Fraga, C. Capdevila, Recuperación en aleaciones ODS base Fe, (2014).
- [153] X. Wu, Y. Zhu, Heterogeneous materials: a new class of materials with unprecedented mechanical properties, *Mater. Res. Lett.* 5 (2017) 527–532. doi:10.1080/21663831.2017.1343208.
- [154] I. Hilger, F. Bergner, T. Weißgärber, Bimodal Grain Size Distribution of Nanostructured Ferritic ODS Fe – Cr Alloys, *J. Am. Ceram. Soc.* 3581 (2015) 3576–3581. doi:10.1111/jace.13833.
- [155] M. Dadé, J. Malaplate, J. Garnier, F. De Geuser, N. Lochet, A. Deschamps, Influence of consolidation methods on the recrystallization kinetics of a Fe-14Cr based ODS steel, *J. Nucl. Mater.* 472 (2016) 143–152. doi:10.1016/j.jnucmat.2016.01.019.
- [156] M.A. Auger, V. De Castro, T. Leguey, A. Muñoz, R. Pareja, Microstructure and mechanical behavior of ODS and non-ODS Fe-14Cr model alloys produced by spark plasma sintering, *J. Nucl. Mater.* 436 (2013) 68–75. doi:10.1016/j.jnucmat.2013.01.331.
- [157] P. Franke, C. Heintze, F. Bergner, T. Weißgärber, Mechanical properties of spark plasma sintered Fe-Cr compacts strengthened by nanodispersed yttria particles, *Mater. Test.* 52 (2010) 133–138. doi:10.3139/120.110115.
- [158] U. Anselmi-Tamburini, J.R. Groza, Critical assessment: electrical field/current application—a revolution in materials processing/sintering?, *Mater. Sci. Technol. (United Kingdom)*. 33 (2017) 1855–1862. doi:10.1080/02670836.2017.1341692.
- [159] Z.A. Munir, U. Anselmi-Tamburini, M. Ohyanagi, The effect of electric field and pressure on the synthesis and consolidation of materials: A review of the spark plasma sintering method, *J. Mater. Sci.* 41 (2006) 763–777. doi:10.1007/s10853-006-6555-2.
- [160] U. Anselmi-Tamburini, J.E. Garay, Z.A. Munir, Fundamental investigations on the spark plasma sintering/synthesis process III. Current effect on reactivity, *Mater. Sci. Eng. A.* 407 (2005) 24–30. doi:10.1016/j.msea.2005.06.066.
- [161] W. Chen, U. Anselmi-Tamburini, J.E. Garay, J.R. Groza, Z.A. Munir, Fundamental investigations on the spark plasma sintering/synthesis process: I. Effect of dc pulsing on reactivity, *Mater. Sci. Eng. A.* 394 (2005) 132–138. doi:10.1016/j.msea.2004.11.020.
- [162] U. Anselmi-Tamburini, S. Gennari, J.E. Garay, Z.A. Munir, Fundamental investigations on the spark plasma sintering/synthesis process: II. Modeling of current and temperature distributions, *Mater. Sci. Eng. A.* 394 (2005) 139–148. doi:10.1016/j.msea.2004.11.019.
- [163] X. Song, X. Liu, J. Zhang, Neck formation and self-adjusting mechanism of neck growth of conducting powders in spark plasma sintering, *J. Am. Ceram. Soc.* 89 (2006) 494–500. doi:10.1111/j.1551-2916.2005.00777.x.
- [164] D.M. Hulbert, A. Anders, J. Andersson, E.J. Lavernia, A.K. Mukherjee, A discussion on the absence of plasma in spark plasma sintering, *Scr. Mater.* 60 (2009) 835–838. doi:10.1016/j.scriptamat.2008.12.059.

- [165] J. Trapp, B. Kieback, Temperature Distribution in Metallic Powder Particles during Initial Stage of Field-Activated Sintering, *J. Am. Ceram. Soc.* 98 (2015) 3547–3552. doi:10.1111/jace.13757.
- [166] D. Tiwari, B. Basu, K. Biswas, Simulation of thermal and electric field evolution during spark plasma sintering, *Ceram. Int.* 35 (2009) 699–708. doi:10.1016/j.ceramint.2008.02.013.
- [167] K. Vanmeensel, A. Laptev, J. Hennicke, J. Vleugels, O. Van Der Biest, Modelling of the temperature distribution during field assisted sintering, *Acta Mater.* 53 (2005) 4379–4388. doi:10.1016/j.actamat.2005.05.042.
- [168] N. Bertolino, J. Garay, U. Anselmi-Tamburini, Z.A. Munir, High-flux current effects in interfacial reactions in Au–Al multilayers, *Philos. Mag. B.* 82 (2002) 969–985. doi:10.1080/13642810208218356.
- [169] S. Diouf, A. Molinari, Densification mechanisms in spark plasma sintering: Effect of particle size and pressure, *Powder Technol.* 221 (2012) 220–227. doi:10.1016/j.powtec.2012.01.005.
- [170] A. Zavaliangos, J. Zhang, M. Krammer, J.R. Groza, Temperature evolution during field activated sintering, *Mater. Sci. Eng. A.* 379 (2004) 218–228. doi:10.1016/j.msea.2004.01.052.
- [171] Z. Shen, M. Johnsson, Z. Zhao, M. Nygren, Spark Plasma Sintering of Alumina, *J. Am. Ceram. Soc.* 27 (2016) 1921–27. doi:10.1111/j.1151-2916.2002.tb00381.x.
- [172] K.N. Allahar, J. Burns, B. Jaques, Y.Q. Wu, I. Charit, J. Cole, D.P. Butt, Ferritic oxide dispersion strengthened alloys by spark plasma sintering, *J. Nucl. Mater.* 443 (2013) 256–265. doi:10.1016/j.jnucmat.2013.07.019.
- [173] Y.P. Xia, X.P. Wang, Z. Zhuang, Q.X. Sun, T. Zhang, Q.F. Fang, T. Hao, C.S. Liu, Microstructure and oxidation properties of 16Cr-5Al-ODS steel prepared by sol-gel and spark plasma sintering methods, *J. Nucl. Mater.* 432 (2013) 198–204. doi:10.1016/j.jnucmat.2012.07.039.
- [174] Q.X. Sun, T. Zhang, X.P. Wang, Q.F. Fang, T. Hao, C.S. Liu, Microstructure and mechanical properties of oxide dispersion strengthened ferritic steel prepared by a novel route, *J. Nucl. Mater.* 424 (2012) 279–284. doi:10.1016/j.jnucmat.2011.12.020.
- [175] M.A. Auger, Y. Huang, H. Zhang, C.A. Jones, Z. Hong, M.P. Moody, S.G. Roberts, P.S. Grant, Microstructural and mechanical characterisation of Fe-14Cr-0.22Hf alloy fabricated by spark plasma sintering, *J. Alloys Compd.* 762 (2018) 678–687. doi:10.1016/j.jallcom.2018.05.196.
- [176] X. Zhou, C. Li, L. Yu, H. Li, Y. Liu, Effects of Ti addition on microstructure and mechanical property of spark-plasma-sintered transformable 9Cr-ODS steels, *Fusion Eng. Des.* 135 (2018) 88–94. doi:10.1016/j.fusengdes.2018.07.019.
- [177] X. Zhou, Y. Liu, L. Yu, Z. Ma, Q. Guo, Y. Huang, H. Li, Microstructure characteristic and mechanical property of transformable 9Cr-ODS steel fabricated by spark plasma sintering, *Mater. Des.* 132 (2017) 158–169. doi:10.1016/j.matdes.2017.06.063.
- [178] Q.X. Sun, Y. Zhou, Q.F. Fang, R. Gao, T. Zhang, X.P. Wang, Development of 9Cr-ODS ferritic-martensitic steel prepared by chemical reduction and mechanical milling, *J. Alloys Compd.* 598 (2014) 243–247. doi:10.1016/j.jallcom.2014.02.030.
- [179] K. Rajan, T. Shanmugasundaram, V. Subramanya Sarma, B.S. Murty, Effect of Y₂O₃ on spark plasma sintering kinetics of nanocrystalline 9Cr-1Mo ferritic oxide dispersion-

- strengthened steels, *Metall. Mater. Trans. A Phys. Metall. Mater. Sci.* 44 (2013) 4037–4041. doi:10.1007/s11661-013-1845-1.
- [180] H. Zhang, Y. Huang, H. Ning, C.A. Williams, A.J. London, K. Dawson, Z. Hong, M.J. Gorley, C.R.M. Grovenor, G.J. Tatlock, S.G. Roberts, M.J. Reece, H. Yan, P.S. Grant, Processing and microstructure characterisation of oxide dispersion strengthened Fe–14Cr–0.4Ti–0.25Y₂O₃ ferritic steels fabricated by spark plasma sintering, *J. Nucl. Mater.* 464 (2015) 61–68. doi:10.1016/j.jnucmat.2015.04.029.
- [181] M.K. Dash, R. Mythili, R. Ravi, T. Sakthivel, A. Dasgupta, S. Saroja, S.R. Bakshi, Microstructure and Mechanical Properties of Oxide Dispersion Strengthened 18Cr-Ferritic Steel Consolidated by Spark Plasma Sintering, *Mater. Sci. Eng. A.* (2018). doi:10.1016/j.msea.2018.08.093.
- [182] I. Bogachev, E. Grigoryev, O.L. Khasanov, E. Olevsky, Fabrication of 13Cr-2Mo ferritic/martensitic oxide-dispersion-strengthened steel components by mechanical alloying and spark-plasma sintering, *Jom.* 66 (2014) 1020–1026. doi:10.1007/s11837-014-0972-5.
- [183] B. Mouawad, X. Boulnat, D. Fabregue, M. Perez, Y. de Carlan, Tailoring the microstructure and the mechanical properties of ultra fine grained high strength ferritic steels by powder metallurgy, *J. Nucl. Mater.* 465 (2015) 54–62. doi:10.1016/j.jnucmat.2015.05.053.
- [184] M.S. Staltsov, I.I. Chernov, I.A. Bogachev, B.A. Kalin, E.A. Olevsky, L.J. Lebedeva, A.A. Nikitina, Optimization of mechanical alloying and spark-plasma sintering regimes to obtain ferrite–martensitic ODS steel, *Nucl. Mater. Energy.* 9 (2016) 360–366. doi:10.1016/j.nme.2016.08.020.



2

Objectives and motivation

2.1. Motivation

The energetic demand promoted during the last few years and the environmental laws legislated on Paris agreement have impulse the energetic industry to evolve into new designs to fulfil a generic objective: less emission and higher efficiency. On first instance renewable energies have been focusing the academia attention; whereas, the nuclear industry is postulated as the energy of present and near future owing to the amount of electricity supplied [1].

However, the term nuclear is always related to serious human and environmental catastrophes related to important accidents (as notorious as Chernovil or Fukushima) or the management of radioactive waste. Therefore, the nuclear research is based on improving safety and durability without losing the efficiency. On this scenery investigations related to structural materials attained a great importance.

Materials science focuses on nuclear reactors must overcome irradiation, corrosion, high temperature behaviour, metal liquid coolant... [2]. Fulfilling the requirements represents one of highest limitations and motivation of this research. In this scenery, Ferritic ODS steels are postulated as an important alternative material to be used on new GENIV reactors.

Indeed, choosing the correct composition was the encouragement of a great part of the researchers in the past [3] and where this thesis was framed. Therefore, beating the irradiation, a BCC crystal structure is selected. Oxidation and corrosion are faced with Cr and Al. Finally, the high temperature resistance is provided by W, Cr and the fine dispersion of oxides, promoted by Y_2O_3 and Ti. Precisely, seeking for smaller and thermally stable precipitates, Zr is added to favour YZrO oxides. This represents one of the central inspirations on this thesis.

Besides, the biggest challenge is to control the different interactions between the oxides formers (Y, Al, Ti, Zr) since the precipitates nature will determine directly the final creep behaviour. Consequently, one particular goal of this manuscript is to regulate the environments and formed precipitates.

Actually, one essential incentive is to understand whose system are determining the great thermal behaviour and why. These phenomena are studied in this work by using different techniques, analysing the main important strengthening mechanisms, as well as the relation between the production procedure and the final microstructure.

On the other side, the production of the material is quite important when costs are faced. Improving the way in which ODS steels are produced is also one of the main interests. Usually, the production starts from mechanical alloying. This important step determines the final microstructure attained. Therefore, an interesting motivation is to understand the effect of milling parameters. On the other side, the sintering process is also under review. Spark plasma sintering is a technique widely extended which has been used during the last years to obtain ferritic steels. One of the main motivations of using these techniques is the shorter sintering times which can provide some specific microstructure (small grain sizes) and reduce the times of production which finally reduce the costs. Precisely, one interesting motivation is to understand the effect of the different SPS parameters since many things are still unknown in ODS steel.

To conclude with, the development of ODS ferritic steels passes through the step followed during this research. Understanding this material represents the biggest challenge and motivation.

2.2. Objectives

This current PhD thesis set out to investigate the development of a competitive ferritic ODS steel (Fe-14Cr-5Al-3W-0.25Y₂O₃-0.6Zr-0.5Ti) to be used in the new GenIV reactors. The project therefore moves on to assess the proper microstructure of the material. It is centred on the production of the material, the study of the microstructure effect and nano-oxides in the mechanical properties, and on the understanding of the final thermal stability. Different partial goals have been established to fulfil all the objective of the thesis.

Starting with the processing route (Chapter 4 and 5) the main goals are:

- To optimize the milling conditions and to analyse their effect on the final microstructure.
- To understand how SPS parameters determine the final densifications and the achieved microstructure.

Continuing with the addition of Zr (Chapter 4, 5 and 7) the main objectives are:

- To study the interaction produced by the different oxides formers (YAlZrTi).
- To develop high stable Y-Zr-O nanoparticles in Al containing alloys (Instead of Y-Al-O compounds).
- To study if some refinement is attained (Small size and higher precipitation state).
- To control the different interactions of the oxides carrier by adding co-precipitated Y-Ti-Zr-O nanoparticles.

Moreover, facing mechanical properties (Chapter 4, 5 and 7)

- To analyse the effect of modifying the microstructure by MA and SPS
- To study the effect of Zr on the final alloy.
- To evaluate the materials behaviour under high temperature conditions.
- To determine the different strengthened method and to understand their influence.

Finally, facing thermal stability (Chapter 6):

- To study new method of evaluation such as In-situ Tem annealing and their viability.
- To analyse the stability of the material, the nanoprecipitates developed and the microstructural stability.

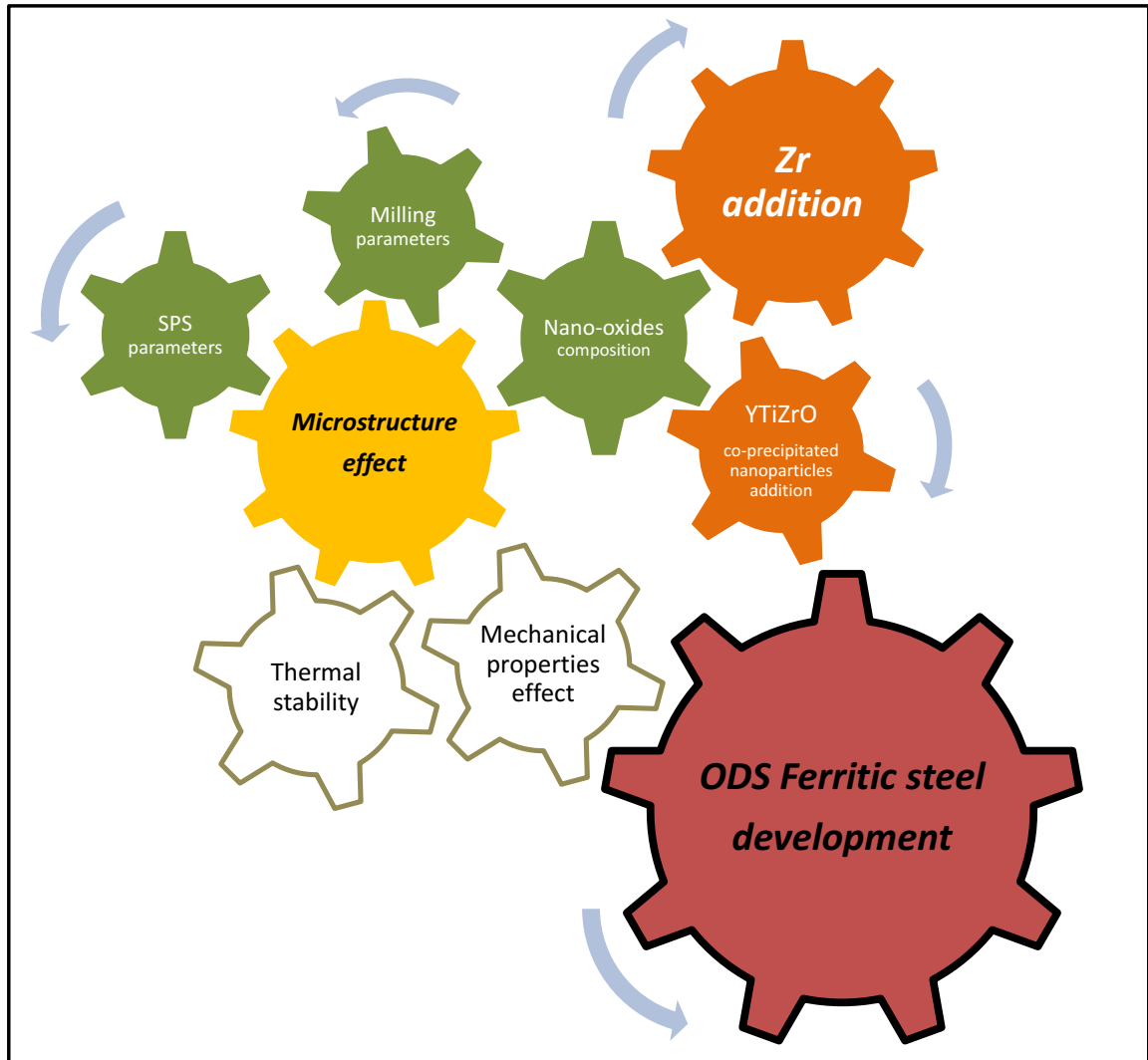


Fig 2.1. Schematic gears of this research.

Bibliography

- [1] S.J. Zinkle, J.T. Busby, Structural materials for fission & fusion energy, *Mater. Today*. 12 (2009) 12–19. doi:10.1016/S1369-7021(09)70294-9.
- [2] D.L. Smith, M.C. Billone, S. Majumdar, R.F. Mattas, D.K. Sze, Materials integration issues for high performance fusion power systems, *J. Nucl. Mater.* 258–263 (1998) 65–73. doi:10.1016/S0022-3115(98)00355-9.
- [3] S.J. Zinkle, A. Möslang, T. Muroga, J.L. Boutard, D.T. Hoelzer, A. Kimura, R. Lindau, G.R. Odette, M. Rieth, L. Tan, H. Tanigawa, Development of next generation tempered and ODS reduced activation ferritic/martensitic steels for fusion energy applications, *Nucl. Fusion*. 57 (2017) 17. doi:10.1088/1741-4326/57/9/092005.

3

*Materials and experimental
procedure*

Contents

3.1. Methodology	53
3.2. Materials	54
3.2.1. Nano-oxides synthesis by co-precipitation	54
3.3. Processing of the powdered ferritic ODS steel by MA	55
3.3.1. Milling parameters optimization	55
3.4. MA powder consolidation	57
3.4.1. Field assisted hot pressing (FAHP).....	57
3.4.2. Spark Plasma Sintering (SPS)	58
3.5. Characterization of sintered samples	59
3.5.1. Density measurement	59
3.5.2. Microstructural characterization.....	59
3.6. Mechanical properties	61
3.6.1. Microhardness	62
3.6.2. Tensile tests.....	62
3.6.3. Small punch test	62
Bibliography	64

3.1. Methodology

This research studies different ODS ferritic stainless steels containing Al, from the development of the alloy until the evaluation of the thermal stability and mechanical properties at high temperatures. ODS steels group four are steels in which the oxide formers are set by four elements with high oxygen activity, in this case by YTiZrAl. Their interaction will be taken into account to understand the final performance of the developed material.

This Thesis was divided into two main blocks. On first part, in order to study the effect of Zr on the ODS Al containing alloy, $Y_2O_3+Ti+Zr$ were introduced as an oxides formers. On the second part, with the main objective of promoting a better interaction among oxide formers by creating an enriched environment in $Y-Ti-Zr$, a new complex compound $Y-Ti-Zr-O$ were synthesized.

In both cases, oxides formers were mechanically alloyed (MA) to the prealloyed Fe-Cr-W-Al powder grade and finally consolidated by FAST techniques.

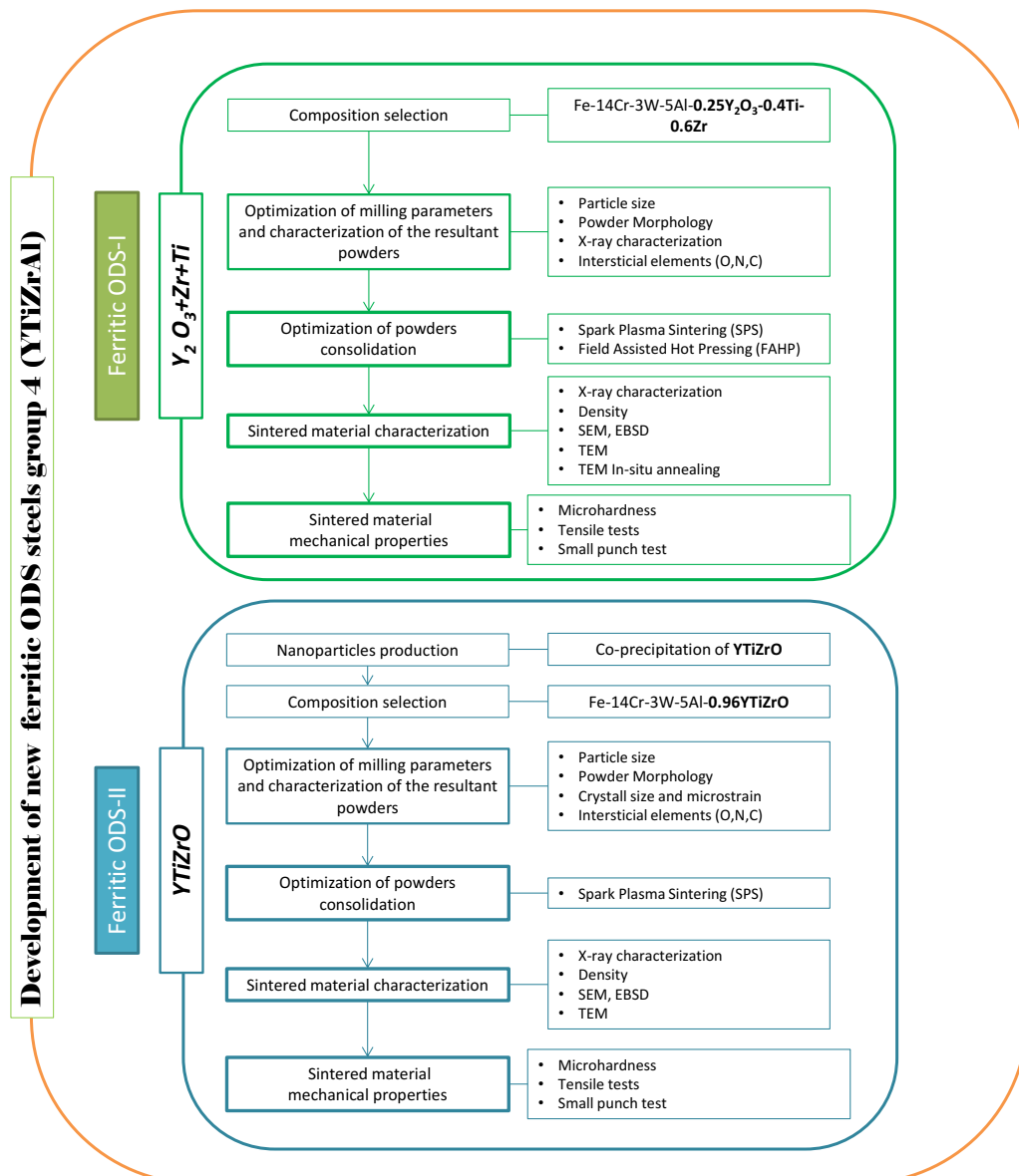


Fig 3.1. Experimental procedure scheme.

The results from Ferritic ODS-I will be discussed on chapter 4, 5 and 6 meanwhile ferritic ODS II will be shown on chapter 7. Each result's chapter allows the understanding of the parameters which are directly determining the microstructure and mechanical properties in ODS alloys.

3.2. Materials

Based on previous studies developed in the research group [1,2] a prealloyed powder (Fe-14Cr-3W-5Al) was mechanical alloyed with 0.25 Y₂O₃ and 0.4 Ti. Besides, in this project the effect of Zr addition (0.6 %) is explored. This research also investigated a ferritic ODS obtained by the addition of one complex oxide Y-Ti-Zr-O nanoparticle synthesized by co-precipitation. Oxide nanoparticles were added to the prealloyed powder (Fe-14Cr-3W-5Al) by using mechanical alloying as well. Powders characteristics are sum up in table 3.1.

Table 3.1. Characteristics of the powders used in this research.

Powder	Composition (wt%)	Supplier	Size
Fe-Cr-W-Al	Fe-14Cr-3W-5Al	Sandvik Osprey	30 μm
Ti	0.4	GfE Gesellsch	50 μm
Y ₂ O ₃	0.25	TJ Tech. & Mater Inc	7 μm
Zr	0.6	Goodfellow	40 μm
YTizrO	0.96	In home production	20 nm

The composition of Ferritic ODS I (F-ODS-I) and Ferritic ODS II (F-ODS-II) families is specified in table 3.2. The amount of complex Y-Ti-Zr-O compound for F-ODS-II was selected as 0.96 wt % trying to maintain the same level of Yttrium (0.20% Y) than in F-ODS-I.

Table 3.2. Composition of the processed ferritic ODS alloys (wt.%).

Tag	Prealloyed Fe-14Cr-5Al-3W	Ti	Zr	Y ₂ O ₃	Complex Y-Ti-Zr-O
F-ODS-I	Balance	0.4	0.6	0.25	-
F-ODS-II	Balance	-	-	-	0.96

3.2.1. Nano-oxides synthesis by co-precipitation

The synthesis of nano complex oxides powders, Y-Ti-Zr-O, was carried out by co-precipitation using as precursors yttrium nitrate (Y(NO₃)₃·6H₂O), titanium isopropoxide (Ti(OCH(CH₃)₂)₄) and zirconium n-butoxides (Zr(OCH(CH₃)₃)₄). Each precursor was individually diluted in 5 ml of isopropanol to avoid unexpected segregations. After that, the three dissolutions were mixed in aqueous solution keeping 10 pH by the addition of concentrated NH₄OH [3]. The co-precipitation was continued for one hour. To remove all the residues produced during the co-precipitation, the precipitates powders (~6 g) were filtered out, washed up several times by using distilled water and a mixture of methanol and ethanol in equal proportion (50% in vol.). Then, powders were dried up in a hot plate and pyrolysed at 700 °C for 1 h in air. To crystallize the powders, another thermal treatment was performed at 850 °C during 30 min using a heating rate of 10 °C/min in air. The whole process is summed up in Fig 3.2.

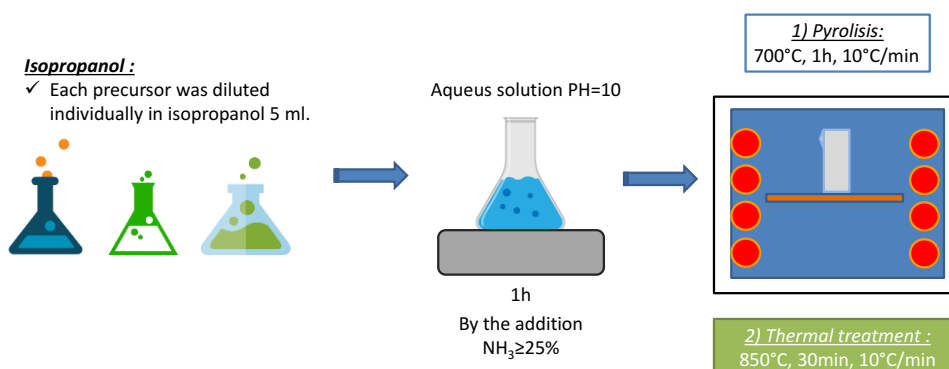


Fig 3.2. Scheme of the co-precipitation followed to obtain Y-Ti-Zr-O nanoparticles.

3.3. Processing of the powdered ferritic ODS steel by MA

Oxides formers were mechanically alloyed to the prealloyed ferritic powder. An *Attritor* type milling was employed (*Simoloyer ZOZ CM01, software Maltoz*) to produce the ODS powders. This type of milling allows to process bigger powder batches than planetary mills (~ 125 g per batch vs. 50 g) and to better control the atmosphere and the temperature inside the vessel during the whole process. Temperature can rise because of the energy released by the impact between balls, blades, vessel and powder.

Several parameters will affect the final powder properties [4]. Among these, can be underline the speed (rpm), the ball to powder ratio, the effective milling time, the atmosphere and the temperature. Trying to limit the contamination coming from grinding media, stainless steels were selected as milling tool material. By using protective atmosphere, oxygen and nitrogen soaking up were controlled. In this case pure Argon (99.9997 vol%) was inlet after vacuum purge the system several times.

Selecting appropriately these parameters, two milling experiments, *MA standard* (M_{st}) and *MA activated* (M_{act}) were designed. Details of milling processes are gathered in Fig 3.3.

Parameters	M_{st}	M_{act}
Ball to powder ratio	20:1	
Milling rate	700 rpm	800 rpm
Effective milling time	60h	50 h
Resting time	10 min	20 min

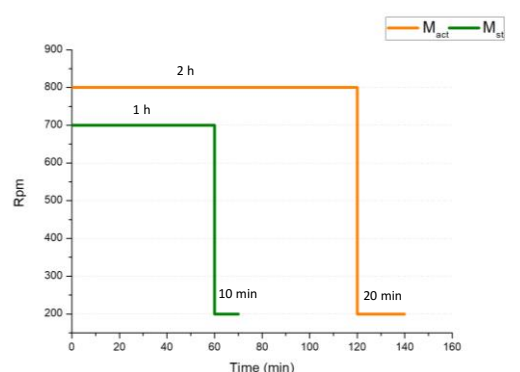


Fig 3.3: Milling parameters for both milling experiments.

In order to step down the energy inside the mill and, consequently, the impact between balls and powder, trying to avoid any kind of overheating inside the mill and hence a welding between powder and balls, it is necessary to reduce the rpm at regular intervals. For example, if the milling was performed at 800 rpm during 2 h, the speed is cut down until 200 rpm during 20 min to avoid this phenomenon.

Besides, attritor type milling allows to extract powder samplings to control MA procedure. For this purpose an extraction tower is used. Subsequent Ar filling and vacuum purges, ensure the atmosphere of the tower. Apart from that, all powder manipulation was conducted in a glove box to delay the contact of the milled powder with the regular atmosphere, trying to control the oxygen and nitrogen absorption.

3.3.1. Milling parameters optimization

Plastic deformation, welding and fracture are the three mechanisms that control the powder evolution with milling time. Milling time has to be set in order to obtain optimum powders for further consolidations. Therefore, different parameters such as particle size distribution, crystallite size and microstrain are used to control the powder progression.

- **Particle size distribution by light diffraction**

Particle size distribution was obtained by using the *DLS Mastersizer 2000 (Malvern instruments Ltd)* equipped with a wet sample dispersion unit Hydro Sm (Malvern Instrument LTD). Laser diffraction is used to measure the size of the particle following the standard ISO13320. Particle size is determined thanks to the light intensity angular variation when a laser beam passes

through a dispersion of solid particles. Larger particles scatter the light at small angles meanwhile smaller particles scatter at low angles. Using this information, the equipment is capable to analyse the scattered pattern obtaining the particle size distribution as a function of the volume. In order to avoid particles agglomerations is necessary to choose the correct dispersant (it could be water or ethanol), and to disperse powders by using ultrasound equipment for 15-20 min.

- ***Particle morphology and microstructure characterization by Scanning Electron Microscopy***

By SEM microscopy it is possible to study the size, morphology and microstructure evolution of the powder as a function of milling time. To analyse the morphology, the powder is deposited in a carbon film. To study the microstructure, powder has to be mounted in resin and conventionally polished in order to obtain a good surface quality. In this research, a Philip XL-30 with a W filament and EDAX DX-4 detector was used. Apart from that a FEG SEM Teneo was operated too.

- ***X-ray diffraction: crystallite size and internal strain***

During the plastic deformation-fracture and welding of the MA powder, structural changes are induced in the Fe base lattice. The evolution of nanostructured materials can be monitored by measuring crystallographic parameters as crystallite size and internal strain by X-Ray diffraction [5,6]. In this case, experiments were done with different instruments:

- ***Ferritic ODS I:***

X'pert Philipps diffractometer (Cu radiation, $\gamma=1.542 \text{ \AA}$) in the range of 35° to 90° using a step size of 0.02° and a time per step 2.4 s. Some diffractometer were also realized in CSIC by using *X-Bruker AXS D discover* provided (Co filament $\gamma=1.78 \text{ \AA}$) and whose conditions were a step size of 0.0148 and a time per step of 307 seconds .

- ***Ferritic ODS II:***

The equipment selected was a *Bruker AXS, D8Advance (Cu filament $\gamma=1.542 \text{ \AA}$)* with a step size of 0.009° and step time per second of 612.

X'pert High Score software was used to identify the different phases. Measurements of both crystallographic parameters were done via the software *Philip Xpert data viewer*.

To obtain these values Scherrer method was used [7]. By this method the crystal size is related to Bragg angle (θ) and to the full width at half maximum intensity (FWHM) by the next equation (1):

$$\beta = \frac{K \times \gamma_{\alpha 1}}{L \times \cos \theta} \quad (\text{Eq 3.1})$$

K is the dimensionless shape factor close to 0.9, β is FWHM, L is the crystallite size, $\gamma_{\alpha 1}$ is the wave length. In this study, β was taken from the most intense peak.

The microstrain value (ϵ) was calculated by using the equation (3.2):

$$\beta = 4\epsilon \tan \theta \quad (\text{Eq 3.2})$$

When it is necessary to evaluate an average microstrain value, Williamson-Hall equation was selected (equation (3.3)). This is the case of strengthening calculations in Chapter 5:

$$\frac{\beta \cos \theta}{\gamma} = \frac{0.9}{L} + 2\epsilon \frac{\sin \theta}{\gamma} \quad (\text{Eq 3.3})$$

- ***Chemical analysis: Measuring the quantity of interstitials elements***

During mechanical alloying process, the obtained milled powder is highly reactive and can pick up easily interstitials elements as oxygen and nitrogen from the atmosphere. Besides, carbon coming also from grinding media could produce carbides that modify the hardness of the milled powders, conditioning the particle evolution. To measure the oxygen, nitrogen and carbon content *LECO TC-500* and *LECO CS-200* equipment were operated.

To analyse oxygen and nitrogen, the sample (300 mg) is deposited in a graphite crucible and introduced into a specific furnace into LECO equipment. After fusion, carbon from the crucible reacts with oxygen coming from the sample, giving as a result CO and CO₂. Besides, nitrogen is released as molecular N₂. He which is flowing inside the LECO system will drag those compounds to an infrared cell which measures the oxygen and nitrogen content.

To measure the carbon content, the sample (300 mg) is deposited in an alumina crucible and after that fuse in an induction furnace inside the LECO CS-200 system. Besides, to achieve the right temperature to induce the combustion it is necessary to add an accelerator agent (Lecocel II). O₂ is flowing inside the equipment deliver CO as soon as carbon reacts with oxygen. At the same time, O₂ drag up CO to an infrared cell in which the quantity of carbon is measured.

The amount of oxygen is evaluated through:

- The amount of oxygen measured by the equipment (%wt).
- The Excess of oxygen (Ex.O) defined as the oxygen quantity measured minus the oxygen amount provided by Y₂O₃. This parameter shows the enrichment of oxygen of the milled powder.

3.4. MA powder consolidation

3.4.1. Field assisted hot pressing (FAHP)

With the aim of obtaining a fully consolidated sample, powders obtained by MA under M_{st} conditions were consolidated by using field assisted hot pressing technique (FAHP) with a Gleeble 3800 equipment. In this technique, the powder is pressed and heated simultaneously, on a graphite die (10 mm diameter) under vacuum (10⁻⁵ Pa). Powders sinter thanks to the Joule effect produced for the alternative current applied into the powdered sample through the punches.

The level of current is automatically regulated because of the difference between the programmed temperature and the powder temperature measured by the thermocouples inserted into the graphite punches. Temperature can be also measured with a thermocouple inserted in the middle of the die. This signal is a better reference of the achieved temperature into the sample. In order to avoid the graphite contamination, a high-purity tungsten foil (%W > 99.97 and 25 µm thickness) was used during the sintering process to cover the die wall and punches [8].

To design the sintering cycle, dilatometry mode was done in the Gleeble equipment. In this case, the applied pressure was 5 MPa, the heating rate was 25 °C/min and the final temperature was 1300 °C. Considering these results, once the compact starts to shrink will be the point in which the load will be increased up to 80 MPa.

Sinterability of MA powders was studied as well by changing the starting point, powder or a preform ('P-Optimized cycle') or when is considered directly powders (addressed as 'single cycle' or 'T-Optimized cycle' (Table 3.3).

Table 3.3. Different cycles followed during the FAHP consolidation

Initial material	Cycle		Labelled
Powder	Dilatometry mode	P: 5MPa; 25 °C/min, 1300 °C (no dwell)	
	Single Cycle	P: 80MPa; 100 °C/min, 1250 °C (10min dwell)	14Zr-t1
	T-Optimized	P1: 20 up to 1050 °C-2min + P2: 80 MPa up to 1250 °C (20min dwell) 100 °C/min	14Zr-t2
Preform	T-Optimized	P1: 20 up to 1050 °C-2min + P2: 80 MPa up to 1250 °C (20min dwell) 100 °C/min	14Zr-opt

3.4.2. Spark Plasma Sintering (SPS)

Looking for a higher densification of the material, SPS was also considered as consolidation technique for powders obtained by high energy milling (M_{std} and M_{act} conditions). SPS is an alternative technique to consolidate metallic or ceramic powder widely extended on the last few years. The shorter sintering times together with the lower sintering temperature allow to consolidate powder with an specific microstructure [9]. A pulsed current passes directly through the powder and the graphite die, and heat the sample due to the Joule effect (Fig 3.5). The level of current is automatically regulated controlling the powder and programmed T [10–12]. Different systems can be used to measure the powder temperature inside the die that will determine the selection of SPS parameters. With the aim of processing a fully dense material, the effect of applied pressure, maximum T, holding time or heating rate will be studied.

To process discs of 20 mm of diameter and 4-5 mm in thickness, 10 g of milled powder was used to fill up the graphite die.

First consolidation was conducted to determine the optimum milling parameters, sintering milled powders – M_{st} and M_{act} - using *SPSSintex Inc. model 3.20 MK-V* (in Daegu Mechatronics & Materials Institute, South Korea). The temperature was controlled by two thermocouples one in the upper punch and the other one inserted in the matrix. To avoid the graphite contamination sprayed BN was used. The operated conditions are summarized on table 3.4.

Table 3.4. Preliminary studies of T effect on F-ODS-I steel family.

	Condition	Temperature (°C)	Labelled Samples (F-ODS-I)
M_{std}	50 MPa, 100 °C/min, 3min	1100	$M_{std,1100}$
		1150	$M_{std,1150}$
M_{act}		1100	$M_{act,1100}$
		1150	$M_{act,1150}$

With the aim of studying the heating rate effect on the final microstructure, specimens were sintered following the parameters of Table 3.5. In this occasion, the equipment was a *FCT system GMBH*, (operated in CINN Asturias, Spain). Pyrometer systems inserted in the upper punch controls the powder temperature. Again, to avoid graphite contamination a W foil was used.

Table 3.5. Heating rate effect on F-ODS-I steel family milled under M_{act} condition.

Fixed parameters	Heating rate (°C/min)	Labelled samples (F-ODS-I)
80 MPa, 1100 °C, 5min	100	Zr100
	200	Zr200
	400	Zr400
	600	Zr600

In addition, the synergetic effect of the maximum temperature and heating rate (HR) on final performance were considered. The sintering tests were done using a FCT-HP D 250/1 SPS equipment in (IFAM, Dresden). The conditions studied are sum up in Table 3.6.

Table 3.6. T and Heating rate effect on F-ODS-II steel family milled under M_{act} condition

Fixed parameters	Heating rate (°C/min)	Temperature (°C)	Labelled samples (F-ODS-II)
57 MPa, dwell 3min	100	1100	YTiZr100-T ₁
		1150	YTiZr100-T ₂
		1200	YTiZr100-T ₄
	300	1150	YTiZr300-T ₂
		1180	YTiZr300-T ₃
		1200	YTiZr300-T ₄
	500	1150	YTiZr500-T ₂

3.5. Characterization of sintered samples

As soon as the samples are consolidated, it is necessary to evaluate the microstructural features achieved to understand the final behaviour at room and high temperature.

3.5.1. Density measurement

Different methods were used to evaluate the final density of the sample. He pycnometer and Archimedes' method were considered to study the final density.

Also density level were analysed by using images analysis method (Fig 3.4) with *J microvision free software* tool. To do this, SEM images are binarized to highlight the material porosity. The software automatically analyses the area (%) related to the red spots which allows to study directly the sample density. In total five micrographs per sample, which represent aprox $9 \cdot 10^5 \mu\text{m}^2$, were considered to estimate the density by this method.

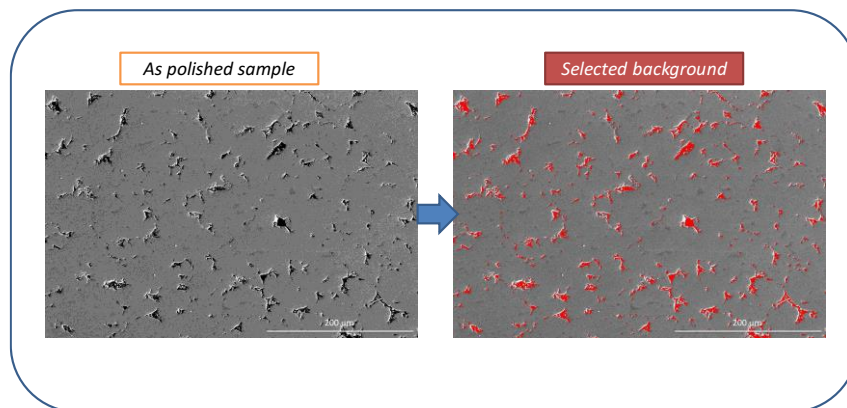


Fig 3.4: Image analysis for density measurements (sample from FAHP process).

3.5.2. Microstructural characterization

Different techniques were studied to evaluate the microstructural properties of the sintered materials: SEM with EBSD detector, TEM and TEM with simultaneous heating.

- **Scanning electron microscopy characterization**

FEG SEM FEI was used to characterize the microstructure of consolidated samples. Indeed, surface preparation was required. Samples were mounted in conductive resin and polished up to silica gel $0.03 \mu\text{m}$. After that, electro polishing was done to enhance the quality of the surface by using Struers Tecnopol using A3 electrolyte (Struers).

EBSD detector was utilised in this research to determine the grain size distribution, crystal size orientation and misorientation maps. EBSD maps are composed by moving an electron beam point by point across a grid of positions [13]. At each point some electrons are backscattered and collected by a detector giving as a result a map. Electrons that fulfil the Bragg equation diffract and form Kikuchi bands, which correspond directly to the atomic lattice planes. To complete these rules, it is necessary to place samples inside SEM at high tilted angles (70-75°).

Achieving the proper surface conditions by electropolishing the samples is mandatory to increase the quality of the indexed patterns. The condition used for this research were 2000x magnification, 15 kV, 5.5 nA, 4x4 high resolution and a step size of 0.08 μm . Grain size were measured by using grain ellipse fitting [14] as it is shown in Fig 3.5. To establish the grain boundaries, frontier were defined as a low misorientation (2-10°) and high misorientation (up to 10°).

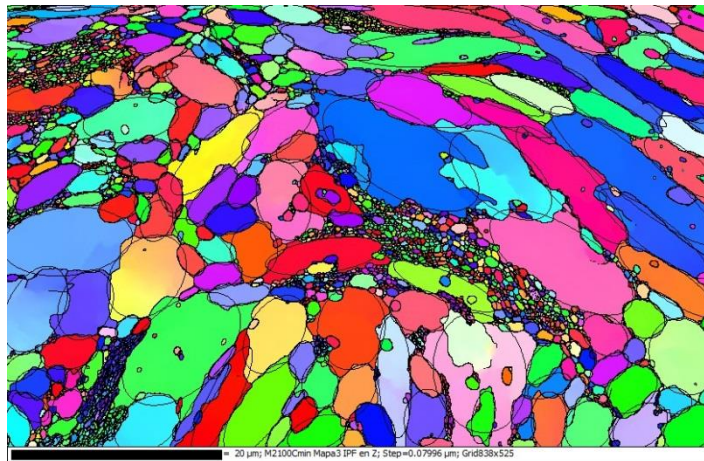


Fig 3.5. Ellipse fitting realized for measuring grains in EBSD technique.

- **TEM characterization**

High resolution TEM images are used to analyse nanometre particles [15]. The behaviour of ODS steels is based on the homogeneity of oxides dispersion, their composition, sizes, structure and location. These characteristics can be only determined by TEM.

This study was done by using a FEG S/TEM (Talos F200X, FEI-IMDEA Materials-). Samples preparation is one of the key issues in this technique. Discs of 3 mm diameter were machined from consolidated sample (transversal to the direction of the SPS) and mechanical polished until 100 μm . Final thinning was performed by using electro polishing at -60 °C and 22 mV in a solution of 5 % perchloric acid in methanol.

Thanks to the possibility of removing material by using FIB milling it is possible to prepare specimens for TEM observations on transparent foils called lamella (Fig 3.6) (FIB-FEGSEM Helios NanoLab 600i, FEI). FIB unlike SEM microscopy, uses accelerated ions instead (Ga^+) of e^- . The collisions of ions with the target material cause material ejection and secondary e^- emission.

Preparation of foils transparent to e^- was performed by using the called lift-out technique (Fig 3.7). Once the area of interest is selected, Pt protective layer is deposited to protect the specimen from the Ga^+ damaging. Rough milling is carried out to remove the surrounding material and left foils of 2 μm thickness. Operational current in that case must be set between 10 and 20 nA. To lower the thickness and polish the surface, beam currents is kept below pA (40 to 80 pA). Finally, the final sample is attached to a TEM grid thanks to a Pt manipulator in which the lamella is fixed. After the right positioning of lamella on the grid the manipulator is removed by using low current beam (0.79 to 2.5 nA).

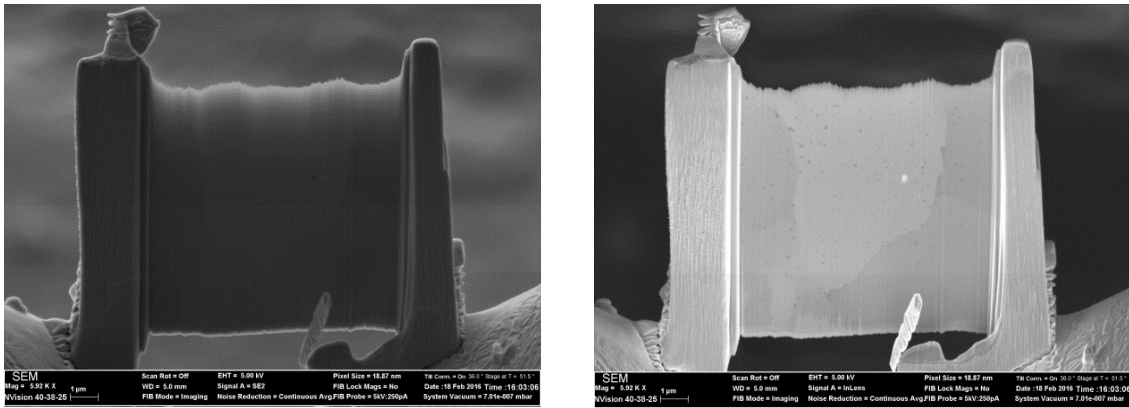


Fig 3.6. Lamella obtained by FIB on ferritic ODS steel.

TEM bright field and dark field images are used to characterize size and morphology of precipitates. Besides weak dark beam field, EDX, and STEM (HAADF detector) were also selected to study the oxides composition and distribution.

In order to evaluate the thermal stability of ODS Ferritic steels, in-situ TEM annealing was performed. This method allows to:

- Study the microstructure evolution after applying the thermal treatment.
- Analyse the morphology size and localization of nanoxides.
- Identify the dislocation structure and the effect of the temperature on them.

In situ TEM annealing was accomplished on a JEOL JEM 2010 equipped by a doubled tilt sample holder furnace with allows achieving temperatures around 1000 °C. Besides, up to 500 °C a water cooling systems is used to evacuate the excessive temperature and avoid damages on the holder.

For this experiment, disc of 3 mm diameter were final thinning by electro polishing at -60°C and 22 mV in a solution of 5% perchloric acid in methanol. Normally, the working temperature of ODS steels is on the range of 500 to 600 °C. For this reason, the maximum temperature was selected up to 600°C. Intervals of 100 °C were set from 200 °C to 600 °C using a heating rate of 20 °C/min (Fig 3.7). During the in-situ test annealing, an isothermal dwell (45') was followed on each step, recording 15' video in the dwell.

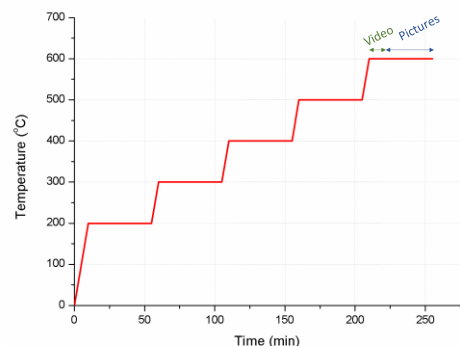


Fig 3.7. Cycle followed during the in-situ TEM annealing test.

Using Bright Field (BF) and Weak Beam Dark Field (WBDF), grain and oxide stability were evaluated. Measurement were done with *Jmicrovision free software*. A total of 2100 oxides were measured to achieve the final distribution reported.

3.6. Mechanical properties

Mechanical properties at room and high T were measured to understand the effect of the obtained bimodal grain microstructure and of the oxide dispersion on the material performance.

3.6.1. Microhardness

Because of its specificity, this type of testing is applicable in those cases where the material shows changes at microstructural level, that is the case of processed ODS where a bi-modal grain size is developed.

Microhardness was determined after 20 indentations. All measurements were done on the complete circular section, drawing a cross on the sample. In order to evaluate the complete microstructure, random measurements were done following the UNE-EN ISO 6507-1:2006 standard. A Zwick Indentec Hardness Testing Machines was used with a load of 200 gf (roughly equivalent to 2 N).

3.6.2. Tensile tests

In this research, miniature tensile specimens were considered to characterize the tensile behaviour due to the material restrictions. Although it is not a normalized test, the results and values can be comparable to the standard one. The geometry of the tensile bones is described in Fig 3.8.

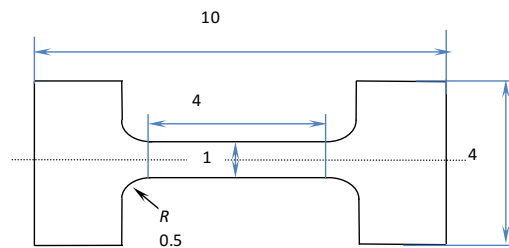


Fig 3.8. Tensile bone sample geometry that assures uniform deformation, cross section of $1 \times 1 \text{ mm}^2$ [16].

A Kammarath and Weiss device (IMDEA materials Institute) was used to perform the tests. The maximum load used was 10 kN and the displacement speed $2 \cdot 10^{-3} \text{ mm} \cdot \text{s}^{-1}$.

The toughness is calculated as the area under the entire stress-strain curve until fracture (equation 3.4). For this reason the units provided are $\text{MPa} \cdot \text{J/m}^3$. It can be considered as the maximum energy per unit volume that the sample can absorb before it fails completely due to fracture. Toughness, measured in this way, can be compared with previous ODS developed in the same research group and analysed in the same way [1].

$$\text{Toughness} = \int_0^{\epsilon_f} \sigma d\epsilon \quad (\text{Eq 3.4})$$

In-situ tensile test on SEM allows to study the crack initiation and propagation. To perform this test, micro-tensile machine is introduced in the SEM by using a special holder. The sample has been polished until mirror like surface quality. To take micrographs, the test must be stopped every certain elongation without release the applied load. In this research, the test was stopped just after stating the plastic deformation, when elongation attained 350, 450, 600, 750, 850, 950 μm until the sample breaks.

3.6.3. Small punch test

The small punch test is a well-established method to evaluate small disc shaped samples on the materials for nuclear applications. This technique provides load deflection curves where it is possible to study four different regions (Fig. 3.9) [17,18]:

- **I:** This is the region corresponding to the elastic deformation.
- **II:** Elastic plastic transition appears in the second region.
- **III:** The slope increases due to the work hardening. Plastic deformation is generally induced on the sample.
- **IV:** The maximum load supported is achieved and damage starts to induce softening on the sample.

- **V**: Finally, micro cracks start to propagate growing in a circular or star shape (depending on the material ductility) around the strength focal point, producing the material failure.

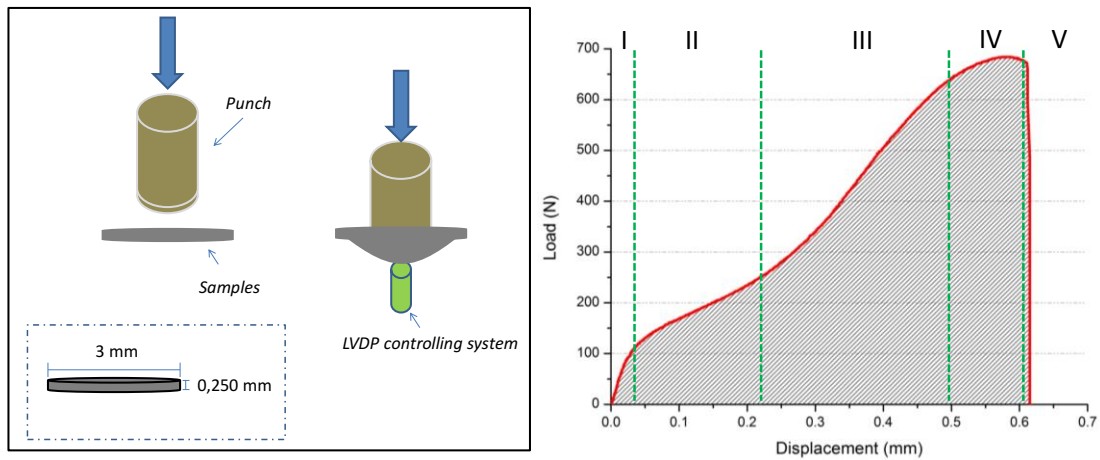


Fig. 3.9. left side: Small punch sketch, Right side: Load-deflection curved obtained [5].

Discs of 3 mm diameter and thickness of 250 μm were prepared for doing the tests. Besides, 7 samples were tested per material to evaluate each composition or SPS condition. The SP experiments were performed up to 25 $^{\circ}\text{C}$, 300 $^{\circ}\text{C}$ and 500 $^{\circ}\text{C}$. The temperature and the real deformation of the material were controlled by an LVDP system, located on the back part of the samples (Fig 3.9 left side).

Finally, the fractography shows the fracture mode of the material. Fragile mode is indicated when the samples breaks as a star shape meanwhile ductile mode as a half-moon shape. Ductile fragile mode is located between the other two (Fig 3.10).

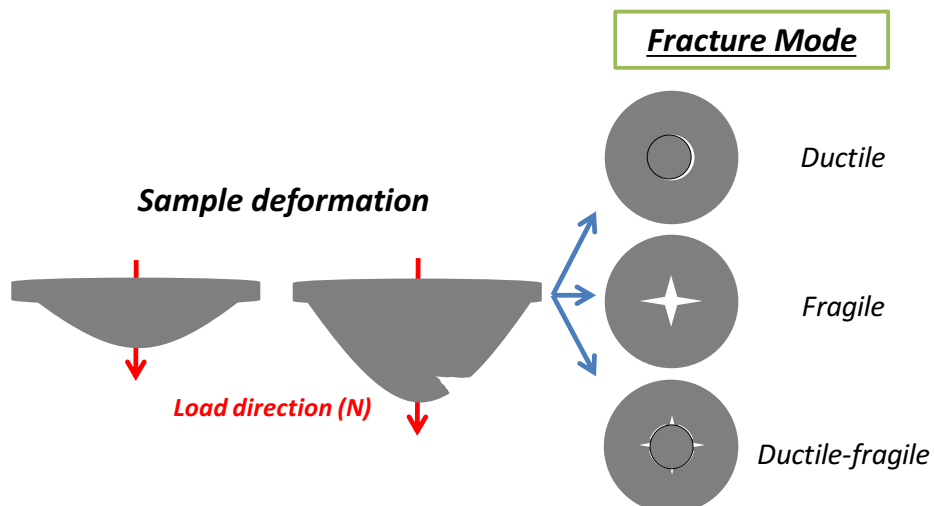


Fig 3.10. Fracture mode on small punch tests [5].

Bibliography

- [1] N. García-Rodríguez, M. Campos, J.M. Torralba, M.H. Berger, Y. Bienvenu, Capability of mechanical alloying and SPS technique to develop nanostructured high Cr, Al alloyed ODS steels, *Mater. Sci. Technol.* 30 (2014) 1676–1684. doi:10.1179/1743284714Y.0000000595.
- [2] N. Garcia, M. Campos, J.M. Torralba, *Desarrollo de Nuevos Aceros Ferríticos ODS para Aplicaciones Nucleares*, 2014.
- [3] T.A. Schaedler, W. Francillon, A.S. Gandhi, C.P. Grey, S. Sampath, C.G. Levi, Phase evolution in the YO_{1.5}-TiO₂-ZrO₂ system around the pyrochlore region, *Acta Mater.* 53 (2005) 2957–2968. doi:10.1016/j.actamat.2005.03.010.
- [4] C. Suryanarayana, Mechanical alloying and milling, *Prog. Mater. Sci.* 46 (2001) 1–184. doi:10.1016/S0079-6425(99)00010-9.
- [5] M.A. Contreras, C. Rodríguez, F.J. Belzunce, C. Betegón, Use of the small punch test to determine the ductile-to-brittle transition temperature of structural steels, *Fatigue Fract. Eng. Mater. Struct.* 31 (2008) 727–737. doi:10.1111/j.1460-2695.2008.01259.x.
- [6] Y.H. Zhao, H.W. Sheng, K. Lu, Microstructure evolution and thermal properties in nanocrystalline Fe during mechanical attrition, *Acta Mater.* 49 (2001) 365–375. doi:10.1016/S1359-6454(00)00310-4.
- [7] J.R. Fermin, D.Y. Salcedo, C.D. Rincon, J.A. Castro, Análisis de tensión/tamaño por RX en Semiconductores InGa₅(VI)₈, *Rev. Mex. Física.* 5 (2017) 345–350.
- [8] A. García-Junceda, N. García-Rodríguez, M. Campos, M. Cartón-Cordero, J.M. Torralba, Effect of Zirconium on the Microstructure and Mechanical Properties of an Al-Alloyed ODS Steel Consolidated by FAHP, *J. Am. Ceram. Soc.* 98 (2015) 3582–3587. doi:10.1111/jace.13691.
- [9] R. Xie, Z. Lu, C. Lu, Z. Li, X. Ding, C. Liu, Microstructures and mechanical properties of 9Cr oxide dispersion strengthened steel produced by spark plasma sintering, *Fusion Eng. Des.* 115 (2017) 67–73. doi:10.1016/j.fusengdes.2016.12.034.
- [10] W. Chen, U. Anselmi-Tamburini, J.E. Garay, J.R. Groza, Z.A. Munir, Fundamental investigations on the spark plasma sintering/synthesis process: I. Effect of dc pulsing on reactivity, *Mater. Sci. Eng. A.* 394 (2005) 132–138. doi:10.1016/j.msea.2004.11.020.
- [11] U. Anselmi-Tamburini, S. Gennari, J.E. Garay, Z.A. Munir, Fundamental investigations on the spark plasma sintering/synthesis process: II. Modeling of current and temperature distributions, *Mater. Sci. Eng. A.* 394 (2005) 139–148. doi:10.1016/j.msea.2004.11.019.
- [12] U. Anselmi-Tamburini, J.E. Garay, Z.A. Munir, Fundamental investigations on the spark plasma sintering/synthesis process III. Current effect on reactivity, *Mater. Sci. Eng. A.* 407 (2005) 24–30. doi:10.1016/j.msea.2005.06.066.
- [13] A.J. Wilkinson, T. Ben Britton, Strains, planes, and EBSD in materials science, *Mater. Today.* 15 (2012) 366–376. doi:10.1016/S1369-7021(12)70163-3.
- [14] L.W.Z. Zhou Weilie, *Scanning Microscopy for Nanotechnology*, Springer Science & Business Media, n.d.
- [15] D. Williams, *Transmission Electron Microscopy*, n.d. doi:10.1007/978-0-387-76501-3_1.
- [16] Y.H. Zhao, Y.Z. Guo, Q. Wei, T.D. Topping, A.M. Dangelewicz, Y.T. Zhu, T.G. Langdon, E.J. Lavernia, Influence of specimen dimensions and strain measurement methods on tensile stress-strain curves, *Mater. Sci. Eng. A.* 525 (2009) 68–77.

doi:10.1016/j.msea.2009.06.031.

- [17] S. Rasche, M. Kuna, Improved small punch testing and parameter identification of ductile to brittle materials, *Int. J. Press. Vessel. Pip.* 125 (2015) 23–34.
doi:10.1016/j.ijpvp.2014.09.001.
- [18] M. Bruchhausen, S. Holmström, I. Simonovski, T. Austin, J.M. Lapetite, S. Ripplinger, F. de Haan, Recent developments in small punch testing: Tensile properties and DBTT, *Theor. Appl. Fract. Mech.* 86 (2016) 2–10. doi:10.1016/j.tafmec.2016.09.012.



4

*Processing ODS ferritic steels:
Preliminary results*

Contents

4. Preamble to this chapter	71
4.1. Validation of MA as powder processing technique	72
4.1.1. Sinterability studies through FAHP.....	73
4.2. MA Optimization for Ferritic-ODS-I	76
4.3. Consolidation by SPS of Ferritic-ODS-I: Temperature effect	78
4.4. Evaluation of mechanical response	83
4.4.1. Room temperature behaviour.....	83
4.4.2. High temperature behaviour.....	83
4.5. Partial discussion of dual size evolution: M_{std} vs M_{act}	85
4.6. Partial remarks	86
Bibliography	87

4. Preamble to this chapter

The Ferritic ODS-I family with Ti, Zr and Y_2O_3 addition was manufactured by using two different mechanical alloying conditions (M_{st} and M_{act}). Since recrystallization depends on the plastic deformation degree, on the composition of each particle and on the oxide dispersion, a heterogeneous grains size evolution can be promoted after FAST consolidation. This Chapter explores the consequences of different mechanical alloyed powders on final microstructure and consequently, on the attained properties. Moreover, as it is stated on Chapter 1, Zr is added seeking for the refinement on the final oxide and for an improvement on the mechanical properties under high temperature conditions. Different percentages are playing a compromise between the promoted strengthening and the final ductility. In Al containing ODS steels the selected amount of Zr varies from 0.3 to 0.6 wt% [1–5]. In this research trying to improve the Y-Zr-O precipitation, Zr is inserted in a 0.6 wt% content.

Besides, all the processed alloys were compared to the ferritic ODS steels developed by N. García Rodríguez et al [6] based on the same prealloyed powder but considering the addition of 0.4 wt% Ti and 0.25 % wt Y_2O_3 (labelled as 14-ODS-Ti). Furthermore, the ferritic GETMAT steel has been considered as a reference for the high temperature experiments using small punch tests.

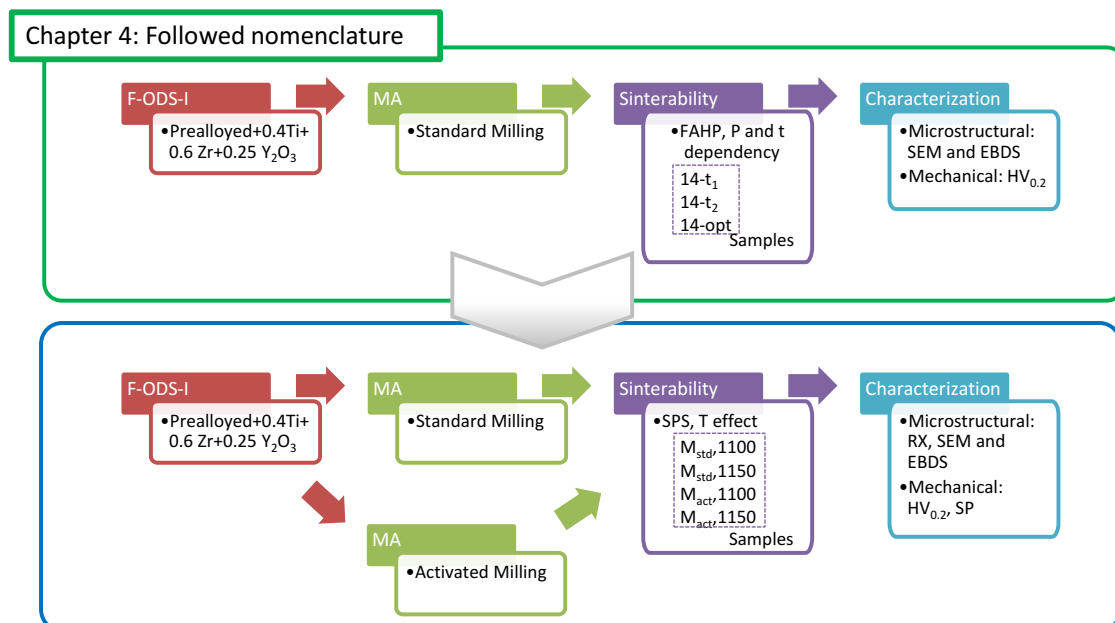


Fig 4.1. Followed nomenclature in Chapter 4.

4.1. Validation of MA as powder processing technique

The results of M_{std} milling conditions show how the milled powders presented an irregular morphology and shape, with a medium value of particle size distribution of 46 μm (Fig 4.2). Besides, by analysing the powder cross section is possible to observe some internal cracks, a sign of the hardening due to the severe plastic deformation.

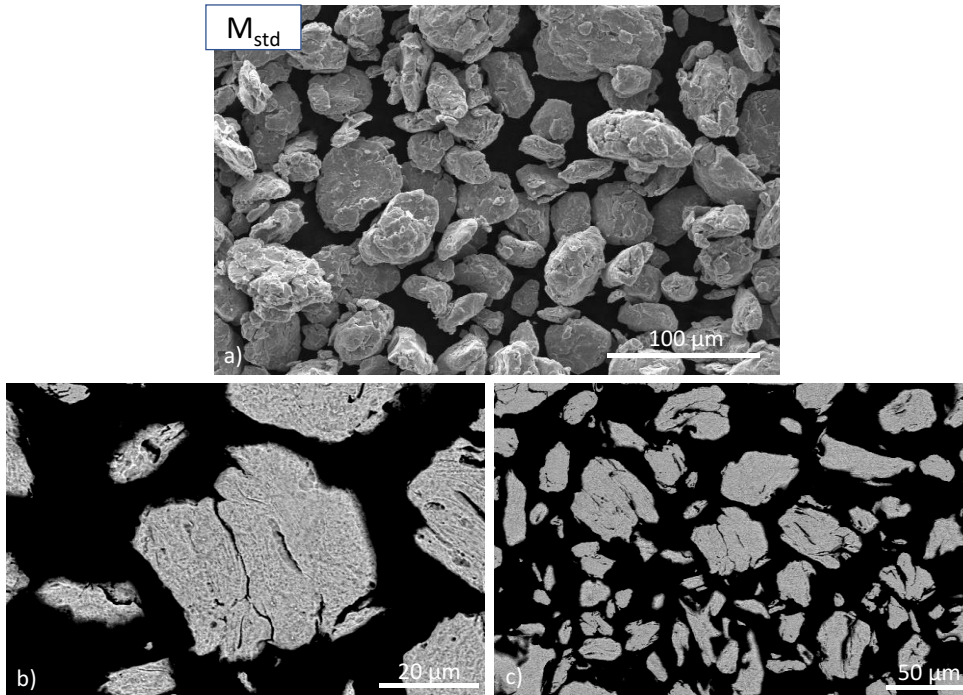


Fig 4.2. F-ODS-I powders morphology (a) and cross section of powders processed by M_{std} conditions (b and c).

This milling consequence could influence on the next FAST sintering step, limiting the penetration depth of the heat promoted by Joule effect. The electrical conductivity of the powder will be reduced as the hardening progress on powders; therefore the sinterability can be conditioned [7].

On the other hand, a high dislocation density on starting powder, could facilitate a higher dislocation density after consolidation. Considering the dislocation hardening from strengthening mechanism contributions, dislocation density can be one of the most important if this parameter increasesⁱ. The next equation was considered to work out (Eq 4.1):

$$\rho_{dis} = 14.4 \frac{\varepsilon^2}{b^2} \quad (\text{eq 4.1})$$

where ε is the microstrain and b burgers vector. Crystallographic features were determined by X-ray diffraction (table 4.1). M_{std} milling has provided powders with higher dislocation strengthening (σ_{dis})ⁱⁱ.

ⁱ Contribution of the different strengthening mechanisms can be described as:

$$\sigma_y = \sigma_0 + \sigma_{ss} + \sigma_{gb} + \sqrt{\sigma_{dis}^2 + \sigma_p^2}$$

ⁱⁱ The dislocation hardening was calculated by the term: $\sigma_{dis} = M\alpha_d Gb\sqrt{\rho}$

where M is the Taylor factor (3.06), G is the shear modulus of iron (85 GPa), b is the burger vector (0.252 nm assumed Fe pure lattice, considered as $a\sqrt{3}/2$, and a is the lattice parameter of pure Fe)[39], α is a constant ($^{1/3}$) [40], and ρ is the dislocation density which is calculated by X-ray diffraction [31]

Table 4.1. Particle size distribution and crystallographic parameters for prealloyed and MA powders.

	d10 (μm)	d50 (μm)	d90 (μm)	L (nm)	ϵ (%)	$\rho_{\text{dis}}(\text{m}^{-2})$	$\sigma_{\text{dis}}(\text{MPa})$
Preal.14Al	12	30	62	43.1	0.217	$1.07 \cdot 10^{15}$	713
14Al-ODS-Ti		49		11.4	0.898	$1.83 \cdot 10^{16}$	2951
F-ODS-I (M_{std})	22	46	92	12.1	0.762	$1.32 \cdot 10^{16}$	2505

The powder quality can be also defined by the interstitials amount. The Ex.O* parameter was determined as it is gathered in table 4.1. S. Ohtsuka et al [8,9] reported the importance to control the Ex.O, setting the maximum value in 0.1 % to ensure the formation of oxides and consequently, to improve the mechanical properties of the ODS steel at high temperature. M_{std} mode has achieved a low Ex.O values (< 0.1 %) which fulfil the literature requirements [10]. Comparing F-ODS-I powders with previous one (14Al-ODS-Ti), it is showed that an accurate control of powder manipulation can reduce the interstitial contents (Table 4.2).

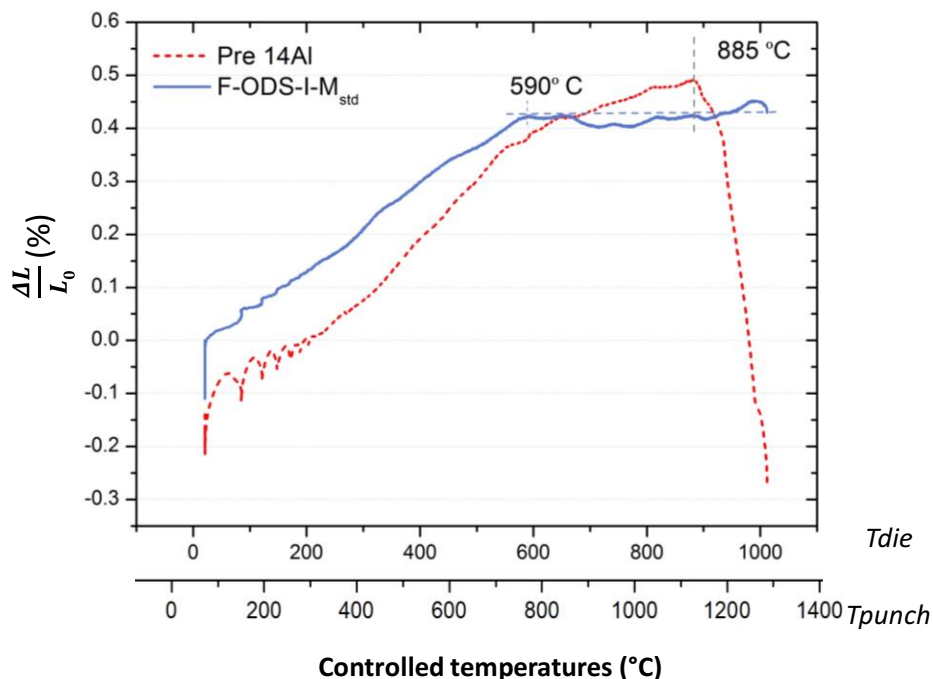
Table 4.2. Carbon, nitrogen and oxygen analysis of the MA powders (LECO).

	%C	%N	%O	%Ex. O*
Prealloyed 14Al	0.012	0.007	0.029	-
14Al-ODS-Ti	0.141	0.220	0.350	0.297
F-ODS-I (M_{std})	0.195	0.015	0.047	0.010

$$* \text{Ex. O} = \text{Total O content} - \frac{48}{226} Y_2O_3 \text{ content (wt\%)}$$

4.1.1. Sinterability studies through FAHP

To evaluate the sinterability of powders by FAST technique, field assisted hot pressing (FAHP) was used by operating the Gleeble system in a dilatometer mode. In order to understand the shrinkage evolution during the sintering step two dilatometry trials were done by using the prealloyed ferritic powder (Preal14Al) and the milled F-ODS-I powders (M_{std} parameters) (Fig 4.3).

**Fig 4.3.** Dilatometry tests: prealloyed powder (Preal14Al) vs MA powders (F-ODS-I M_{std}).

The dimensional change is considered as the axial shrinkage. In case of prealloyed powder, the starting temperature for shrinkage is close to 885 °C and thanks to the plasticity of the powder, the sample registers the highest shrinkage.

As it could be observed, MA powders (F-ODS-I) have experimented a lower shrinkage during the heating. The MA powder size, shape, composition and the structural defects produced during milling are determining the sintering kinetics during FAHP process [11]. Not only the increase on lattice defects, but also the solid solution hardening promoted during MA leads to a brittle powder with a low plastic range. Besides, the ability of packing the MA powders is also lower; the apparent density is not as good as for the prealloyed powders.

It has been also recorded that the difference between the T registered at the upper punch (which controls the current intensity of the experiment) and at the centre of the matrix, is close to 250 °C. Even by using an improved cycle, it seems that the temperature attained in the middle is just around 1000 °C (Fig 4.3).

Taking into consideration the dilatometry results, it was possible to design an appropriate thermal cycle. After the consolidation attempt (see table 3.3, p. 58), the microstructures were studied by using SEM (Fig 4.4).

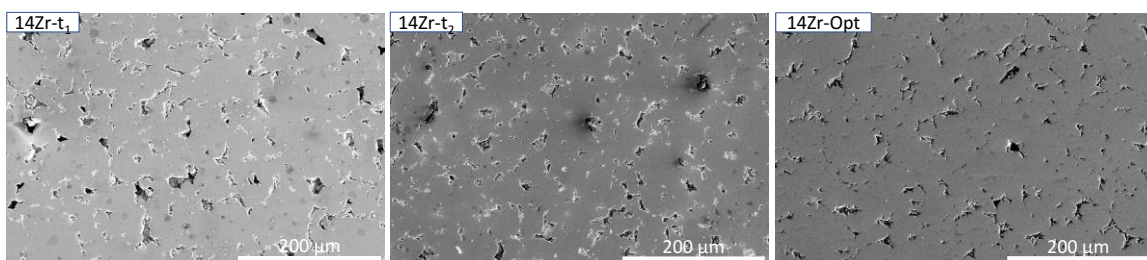


Fig 4.4. F-ODS-I SEM micrographs from material consolidated by FAHP by using different cycles: a) 14Zr-t1- b) 14Zr-t2 c) 14Zr-opt.

As it could be observed, the level of densification must be improved since full density materials were not obtained (Table 4.3). The prior particles shape coming from MA are appreciable on the whole microstructure (independently on the cycle used) and generally, sinter necks are poorer. Even though 14Zr-opt cycles allow to produce full dense regions, especially on the middle of the samples.

As it has been widely reported [12–14] to ensure full consolidated samples sintering temperature should be >1100 °C (more than the 1000 °C achieved in the Gleeble FAST sintering). On the other side, the use of alternative current (typical in Gleeble device) could determine the Joule effect obtained leading into lower density values [15].

Table 4.3. F-ODS-I samples densities using the different consolidation cycles (%).

Nomenclature	14Zr-t ₁	14Zr-t ₂	14Zr-opt
Density (%)	95.8 ± 0.2	97.2 ± 0.3	96 ± 0.2

Apart from that, FAHP technique can retain the nanostructured powder characteristics. One of the main objectives of using FAST methods is to limit the grain growth. These features are studied by EBSD maps, grain boundaries and inverse pole figures (IPF) maps on x axis (Pressure direction on FAHP process) (Fig 4.5).

The importance of the thermal activation (determined by the time and the final temperature reached) has a clear influence on the achieved final grain structure. The consolidated F-ODS-I exhibits a dual grain size distribution with ultrafine grains colonies disperse over the micro grains. Fig 4.5 (left) shows how F-ODS-I sintered under 14Zr-t₂ conditions, has reached this bimodal microstructure.

Although the use of double cycle process (14Zr-opt) reports small difference on the final densification, the material grain structure has changed. The grains population is composed almost entirely by micrometric grains sizes reducing the ultrafine regions (UF). Samples coming from this cycle have been submitted to a double thermal treatment which is translated into a

higher recrystallization and further grain growing. No texture is appreciated for both materials as it is reported for ODS samples consolidated by field electrical current methods [14].

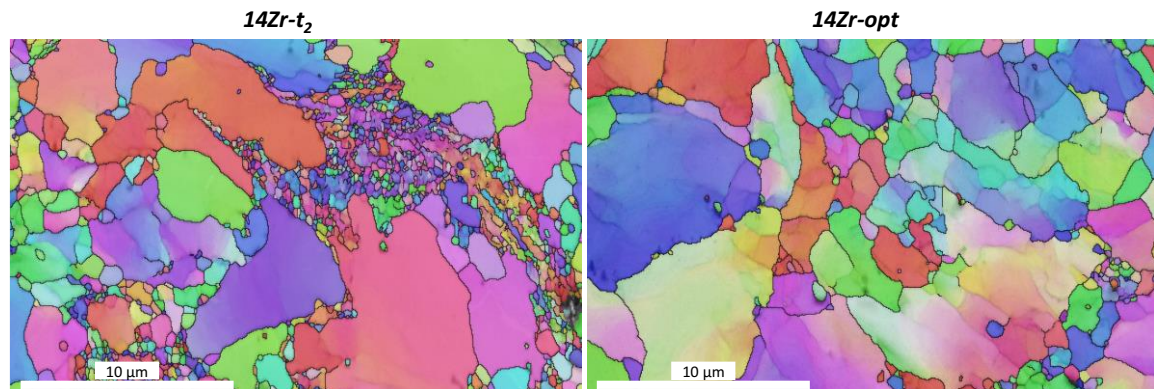


Fig 4.5. EBSD YPF Y maps obtained for 14Zr-opt and 14Zr-t2.

The final pressure used and the moment in which the pressure is applied drive the recrystallization, that can be studied by the microstrain level and the crystallite size (Fig 4.6). 14Zr-t₁ cycle applies the maximum pressure (80 MPa) from RT until the cooling step starts that means a higher level of deformation and a decrease on the recrystallization T. Hence, a lower value of microstrain and a higher crystallite size are attained. When the maximum pressure is applied from 1050 °C, the amount of deformation is reduced and therefore, crystal size achieves a minor value and the microstrain remains higher.

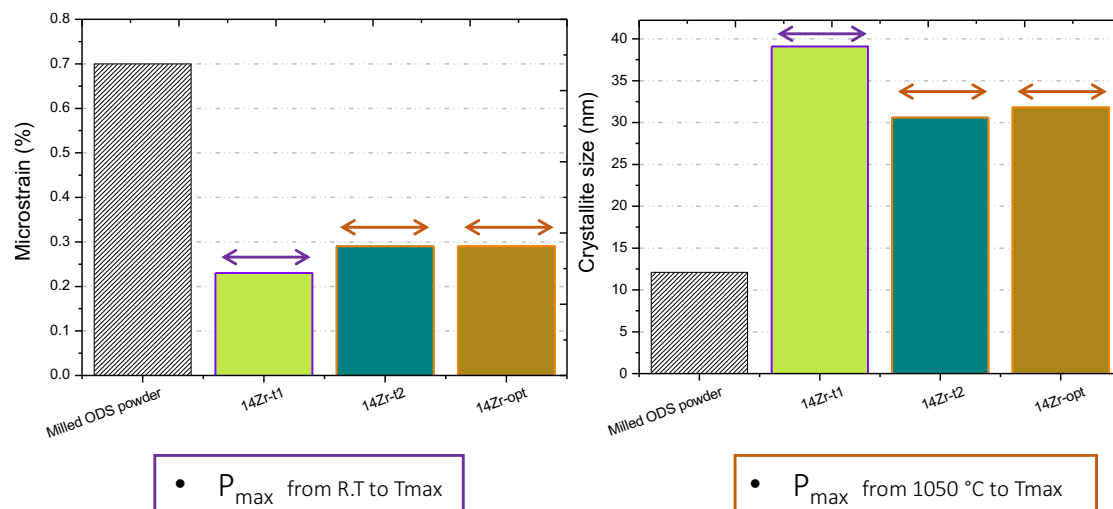


Fig 4.6. Microstrain (%) and crystallite size (nm) values for the FAHP samples obtained.

The Fig 4.7 shows the obtained microhardness. The measurements reflect the structural modifications produced by MA and the capability for strengthening the material and stabilizing the grain structure of ODS alloys. Although the achieved density level is low, the microhardness presents similar values to the Ferritic ODS previously produced [6]. The Zr effect does not arise due to the porosity of the material (notice the high standard deviation of the measurement). In case of optimize the densification, values should be shifted to higher ranges [4].

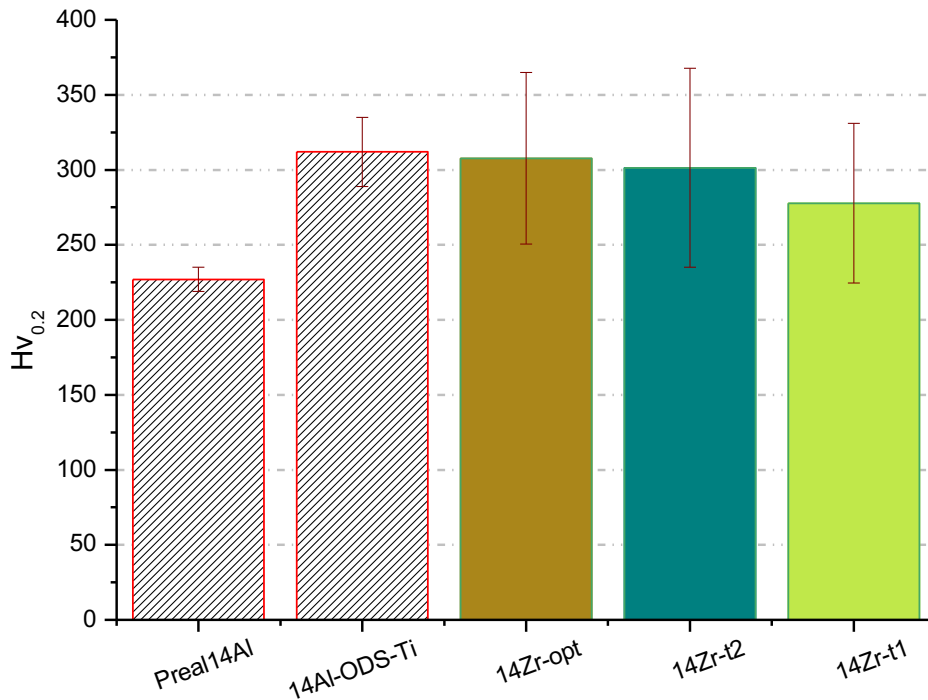


Fig 4.7. F-ODS-I consolidated by FAHP: Microhardness at room temperature [6].

It is possible to obtain a yield strength estimation (Table 4.4), by using the relationship between hardness and yield strength, $HV \sim 3 \sigma_y$ (transferring HV units to MPa) [16,17].

Table 4.4. Estimation of F-ODS-I yield strength by microhardness measurement.

	Preal14Al	14Al-ODS-Ti	14Zr-opt	14Zr-t2	14-Zr-t1
σ_y (MPa)	742	1019	1005	985	907

4.2. MA Optimization for Ferritic-ODS-I

The final purpose is to optimize the milling energy involved, that it is defined by collisions efficiency, i.e., by the rotational speed and the overheating generated during the collisions when grinding media remains constant. To do that, another batch will be produced (under M_{act} conditions Fig 3.3) to assess the milling effect.

During MA, the collisions of the grinding tools with the initial powder mixture provide the transfer of kinetic energy needed to modify the characteristics of the powder. Subsequent process of plastic deformation causes a repeated fracturing and cold welding of particles that will condition the progression of the alloying. During the first milling steps, particles start to adopt a flake-like shape and from that point cold welding will be the dominant mechanisms. As the milling process continues, the powder is hardened and consequently fracture step starts, leading into a reduction of the mean particle size obtained. Further collisions promote welding between particles as well. M_{act} milling mode was selected as optimum milling process. To study the evolution, milling was monitored at certain milling times. Fig 4.8 shows the shape and size evolution.

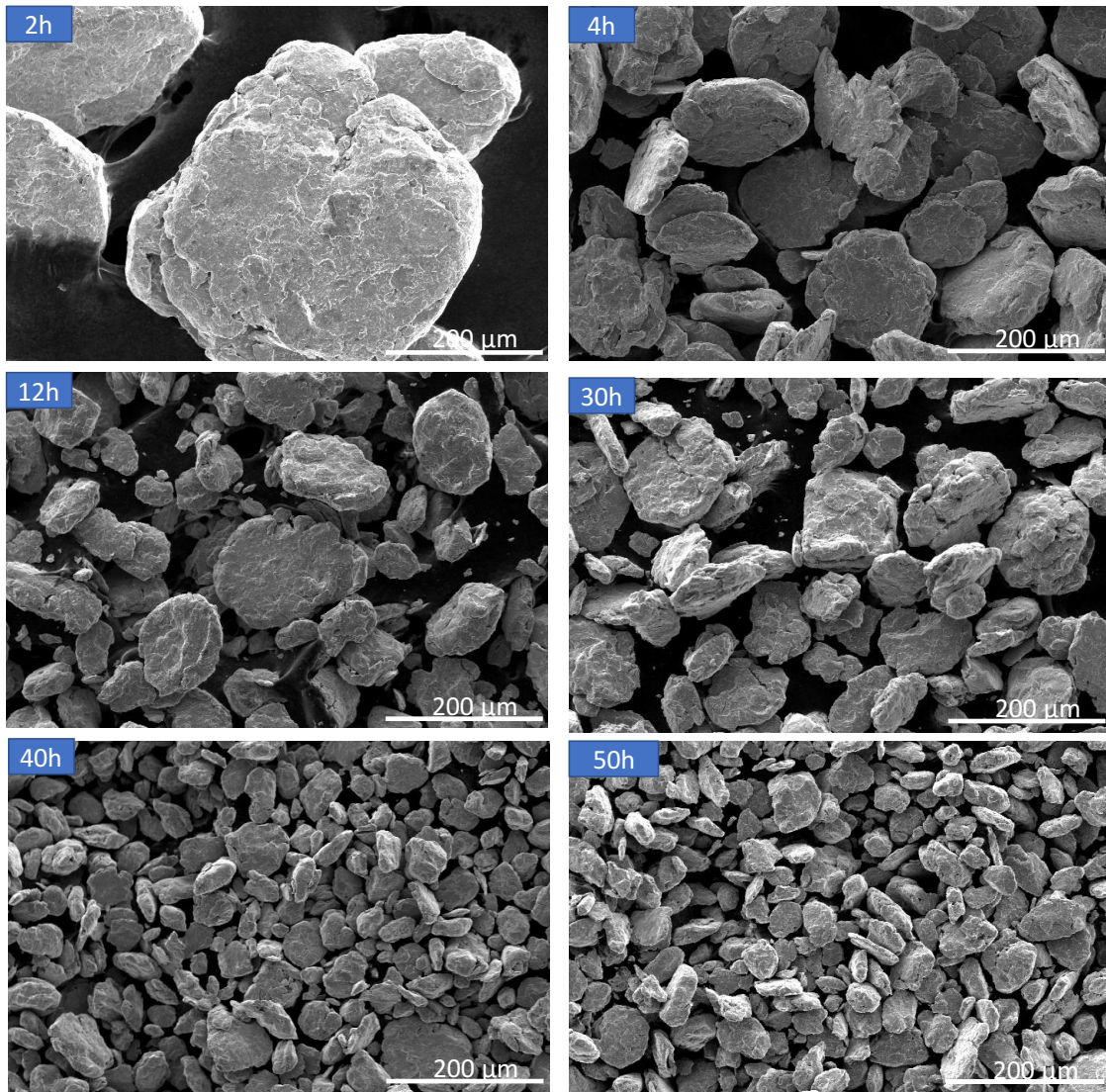


Fig 4.8.F-ODS-I powder morphology and size evolution during mechanical alloying using M_{act} parameters.

As stated on Chapter 1, two parameters enable to follow the MA evolution: crystallite size (nm) and microstrain of the lattice (%). Structural defects or modifications produced during milling, such as solid solution formation, vacancies, dislocations, and stacking faults, induce an inhomogeneous strain into the crystalline structure. As a result, the lattice distortion increases and the crystalline coherence zone decreases and therefore the crystallite size is reduced [18,19].

To obtain a nanostructured powder it is necessary to ensure a high microstrain level and low crystallite size as milling time progresses (as show in Fig 4.9, right). The minimum crystallite value after 50 h of milling is close to that reported in [20] for pure Fe, where the minimum average grain size possible by milling was calculated.

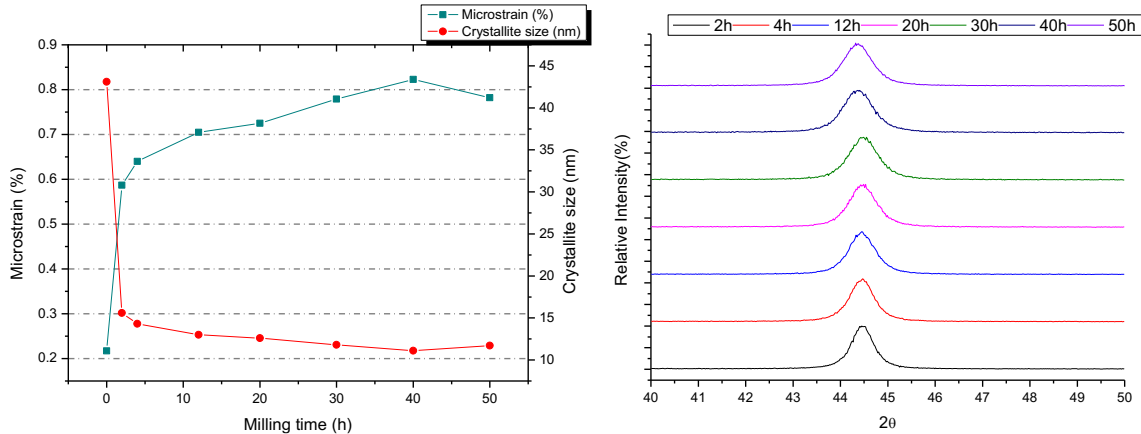


Fig 4.9. Microstrain and crystallite size evolution during the milling time calculated by Scherrer method on the peak (110) of the bcc lattice (right side).

The microstrain level will determine the final grain size of the consolidated powders, since the minimum average grain size achieved can be attributed to the balance between the dislocations density and its recovery by thermal processes, as stated in [21]. Once a critical level of microstrain is reached, the crystallite size remains stable, attaining a steady state with milling time [19,22]. Table 4.5 compares the final characteristics' of milled powders. Following the same approximations as in p. 72, strengthening due to dislocation density is also calculated. In this case, the enhancement attained with M_{act} milling mode is clear.

Table 4.5. Particle size distribution and crystallographic parameters MA powders under M_{std} and M_{act} conditions.

	d10 (μm)	d50 (μm)	d90 (μm)	L (nm)	$\mu\epsilon$ (%)	$\rho_{dis}(\text{m}^{-2})$	$\sigma_{dis}(\text{MPa})$
F-ODS-I (M_{std})	22	46	92	12.1	0.762	$1.32 \cdot 10^{16}$	2505
F-ODS-I (M_{act})	40	77	151	11.7	0.782	$1.39 \cdot 10^{16}$	2570

At the end of MA, even if a steady state is obtained, the plastic deformation stored on each particle is different, as the achieved alloying degree does. In addition, the difference in particle size will have a strong influence on the way in which the material will recrystallize during the next SPS consolidation step. The thermal activation will be used first on reducing the crystallite strain and then on the grain growth. But the temperature will be more homogeneous in the smaller particles than in the bigger ones and hence, the recrystallization will progress heterogeneously.

Again, the Ex.O parameter and the interstitial levels indicate a good powder quality (table 4. 6)

Table 4.6. Carbon, nitrogen and oxygen analysis of the MA powders (LECO).

	%C	%N	%O	%Ex. O*
F-ODS-I (M_{std})	0.195	0.015	0.047	0.010
F-ODS-I (M_{act})	0.149	0.059	0.160	0.110

* $Ex. O = \text{Total O content} - \frac{48}{226} Y_2O_3 \text{ content (wt\%)}$

4.3. Consolidation by SPS of Ferritic-ODS-I: Temperature effect

To maintain the nanostructure obtained during the mechanical alloying step, the use of SPS is quite common as an alternative to HIP or HE [14,23,24]. Optimizing the different parameters is required to achieve a good equilibrium between final consolidation and the optimized microstructure. To evaluate the effect of temperature on the final densification and on the final microstructure, the effect of the milling parameters (M_{std} vs M_{act}) and the selected consolidation temperature will be analysed (see table 3.4 on p. 58).

Increasing the maximum temperature during the consolidation could favour diffusion process leading into a better densification of the material. Studying the cross section of the samples allows to evaluate the reached densities (Fig 4.10).

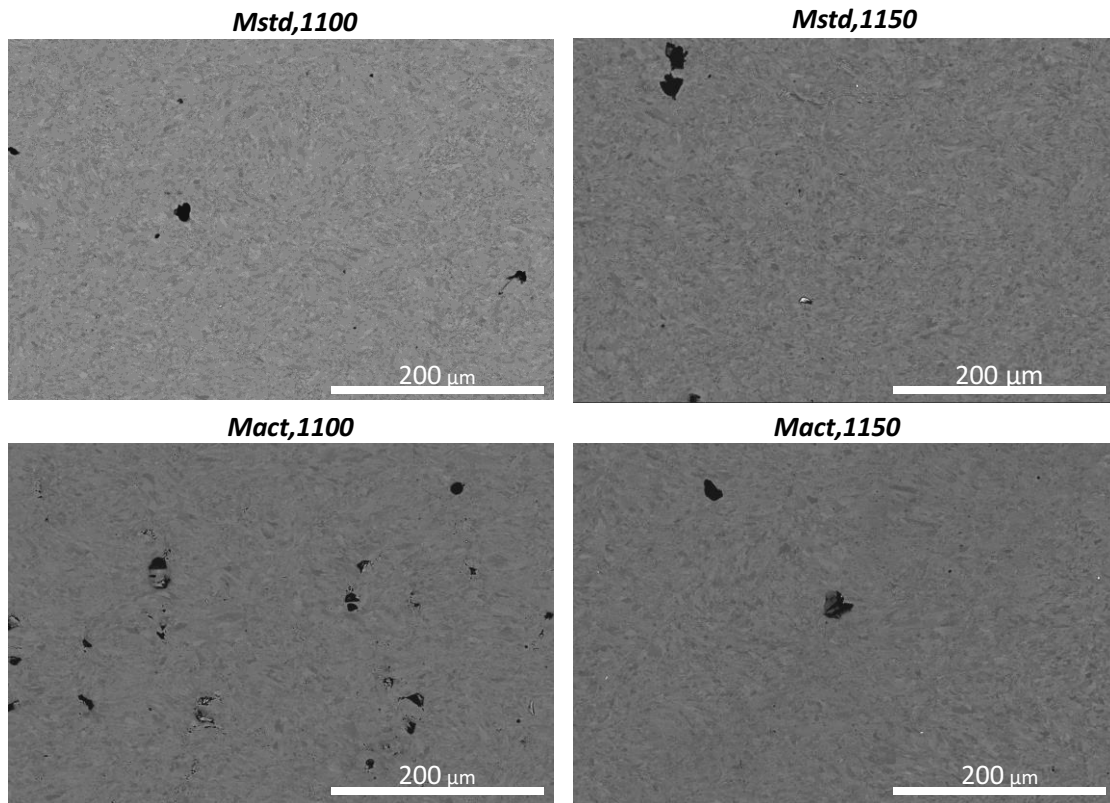


Fig 4.10. F-ODS-I SPS consolidation evolution as a function of the temperature and milling parameters.

Density is slightly influenced by milling parameters (table 4.7) only noticeable for lower SPS temperatures. Initial difference on particle size ($47\ \mu\text{m}$ vs $77\ \mu\text{m}$) is strongly related to the temperature in which the powder starts to consolidate. Smaller particles size provide a better temperature homogenization, leading into higher consolidation at lower temperatures ($1100\ ^\circ\text{C}$). The mass transport phenomenon, responsible of the growth on the sintering necks is favoured by smaller particles something that was reported by A. Molinari et al [25].

As soon as the temperature rises ($1150\ ^\circ\text{C}$) almost fully dense materials are attained independently on the used milled powder [23]. Thanks to the $50\ ^\circ\text{C}$ difference, sintering necks growth has reduced the porosity in $0.9\ \%$ [7]. Nonetheless, independently on the temperature or milling mode used all densities have achieved accurate values. This should lead into reproducible mechanical properties.

Table 4.7. F-ODS-I SPS samples densities as a function of SPS temperatures and milling parameters (%).

Nomenclature	M_{std}, 1100	M_{std}, 1150	M_{act},1100	M_{act}, 1150
Density (%)	99.8 ± 0.2	99.7 ± 0.3	98.7 ± 0.5	99.6 ± 0.33

During the sintering process, each particle recovers and recrystallizes in different stages following an inhomogeneous recrystallization. The sintered ODS steel evolves into a dual grain size microstructure (Fig 4.11) that can provide a material with a better balance between toughness/strength, that means a high performance material at room and high temperature.

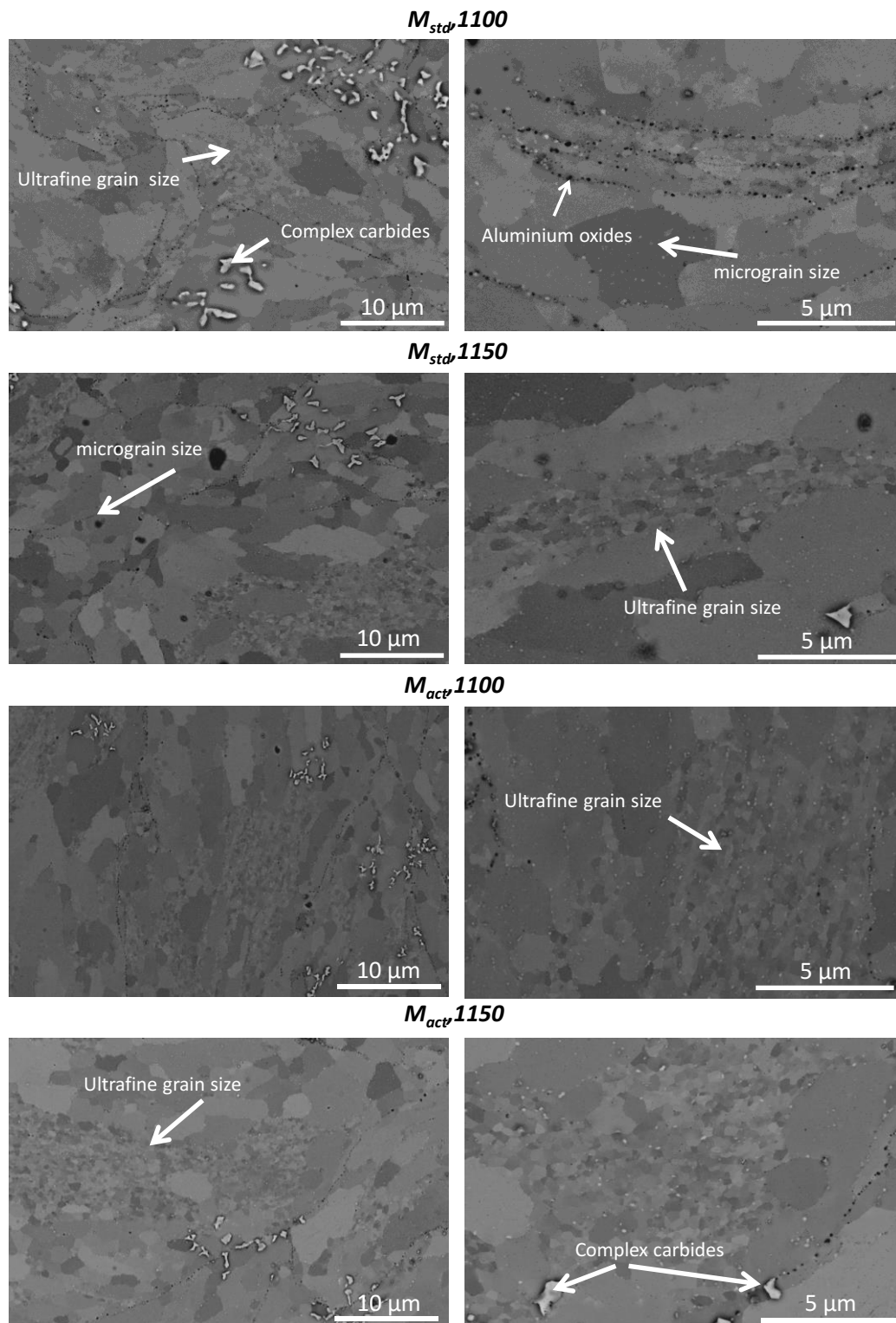


Fig 4.11. F-ODS-I steels consolidation at different temperatures, depending on milling conditions.

On first instance, it seems that M_{std} provides a microstructure mainly composed by grains of micrometric sizes (micrograins) with some ultrafine regions, which represent less than 3 % of the whole microstructure (Fig 4.12, left side). On the contrary, M_{act} provides a marked dual grain size microstructure, where almost 10% of the entire microstructure are ultrafine regions or colonies (Fig 4.12, right side).

As the same composition is used independently on the milling parameters, it is supposed that the oxides dispersion would be equal for both powders [26]. Therefore, this bimodal microstructure will be related to the accumulated amount of plastic deformation during the MA step, rather than to the final oxide dispersion. A slight increase of dislocation density was detected as it was stated in table 4.5.

The EBSD inverse pole figures maps (IPF Y) show the different crystal orientation provided by the mechanical alloying process where the absence of texture is also reported. Grain size distribution is conditioned by the selected milling mode. Ultrafine areas contain smaller grains in case of M_{std} materials.

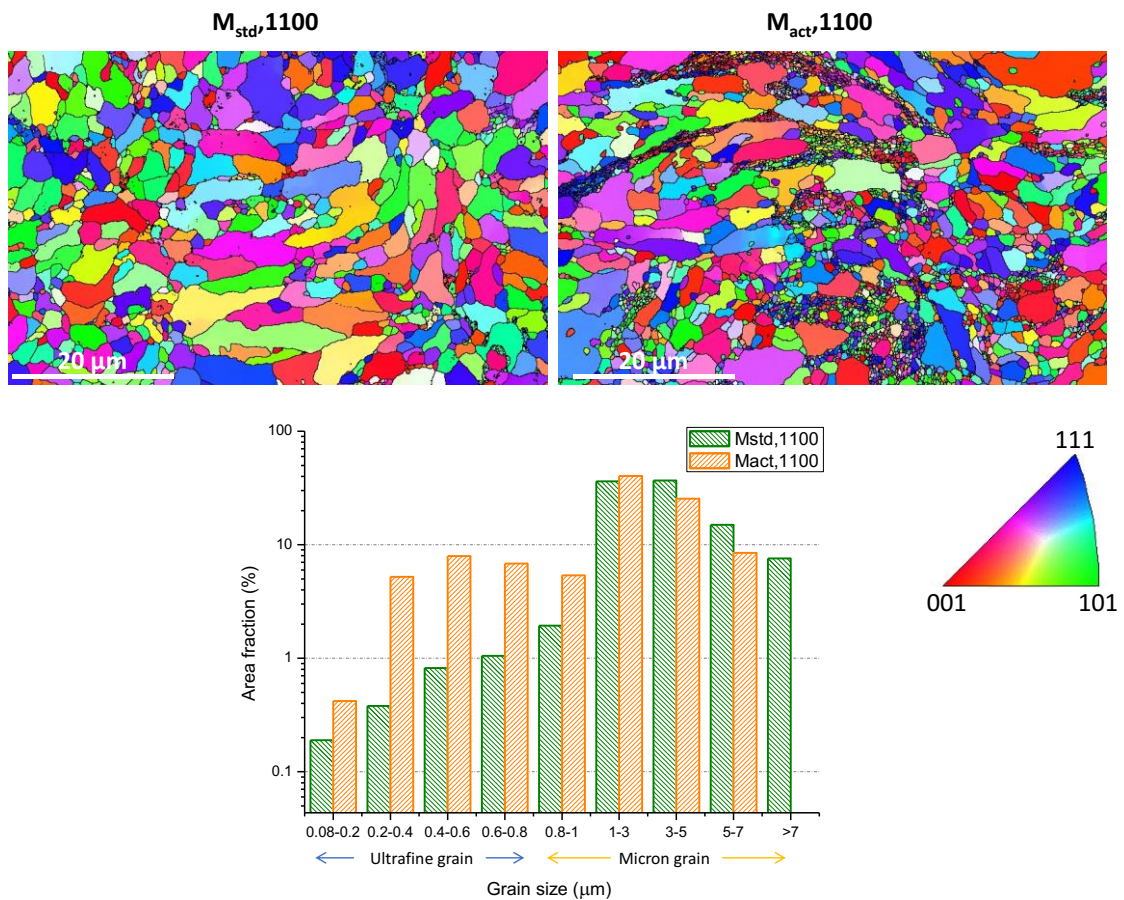


Fig 4.12. F-ODS-I steels consolidated at 1100 °C by using different milling parameters.

The thermal activation promoted by the higher SPS temperatures (1150 °C vs 1100 °C) does not affect the final dual microstructure as it is stated in Fig 4.13 [27]. Measuring the area fraction covered by ultrafine regions highlight how M_{act} provides higher volumes of nanograins (Fig. 4.13).

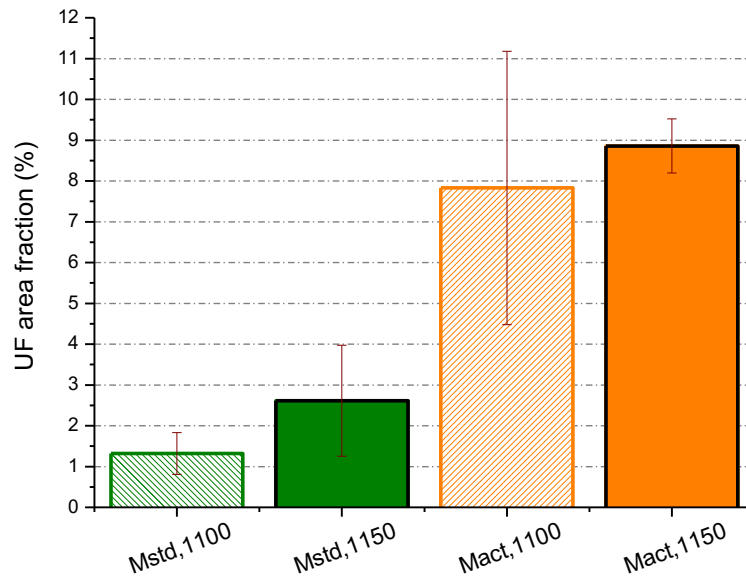


Fig 4.13. F-ODS-I ultrafine (UF) area fraction as a function of milling parameters and SPS temperature. It has been measured by covering different areas using SEM.

SPS consolidation may reduce the grain growth of the material, nevertheless it could not avoid the recrystallization [28]. The thermal activation leads to crystallite growth meanwhile the internal strain decreases. Consequently, the final values attained are similar to the ones presented on the prealloyed powder as stated on Fig 4.14.

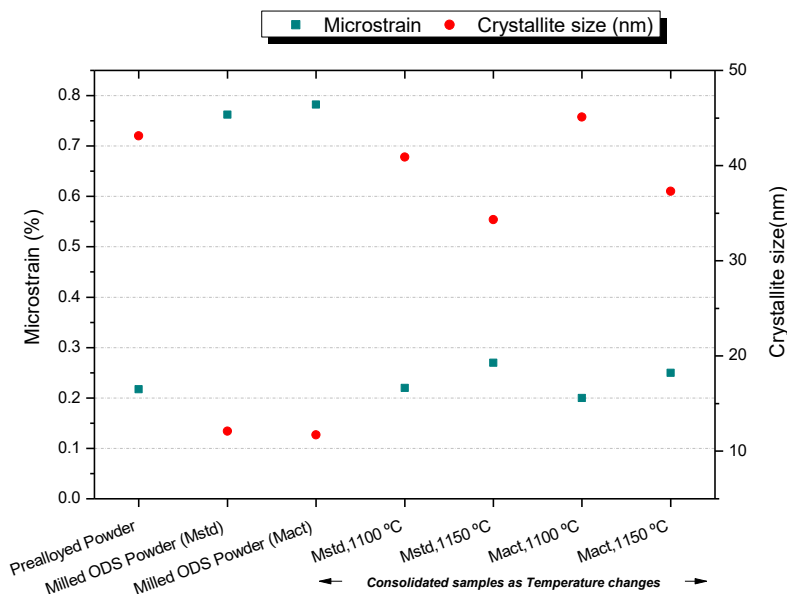


Fig 4.14. F-ODS-I Microstrain (%) and crystallite size (nm) values in prealloyed/milled powders and after consolidation by SPS at different temperatures.

The recrystallization and grain growth are directly related to the reached SPS temperature. Consequently, it is supposed that by using higher temperature lower microstrain and higher crystallite size will be attained. This tendency is not reported in this study probably due to the dual character of grain size distribution and the size of UF grains inside the colonies (Fig 4.14).

Even if the use BN layer during SPS tries to prevent the carbon diffusion from the graphite die, some carbides (from 1 to 5 μm) are dispersed at grain boundaries and inside of grains (see Fig 4.11). Normally their shape is large and polygonal. As N. Garcia et al reported [6] these carbides with MC and M_6C stoichiometry, contain Cr and Cr-W and they are frequently located in ODS alloys coming from MA powders, regardless of the method used for consolidating the material (HIP, SPS or HE) as it was stated in [29,30].

4.4. Evaluation of mechanical response

4.4.1. Room temperature behaviour

Despite the SPS temperature, all the consolidated ODS steels presented a good microhardness level, thanks to the proper densification and to the ODS mechanism.

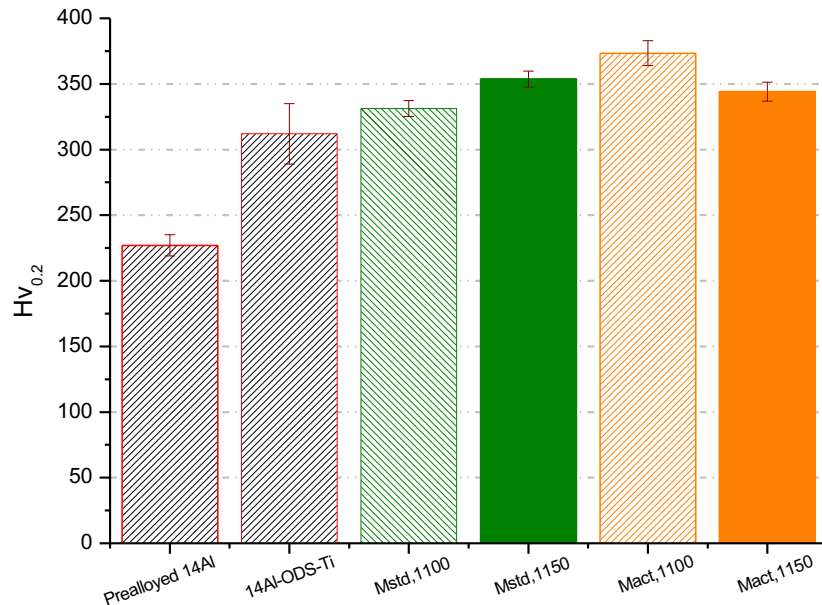


Fig 4.15. F-ODS-I Microhardness as a function of milling parameters and temperature.

Zr addition seems to improve the microhardness respect 14Al-ODS-Ti. However, the best value was the one obtained for M_{act} conditions consolidated at 1100 °C. Although it is necessary to consider that micro HV is not as accurate measurements as this material requires. The size of the indentation also covers the contribution of formed carbides (promoted depending on final C content) affecting the values scattering.

By using again, the relationship between hardness and strength where $HV \sim 3 \sigma$ (as in p. 10) to get an approximate value of Yield Strength, it is possible to connect these results with the UF area developed on each F-ODS-I steel (table 4.8). The enhancement on density and the presence of Zr contribute to the performance improvement.

Table 4.8. F-ODS-I Yield Strength evaluated by microhardness as a function of milling and temperature parameters and percentage of the area covered with UF grains.

Nomenclature	$M_{std,1100}$	$M_{std,1150}$	$M_{act,1100}$	$M_{act,1150}$
σ_y (MPa)	1081	1155	1219	1124
%UF Area	1.32 ± 0.51	2.61 ± 1.36	7.83 ± 3.35	7.27 ± 2.8

4.4.2. High temperature behaviour

The load-deflection curves show the results of the SP tests (Fig 4.16). In spite of milling conditions or the SPS temperature, the mechanical behaviour is determined by Zr addition. As it was stated in [31] the bimodal microstructure of F-ODS-I together with the oxides pinning effect are responsible of the different behaviour when they are compared with 14AlODS-Ti (Zr free).

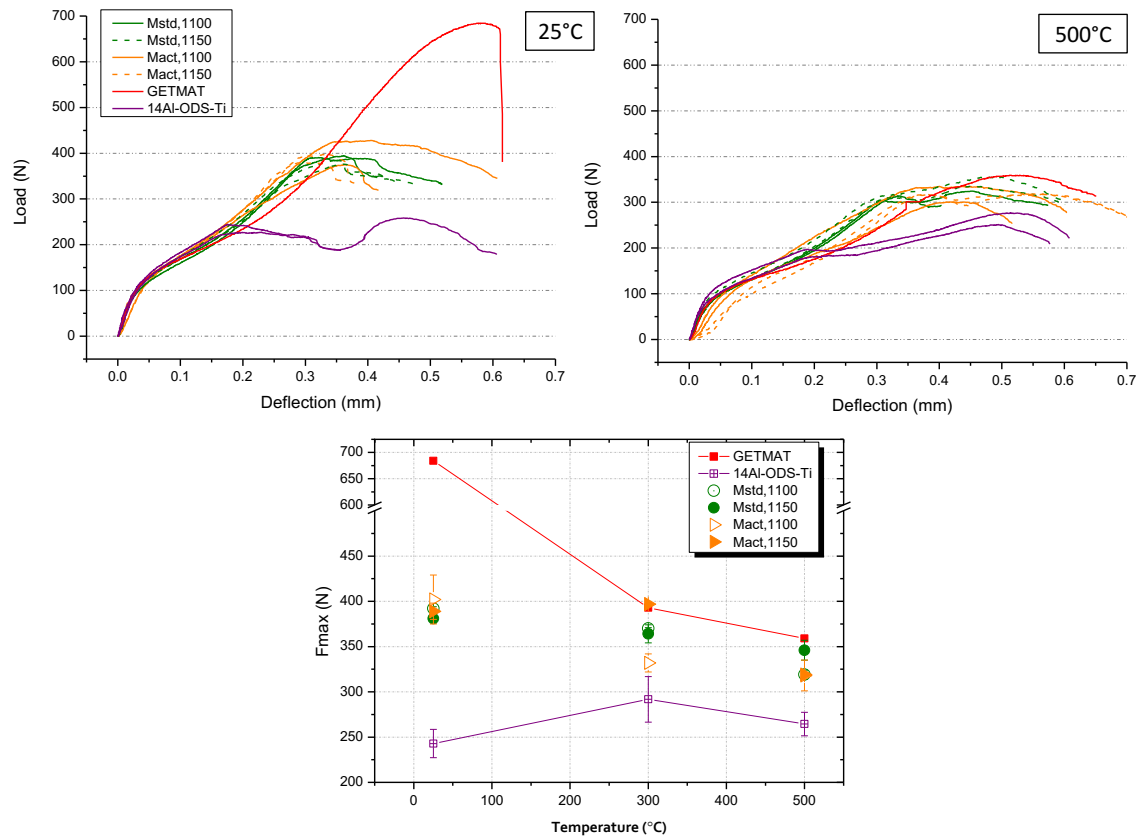


Fig 4.16. SP test from RT to 500 °C and maximum load values achieved at different temperatures. Graphs show the comparison between the different milling and SPS conditions on F-ODS-I material as well as the relation between Zr- ODS, Free Zr-ODS and GETMAT steel (processed by HE) [32,33].

Both milling conditions (M_{act} and M_{std}) promote higher performance at RT and 500 °C compare to Zr free ODS (14Al-ODS-Ti). Even if at room temperature GETMAT (reference steel processed by MA and HE at 1100 °C and finally annealed for 1.5 h at 1050 °C) is far better than F-ODS-I steels (Fig 4.16, top left side) when test temperature rises up to 300 °C and 500 °C the maximum load and deflection achieved are totally comparable. The refinement of the microstructure reached by using FAST consolidation techniques and by the Zr addition is increasing the behaviour under high temperature.

Nevertheless, at high temperature, the grain refinement of steels processed by M_{act} conditions provides a minimal effect the final properties attained, contrary of what it was expected by the results obtained by micro hardness test (Fig 4.16, bottom).

Fractured specimens (Fig 4.17) were divided into two groups according to cracks morphology, (described in Chapter 3). The cracks shape is opened and circumferentially oriented, this is the fracture mode for ductile-fragile samples [33,34]. The Zr addition and the grain size distribution support the ductility of the material.

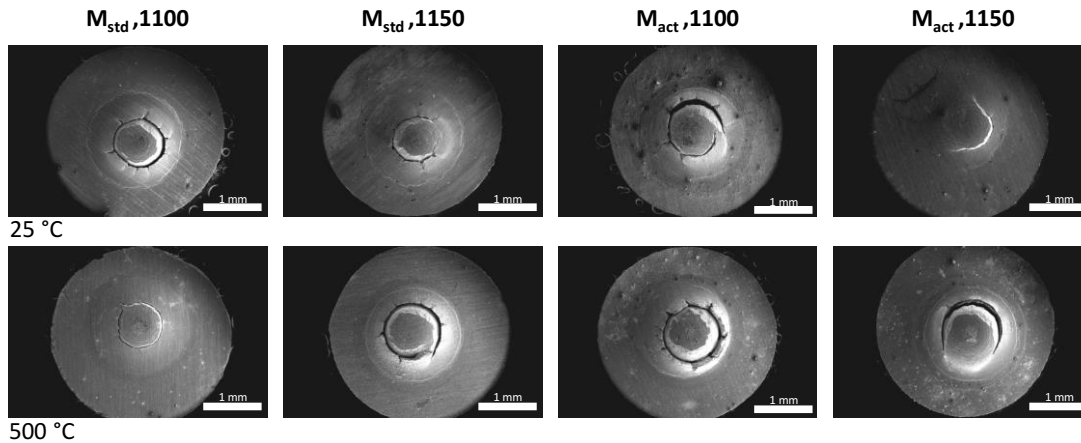


Fig 4.17. F-ODS-I SP fracture specimens as a function of milling parameters and SPS Temperature.

4.5. Partial discussion of dual size evolution: M_{std} vs M_{act}

The bimodal grain size microstructure is characteristic of ODS ferritic steels processed by MA, independently of using HIP or SPS as it is reported by I. Hilger et al in [35]. Generally, the final microstructure for F-ODS-I steels is determined by two parameters which are controlling the grain growth. First, after alloying the powder, the oxide formers are ready to combine with oxygen and to precipitates in small nanoclusters and nano-oxides. Both produce a strong pinning effect blocking the grain growth. Second, during MA particles are unequally deformed determining the heterogeneous stored energy and the ability of recrystallization [14,27,35–38]. In this case, M_{std} and M_{act} milling conditions have developed ODS steels whose microstructures are reasonably different. M_{act} parameters favours microstructures composed by UF grain areas (around 10 %), meanwhile M_{std} conditions promotes a microstructure composed specially by micrometric grains (less than 3 % is covered by UF regions).

N. Sallez et al [28] observed that nanocluster precipitates on the alloy around 800 °C, therefore from this point, the grain growth is highly determined by this nano-precipitation. As the M_{std} and M_{act} conditions have the same composition (see Chapter 3) an equivalent nanoclusters nature, density and size could be developed producing a similar pinning effect independently on the used conditions (at least on first instance). Consequently, this phenomenon alone cannot clarify the differences reached for both microstructures.

It should be also considered the influence of the attained particles size distribution for each milling conditions. The temperature will be more homogeneous in the smaller particles than in the bigger ones and hence, the recrystallization will progress heterogeneously depending on the size. The narrower particles distribution attained on M_{std} conditions (see table 4.5) could promote a more homogeneous temperature distribution inside the sample and consequently favoured the micrometric grain.

Besides, the way in which the plastic deformation is stored on each particle after the MA, could determine the final microstructure. The measured dislocation density for both milled powders is similar (see table 4.5). Different forces drive the recrystallization. Usually the primary recrystallization is led by the strain energy of cold work meanwhile the abnormal grain growth is led by merely surfaces energies. Primary recrystallization occurs in the whole material but since an heterogeneous deformation is attained during the attrition milling, recovery and recrystallization occurs at different consolidation temperature and consequently, different times. Particles highly deformed will have a lower recrystallization temperature. This phenomenon provides a driving force for recrystallization.

An inhomogeneous and competitive recovery appears on the material during consolidation. And hence, new nuclei are formed at expenses to growth to the unrecovered ones, consequently recrystallized grains will grow at expenses of the brandnew deformed ones low deformed ones [14,27]. This phenomenon leads into bimodal grain size microstructure.

As M_{act} promote higher bimodal microstructure, on first instance, M_{act} milling conditions has provided an heterogeneous deformed particles, meanwhile under M_{std} parameters particles have been more uniformly deformed.

Both I. Higler et al in [36] and X. Boulmat et al in [14] reported a similar grain size distribution to the one studied here. In their case, they observed how uniform deformed particles lead to narrower bimodal microstructure.

Apart from that, changing the sintering temperature from 1100 to 1150 °C no differences are observed on the final microstructure (as it is observed in Fig 4.7). Precipitation as stated by N. Salliez et al [28] is not the only factor influencing the abnormal grain growth; nevertheless, it is the biggest responsible of the stability of the microstructure as soon as it is developed. This should explain why bimodal microstructure is observed even on samples consolidated by HIP and why there is no difference between steels consolidated up to 1100 or 1150 °C [14,35].

4.6. Partial remarks

In this chapter a prealloyed powders (Fe-14Cr-3W-5Al) has been mechanically alloyed with Y_2O_3 , Ti and Zr (F-ODS-I) to improve the efficiency in the ODS ferritic steels production, milled powders have been consolidated by FAHP and SPS. It was demonstrated:

- Spark plasma sintering provides full dense materials when the proper parameters are chosen. Temperature is determining the final sample consolidation.
- Different milling parameters provided different microstructure and different consolidation when 1100 °C is used. Probably the way in which the particles are deformed during the process promote this behaviour.
- M_{act} milling parameters favour the dual size microstructure on the sample, leading to better mechanical properties by using microhardness as evaluation method.

M_{std} milled powder was used to evaluate **FAHP** as a consolidation method. The main conclusions are:

- During the MA the powder was extremely hardened. This is shown by the higher number of fractured particles obtained. As a result, consolidation becomes more complicated due to the low particles plasticity, low packing.
- The results obtained shows that even in the 14Zr-opt cycle the sample retain the porosity, so the sintering of the material is still limited. The final temperature achieved by using alternative current is no higher enough to ensure full dense samples.
- Microhardness test are performed in order to analyse the properties of the material. The steels 14Zr-t₂ and 14Zr-opt have achieved a Vickers microhardness value similar to those obtained in previous ODS steels consolidated by SPS [6].
- The defined cycle for this process needs to be optimize by study other parameters as: heating rate or delimit the milling time to better control the hardening effect.

Bibliography

- [1] H. Dong, L. Yu, Y. Liu, C. Liu, H. Li, J. Wu, Enhancement of tensile properties due to microstructure optimization in ODS steels by zirconium addition, *Fusion Eng. Des.* 125 (2017) 402–406. doi:10.1016/J.FUSENGDES.2017.03.170.
- [2] P. Dou, A. Kimura, R. Kasada, T. Okuda, M. Inoue, S. Ukai, S. Ohnuki, T. Fujisawa, F. Abe, TEM and HRTEM study of oxide particles in an Al-alloyed high-Cr oxide dispersion strengthened steel with Zr addition, *J. Nucl. Mater.* 444 (2014) 441–453. doi:10.1016/j.jnucmat.2013.10.028.
- [3] R. Gao, T. Zhang, X.P. Wang, Q.F. Fang, C.S. Liu, Effect of zirconium addition on the microstructure and mechanical properties of ODS ferritic steels containing aluminum, *J. Nucl. Mater.* 444 (2014) 462–468. doi:10.1016/j.jnucmat.2013.10.038.
- [4] A. García-Junceda, N. García-Rodríguez, M. Campos, M. Cartón-Cordero, J.M. Torralba, Effect of Zirconium on the Microstructure and Mechanical Properties of an Al-Alloyed ODS Steel Consolidated by FAHP, *J. Am. Ceram. Soc.* 98 (2015) 3582–3587. doi:10.1111/jace.13691.
- [5] J. Isselin, R. Kasada, A. Kimura, T. Okuda, M. Inoue, S. Ukai, S. Ohnuki, T. Fujisawa, F. Abe, Effects of Zr Addition on the Microstructure of 14%Cr4%Al ODS Ferritic Steels, *Mater. Trans.* 51 (2010) 1011–1015. doi:10.2320/matertrans.MBW200923.
- [6] N. García-Rodríguez, M. Campos, J.M. Torralba, M.H. Berger, Y. Bienvenu, Capability of mechanical alloying and SPS technique to develop nanostructured high Cr, Al alloyed ODS steels, *Mater. Sci. Technol.* 30 (2014) 1676–1684. doi:10.1179/1743284714Y.0000000595.
- [7] X. Song, X. Liu, J. Zhang, Neck formation and self-adjusting mechanism of neck growth of conducting powders in spark plasma sintering, *J. Am. Ceram. Soc.* 89 (2006) 494–500. doi:10.1111/j.1551-2916.2005.00777.x.
- [8] S. Ohtsuka, S. Ukai, M. Fujiwara, T. Kaito, T. Narita, Improvement of 9Cr-ODS martensitic steel properties by controlling excess oxygen and titanium contents, *J. Nucl. Mater.* 329–333 (2004) 372–376. doi:10.1016/j.jnucmat.2004.04.043.
- [9] S. Ohtsuka, S. Ukai, M. Fujiwara, T. Kaito, T. Narita, Nano-structure control in ODS martensitic steels by means of selecting titanium and oxygen contents, *J. Phys. Chem. Solids.* 66 (2005) 571–575. doi:10.1016/j.jpcs.2004.06.033.
- [10] P. Olier, J. Malaplate, M.H. Mathon, D. Nunes, D. Hamon, L. Toualbi, Y. De Carlan, L. Chaffron, Chemical and microstructural evolution on ODS Fe-14CrWTi steel during manufacturing stages, *J. Nucl. Mater.* 428 (2012) 40–46. doi:10.1016/j.jnucmat.2011.10.042.
- [11] K. Rajan, T. Shanmugasundaram, V. Subramanya Sarma, B.S. Murty, Effect of Y₂O₃ on spark plasma sintering kinetics of nanocrystalline 9Cr-1Mo ferritic oxide dispersion-strengthened steels, *Metall. Mater. Trans. A Phys. Metall. Mater. Sci.* 44 (2013) 4037–4041. doi:10.1007/s11661-013-1845-1.
- [12] H. Zhang, Y. Huang, H. Ning, C.A. Williams, A.J. London, K. Dawson, Z. Hong, M.J. Gorley, C.R.M. Grovenor, G.J. Tatlock, S.G. Roberts, M.J. Reece, H. Yan, P.S. Grant, Processing and microstructure characterisation of oxide dispersion strengthened Fe–14Cr–0.4Ti–0.25Y₂O₃ ferritic steels fabricated by spark plasma sintering, *J. Nucl. Mater.* 464 (2015) 61–68. doi:10.1016/j.jnucmat.2015.04.029.
- [13] Y.P. Xia, X.P. Wang, Z. Zhuang, Q.X. Sun, T. Zhang, Q.F. Fang, T. Hao, C.S. Liu, Microstructure and oxidation properties of 16Cr-5Al-ODS steel prepared by sol-gel and

- spark plasma sintering methods, *J. Nucl. Mater.* 432 (2013) 198–204. doi:10.1016/j.jnucmat.2012.07.039.
- [14] X. Boulnat, M. Perez, D. Fabregue, T. Douillard, M.H. Mathon, Y. De Carlan, Microstructure evolution in nano-reinforced ferritic steel processed by mechanical alloying and spark plasma sintering, *Metall. Mater. Trans. A Phys. Metall. Mater. Sci.* 45 (2014) 1485–1497. doi:10.1007/s11661-013-2107-y.
- [15] W. Chen, U. Anselmi-Tamburini, J.E. Garay, J.R. Groza, Z.A. Munir, Fundamental investigations on the spark plasma sintering/synthesis process: I. Effect of dc pulsing on reactivity, *Mater. Sci. Eng. A.* 394 (2005) 132–138. doi:10.1016/j.msea.2004.11.020.
- [16] P. Zhang, S.X. Li, Z.F. Zhang, General relationship between strength and hardness, *Mater. Sci. Eng. A.* 529 (2011) 62–73. doi:10.1016/j.msea.2011.08.061.
- [17] X. Zhou, Y. Liu, L. Yu, Z. Ma, Q. Guo, Y. Huang, H. Li, Microstructure characteristic and mechanical property of transformable 9Cr-ODS steel fabricated by spark plasma sintering, *Mater. Des.* 132 (2017) 158–169. doi:10.1016/j.matdes.2017.06.063.
- [18] J.M. Torralba, L. Fuentes-Pacheco, N. García-Rodríguez, M. Campos, Development of high performance powder metallurgy steels by high-energy milling, *Adv. Powder Technol.* 24 (2013) 813–817. doi:10.1016/j.apt.2012.11.015.
- [19] H.J. Fecht, Nanoparticle formation by mechanical attrition, *Nanostructured Mater.* 6 (1995) 33–42. doi:10.1016/0965-9773(95)00027-5.
- [20] F.A. Mohamed, Y. Xun, Correlations between the minimum grain size produced by milling and material parameters, *Mater. Sci. Eng. A.* 354 (2003) 133–139. doi:10.1016/S0921-5093(02)00936-X.
- [21] J. Eckert, J.C. Holzer, C. III E., Krill, W. Johnson L., C. Krill E., W. Johnson L., Structural and thermodynamic properties of nanocrystalline fcc metals prepared by mechanical attrition, *J. Mater. Res.* 7 (1992) 1751–1761. doi:10.1557/JMR.1992.1751.
- [22] Y.H. Zhao, H.W. Sheng, K. Lu, Microstructure evolution and thermal properties in nanocrystalline Fe during mechanical attrition, *Acta Mater.* 49 (2001) 365–375. doi:10.1016/S1359-6454(00)00310-4.
- [23] I. Bogachev, E. Grigoryev, O.L. Khasanov, E. Olevsky, Fabrication of 13Cr-2Mo ferritic/martensitic oxide-dispersion-strengthened steel components by mechanical alloying and spark-plasma sintering, *Jom.* 66 (2014) 1020–1026. doi:10.1007/s11837-014-0972-5.
- [24] X. Boulnat, D. Fabregue, M. Perez, M.H. Mathon, Y. De Carlan, High-temperature tensile properties of nano-oxide dispersion strengthened ferritic steels produced by mechanical alloying and spark plasma sintering, *Metall. Mater. Trans. A Phys. Metall. Mater. Sci.* 44 (2013) 2461–2465. doi:10.1007/s11661-013-1719-6.
- [25] S. Diouf, A. Molinari, Densification mechanisms in spark plasma sintering: Effect of particle size and pressure, *Powder Technol.* 221 (2012) 220–227. doi:10.1016/j.powtec.2012.01.005.
- [26] X. Boulnat, D. Fabrègue, M. Perez, S. Urvoy, D. Hamon, Y. de Carlan, Assessment of consolidation of oxide dispersion strengthened ferritic steels by spark plasma sintering: from laboratory scale to industrial products, *Powder Metall.* 57 (2014) 204–211. doi:10.1179/1743290114Y.0000000091.
- [27] X. Boulnat, N. Sallez, M. Dadé, A. Borbély, J. Béchade, Y. De Carlan, J. Malaplate, Y. Brechet, F. de Geuser, A. Deschamps, P. Donnadiou, D. Fabregue, M. Perez, Influence of

- oxide volume fraction on abnormal growth of nanostructured ferritic steels during non-isothermal treatments: An in situ study, *Acta Mater.* 97 (2015) 124–130. doi:10.1016/j.actamat.2015.07.005.
- [28] N. Sallez, X. Boulnat, A. Borbély, J.L. Béchade, D. Fabregue, M. Perez, Y. De Carlan, L. Henet, C. Mocuta, D. Thiaudiere, Y. Brechet, In situ characterization of microstructural instabilities: Recovery, recrystallization and abnormal growth in nanoreinforced steel powder, 87 (2015) 377–389. doi:10.1016/j.actamat.2014.11.051.
- [29] M.A. Auger, V. de Castro, T. Leguey, M.A. Monge, A. Muñoz, R. Pareja, Microstructure and tensile properties of oxide dispersion strengthened Fe–14Cr–0.3Y₂O₃ and Fe–14Cr–2W–0.3Ti–0.3Y₂O₃, *J. Nucl. Mater.* 442 (2013) S142–S147. doi:10.1016/j.jnucmat.2012.11.001.
- [30] M.A. Auger, V. De Castro, T. Leguey, A. Muñoz, R. Pareja, Microstructure and mechanical behavior of ODS and non-ODS Fe-14Cr model alloys produced by spark plasma sintering, *J. Nucl. Mater.* 436 (2013) 68–75. doi:10.1016/j.jnucmat.2013.01.331.
- [31] E. Macía, A. García-Junceda, M. Serrano, M. Hernández-Mayoral, L.A. Diaz, M. Campos, Effect of the heating rate on the microstructure of a ferritic ODS steel with four oxide formers (Y-Ti-Al-Zr) consolidated by spark plasma sintering (SPS), *J. Nucl. Mater.* 518 (2019) 190–201. doi:10.1016/j.jnucmat.2019.02.043.
- [32] M. Serrano, M. Hernández-Mayoral, A. García-Junceda, Microstructural anisotropy effect on the mechanical properties of a 14Cr ODS steel, *J. Nucl. Mater.* 428 (2012) 103–109. doi:10.1016/j.jnucmat.2011.08.016.
- [33] M. Serrano, A. García-Junceda, R. Hernández, M.H. Mayoral, On anisotropy of ferritic ODS alloys, *Mater. Sci. Technol.* 30 (2014) 1664–1668. doi:10.1179/1743284714Y.0000000552.
- [34] K. Guan, L. Hua, Q. Wang, X. Zou, M. Song, Assessment of toughness in long term service CrMo low alloy steel by fracture toughness and small punch test, *Nucl. Eng. Des.* 241 (2011) 1407–1413. doi:10.1016/j.nucengdes.2011.01.031.
- [35] I. Hilger, X. Boulnat, J. Hoffmann, C. Testani, F. Bergner, Y. De Carlan, F. Ferraro, A. Ulbricht, Fabrication and characterization of oxide dispersion strengthened (ODS) 14Cr steels consolidated by means of hot isostatic pressing, hot extrusion and spark plasma sintering, *J. Nucl. Mater.* 472 (2015) 206–214. doi:10.1016/j.jnucmat.2015.09.036.
- [36] I. Hilger, F. Bergner, T. Weißgärber, Bimodal Grain Size Distribution of Nanostructured Ferritic ODS Fe – Cr Alloys, *J. Am. Ceram. Soc.* 3581 (2015) 3576–3581. doi:10.1111/jace.13833.
- [37] N. Sallez, C. Hatzoglou, F. Delabrouille, D. Sornin, L. Chaffron, M. Blat-Yrieix, B. Radiguet, P. Pareige, P. Donnadieu, Y. Bréchet, Precipitates and boundaries interaction in ferritic ODS steels, *J. Nucl. Mater.* 472 (2016) 118–126. doi:10.1016/j.jnucmat.2016.01.021.
- [38] M. Dadé, J. Malaplate, J. Garnier, F. De Geuser, N. Locket, A. Deschamps, Influence of consolidation methods on the recrystallization kinetics of a Fe-14Cr based ODS steel, *J. Nucl. Mater.* 472 (2016) 143–152. doi:10.1016/j.jnucmat.2016.01.019.
- [39] F. Bergner, C. Heintze, I. Hilger, M. Serrano, Elastic properties of Fe-Cr and ODS Fe-Cr alloys, (2016) 1–2. doi:10.13140/RG.2.1.3783.5281.
- [40] M. Praud, F. Momprou, J. Malaplate, D. Caillard, J. Garnier, A. Steckmeyer, B. Fournier, Study of the deformation mechanisms in a Fe-14% Cr ODS alloy, *J. Nucl. Mater.* 428 (2012) 90–97. doi:10.1016/j.jnucmat.2011.10.046.

5

*Processing ODS ferritic steels:
Promoting bimodal grain size
with Zr addition*

Contents

5. Preamble to this chapter	95
5.1. Characterization of consolidated samples: Effect of heating rate on the microstructure	96
5.2. Nano-structured ferritic alloy microstructure: Study of the oxide dispersion	98
5.2.1. Analysis of precipitates on the ultrafine grain area	99
5.2.2. Analysis of precipitates on the micrometric grain.....	101
5.2.3. SPS Heating rate effect: Low HR vs high HR	102
5.2.4. Effect of Zr addition on the precipitates size distribution.....	104
5.3. Evaluation of the mechanical behaviour	105
5.3.1. Room temperature behaviour.....	105
5.3.2. High temperature behaviour by SP test	107
5.4. Partial discussion	108
5.4.1. Influence of processing conditions.....	108
5.4.2. Effect of Zr addition on the nature of the nano-precipitates.....	108
5.4.3. Effect of Zr addition on the nano-precipitates size and density	110
5.4.4. Strengthened mechanisms	111
5.4.5. Evaluation of the material under high temperature	113
5.5. Partial remarks	114
Bibliography	115

5. Preamble to this chapter

The proposed ODS ferritic steel, F-ODS-I, was produced by mechanical alloying (MA) and spark plasma sintering (SPS) to obtain a complex nanostructure. To densify the material by SPS, a sintering cycle was performed at 1100 °C by using fast heating rates (from 100 to 600 °C/min). During the attrition of MA powders, the uneven deformation level distribution and the alloying elements have produced an inhomogeneous recrystallization during the consolidation step.

The influence of processing conditions was studied by modifying the heating rate of SPS to promote a heterogeneous material with bimodal grain size distribution. The final microstructures were characterized by X-ray diffraction and electron microscopy (SEM and TEM).

The mechanical behaviour at R.T. was characterized by means of the Vickers microhardness and micro tensile tests. The good balance obtained between ductility (~22-26%) and yield stress (800-910 MPa) at room temperature is provided by the bimodal grain size distribution. To predict the experimental values depending on the processing conditions, a yield strength model is presented. This model covers the contribution of different strengthening mechanism from solid solution, grain size, dislocation density and oxides precipitation. The model indicates the dislocation density as the major strengthening contribution. In addition, small punch (SP) tests were performed to analyse the response of the material at high temperatures where remarkable properties have been achievedⁱ.

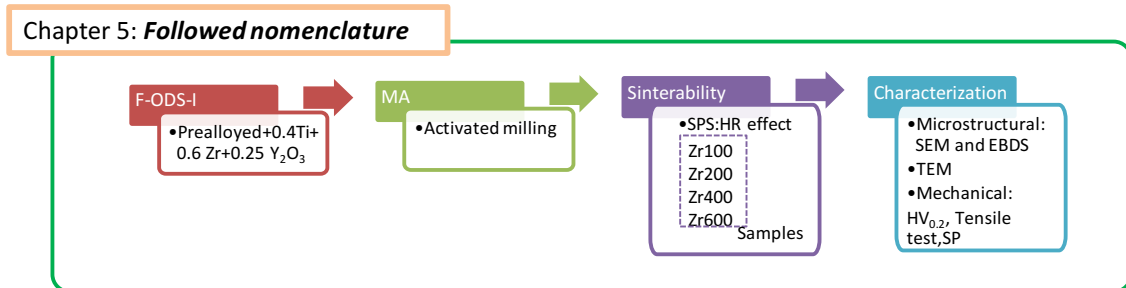


Fig 5.1. Followed nomenclature in Chapter 5.

ⁱ Part of the information compiled on this chapter was displayed in:

“Effect of the heating rate on the microstructure of a ferritic ODS steel group four (Y-Ti-Al-Zr) consolidated by Spark Plasma Sintering (SPS)” **E.Macia,A.García-Junceda,M.Serrano,M.Hernandez-Mayoral,L.A.Diaz,M.Campos** doi.org/10.1016/j.jnuamat.2019.02.043

5.1. Characterization of consolidated samples: Effect of heating rate on the microstructure

One of the most interesting points on using SPS is the peculiarity of heating the material by using faster heating rates (in the order of 1000 °C/min depending on the equipment). Precisely, the influence of heating rate on the consolidation and the microstructure is not yet well understood [1], moreover on mechanically alloyed materials. To understand the consequences of fast consolidation rates, milled powders have been sintered from 100 °C/min to 600 °C/min.

Starting with the crystallographic parameters once the F-ODS-I was consolidated, as a result of recrystallization during the SPS, the crystallite size and microstrain level change and consequently the crystallite size increases while the internal strain decreases (see Fig 5.2 where processed samples were compare with milled ODS powders and raw prealloyed grade) [2].

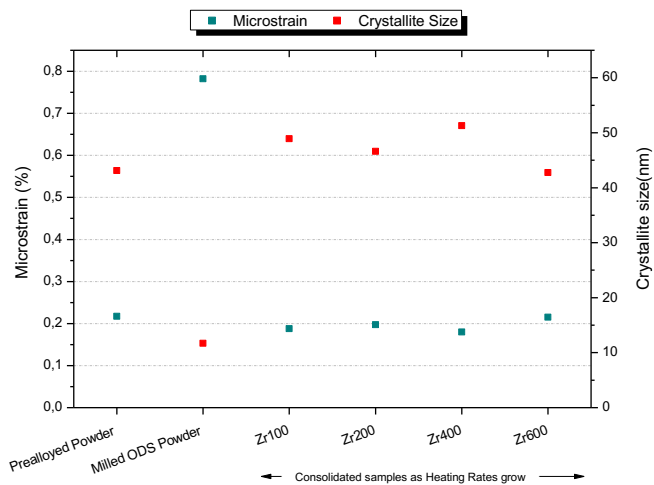


Fig 5.2. Microstrain (%) and crystallite size (nm) values in prealloyed/milled powders and after consolidation by SPS at different heating rates (ZrX00).

In the end, the values are close to those obtained for the starting prealloyed grade powder, which has a fine grain microstructure due to the fast cooling rate achieved during the gas atomization process.

In the course of the sintering process, independently of the heating rate, each individual powder particle recovers and recrystallizes in a different degree, following an inhomogeneous recrystallization. Therefore, as stated on Chapter 4, the sintered ODS steel evolves into a dual grain size microstructure comprising colonies of ultrafine (UF)

grains and micro size grains. As the heating rate increases the area taken up by the UF colonies is greater and, at the same time, the mean grain size decreases inside the colony (Fig 5.3).

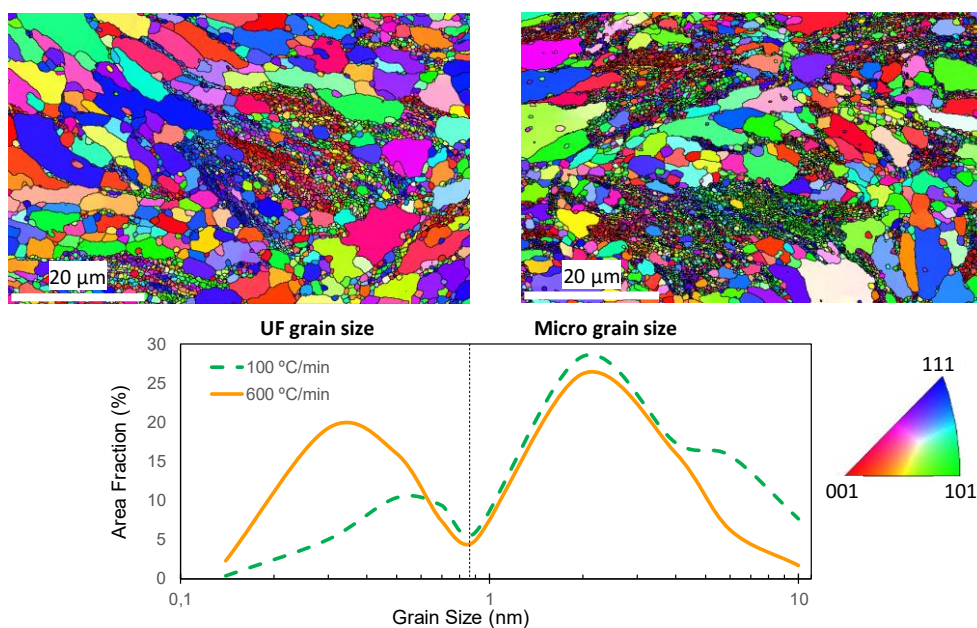


Fig 5.3. Zr100 (left side) and Zr600 (right side) of the Y IPF (SPS compression direction). Graph of grain size distribution depending on the heating rate.

To characterize the completely transversal section of the specimen, a total area of $9000 \mu\text{m}^2$ per SPS sample was considered. In Fig 5.4 the maximum and minimum value attained is reported. The heating rate effect the on the extension of the UF grain colonies is clear when faster heating rates are used ($600 \text{ }^\circ\text{C}/\text{min}$ promotes the higher UF area).

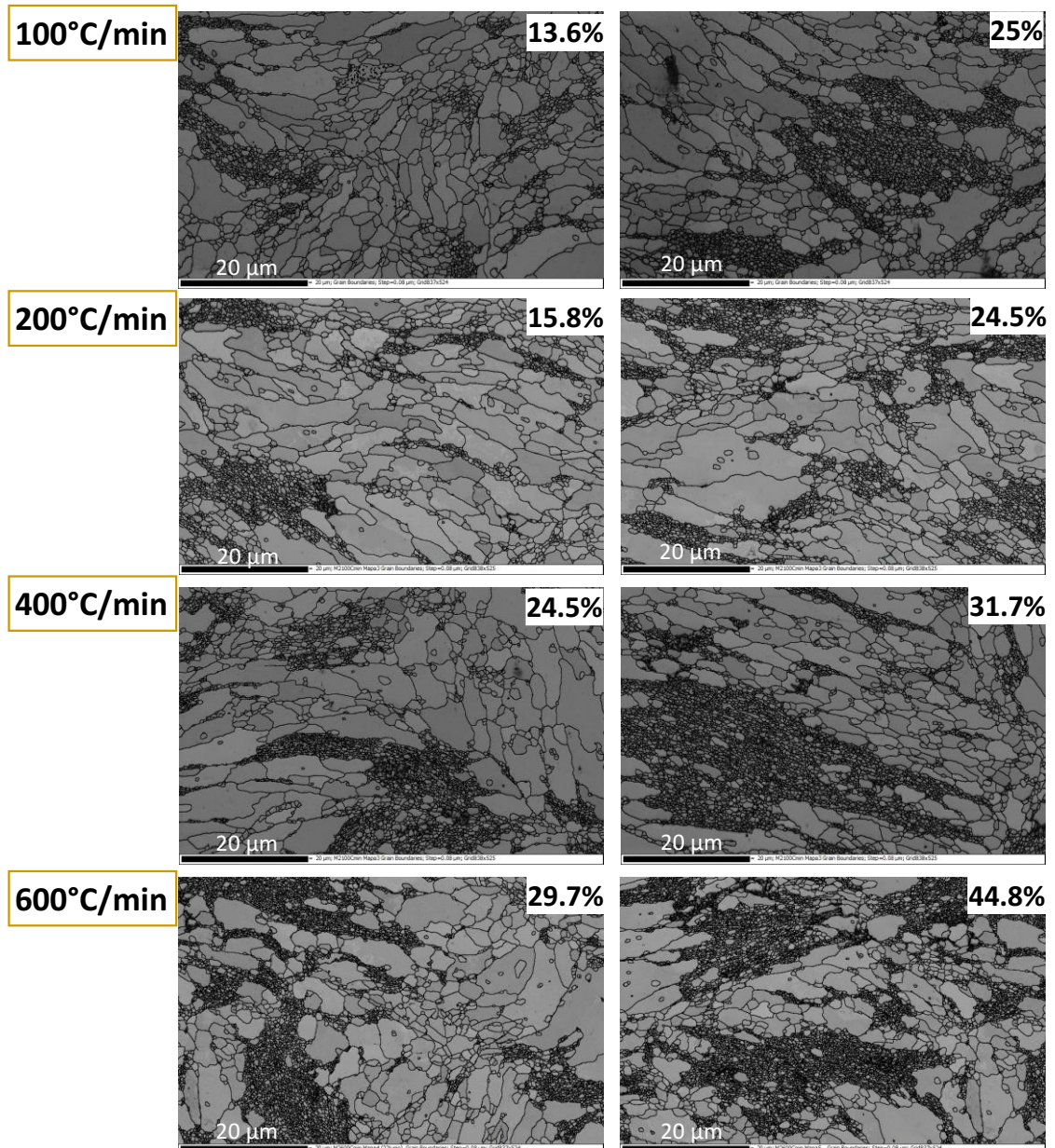


Fig 5.4. F-ODS-I grain size map based on the different heating rates where the ultrafine areas per heating rate are represented. The minimum of UF is represented on the left side and the maximum attained on the right side.

Higher heating rates have a direct effect not only on the presence of ultrafine colonies, but also on the average grain size inside those areas, reducing the value as soon as the heating rate is increased (Fig 5.5 and table 5.1). On the other hand, the micrometric grain is also affected. The average micrometric grain size in this region is also reduced, when the heating rate is increased from $100 \text{ }^\circ\text{C}/\text{min}$. Therefore, the UF grains characteristics combined with those of micrometric grains could enhance the mechanical behaviour, providing good toughness without strength losses [3].

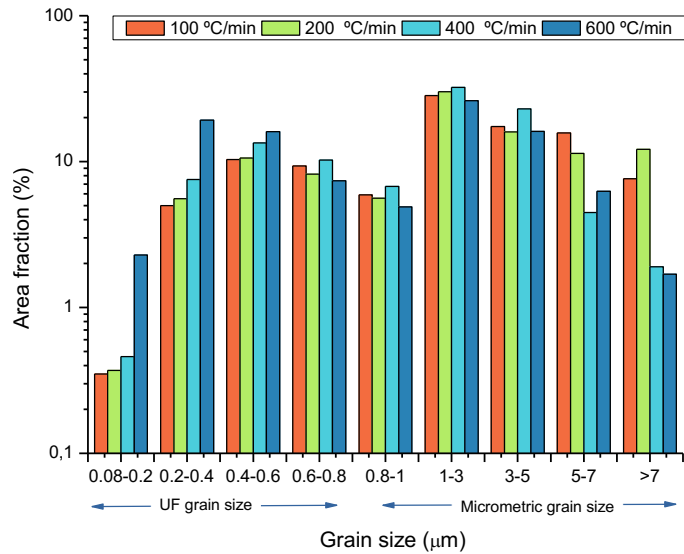


Fig 5.5. Grain size distribution by using different heating rates: UF grain and micrometric grain size. It was considered the images with maximum UF colonies in all the cases.

Besides, Table 5.1 shows the effect on the final dislocation density (calculated from eq 4.1). In this case, trying to perform a more accurate measurement, the microstrain (ϵ) was calculated by means of Williamson-Hall equation [4]. Higher dislocation density remains when 600 °C/min heating rate is selected (Table 5.1) as the material undergoes a shorter thermal history.

Table 5.1. Average grain size, particle size, volume fraction of nanoparticles and dislocation density of the different steels consolidated with different heating rates.

Nomenclature	Zr100	Zr200	Zr400	Zr600
Ultrafine area fraction	19 ± 8	18 ± 6	27 ± 4	32 ± 13
Mean UF grain size (µm)	0.40	0.40	0.39	0.30
Mean micrograin size (µm)	1.57	1.50	1.51	1.51
Microstrain (%) [W-H]	0.17	0.15	0.18	0.20
Dislocation density (m^{-2})	6.55 · 10 ¹⁴	5.10 · 10 ¹⁴	7.34 · 10 ¹⁴	9.07 · 10 ¹⁴

In the literature, it is reported how the heating rate could also has an effect on the final densification of the material, increasing it as the heating rate does [5,6]. In this case, the equilibrium achieved between temperature and pressure has the largest effect on the final consolidation. The values of final density are almost the same, despite of the heating rate used as it is shown on Table 5.2.

Table 5.2. Samples densities using different heating rates (%).

Nomenclature	Zr100	Zr200	Zr400	Zr600
Density (%)	99.4±0.5	99.2±0.5	98.7±0.2	98.6±0.1

5.2. Nano-structured ferritic alloy microstructure: Study of the oxide dispersion

Mechanical properties are closely related to the final oxide dispersion. Therefore, the analysis of oxides composition, dispersion and size is mandatory to understand how this steel is working at room and high temperature. Seeking for the precipitates' refinement, Zr is added to the alloy, besides it would contribute to increase the amount of nano oxides on the material and to form a specific oxide composition Y-Zr-O, instead of larger Y-Al-O, which is supposed to provide higher stability of properties at high temperature.

In this research, trying to understand the effects of the oxide composition and the volumetric fraction on the final attained microstructure, the analysis of precipitates was divided into two parts: ultrafine grains colonies and micrometric grains regions. To analyse the obtained precipitates the F-ODS-I-Zr600 steel is used. To get this, one lamella was produced by ion milling by FIB, containing the dual grain size microstructure (see Fig. 5.6).

5.2.1. Analysis of precipitates on the ultrafine grain area

Oxides at ultrafine grains are located decorating the grain boundaries and inside of the grain, with sizes from 3 to 80 nm and with a precipitation density (N_p^{ii}) of $3 \cdot 10^{22}$ oxd/m³. Their compositions show the high possibilities of interaction among the four oxide formers (Y, Al, Zr, Ti). Several TEM-EDS analysis display five types of precipitates (see table 5.3).

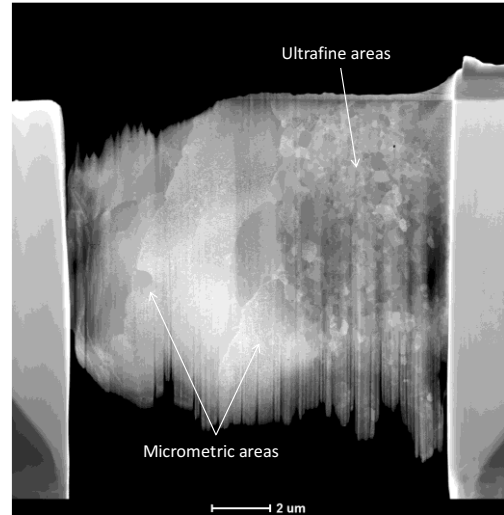


Fig 5.6. Lamella carved on Zr600 material, containing both micrometric and ultrafine regions.

Table 5.3. Main composition of precipitates in Zr600 material.

Precipitate type	Main Composition	Size range (nm)
1	TiZr, WTiZr, WTi, WZr	60-80
2	Y-Al-O	8-20
3	Y-Al-Zr-O	8-20
4	Y-Al-Ti-Zr-O	8-20
5	Y-Zr-O	3-10

Type 1 precipitates are composed by TiZr, WTiZr, WTi, WZr, forming coarse particles, whose diameter varies from 60 and 80 nm (Fig 5.7). Other authors have reported how the Zr can react also with C or N forming compounds different from the expected oxides. These have been reported by J. Isselin et al [7] in a micrometric scale (nevertheless not at this nanometric size) and by K. A. Unocic et al [8], but in their case they argued about Zr C/N formation.

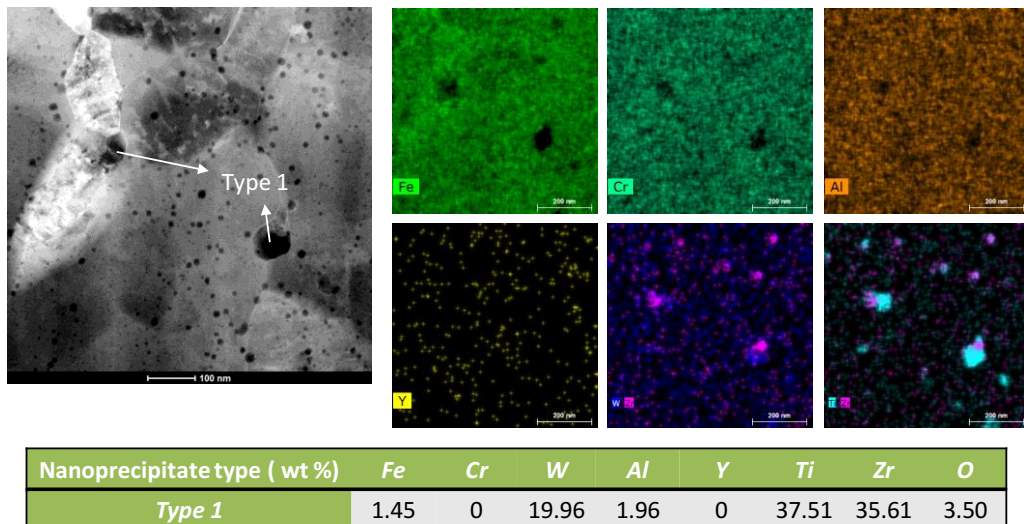
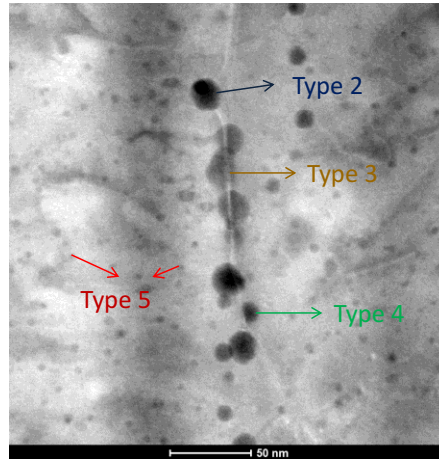


Fig 5.7. Steel Zr600 EDX Mapping and composition oxide type 1.

ⁱⁱ $N_p = \frac{\text{number oxides}}{\text{area-e}}$ considering e = 100nm

In a smaller scale (under 20 nm), particles are composed entirely by oxides. These oxides are distributed along the material and the grain boundary (see fig 5.8). Oxides type 2, 3 and 4 are composed respectively by Y-Al-O, Y-Al-Zr-O and Y-Al-Ti-Zr-O. Their diameter varies from 8 to 20 nm (Fig 5.9) [9]. Therefore, in the view of the results, Zr is not avoiding the formation of Y-Al-O as it was expected by the conclusions reported in the literature [7,10–13].



Nanoparticle type (wt %)	Fe	Cr	W	Al	Y	Ti	Zr	O
Type 2	54.51	8.39	1.88	19.11	5.76	0	0	10.35
Type 3	67.28	13.93	2.05	7.71	1.46	0.3	1.58	5.69
Type 4	64.99	10.91	2.13	9.33	4.43	0.64	0.63	6.94
Type 5	70.92	14.51	2.81	4.24	3.07	0.3	1.12	3.02

Fig 5.8. Detail of oxide compounds on Zr600 materials.

Type 2 (Y-Al-O) and type 3 (Y-Al-Zr-O) are distributed homogenously along the grain’s boundaries and inside of them (see Fig 5.8) meanwhile type 4 are rarely found. These findings were also reported by R. Rahmanifard et al [14] in which a complex Y-Ti-Zr-O complex oxide was analysed. Moreover, R. Gao et al [10] located a solid solution composed by Y-Al-Zr-O, similar to the one observed in this research (type 3).

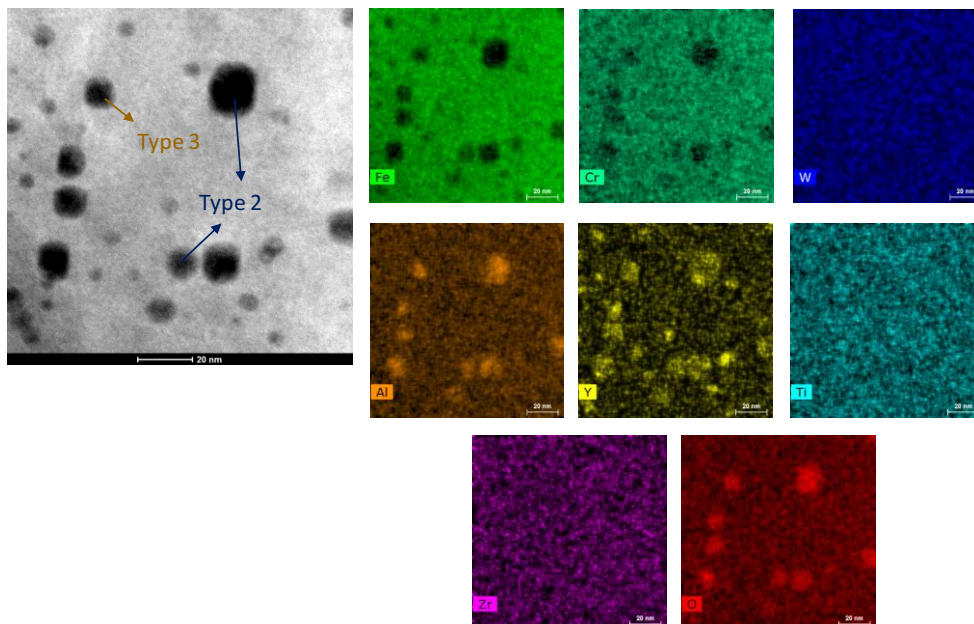


Fig 5.9. Zr600 EDX Mapping, oxide type 2 and 3.

Oxides type 5 are particles of 3-10 nm with a Y-Zr-O composition. The higher binding energy of Zr respect Al enhance the formation of these nano-oxides (see Fig 5.10). The Zr addition has refined the nano-oxides, reducing the size, less than 10 nm.

Other investigations have found the formation of equivalents nano oxides. H. Dong et al [13] whose research is focus on 16Cr ODS steels with 3% Al and 0.5% Zr, observed that Y-Al-O and Y-Zr-O coexist, although $Y_4Zr_3O_{12}$ is the most prone to form. P. Dou et al [15] studied a 4% Al containing ODS steels with 0.6% of Zr addition where the formation Y-Al-O was almost entirely reduced and induced the formation of $Y_4Zr_3O_{12}$ and Y_2TiO_5 with an average size of 3.7 nm. R. Gao et al [10] studied the effect of Zr by producing an Al containing ODS steel through sol gel techniques. The mean size of Zr-precipitates is larger than the one obtained in this Thesis (25 nm), nevertheless, in that steel, precipitates are practically formed by Y-Zr-O.

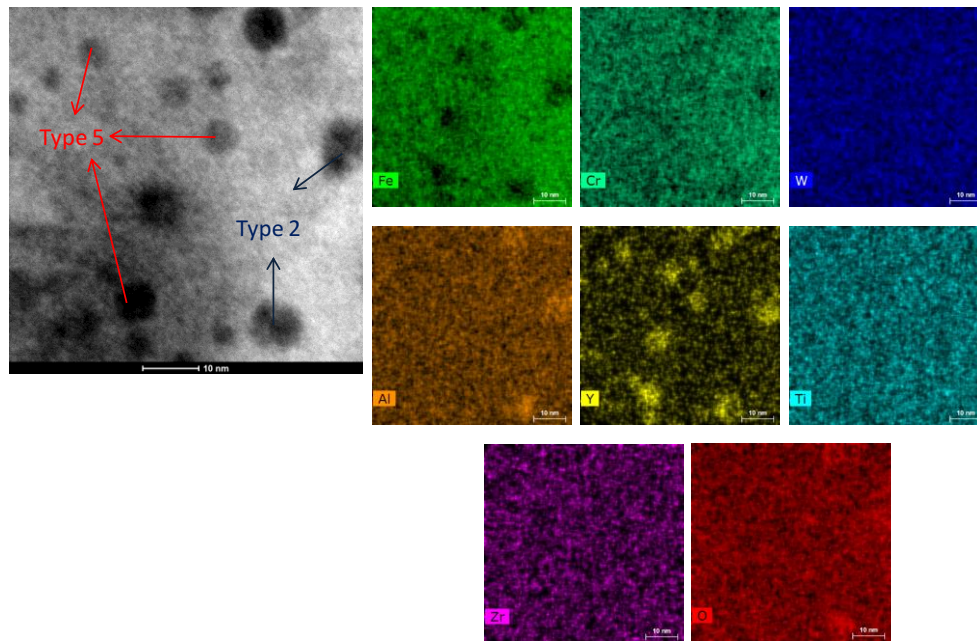


Fig 5.10. Zr600 EDX Mapping, type 5 oxide.

Table 5.4 displays the frequency of different precipitates compositions on the alloy. The 65 % of the particles analysed under 10 nm contains Zr.

Table 5.4. Total number of analysed particles and fraction containing Y, Zr, Ti or Al under 10 nm.

Total number of particles analysed	Y containing nanoparticles	Zr containing nanoparticles	Ti containing nanoparticles	Al containing nanoparticles
14	14	9	0	4

5.2.2. Analysis of precipitates on the micrometric grain

Micrometric regions were also analysed trying to find if the composition, size or nano-oxides localization have conditioned the attained microstructure (Fig 5.11).

However, no differences on precipitates features were observed. Oxides type 1 are clearly identified on these regions, even if in this case, the most frequent detected composition was TiZr or ZrTi, with sizes between 30 to 60 nm. However, this type tends to form agglomerates, making difficult the precise measurement. In this region, 20 particles were analysed among which 14 fulfil the composition previously mentioned.

On the other side, the compositions of smaller particles (less than 20 μm) are in accordance with oxides type 2, 3 and 4. Besides, oxide type 5 was also detected.

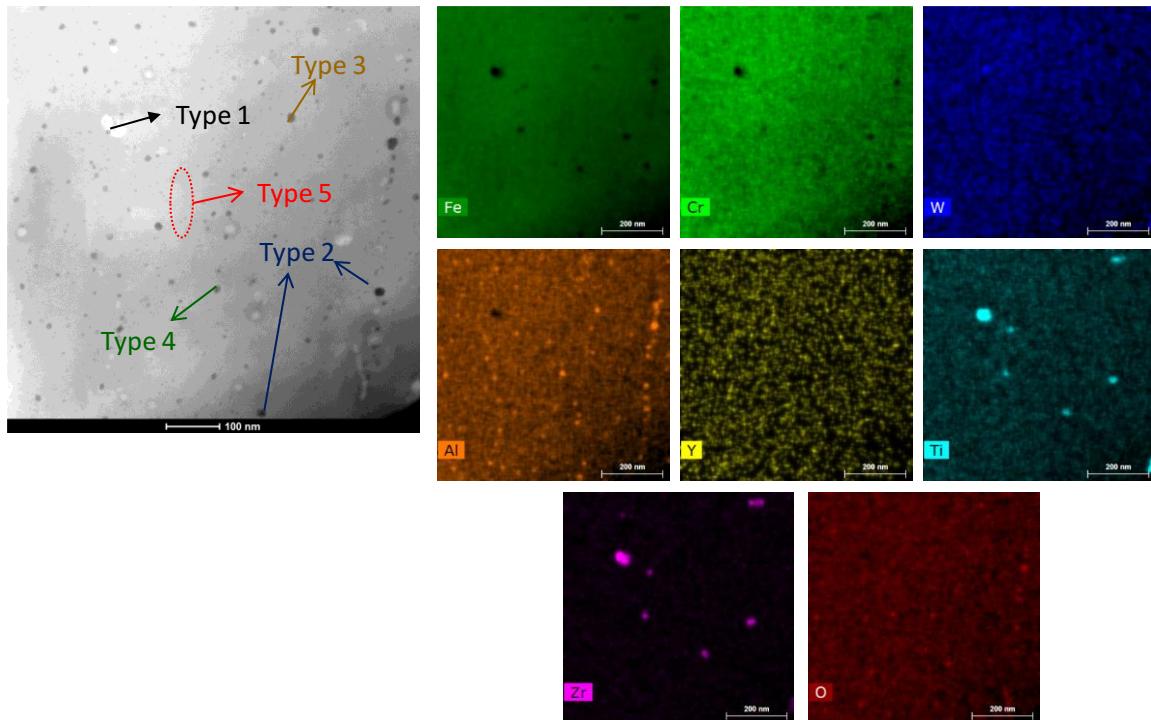


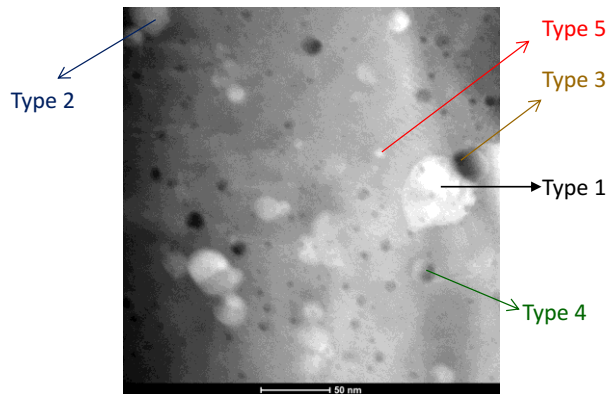
Fig 5.11. Zr600 EDX mapping on micrometric grains.

Therefore, micrometric areas and UF colonies have the same oxide characteristic, the only different relay on the density of oxides where UF colonies attain a $3 \cdot 10^{22}$ oxd/m³ and micrometric regions $1.6 \cdot 10^{22}$ oxd/m³.

5.2.3. SPS Heating rate effect: Low HR vs high HR

To assess the effect of the heating rate on the final oxide precipitation, the steel Zr100 was studied to compare the results reported in the previous section for Zr600.

Taking into account the composition of nano-precipitates, all types of oxides previously mentioned were also detected in Zr100 material (see Fig 5.12 and 5.13).



Nanoparticle type (wt %)	Fe	Cr	W	Al	Y	Ti	Zr	O
Type 1	27.91	5.6	2.39	1.91	3.47	6.83	47.11	4.78
Type 2	59.16	10.44	2.48	12.46	3.04	0.19	0.33	11.91
Type 3	56.69	11.75	2.7	10.38	4.34	0	3.37	10.78
Type 4	62.55	15.15	2.44	5.67	2.79	1.16	3.28	6.96
Type 5	73.28	12.04	3.04	2.22	1.67	0.83	3.44	3.49

Fig 5.12. Precipitates composition on Zr100 material.

Nevertheless, unlike Zr600 steel, a reduction on the Al reaction with Y-Zr-O is observed, highlighting a highest number of precipitates composed entirely by Y-Zr-O. Considering the analysed region, it was possible to find coarser type 5 oxides with sizes from 11 nm to 20 nm (in Zr600, type 5 oxides are between 5-10 nm).

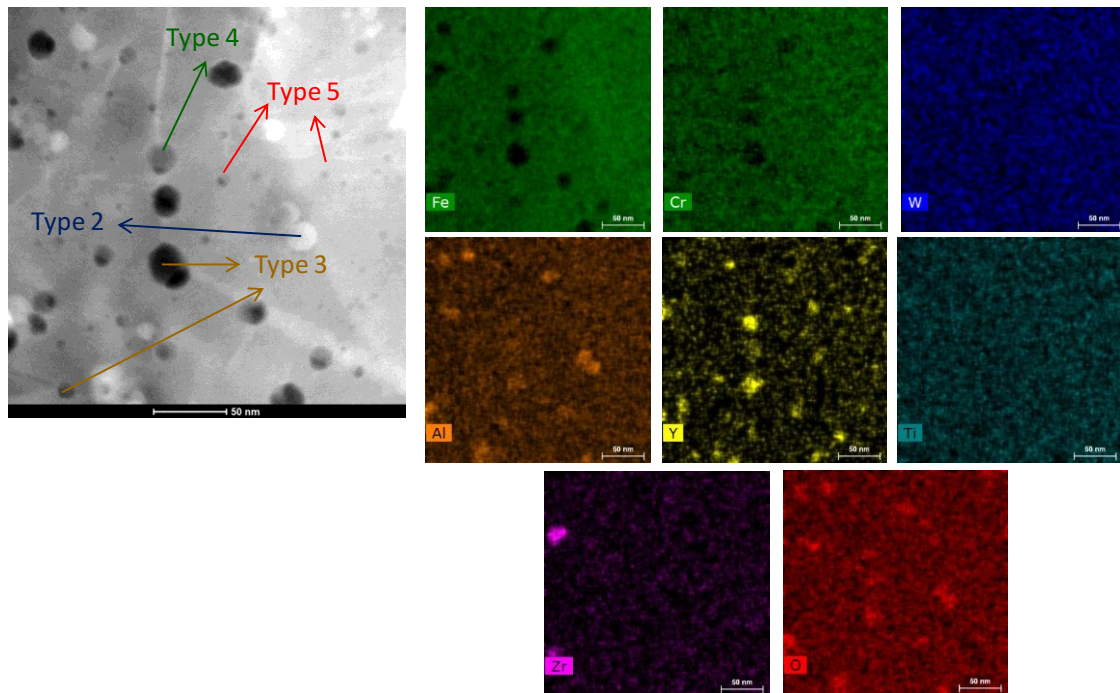


Fig 5.13. Oxide nature on Zr100 materials: Tem EDS mapping.

It seems that at least on terms of the oxide density, the values are in the same order of magnitude for both steels: $N_p]^{100Zr}$ is between 1 to $2 \cdot 10^{22}$ oxd/m³ and $N_p]^{600Zr}$ varies from 1 to $3 \cdot 10^{22}$ oxd/m³.

If oxide size distribution is considered, similar results are detected (Fig 5.14). The mean size for both materials, Zr100 steel 5.3 nm and Zr600 steel 5.6 nm, indicates that the heating rate does not have a remarkable influence.

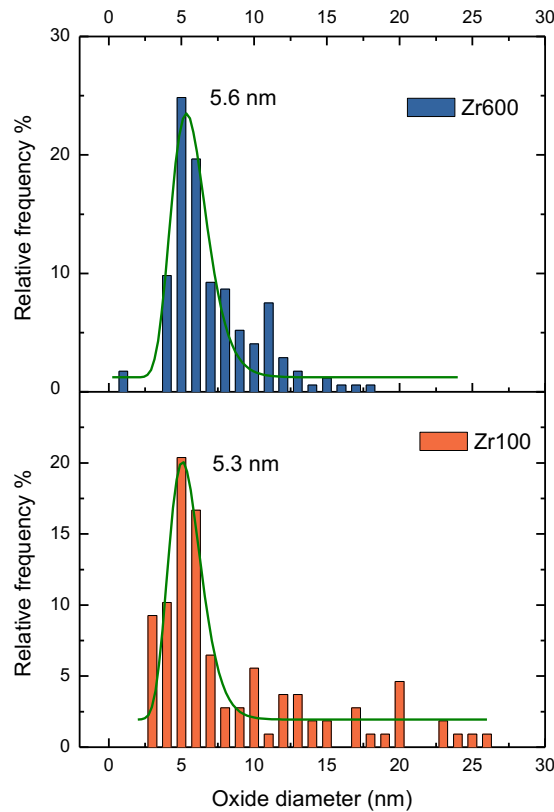


Fig 5.14. Precipitates dimension on Zr100 and Zr600 material.

5.2.4. Effect of Zr addition on the precipitates size distribution

Zr addition should determine the grain growth and consequently the mechanical properties. Fig 5.15 shows the obtained grain size distribution, comparing 14Al-ODS-Ti, with F-ODS-I (Zr100 and Zr600).

Considering only the ultrafine regions (with grain sizes below 800 nm) it is visible how the F-ODS-I containing Zr has a higher UF area fraction (Zr 600 a 45%; Zr100 a 25%, 14AlODS a 19.5 %). The use of faster heating rates, along with Zr addition have promoted a wide extension of UF grain microstructure.

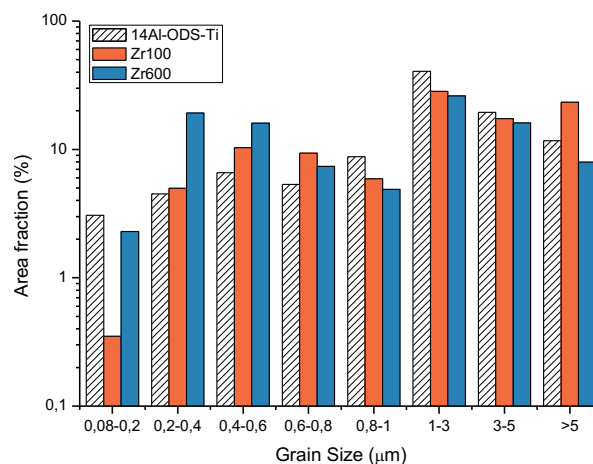


Fig 5.15. Grain size distribution comparison: Zr600 and Zr100 vs 14Al-ODs-Ti. It was considered the images with the maximum UF colonies for all the steels.

TEM study of F-ODS-I alloys and the equivalent Zr-free grade (14Al-ODS-Ti) has proved the refinement of precipitated oxides. Image of F-ODS-I has an oxide size distribution centred on 5.5 nm meanwhile the one of 14Al-ODS-Ti has achieved a distribution centred on 12 nm sizes (Fig

5.16). Besides, the densities of oxide precipitation varies from $1.66 \cdot 10^{22} \text{ oxd}/\text{m}^3$ to $5.57 \cdot 10^{21} \text{ oxd}/\text{m}^3$ respectively [16].

The morphology obtained is similar for both alloys indeed, composed especially by almost rounded particles. However, 14Al-ODS-Ti precipitates are almost completely formed by Y-Al-O nano-oxides [16]. The precipitate's nature could also influence the grain growth.

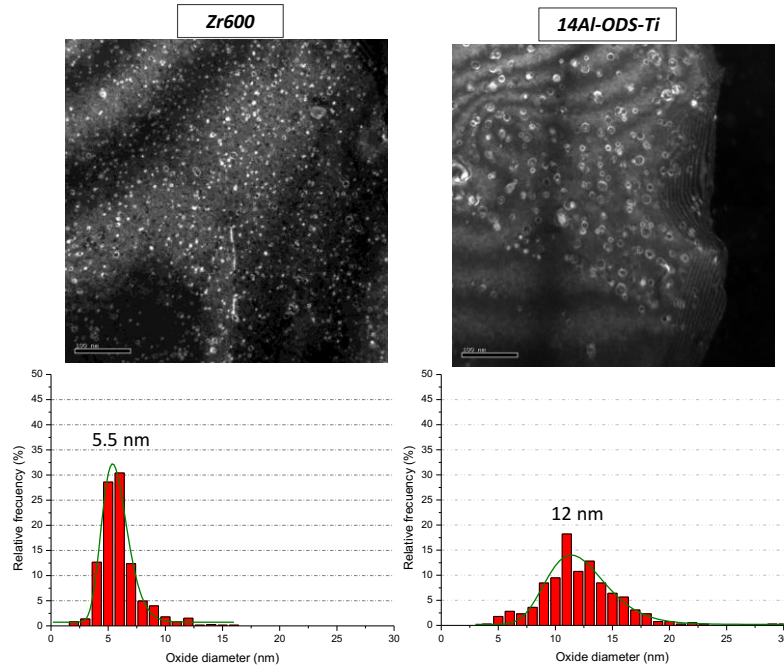


Fig 5.16. Nano oxides precipitates on Zr600 vs 14Al-ODS-Ti size distribution.

5.3. Evaluation of the mechanical behaviour

As in Chapter 4, to understand the effect Zr on the mechanical response, the F-ODS-I will be compared to 14Al-ODS-Ti (Zr free). Both samples were consolidated by SPS using a heating rate of $100 \text{ }^\circ\text{C}/\text{min}$ [16]. Besides, to evaluate the material under high temperature, F-ODS-I materials were compared to GETMAT using small punch tests [17,18].

5.3.1. Room temperature behaviour

The materials resistance to local plastic deformation was tested by microhardness. Fig 5.17 shows how the consolidated ODS steels with Zr additions have reached a comparable level to ODS RAF, consolidated following a complex processing route (HIP plus thermomechanical treatment, detailed on figure as Sci. literature) [19]. The reduction of the grain size, the precipitation of new nano-oxides and the efficient solid solution strengthening leads to an increase in the obtained hardness. These values are of the same order as those reported in the literature [20,21].

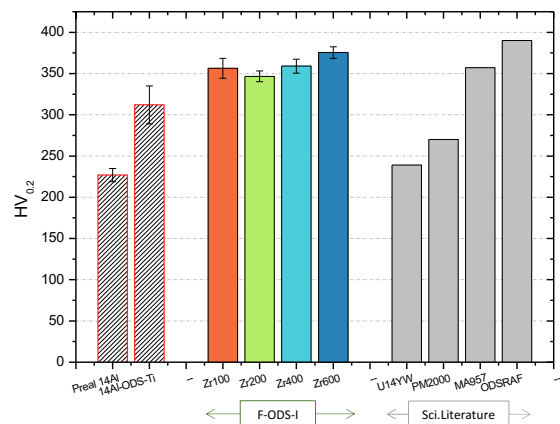


Fig 5.17. Microhardness of different ODS steels.

Yield Strength is also estimated through the hardness following the eq. on page 76 (table 5.5) [22].

Table 5.5. F-ODS-I Yield Strength calculated from microhardness measurements.

Nomenclature	Zr100	Zr200	Zr400	Zr600
σ_y (MPa)	1163	1132	1172	1226

Moreover, microtensile test allows to evaluate the maximum resistance of the material under an uniaxial load as well as the capability of the material to be deformed.

Independently of the used heating rate, F-ODS-I steels have demonstrated an extraordinary UTS values (Fig 5.18). The UTS increases when the area fraction of UF grains increases too (table 5.1). The YS calculated by tensile test confirm the tendency of the YS estimated by microhardness data.

Toughness is essentially affected by the balance between UF and micrometric grains and by the final density of sintered specimens. Although all the consolidated materials, from Zr100 to Zr600, present a good equilibrium between toughness and UTS, the higher results are achieved for the material processed at 600 °C/min, which exhibit the largest area of ultrafine grains.

The in-situ tests help to understand the mechanical behaviour of these ODS steels (Fig 5.18). The pictures correspond to the tensile evolution of Zr200 once the necking has begun. Just before break, cracks appear at 45° to the loading direction. This phenomenon, together with the necking on the sample in the gauge section, proves the ductility of the material.

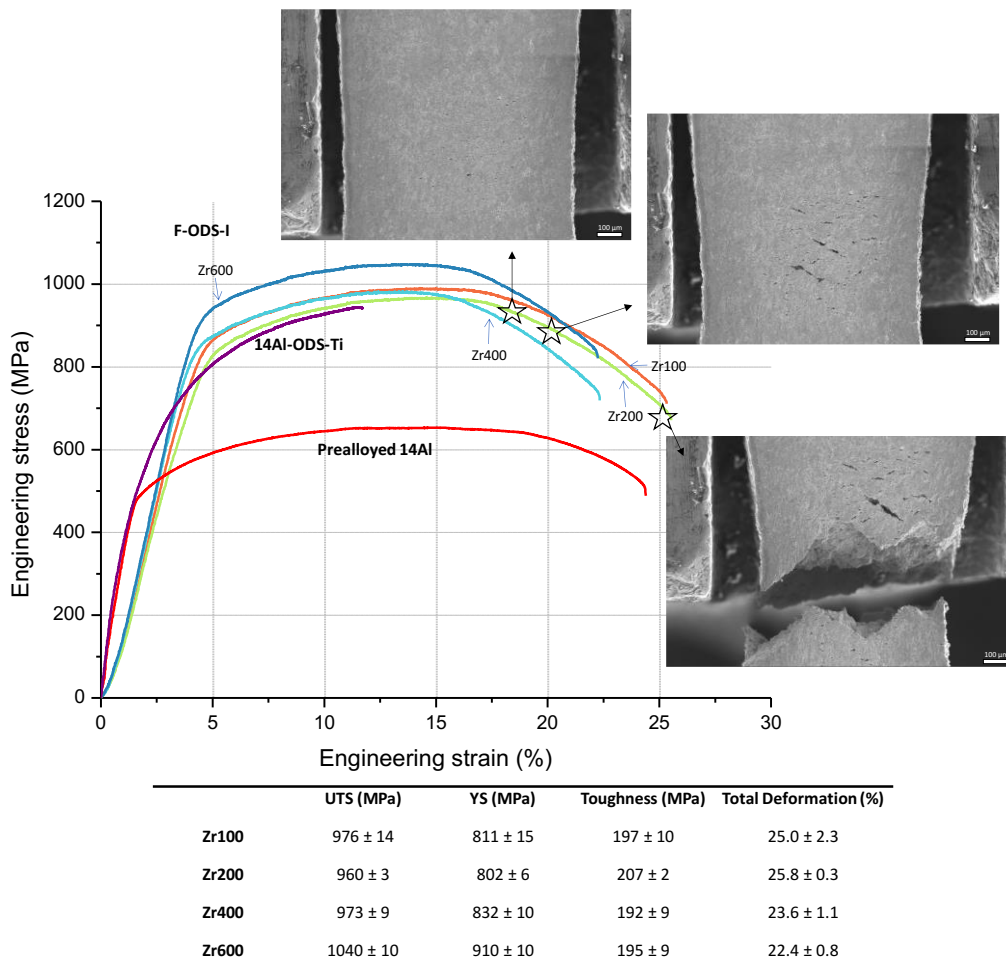


Fig 5.18. Comparison of engineering tensile stress-strain curves for the SPS ODS steels with Zr addition ZrX00, ODS Zr free (14Al-ODS-Ti) and free ODS ferritic steel (Prealloyed 14Al). SEM micrographs showed the cracks formed during the tensile test of Zr200 ODS steel depending on tensile deformation.

5.3.2. High temperature behaviour by SP test

The results of the SP tests are plotted on the load-deflection curves (Fig 5.19). Considering the materials' response at RT and 500 °C is well defined the influence of the Zr addition and the bimodal grain size distribution effect. Zr600 ODS steel maintains the maximum load (F_m) until 300 °C, and for 500 °C F_m only decreases a 13%. The response in terms of ductility (deflection) and F_{max} is comparable to that observed for the hot extruded ODS steel analysed in GETMAT project [17,18].

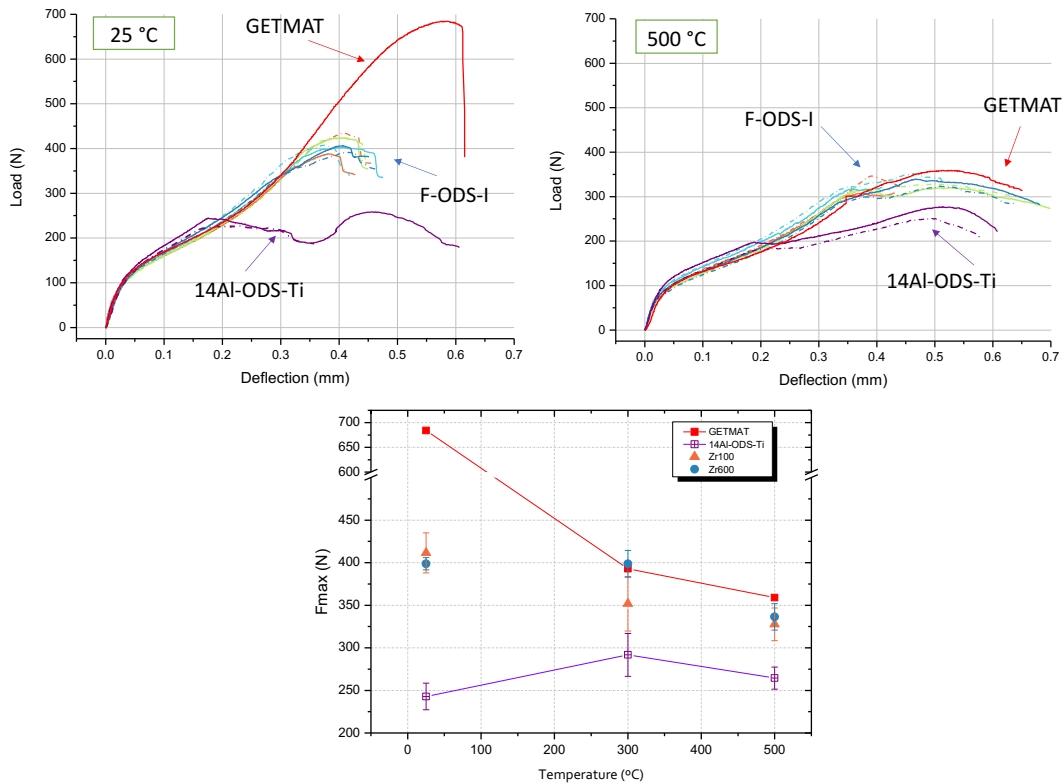


Fig 5.19. SP test at RT and 500 °C and maximum load values achieved at different temperatures. Graphs show the comparison between Zr- ODS, Free Zr-ODS and GETMAT steel (processed by HE [17,18]).

Fractography of the SP tested specimens has shown two different behaviours (Fig 5.20). A typical ductile- fragile fracture mode with open and circumferentially oriented cracks for the F-ODS-I group, and a fragile fracture mode with radial cracks in the case of Zr-free ODS steel - 14Al-ODS-Ti [18,23].

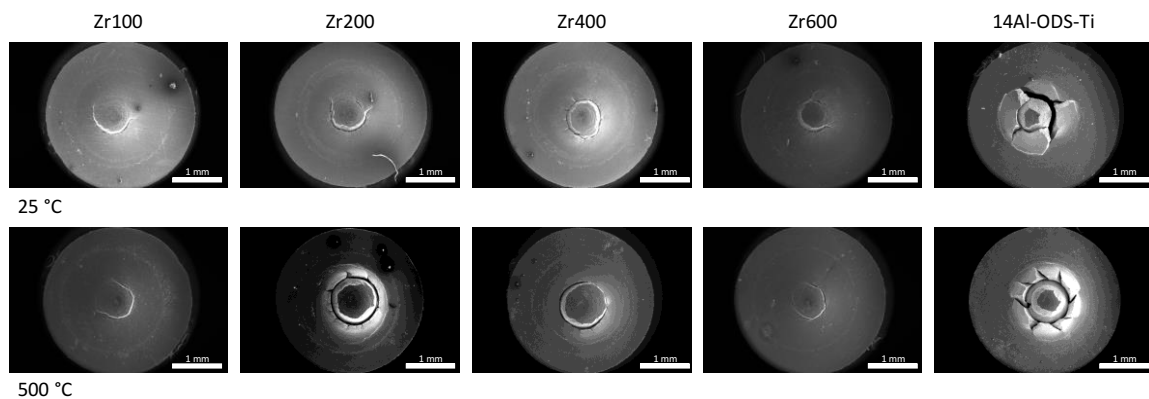


Fig 5.20. Small punch fracture specimens.

The fractography of the sample is directly related to the final microstructure and to the densification (higher than 98% for F-ODS-I). Clearly, the Zr addition has changed the fractography (rounded shape instead of star shape).

5.4. Partial discussion

5.4.1. Influence of processing conditions

The sintered ODS steel evolves into a dual grain size microstructure, comprising colonies of UF grains and areas of micro size grains. Three parameters control the grain growth. First, the nano-oxide precipitation, which produces a strong pinning effect on the grain boundaries that will transform into an abnormal growth [24]. Second, the unequal plastic deformation and alloying distribution achieved during the MA that will determine the stored energy and the ability of recrystallization [24–26]. Finally, the heating rate. This parameter is increased as the current intensity does, so, the heat generated by the Joule effect on particles rises as well. At the same time, the high density of lattice defects decreases the conductivity of the milled powder, limiting the penetration depth of the Joule effect. Consequently, the temperature gradient on the former particle could be increased for higher HR. Hence, grains close to the particle surface could recrystallize before the core of the former particle, contributing to the abnormal growth [27–29].

On the other side, consolidation time and temperature are determining the grain growth, so limiting the time for sintering (diffusion) by using SPS with higher HR could limit the diffusion processes and finally the grain growth, explaining why Zr600 presents the higher area covered by UF.

5.4.2. Effect of Zr addition on the nature of the nano-precipitates

The precipitates Y-Zr-Al-O (type 3) are not widely reported on similar ferritic ODS steels, and only few authors have detected or at least mentioned [10]. According to previous theories proposed, Zr addition improves the nucleation rate and consequently decreases the size and increases the density of nano-precipitates, besides promotes oxides with higher stability which usually are composed by Y-Zr-O [9,12,14,30–34]. Nevertheless, as it was recorded during this Chapter, there is a high variability of interactions between the four oxide formers (Y,Ti,Zr,Al) on F-ODS-I-Zr600 material. Consequently, the highest population is composed by Y-Zr-Al-O (type 3) complex oxides, some by Y-Al-O oxides (type 2) and others or at least the smallest ones by Y-Zr-O (type 4) and just in a few cases forming large precipitates (60-80 nm) ZrTi, ZrW, TiW (Type 1). Therefore, the effectivity of Zr on forming Y-Zr-O is limited since part of Zr reacts creating other precipitates.

S.Mohan et al [12] among others related the formation of the different precipitates to the bonding energy between the oxides formers, vacancies, medium in which they are inserted (in ferritic matrix) and oxygen. Therefore, the explanation given on the next paragraphs is based on their investigations. Indeed, the solute elements reaction with oxygen will lead into the production of one precipitate with one specific composition. In case Y, Zr and Ti are in free state (without the ferritic matrix), their interaction with oxygen is granted and the binding energy (between the element and O) follows the next trend $Zr-O > Y-O > Al-O$ ⁱⁱⁱ. However, Y, Zr and Al are highly influenced by the environment in which they are inserted (in this case the BCC Fe structure), and their behaviour changes following the next tendency $Y-O > Zr-O > Al-O$. This phenomena is explained in [12] through the formation energy of the solute element into Fe

ⁱⁱⁱ -O=The link with oxygen

matrix, since $\text{Fe-Y} > \text{Fe-Zr} > \text{Fe-Al}^{\text{iv}}$. Under these rules, Y and Zr have the advantage on the precipitation of nano-oxides respect Al.

Additionally, during the alloying step, MA promotes a high concentration of vacancies. Many authors [35–39] connect the formation of nanoclusters (or nano-oxides) with that vacancies obtained during milling. Furthermore, S. Mohan et al [12] studied the relationship established between different solute atoms with vacancies, oxygen-vacancy and Yttrium -oxygen -vacancy through their binding energy and the capacity to form easily one specie respect the others. They concluded that the binding energy when a solute atom interacts with the vacancy, follows the next trend $\text{Y-O}^{\text{v}} > \text{Zr-O}^{\text{v}} > \text{Al-O}^{\text{v}}$ (-1.20 eV, -0.73 eV and -0.30 eV respectively).

Moreover, if the trend solute atom-oxygen-vacancy are studied together, the maximum binding energy for Zr-O^{v} was -2.55 eV comparing to -2.01 for Al-O^{v} [12]. The binding energy related to Zr compounds is higher than the one related to Al compounds since the interaction between Al-O and Al-O^{v} is smaller than Zr-O or Zr-O^{v} . Moreover, the binding energy between Y-O^{v} is far superior than $\text{Solute-O}^{\text{v}}$ being the more prone to form. Usually, if a solute element reacts with Y there is a repulsion which is compensated by the high binding energy promoted by Y-O and Y-O^{v} . Certainly, this explains why Y-Zr-O or Y-Al-O or YZrAlO represent almost the totality of the formed nano-precipitates and it was not possible to detect Zr-O or Y-O or Ti-O or Al-O or ZrY , TiY formations.

It should be noted that the content of Y, Ti and Zr (0.2, 0.4, 0.6 –wt %- respectively) is quite small regarding to the 5% of Al content. Consequently, as stated by K. Unocic et al [8], the diffusion rate, starts to be an important parameter which has to be taken into account. The 5 wt % of Al indicates that around 1 in 10 atoms is Al or in 5 units cells there should be Al atom in a solid solution. Therefore, the distance presented by Al to react with O is shorter than the one presented by Y, Ti or Zr. Besides, Al has a diffusion rate similar to the self-diffusion of Fe in the BCC matrix with as a consequence could favour the reaction of Al over the rest of the elements. Moreover, M. Palm et al [40] reported that in the BCC matrix the solubility of Al around a 45 % at can be dissolved depending on the temperature. Nevertheless the solubility of Zr is far reduced 0.16 at % [41] as well as the one presented by Y which represent less than 1 at % [42]. Definitely, this could explain why it is not possible to prevent the formation of Y-Al-O or the compound composed by Y-Zr-Al-O [13] even if the binding energy between Y and Zr is far superior.

On the other side, it is interesting to observe how Ti has a lower effect on the refinement of precipitates on Al containing ODS steels [43]. Considering the relationship between Ti and vacancies (0.26 eV), is observed that $\text{Y-O}^{\text{v}} > \text{Zr-O}^{\text{v}} > \text{Al-O}^{\text{v}} > \text{Ti-O}^{\text{v}}$. Consequently, Y-Al-O will precipitate first than Y-Ti-O . Only when the composition does not include Al, the competition establish between Zr and Ti to form a solid solution with Y and O can shift the formation of Ti-Y-O to Zr-Y-O [44]. The bond length of Zr-O in $\text{Y-O}^{\text{v}}\text{-O-Ti}$ is shorter than that of Ti-O in $\text{Y-O}^{\text{v}}\text{-Zr-O}$ providing stronger interaction between Y and Zr and consequently finer and higher stable oxide [30,38]. Besides, D.Murali et al [37,38] reported that the binding energy between Y-O^{v} rises when Ti was substituted by Zr which promotes high stable nanoclusters. Moreover they clearly observed how the binding energy between Y and Zr in a BCC matrix is 0.12 eV respect the one attained for Y-Ti which is -0.21 eV.

Symbols:

$^{\text{iv}}\text{Fe-Solute element}$ =The formation energy into the matrix

$^{\text{v}}\text{-O}^{\text{v}}$ =The link with the vacancy

5.4.3. Effect of Zr addition on the nano-precipitates size and density

As it was described during the Chapter, independently on the composition, smaller and higher density of precipitates are attained when Zr is added to the alloy (p. 105). When F-ODS-I is compared to 14Al-ODS-Ti (without Zr addition) the size of precipitates is reduced from 12 nm to 5.5 (55%) and the density increases its value in an order of magnitude (from 10^{21} to 10^{22} oxd/m^3). Similar results are reported on these researchers whose investigation are based on Al containing ODS steels.

Starting from these authors whose Cr percentage is higher than F-ODS-I-Zr600 (16 vs 14) and the Al amount is a little bit lower (1-2% less), R. Gao et al [10] (16 Cr ODS alloys with 4wt% of Al), reported an oxide diameter of 25 nm and a particles density of $2.1 \cdot 10^{21} oxd/m^3$ ($10^{19} oxd/m^3$ without Zr) by using sol gel precursors. Furthermore, C.Z.Yu et al [45] (16 Cr ODS steels with 4 % Al addition) observed a reduction of the particle size from 8.1 to 7.1 and an increase on the oxide density (from 1.2 to $2.0 \cdot 10^{22} oxd/m^3$). H. Dong et al [13] (16 Cr ODS steels with a 3% of Al) , get a reduction on the oxide diameter, from 9.8 to 8nm and a increment on the oxide density ,from 2.1 to $3.2 \cdot 10^{23} oxd/m^3$.

Furthermore, in these materials whose Cr content is on the same range of F-ODS-I , P. Dou et al [15,46,47] (15 Cr ODS steels with a 3% of Al) disclosed how by adding Zr an average oxide size of 4.75 nm and a density of $7.16 \cdot 10^{22} oxd/m^3$ is attained (The oxide size average is 6.78 nm and a density of $1.72 \cdot 10^{22} oxd/m^3$ the same alloy without Zr).

Finally, using the same amount of Al as the one presented for F-ODS-I ,K.A.Unocic et al [8](12 Cr ODS steels with 5 wt % of Al) showed that the addition of Zr promotes oxides whose dimension are 10.2 nm respect 10.5 nm of these steels without this element. They also observed modifications on the oxide density from $2.5 \cdot 10^{23} oxd/m^3$ to $1.4 \cdot 10^{23} oxd/m^3$.

Undoubtedly, Zr is determining the final precipitation and particle density obtained, independently on the addition of Al or the amount of Cr as it is described in all the investigations analysed in this section. [10,13,15,45–47].

However, it is not clear that Zr has a direct effect on the grain refinement. During this Chapter it was described how the grain size does not depend only on the precipitation state (which is the one determined by Zr) but also on the final condition used to consolidate the material and on the plastic deformation degree attained during the mechanical alloying step (See Chapter 4, p. 85). From the previous authors, H. Dong et al [13] analysed a reduction on the grain size from 1795 nm to 756 nm. A. García-Junceda et al [48], using the same composition as in F-ODS-I by adding ZrO_2 have also reported a reduction of 500 nm in grain size by the addition of 0.6 ZrO_2 . K.A.Unocic et al [8] reported also a refinement of the grain on these material that contains Zr. However, J. Isselin et al [7] (14 Cr ODS steels with 4% Al) observed that the improvement on the grain promoted by the Zr addition is not clear respect to the base material. This phenomenon might be demonstrated by the Zener equation (Eq 5.1), which shows the critical grain radius R_c^{Zener} as function of the precipitate state (oxide radius r_p and volumetric fraction f_p):

$$R_c^{Zener} = \frac{4r_p}{3f_p} \quad (\text{eq 5.1})$$

Comparing F-ODS-I-Zr600 and 14Al-ODS-Ti through this equation gives as a result Fig 5.21.

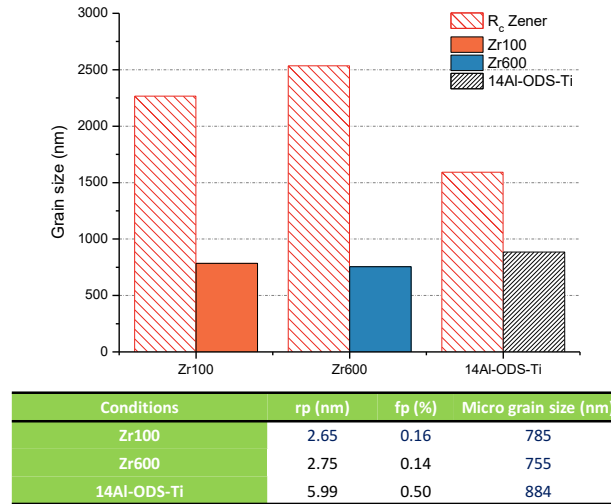


Fig 5.21. Zener pinning effect on Zr100 and Zr600 vs 14Al-ODS-Ti.

As it was described in Fig 5.3, the grain size distribution of F-ODS-I is composed by smaller grains than the result obtained by R_C^{Zener} (See in Fig 5.21 Zr100 and Zr600) which consequently highlight the importance of using the heating rate to limit the grain growth. Without the use of HR the grain will grow until the particles pin the grain border.

On the other side the R_C^{Zener} provided by 14Al-ODS-Ti (consolidated by using SPS and an HR of 100 °C/min) attains lower values than F-ODS-I materials. Undoubtedly, Zr is directly determining the precipitation state (less size and higher density) but the grain size structure is not completely determined by this element. As it was affirmed by J. Iselin et al [7] it is difficult to correlate the refining of the grain with the presence of Zr.

5.4.4. Strengthened mechanisms

Changes produced on the microstructure are not clearly noticeable on the final mechanical properties achieved unless the selected heating rate is 600 °C/min. For this reason, the contribution of the different strengthening mechanism is required. For this purpose, following the reported results in other works [4,49–51] the equation 5.2 collects the mechanisms that influence the yield strength, σ_y , of the ferritic ODS :

$$\sigma_y = \sigma_0 + \sigma_{ss} + \sigma_{gb} + \sqrt{\sigma_{dis}^2 + \sigma_p^2} \quad (\text{eq 5.2})$$

σ_0 is the lattice friction stress of pure iron whose value was taken as 53.9 MPa as it is described in [51].

The σ_{ss} is the solid solution contribution. First, the solid solution strengthening can be divided into the interstitial and substitutional strengthening. In this work, it is assumed that the input of Ti, Al or Zr to solid solution strengthening or the one provided by C or N due to the milling step are negligible. Thus, Cr and W are the main alloying elements for solid solution strengthening. This parameter is given by the equation 5.3 [52]:

$$\sigma_{ss} = 0.00689 \sum K_i \cdot c_i^z \quad (\text{eq 5.3})$$

Where K is the strengthened coefficient and c_i is the atomic percent of the different substitutional elements. As it is stated in [51,52] the value of K_i for Cr is 1400 and for W is 11000 and for the substitutional elements the exponent z is equal to 0.75 as stated in [4,49,50]. In this work, the atomic percentage of Cr is 14%, and it is 0.83% for W, which gives a total value for σ_{ss} of 140 MPa.

The strengthening promoted by grain boundaries in this dual microstructure depends on the analysed area (micro or ultrafine colonies). It was considered the mean value of each region to calculate the total contribution (equation 5.4). [53]:

$$\sigma_{gb} = f_{area} \cdot \left(\frac{1}{5} G \sqrt{\frac{b}{d_g}}\right) \quad (\text{eq 5.4})$$

Equation 5.3 was slightly modified adding f_{area} which represent the area fraction covered by ultra fine or micrometric grain size, trying to perform an accurate measurement as it was proposed in [50]. G is the iron shear modulus (85 GPa) [54], b is the Burgers vector (in this case 0.252 nm calculated for a pure Fe lattice).

The dislocation hardening (σ_{disl}) was calculated by equation 5.5 [55]:

$$\sigma_{disl} = \alpha_d M G b \sqrt{\rho} \quad (\text{eq 5.5})$$

Where M is the Taylor factor (3.06) [56], α_d is a constant (1/3) [53], and ρ is the dislocation density. Table 5.1 summarizes all the parameters necessary to perform this calculation.

Finally, the oxide contribution usually was estimated by the Orowan bypass mechanism [4]. However, this theory supposed that the oxides particles are impenetrable without taken into account the range of coherency of the different oxides. Chauhan et all [51] proposed the use of another equation based on the formulation of Seeger [57,58]:

$$\sigma_p = \alpha_p M G b \sqrt{N_p d_p} \quad (\text{eq 5.6})$$

Where α_p is the obstacle strength for oxide nanoparticles which could vary from 0.1 to 0.5 (depending on the particle type and the degree of coherency). Following the parameters used by Chauhan et all in [51], α_p was taken as 1/3. Besides, N_p represent the density of nano-oxides and d_p is the mean particle diameter, which was determined by TEM observation (Fig 5.21). In a ODS steel by refining the size and increasing the oxide volume fraction is possible to increase the contribution of that term σ_p . As the heating rate does not show an effect on the oxide precipitation, the system was simplified assuming the same volume fraction and mean oxide diameters for each material. If the mean oxide size is 5.5 nm and the precipitation density is $1.63 \cdot 10^{22} \text{ oxd}/m^3$, then the volume fraction is 0.142%. This gives a contribution by precipitation hardening of 205 MPa.

The input of each term of eq. 5.2 is gathered in table 5.6. The theoretical calculations highlight that the grain size has a small influence on the final yield strength (see Fig 5.22.). However, the dual grain size distribution has shown a greater influence for balancing the mechanical response, allowing a higher strain level in the processed ODS steel.

Table 5.6. Strengthening contributions and experimental vs calculated Yield Strength for the F-ODS-I steel.

Strength. Contribution (MPa)	Zr100	Zr200	Zr400	Zr600
σ_{gb}	268	271	288	339
σ_{dislo}	559	493	592	657
σ_p	205	205	205	205
Yield Strength (MPa)				
$\sigma_{y,calc}$	1057	999	1108	1221
$\sigma_{y,experimental}$	811	802	832	910

By plotting all the contributions to σ_y , it is possible to notice how the processed ODS material is specially conditioned by the hardening produced by the dislocation density and particle pinning.

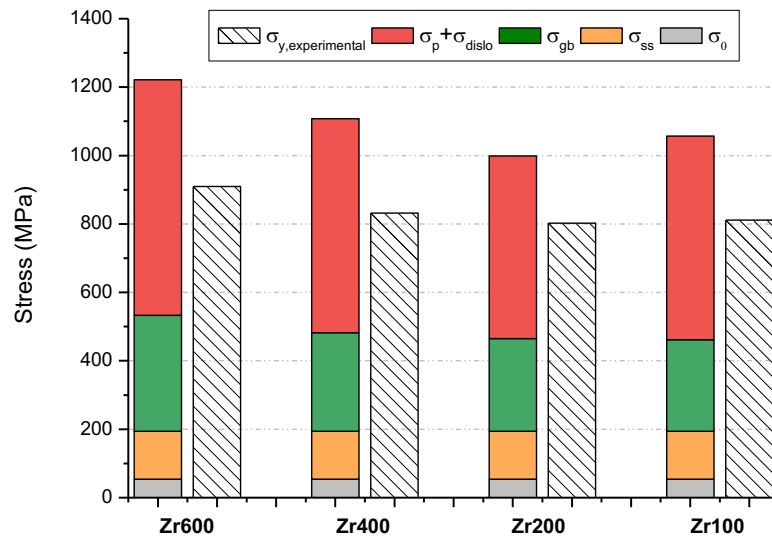


Fig 5.22. F-ODS-I experimental and estimated Yield Strength at room temperature.

The difference between experimental results and theoretical calculations could be due to the strengthened promoted by lattice friction and solid solution hardening. Lattice friction stress depends directly on the type of dislocation slip system and temperature, for this reason, friction stress value could suffer modifications [59]. Apart from that, Cr and W content determines the solid solution strengthening term, but both elements have formed carbides along the material which could lead to a decrease of the real combined amount in solid solution [60]. Hence, the σ_{ss} value could be lower. If these two terms are neglected and it is only considered as dominant the contributions of σ_{gb} , σ_{dislo} and σ_p , the theoretical calculation has shown a superior accuracy with regards to experimental data as stated in [51] (table 5.7).

Table 5.7. Comparison of theoretical contribution (in MPa) considering two approach vs experimental results.

Nomenclature	Zr100	Zr200	Zr400	Zr600
$\sigma_{y,calc} = f(\sigma_0, \sigma_{ss}, \sigma_{gb}, \sigma_{dis}, \sigma_p)$	1057	999	1108	1221
$\sigma'_{y,calc} = f(\sigma_{gb}, \sigma_{dis}, \sigma_p)$	863	805	914	1028
$\sigma_{y,experimental}$	811	802	832	910

5.4.5. Evaluation of the material under high temperature

The results of the small punch tests suggest small differences with the variation of the heating rate from room temperature to 500 °C, making the grain refinement insufficient to be detected by this method [61]. Independently of the heating rate used, all the materials processed are hardened by dislocation density and oxides precipitation. Both terms allow those materials to present a stable behaviour under high temperature service. It is assumed from previous studies performed at high temperature, that until 400 °C the contribution to the strengthening produced by the dislocations is constant. Solid solutions follow the same path but until 600 °C [50]. This explains why at 500 °C there is a drop in the mechanical properties (F_{max}) since the dislocation density seems to be reduced at this temperature [50]. What is not clear is the effect of the precipitates at high temperatures. Nano-oxides present high thermal stability, avoiding the coarsening at temperatures near to $0,8T_m$ [62]. If those oxides are refined by Zr addition [12–15,31,32,63] and coherent oxides are obtained, the pinning effect at high temperature could be maintained and it allows the material to present good properties under those conditions. Then, the Zr addition is the key-factor in the improvement of the mechanical properties at high temperature.

5.5. Partial remarks

An ODS steel has been developed by the addition of Zr, and it has been successfully processed by using SPS as a consolidation technique. It is demonstrated that:

- The selection of the SPS processing conditions can modify the grain size distribution. A large effect on the grain size is obtained by fixing an optimum heating rate. Higher heating rates increase the area of ultra-fine regions and cut down the grain size inside these areas, while the micrometric grain coarsening is reduced.
- Zr is refining the attained nano-precipitates (achieving a distribution mean size of 5.5 nm) compares to the same material without Zr addition taken as a reference (14Al-ODS-Ti, 12 nm), besides increasing the precipitation density from 10^{21} to 10^{22} oxd/m³.
- F-ODS-I presents a wide variation on the composition of precipitates. Besides, Y-Al-O (type 2 oxides) are not avoided and a solid solution with Zr is observed (Y-Zr-Al-O type 3). Moreover, under 10 nm, Y-Zr-O nano-oxides have been analysed.
- Zr addition has the strongest effect on improving the mechanical behaviour of the material, offering an extraordinary balance between toughness and UTS and also, good properties at high temperatures (500 °C).
- The analysis of the mechanical properties proves that SPS ODS steels with Zr have similar characteristic to the ones obtained by traditional consolidation method such as HIP or HE.
- The material consolidated at 600 °C/min (Zr600) achieves the best values of microhardness and UTS. Although the grain refinement contributes to the increase of these properties, the mechanical behaviour is not totally determined by this factor. Dislocation and oxide hardening are the parameters that determine the final mechanical properties.
- Small punch tests demonstrate how Zr600 can keep the maximum load until 300 °C. However, at 500 °C, Zr100 and Zr600 have almost the same behaviour.

Bibliography

- [1] U. Anselmi-Tamburini, J.R. Groza, Critical assessment: electrical field/current application—a revolution in materials processing/sintering?, *Mater. Sci. Technol.* (United Kingdom). 33 (2017) 1855–1862. doi:10.1080/02670836.2017.1341692.
- [2] N. Sallez, X. Boulnat, A. Borbély, J.L. Béchade, D. Fabregue, M. Perez, Y. De Carlan, L. Hennet, C. Mocuta, D. Thiaudiere, Y. Brechet, In situ characterization of microstructural instabilities : Recovery , recrystallization and abnormal growth in nanoreinforced steel powder, 87 (2015) 377–389. doi:10.1016/j.actamat.2014.11.051.
- [3] X. Wu, Y. Zhu, Heterogeneous materials: a new class of materials with unprecedented mechanical properties, *Mater. Res. Lett.* 5 (2017) 527–532. doi:10.1080/21663831.2017.1343208.
- [4] J. Shen, Y. Li, F. Li, H. Yang, Z. Zhao, S. Kano, Y. Matsukawa, Y. Satoh, H. Abe, Microstructural characterization and strengthening mechanisms of a 12Cr-ODS steel, *Mater. Sci. Eng. A.* 673 (2016) 624–632. doi:10.1016/j.msea.2016.07.030.
- [5] I. Bogachev, E. Grigoryev, O.L. Khasanov, E. Olevsky, Fabrication of 13Cr-2Mo ferritic/martensitic oxide-dispersion-strengthened steel components by mechanical alloying and spark-plasma sintering, *Jom.* 66 (2014) 1020–1026. doi:10.1007/s11837-014-0972-5.
- [6] M.S. Staltsov, I.I. Chernov, I.A. Bogachev, B.A. Kalin, E.A. Olevsky, L.J. Lebedeva, A.A. Nikitina, Optimization of mechanical alloying and spark-plasma sintering regimes to obtain ferrite–martensitic ODS steel, *Nucl. Mater. Energy.* 9 (2016) 360–366. doi:10.1016/j.nme.2016.08.020.
- [7] J. Isselin, R. Kasada, A. Kimura, T. Okuda, M. Inoue, S. Ukai, S. Ohnuki, T. Fujisawa, F. Abe, Effects of Zr Addition on the Microstructure of 14%Cr4%Al ODS Ferritic Steels, *Mater. Trans.* 51 (2010) 1011–1015. doi:10.2320/matertrans.MBW200923.
- [8] K.A. Unocic, B.A. Pint, D.T. Hoelzer, Advanced TEM characterization of oxide nanoparticles in ODS Fe–12Cr–5Al alloys, *J. Mater. Sci.* 51 (2016) 9190–9206. doi:10.1007/s10853-016-0111-5.
- [9] J. Ren, L. Yu, Y. Liu, C. Liu, H. Li, J. Wu, Effects of Zr addition on strengthening mechanisms of Al-alloyed high-Cr ODS steels, *Materials (Basel).* 11 (2018) 1–13. doi:10.3390/ma11010118.
- [10] R. Gao, T. Zhang, X.P. Wang, Q.F. Fang, C.S. Liu, Effect of zirconium addition on the microstructure and mechanical properties of ODS ferritic steels containing aluminum, *J. Nucl. Mater.* 444 (2014) 462–468. doi:10.1016/j.jnucmat.2013.10.038.
- [11] S. Takaya, T. Furukawa, M. Inoue, T. Fujisawa, T. Okuda, F. Abe, S. Ohnuki, A. Kimura, Corrosion resistance of Al-alloying high Cr–ODS steels in stagnant lead–bismuth, *J. Nucl. Mater.* 398 (2010) 132–138. doi:10.1016/j.jnucmat.2009.10.023.
- [12] S. Mohan, G. Kaur, B.K. Panigrahi, C. David, G. Amarendra, Effect of Zr and Al addition on nanocluster formation in oxide dispersion strengthened steel - An ab initio study, *J. Alloys Compd.* 767 (2018) 122–130. doi:10.1016/j.jallcom.2018.07.047.
- [13] H. Dong, L. Yu, Y. Liu, C. Liu, H. Li, J. Wu, Enhancement of tensile properties due to microstructure optimization in ODS steels by zirconium addition, *Fusion Eng. Des.* 125 (2017) 402–406. doi:10.1016/J.FUSENGDES.2017.03.170.
- [14] R. Rahmanifard, H. Farhangi, A.J. Novinrooz, Effect of zirconium and tantalum on the microstructural characteristics of 12YWT ODS steel nanocomposite, *J. Alloys Compd.* 622

- (2015) 948–952. doi:10.1016/j.jallcom.2014.11.018.
- [15] P. Dou, A. Kimura, R. Kasada, T. Okuda, M. Inoue, S. Ukai, S. Ohnuki, T. Fujisawa, F. Abe, TEM and HRTEM study of oxide particles in an Al-alloyed high-Cr oxide dispersion strengthened steel with Zr addition, *J. Nucl. Mater.* 444 (2014) 441–453. doi:10.1016/j.jnucmat.2013.10.028.
- [16] N. García-Rodríguez, M. Campos, J.M. Torralba, M.H. Berger, Y. Bienvenu, Capability of mechanical alloying and SPS technique to develop nanostructured high Cr, Al alloyed ODS steels, *Mater. Sci. Technol.* 30 (2014) 1676–1684. doi:10.1179/1743284714Y.0000000595.
- [17] M. Serrano, M. Hernández-Mayoral, A. García-Junceda, Microstructural anisotropy effect on the mechanical properties of a 14Cr ODS steel, *J. Nucl. Mater.* 428 (2012) 103–109. doi:10.1016/j.jnucmat.2011.08.016.
- [18] M. Serrano, A. García-Junceda, R. Hernández, M.H. Mayoral, On anisotropy of ferritic ODS alloys, *Mater. Sci. Technol.* 30 (2014) 1664–1668. doi:10.1179/1743284714Y.0000000552.
- [19] Z. Oksiuta, N. Baluc, Optimization of the chemical composition and manufacturing route for ODS RAF steels for fusion reactor application, *Nucl. Fusion.* 49 (2009). doi:10.1088/0029-5515/49/5/055003.
- [20] Z. Oksiuta, N. Baluc, Effect of mechanical alloying atmosphere on the microstructure and Charpy impact properties of an ODS ferritic steel, *J. Nucl. Mater.* 386–388 (2009) 426–429. doi:10.1016/j.jnucmat.2008.12.148.
- [21] M.J. Alinger, G.R. Odette, D.T. Hoelzer, On the role of alloy composition and processing parameters in nanocluster formation and dispersion strengthening in nanostructured ferritic alloys, *Acta Mater.* 57 (2009) 392–406. doi:10.1016/j.actamat.2008.09.025.
- [22] P. Zhang, S.X. Li, Z.F. Zhang, General relationship between strength and hardness, *Mater. Sci. Eng. A.* 529 (2011) 62–73. doi:10.1016/j.msea.2011.08.061.
- [23] K. Guan, L. Hua, Q. Wang, X. Zou, M. Song, Assessment of toughness in long term service CrMo low alloy steel by fracture toughness and small punch test, *Nucl. Eng. Des.* 241 (2011) 1407–1413. doi:10.1016/j.nucengdes.2011.01.031.
- [24] X. Boulnat, N. Sallez, M. Dadé, A. Borbély, J. Béchade, Y. De Carlan, J. Malaplate, Y. Brechet, F. de Geuser, A. Deschamps, P. Donnadieu, D. Fabregue, M. Perez, Influence of oxide volume fraction on abnormal growth of nanostructured ferritic steels during non-isothermal treatments: An in situ study, *Acta Mater.* 97 (2015) 124–130. doi:10.1016/j.actamat.2015.07.005.
- [25] M. Dadé, J. Malaplate, J. Garnier, F. De Geuser, N. Lochet, A. Deschamps, Influence of consolidation methods on the recrystallization kinetics of a Fe-14Cr based ODS steel, *J. Nucl. Mater.* 472 (2016) 143–152. doi:10.1016/j.jnucmat.2016.01.019.
- [26] N. Sallez, C. Hatzoglou, F. Delabrouille, D. Sornin, L. Chaffron, M. Blat-Yrieix, B. Radiguet, P. Pareige, P. Donnadieu, Y. Bréchet, Precipitates and boundaries interaction in ferritic ODS steels, *J. Nucl. Mater.* 472 (2016) 118–126. doi:10.1016/j.jnucmat.2016.01.021.
- [27] R. Xie, Z. Lu, C. Lu, Z. Li, X. Ding, C. Liu, Microstructures and mechanical properties of 9Cr oxide dispersion strengthened steel produced by spark plasma sintering, *Fusion Eng. Des.* 115 (2017) 67–73. doi:10.1016/j.fusengdes.2016.12.034.
- [28] K. Vanmeensel, A. Laptev, J. Hennicke, J. Vleugels, O. Van Der Biest, Modelling of the temperature distribution during field assisted sintering, *Acta Mater.* 53 (2005) 4379–

4388. doi:10.1016/j.actamat.2005.05.042.
- [29] U. Anselmi-Tamburini, S. Gennari, J.E. Garay, Z.A. Munir, Fundamental investigations on the spark plasma sintering/synthesis process: II. Modeling of current and temperature distributions, *Mater. Sci. Eng. A*. 394 (2005) 139–148. doi:10.1016/j.msea.2004.11.019.
- [30] H. Xu, Z. Lu, S. Ukai, N. Oono, C. Liu, Effects of annealing temperature on nanoscale particles in oxide dispersion strengthened Fe-15Cr alloy powders with Ti and Zr additions, *J. Alloys Compd.* 693 (2017) 177–187. doi:10.1016/j.jallcom.2016.09.133.
- [31] L. Zhang, L. Yu, Y. Liu, C. Liu, H. Li, J. Wu, Influence of Zr addition on the microstructures and mechanical properties of 14Cr ODS steels, *Mater. Sci. Eng. A*. 695 (2017) 66–73. doi:10.1016/J.MSEA.2017.04.020.
- [32] H. Xu, Z. Lu, D. Wang, C. Liu, Effect of zirconium addition on the microstructure and mechanical properties of 15Cr-ODS ferritic Steels consolidated by hot isostatic pressing, *Fusion Eng. Des.* 114 (2017) 33–39. doi:10.1016/J.FUSENGDES.2016.11.011.
- [33] A. Kimura, R. Kasada, N. Iwata, H. Kishimoto, C.H. Zhang, J. Isselin, P. Dou, J.H. Lee, N. Muthukumar, T. Okuda, M. Inoue, S. Ukai, S. Ohnuki, T. Fujisawa, T.F. Abe, Development of Al added high-Cr ODS steels for fuel cladding of next generation nuclear systems, *J. Nucl. Mater.* 417 (2011) 176–179. doi:10.1016/j.jnucmat.2010.12.300.
- [34] H. Xu, Z. Lu, D. Wang, C. Liu, Microstructure Refinement and Strengthening Mechanisms of a 9Cr Oxide Dispersion Strengthened Steel by Zirconium Addition, *Nucl. Eng. Technol.* 49 (2017) 178–188. doi:10.1016/j.net.2017.01.002.
- [35] C.L. Fu, M. Krčmar, G.S. Painter, X.Q. Chen, Vacancy mechanism of high oxygen solubility and nucleation of stable oxygen-enriched clusters in Fe, *Phys. Rev. Lett.* 99 (2007) 1–4. doi:10.1103/PhysRevLett.99.225502.
- [36] A. Claisse, P. Olsson, First-principles calculations of (Y, Ti, O) cluster formation in body centred cubic iron-chromium, *Nucl. Instruments Methods Phys. Res. Sect. B Beam Interact. with Mater. Atoms.* 303 (2013) 18–22. doi:10.1016/j.nimb.2013.01.016.
- [37] D. Murali, B.K. Panigrahi, M.C. Valsakumar, C.S. Sundar, Diffusion of γ and Ti/Zr in bcc iron: A first principles study, *J. Nucl. Mater.* 419 (2011) 208–212. doi:10.1016/j.jnucmat.2011.05.018.
- [38] D. Murali, B.K. Panigrahi, M.C. Valsakumar, S. Chandra, C.S. Sundar, B. Raj, The role of minor alloying elements on the stability and dispersion of yttria nanoclusters in nanostructured ferritic alloys: An ab initio study, *J. Nucl. Mater.* 403 (2010) 113–116. doi:10.1016/j.jnucmat.2010.06.008.
- [39] Y. Jiang, J.R. Smith, G.R. Odette, Formation of Y-Ti-O nanoclusters in nanostructured ferritic alloys: A first-principles study, *Phys. Rev. B - Condens. Matter Mater. Phys.* 79 (2009) 1–7. doi:10.1103/PhysRevB.79.064103.
- [40] M. Palm, Concepts derived from phase diagram studies for the strengthening of Fe-Al-based alloys, *Intermetallics*. 13 (2005) 1286–1295. doi:10.1016/j.intermet.2004.10.015.
- [41] C. Servant, C. Gueneau, I. Ansara, Experimental and thermodynamic assessment of the FeZr system, *J. Alloys Compd.* 220 (1995) 19–26. doi:10.1016/0925-8388(94)06036-3.
- [42] Kubaschewski, O, *Iron-binary Phase Diagrams*, 1 ed, 1982, n.d.
- [43] L.L. Hsiung, M.J. Fluss, S.J. Tumey, B.W. Choi, Y. Serruys, F. Willaime, A. Kimura, Formation mechanism and the role of nanoparticles in Fe-Cr ODS steels developed for radiation tolerance, *Phys. Rev. B - Condens. Matter Mater. Phys.* 82 (2010) 1–13. doi:10.1103/PhysRevB.82.184103.

- [44] T.A. Schaedler, W. Francillon, A.S. Gandhi, C.P. Grey, S. Sampath, C.G. Levi, Phase evolution in the YO_{1.5}-TiO₂-ZrO₂ system around the pyrochlore region, *Acta Mater.* 53 (2005) 2957–2968. doi:10.1016/j.actamat.2005.03.010.
- [45] C.Z. Yu, H. Oka, N. Hashimoto, S. Ohnuki, Development of damage structure in 16Cr–4Al ODS steels during electron-irradiation, *J. Nucl. Mater.* 417 (2011) 286–288. doi:10.1016/j.jnucmat.2011.02.037.
- [46] P. Dou, A. Kimura, T. Okuda, M. Inoue, S. Ukai, S. Ohnuki, T. Fujisawa, F. Abe, Polymorphic and coherency transition of Y–Al complex oxide particles with extrusion temperature in an Al-alloyed high-Cr oxide dispersion strengthened ferritic steel, *Acta Mater.* 59 (2011) 992–1002. doi:10.1016/j.actamat.2010.10.026.
- [47] P. Dou, A. Kimura, T. Okuda, M. Inoue, S. Ukai, S. Ohnuki, T. Fujisawa, F. Abe, Effects of extrusion temperature on the nano-mesoscopic structure and mechanical properties of an Al-alloyed high-Cr ODS ferritic steel, *J. Nucl. Mater.* 417 (2011) 166–170. doi:10.1016/j.jnucmat.2011.01.061.
- [48] A. García-Junceda, N. García-Rodríguez, M. Campos, M. Cartón-Cordero, J.M. Torralba, Effect of Zirconium on the Microstructure and Mechanical Properties of an Al-Alloyed ODS Steel Consolidated by FAHP, *J. Am. Ceram. Soc.* 98 (2015) 3582–3587. doi:10.1111/jace.13691.
- [49] X. Zhou, Y. Liu, L. Yu, Z. Ma, Q. Guo, Y. Huang, H. Li, Microstructure characteristic and mechanical property of transformable 9Cr-ODS steel fabricated by spark plasma sintering, *Mater. Des.* 132 (2017) 158–169. doi:10.1016/j.matdes.2017.06.063.
- [50] M. Dadé, J. Malaplate, J. Garnier, F. De Geuser, F. Barcelo, P. Wident, A. Deschamps, Influence of microstructural parameters on the mechanical properties of oxide dispersion strengthened Fe-14Cr steels, *Acta Mater.* 127 (2017) 165–177. doi:10.1016/j.actamat.2017.01.026.
- [51] A. Chauhan, F. Bergner, A. Etienne, J. Aktaa, Y. De Carlan, C. Heintze, D. Litvinov, M. Hernandez-Mayoral, E. Oñorbe, B. Radiguet, A. Ulbricht, Microstructure characterization and strengthening mechanisms of oxide dispersion strengthened (ODS) Fe-9 % Cr and Fe-14 % Cr extruded bars, *J. Nucl. Mater.* 495 (2017) 6–19. doi:10.1016/j.jnucmat.2017.07.060.
- [52] C.E. Lacy, M. Gensamer, The tensile properties of alloyed ferrites, *Trans. Amer. Soc. Met.* 32 (1944) 88–110. doi:10.1016/j.molcatb.2003.10.012.
- [53] M. Praud, F. Momprou, J. Malaplate, D. Caillard, J. Garnier, A. Steckmeyer, B. Fournier, Study of the deformation mechanisms in a Fe-14% Cr ODS alloy, *J. Nucl. Mater.* 428 (2012) 90–97. doi:10.1016/j.jnucmat.2011.10.046.
- [54] F. Bergner, C. Heintze, I. Hilger, M. Serrano, Elastic properties of Fe-Cr and ODS Fe-Cr alloys, (2016) 1–2. doi:10.13140/RG.2.1.3783.5281.
- [55] J.E. Bailey, P.B. Hirsch, The dislocation distribution, flow stress, and stored energy in cold-worked polycrystalline silver AU -, *Philos. Mag. A J. Theor. Exp. Appl. Phys.* 5 (1960) 485–497. doi:10.1080/14786436008238300.
- [56] R.E. Stoller, S.J. Zinkle, On the relationship between uniaxial yield strength and resolved shear stress in polycrystalline materials, *J. Nucl. Mater.* 283–287 (2000) 349–352. doi:10.1016/S0022-3115(00)00378-0.
- [57] A.K. Seeger, On the theory of radiation damage and radiation hardening, *Proc. Second United Nations Int. Conf. Peac. Uses At. Energy, Vol. 6.* 6 (1958) 250–273. doi:10.1007/BF03223261.

- [58] J.H. Kim, T.S. Byun, D.T. Hoelzer, C.H. Park, J.T. Yeom, J.K. Hong, Temperature dependence of strengthening mechanisms in the nanostructured ferritic alloy 14YWT: Part II—Mechanistic models and predictions, *Mater. Sci. Eng. A.* 559 (2013) 111–118. doi:10.1016/j.msea.2012.08.041.
- [59] Z. Chen, Modeling the plastic deformation of iron, 2012. doi:10.5445/KSP/1000032216.
- [60] F. Pickering, Structure-Property Relationships in Steels, *Mater. Sci. Technol.* (2006). doi:10.1002/9783527603978.mst0062.
- [61] J. Isselin, R. Kasada, A. Kimura, T. Okuda, M. Inoue, S. Ukai, S. Ohnuki, T. Fujisawa, F. Abe, Evaluation of fracture behavior of recrystallized and aged high-Cr ODS ferritic steels, *J. Nucl. Mater.* 417 (2011) 185–188. doi:10.1016/j.jnucmat.2010.12.061.
- [62] X. Boulnat, M. Perez, D. Fabregue, T. Douillard, M.H. Mathon, Y. De Carlan, Microstructure evolution in nano-reinforced ferritic steel processed by mechanical alloying and spark plasma sintering, *Metall. Mater. Trans. A Phys. Metall. Mater. Sci.* 45 (2014) 1485–1497. doi:10.1007/s11661-013-2107-y.
- [63] W. Li, T. Hao, R. Gao, X. Wang, T. Zhang, Q. Fang, C. Liu, The effect of Zr, Ti addition on the particle size and microstructure evolution of yttria nanoparticle in ODS steel, *Powder Technol.* 319 (2017) 172–182. doi:10.1016/J.POWTEC.2017.06.041.

6

*Microstructural evaluation
under high temperature conditions:
In-situ TEM annealing*

Contents

6. Preamble to this chapter	125
6.1. Introduction to in-situ TEM annealing test	126
6.2. Ultrafine grain evaluation: Tracking the nano-oxides size and location	127
6.3. Micrometric area analysis: Tracking precipitates and grain size	134
6.4. Microstructural features after the annealing	135
6.5. Partial discussion	137
6.5.1. Effect of temperature on microstructure	137
6.5.2. Effect of temperature on mechanical properties.....	139
6.6. Partial remarks	140
Bibliography	141

6. Preamble to this chapter

Oxide dispersion strengthened ferritic steels are one promising material to be used under high temperature applications. Normally, their good behaviour under extreme conditions (irradiation and high temperatures) is related to the high dispersion density of nano-oxides which are responsible for blocking the motion of dislocation and for reducing the grain growth. Evaluating the stability of the oxides precipitation and grain growing is mandatory to ensure a good behaviour under high temperature conditions. Traditionally, these kinds of materials were evaluated after long annealing tests at different temperatures (between 100 and 10000 h). Subsequently the microstructural and nano-oxides evolution were analysed by TEM characterization.

This chapter presents a new way to examine ferritic ODS steels by using *In-situ TEM annealing*. This method offers the advantage of heating one thin TEM disc (below 100 nm) from room temperature to 600 °C under high vacuum conditions, evaluating at all time the evolution of the reinforced nano-precipitates and the grain stability.

Thus, the **F-ODS-I ODS (Zr600)** is used as a material to be assessed. The chapter is split up into two main parts: the first one shows the in-situ TEM test and the second one the final check-up after the annealing test by using a lamella carved by FIB. The stability showed by F-ODS-I-Zr600 at 600 °C in terms of grain size evolution and oxide stability are promising for future applications.

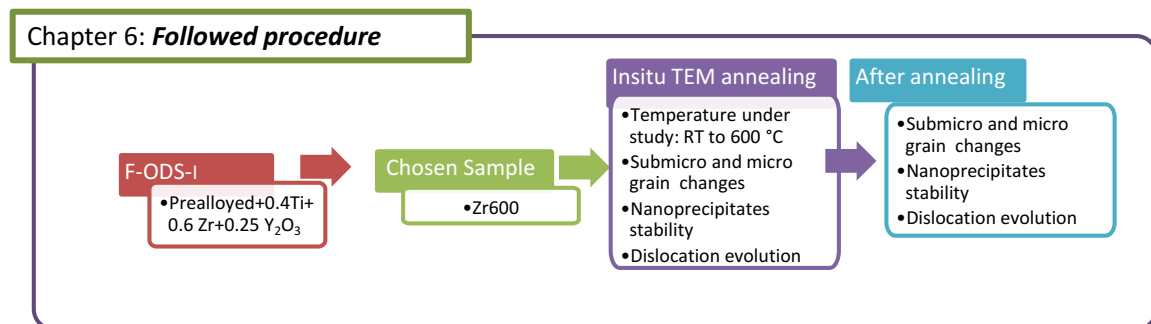


Fig 6.1. Followed procedure in Chapter 6.

6.1. Introduction to in-situ TEM annealing test

As it was stated in Chapter 5, F-ODS-I-Zr600 presents one of the most marked bimodal microstructure reached in this Thesis, with a 32% of the area covered by UF grain colonies where it is possible to observe the high dispersion of nano-precipitates, (see Fig 6.2).

Regions composed by UF grain size can be connected to prior highly deformed powders and consequently, inheriting a large amount of lattice defects; therefore UF grains should be more prone to experiment modifications during the annealing treatment. Hence, one ultrafine grain has been selected to be monitored as T rises. Heating the material induces growing on those grains which are recovered and ready to grow at expenses of others. Micrometric grains are the main candidates to follow this behaviour. Consequently, the in-situ study was performed on the micro grain as well (Fig 6.2).

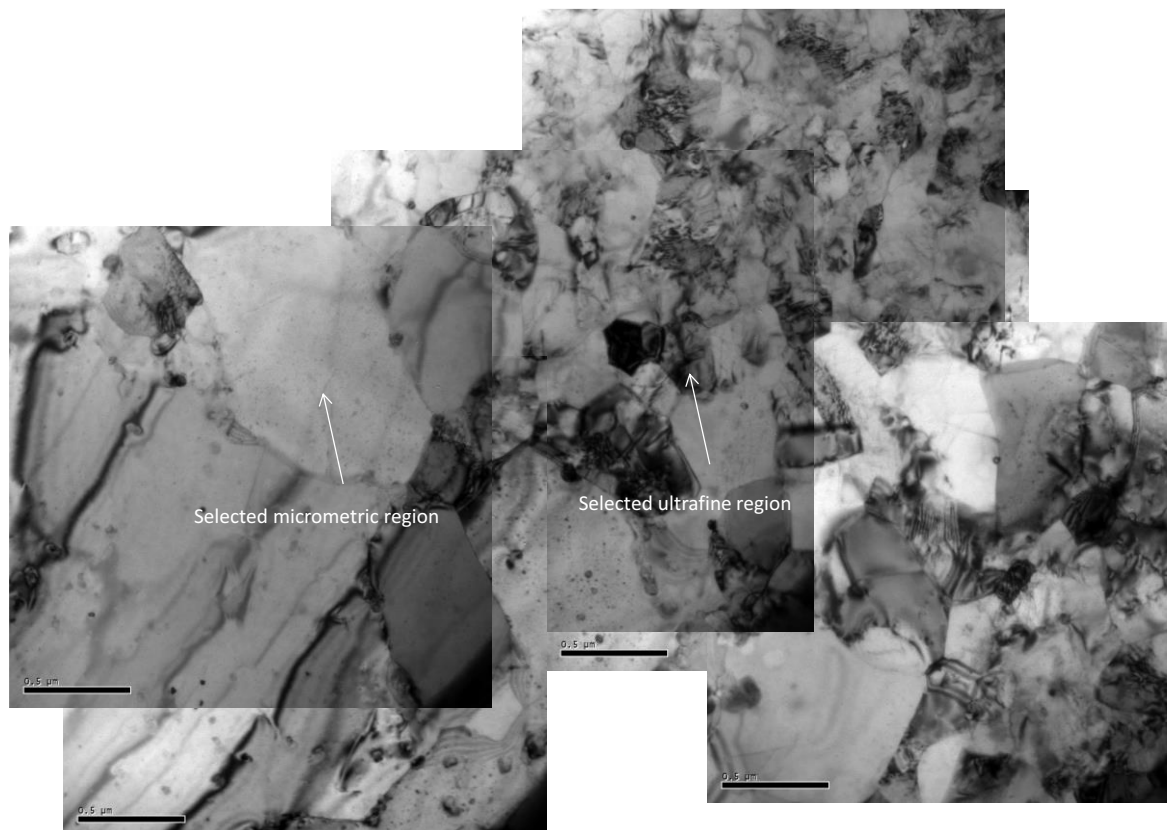


Fig 6.2. Generic view of material microstructure of Zr600 ODS. Selected regions to perform the tracking during the in-situ TEM annealing.

Besides, the stability of the grain is directly related to the dispersion of the precipitated nano-oxides. For this reason, both in the micrometric and UF areas the nano-oxide position, morphology and size are evaluated. As it was stated in Chapter 5, precipitates (from 3 nm to 80 nm) are located at the grain boundaries and inside the grain (see p. 99). Since it is not possible to analyse the nature of precipitates during the in-situ TEM test, the composition was estimated through the diameter.

The effectivity of the nano-oxides on the retention of dislocation is studied through the local dislocation density on studied TEM grains. The minimum value of this parameter is calculated considering the grain area and the length of dislocations inside¹.

¹ $\rho_{disl.} = \frac{lenght}{Area \cdot e}$ considering $e=100nm$

6.2. Ultrafine grain evaluation: Tracking the nano-oxides size and location

Studying the grain evolution under the different temperatures passes through the evaluation of three factors once the UF region is located (Fig 6.3).

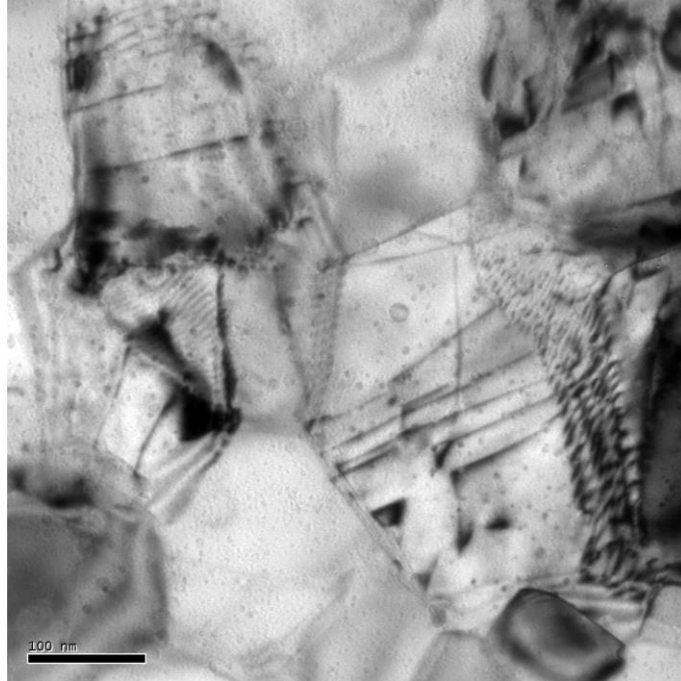


Fig 6.3. Generic view of the selected ultrafine grain area at room temperature on Zr600.

The attention is focused on differences on grain boundaries (whose frontier is marked by green lines), on the oxides dispersion size and morphology (15 types of oxides are followed highlighted, by red circles) and finally, on the movement of dislocations (followed up by blue arrows and the study of the dislocation density) (see Fig. 6.4, 6.5 and 6.6).

Fig 6.4 shows the evolution of the ultrafine region selected, from 200 to 300 °C, where no change on dislocations, precipitates or grain frontier are reported. From 400 to 500 °C (see Fig 6.5) small differences on dislocations are observed but without any remarkable dissimilarity in the final dislocation density. Once again, the tracked nano-oxides and grain frontier do not show variation. However, at 500 °C the evaluated surface starts reducing its quality, (see Fig 6.5) showing indications of the applied annealing. Finally, at 600 °C, some dislocations have completely disappeared, and the final surface quality is clearly reduced (see Fig 6.6).

Any oxide decomposition was observed; the recorded 15 oxides remains once the in-situ test is finished (see Fig 6.4 and 6.6). With the accuracy of the used magnification, the shape of all of them is rounded over the total range of temperatures (up to 600 °C) All those oxides whose size is under 10 nm, correspond to type 2, 3, 4, 5. Besides, the oxides labelled as 1, 2 and 9 are type 2 and type 3 and 4 (following the classification made in Chapter 5 p. 99).

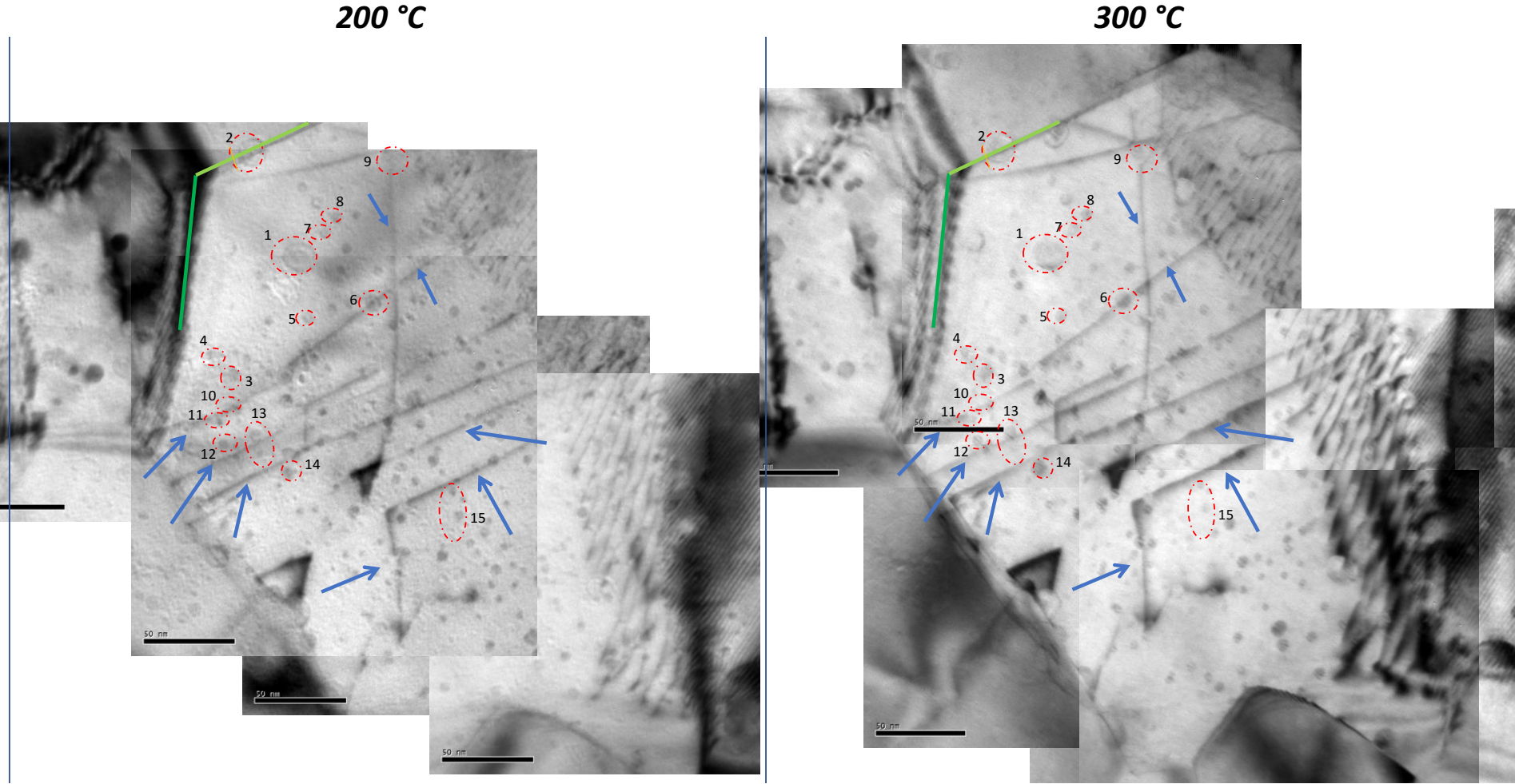


Fig 6.4. Zr600 tracking on ultrafine grain from 200 °C (left) to 300 °C (Right).

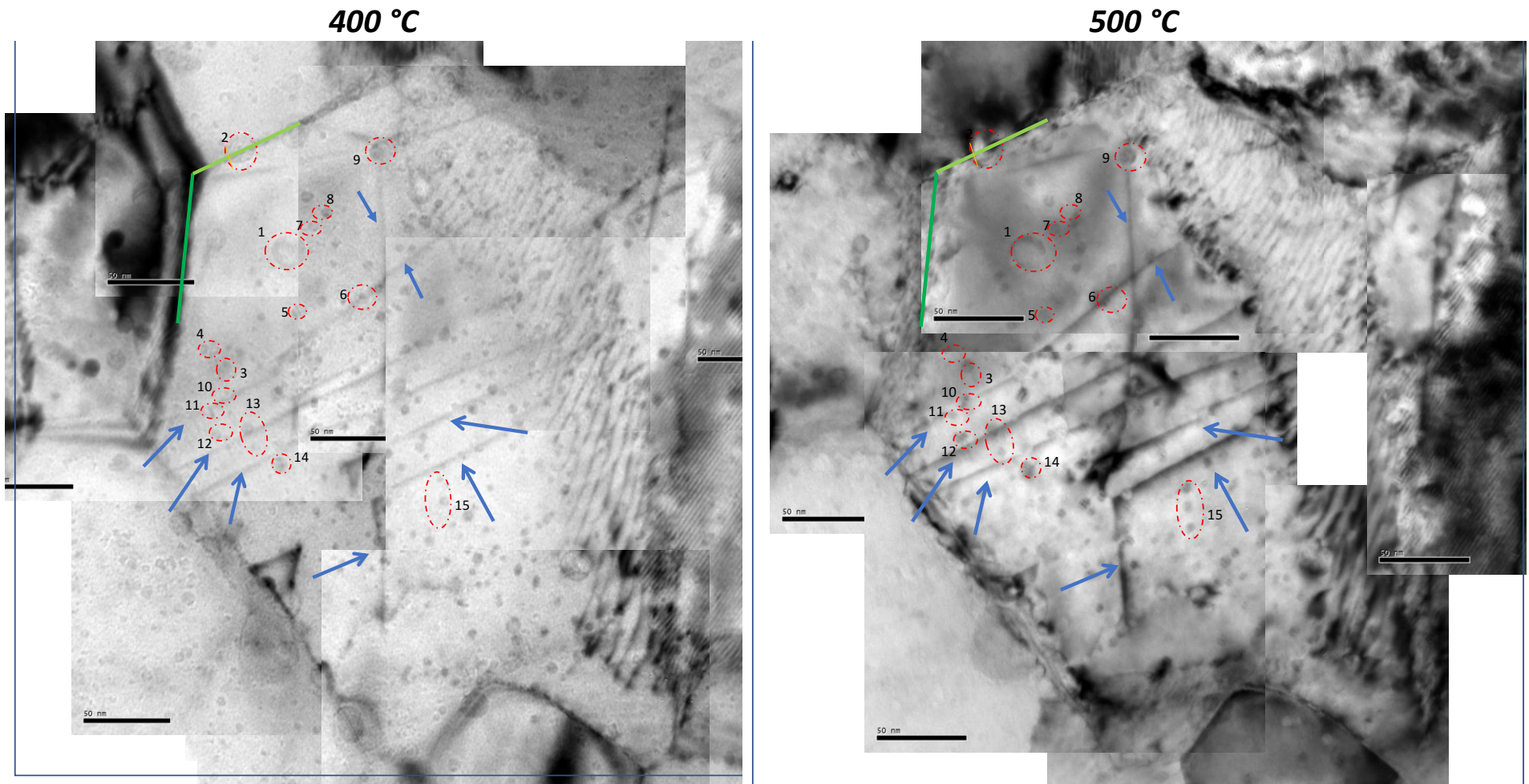


Fig 6.5. Zr600 tracking on ultrafine grain from 400 °C (left) to 500 °C (Right).

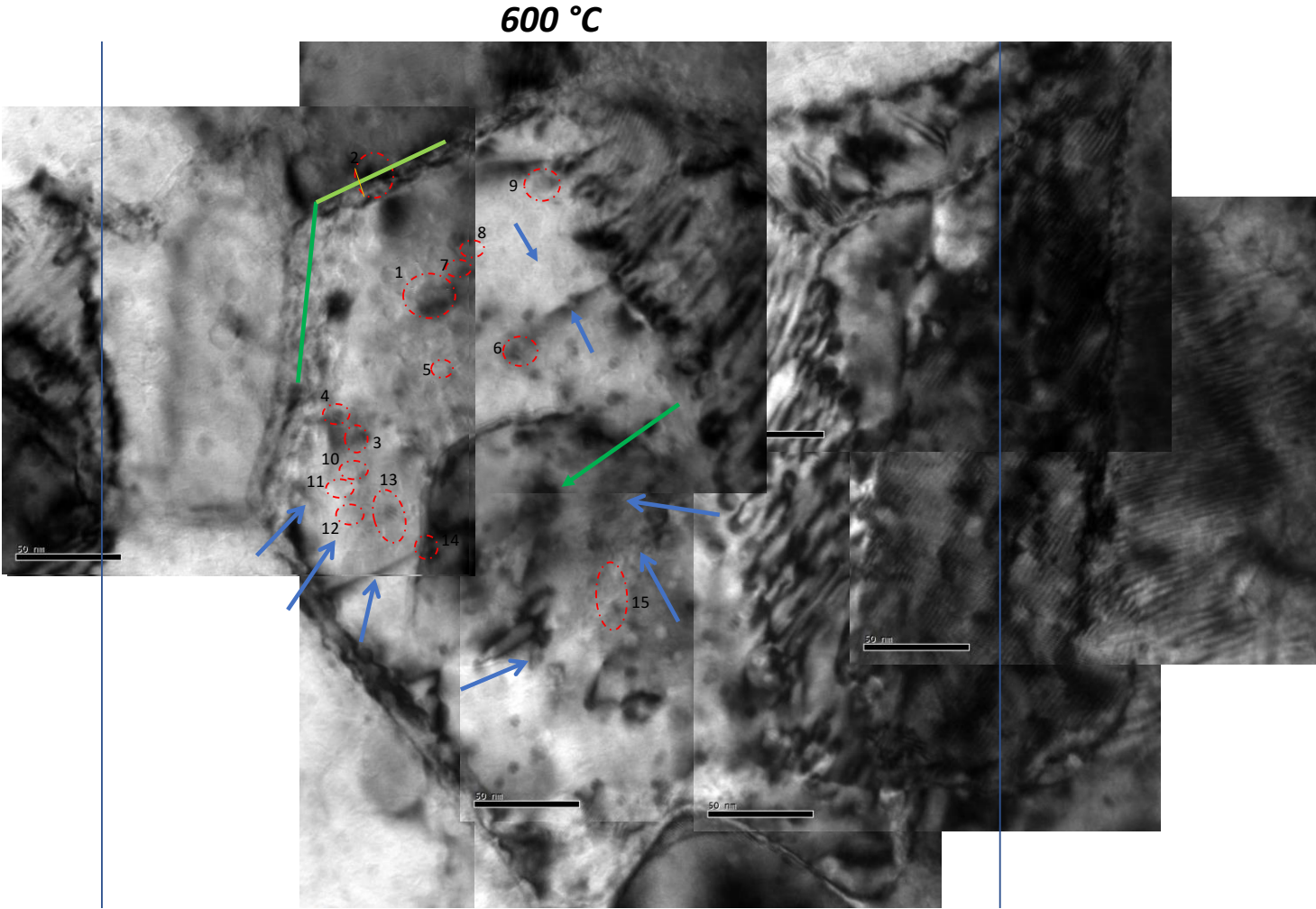


Fig 6.6. Zr600 tracing ultrafine grain at 600 °C.

Moreover, around 100 nano-precipitates were measured to obtain the final plotted size distribution at different T. The mean size of the distribution measured on TEM images from Fig. 6.4, 6.5 and 6.6 is almost the same despite of the annealing temperature (Fig 6.7).

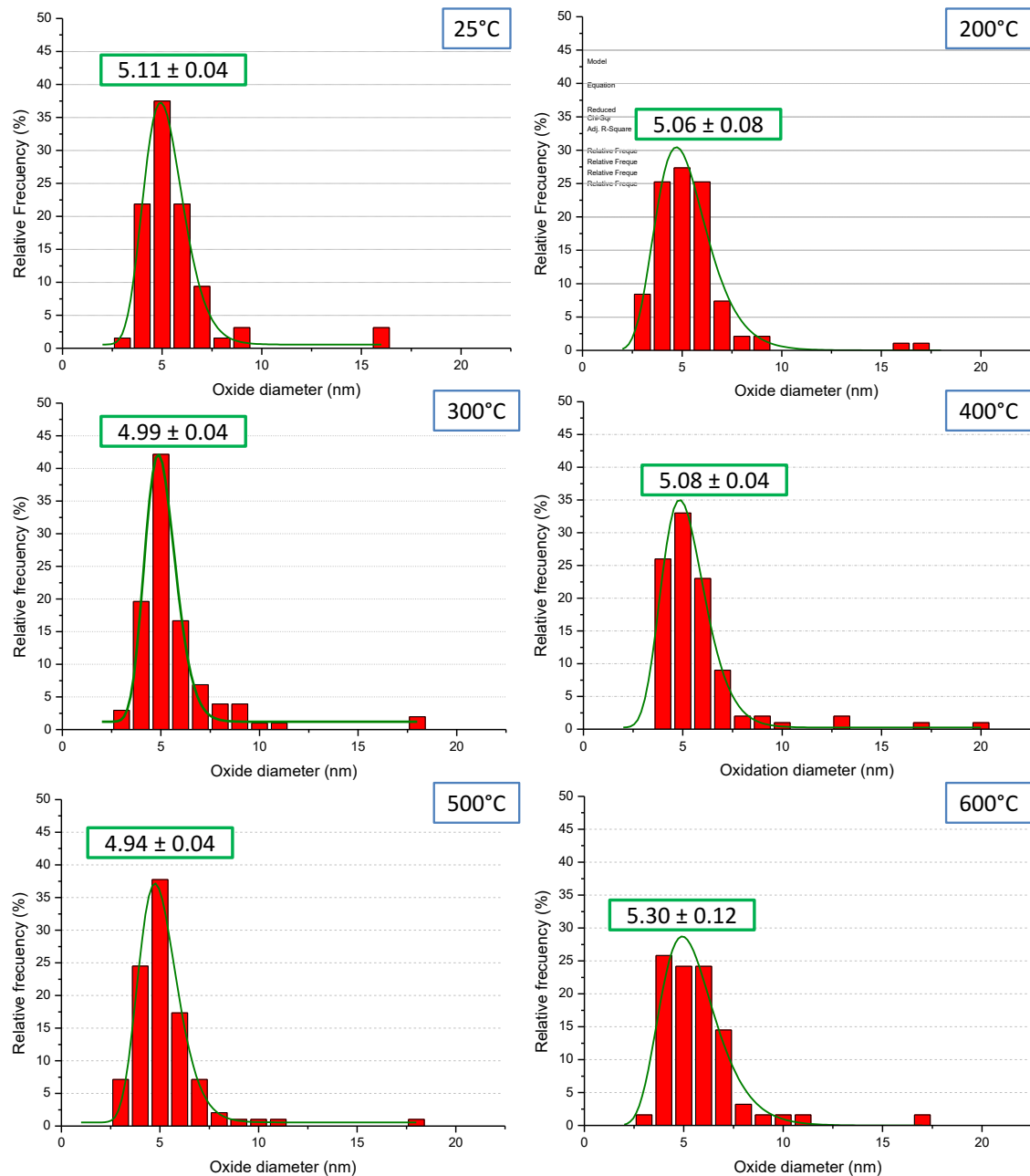


Fig 6.7. Evolution of oxides size distribution during the thermal treatment on Zr600.

If the oxide size distributions at different T are considered, it is not possible to draw a tendency depending on the thermal activation. The degradation of the surface quality during the annealing process, along with the small differences in the orientation on TEM sample, could induce some changes on the measurement, observed on the oxide size distribution measured at 600 °C. This could be one of the observed limitations by using in-situ TEM annealing.

In addition, precipitates were also followed by considering the density of precipitated oxides (N_p , -oxd/ m^3 -) and the volumetric fraction, showed on table 6.1. Clearly, reported oxides are stable and do not disappear during the thermal treatment. Indeed, differences between temperatures could be considered negligible.

Table 6.1. Zr600 ultrafine region: precipitates density as a function of the temperature (minimum of 100 precipitated was measured).

Temperature (°C)	$\rho_{\text{precipitates}} \text{ (oxd/m}^3\text{)}$	Volumetric fraction (%)
25	$2.6 \cdot 10^{22}$	0.18
200	$3.0 \cdot 10^{22}$	0.20
300	$3.1 \cdot 10^{22}$	0.20
400	$3.2 \cdot 10^{22}$	0.22
500	$2.6 \cdot 10^{22}$	0.16
600	$2.1 \cdot 10^{22}$	0.16

On the other side, the dislocation density is reduced when the temperature reaches 600 °C (Fig 6.8, measured on TEM images of Fig. 6.4, 6.5 and 6.6). This could influence directly the mechanical properties at this temperature as it stated on chapter 5.

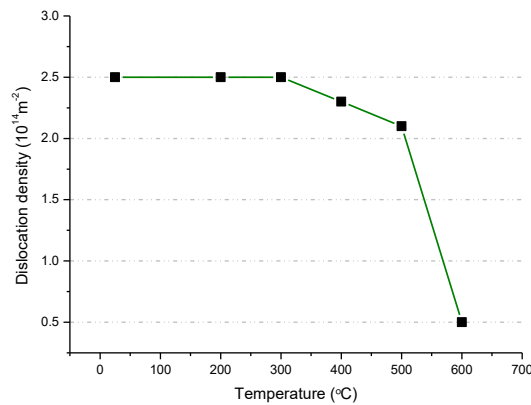


Fig 6.8. Dislocation density evolution on the ultrafine grain selected.

Fig 6.9 reports the dislocation movement at 600 °C (marked by the blue arrow) and the interaction between some precipitates (marked by the red arrow).

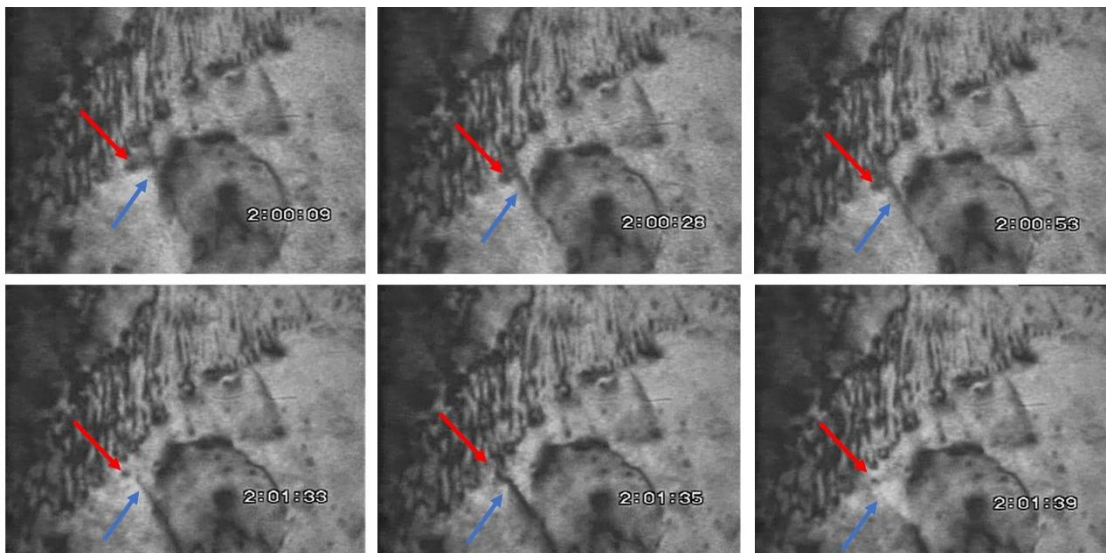


Fig 6.9. Dislocation movement on Zr600 when 600 °C is reached.

The movement of dislocations is related to the interaction with the precipitates of the ODS steel as it was stated on Chapter 1. When the dislocation line is about to pass through the oxides, their nature will determine coherency and misfit with the matrix which will influence the dislocation interaction. If dispersed precipitates are impenetrable, dislocations bypass the oxides by Orowan looping or bowing. Meanwhile for weak precipitates that will leave a low degree of strengthening; the dislocation begins to pass through the precipitate by shearing

mechanism, and will cut them. In Fig 6.10 it can be observed how the dislocation line interacts with the oxides.

Since Orowan equation (see Chapter 1) directly depends on the precipitates distance, and no change was reported on the final positions, it is supposed that this hardening would be stable under high temperature.

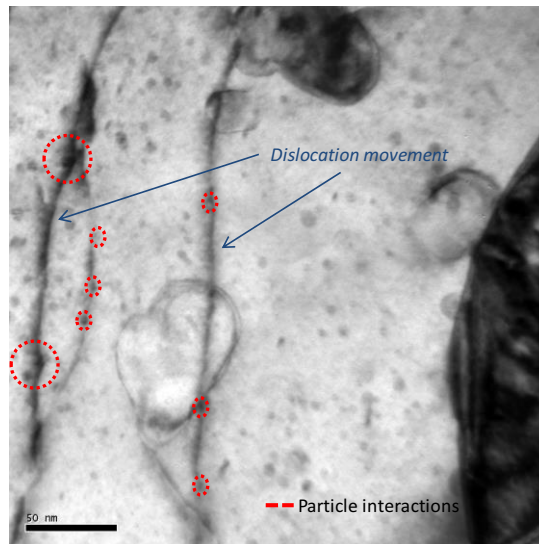


Fig 6.10. Dislocations movement through nano-precipitates depending on their diameter.

To study the effect of temperature on the UF grains colonies it was selected the area gathered in Fig 6.11, marked on green. Indeed, figure shows that no appreciable change on size was attained after the thermal treatment. The studied ultrafine grain is stable on the range of considered temperature.

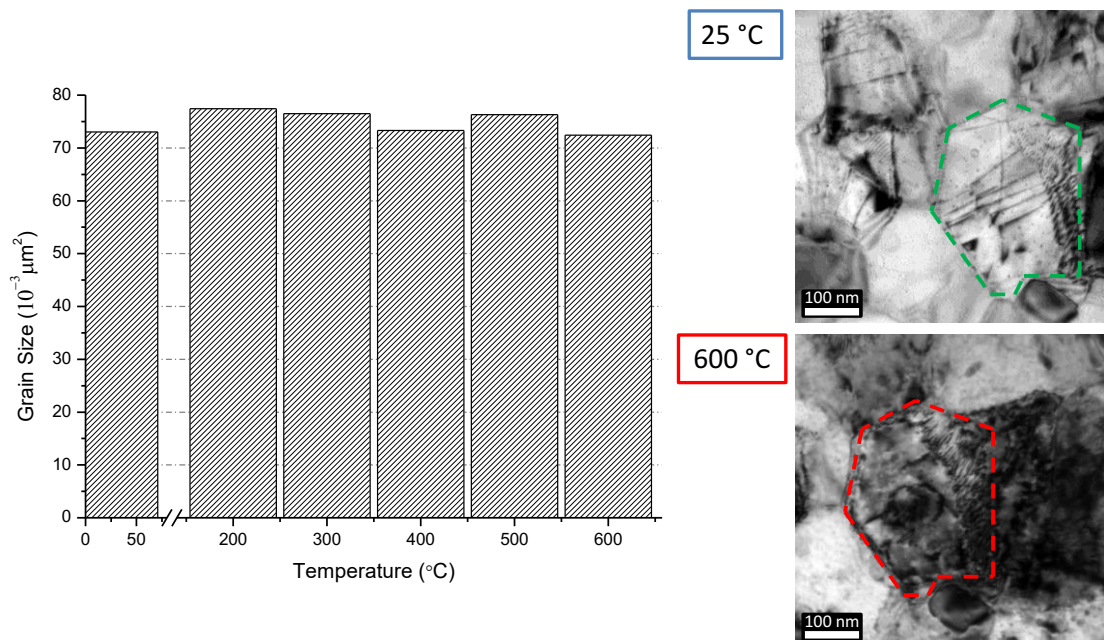


Fig 6.11. Grain size evolution during the thermal annealing.

6.3. Micrometric area analysis: Tracking precipitates and grain size

Considering micrometric grain, the grain size is measured without reporting any significant evolution. A small difference in size of $14 \cdot 10^{-3} \mu\text{m}^2$ is observed which can be totally negligible (see Fig 6.12). It is possible to note, how the surface quality falls at 600 °C, which make more difficult the analysis of precipitates morphology and size.

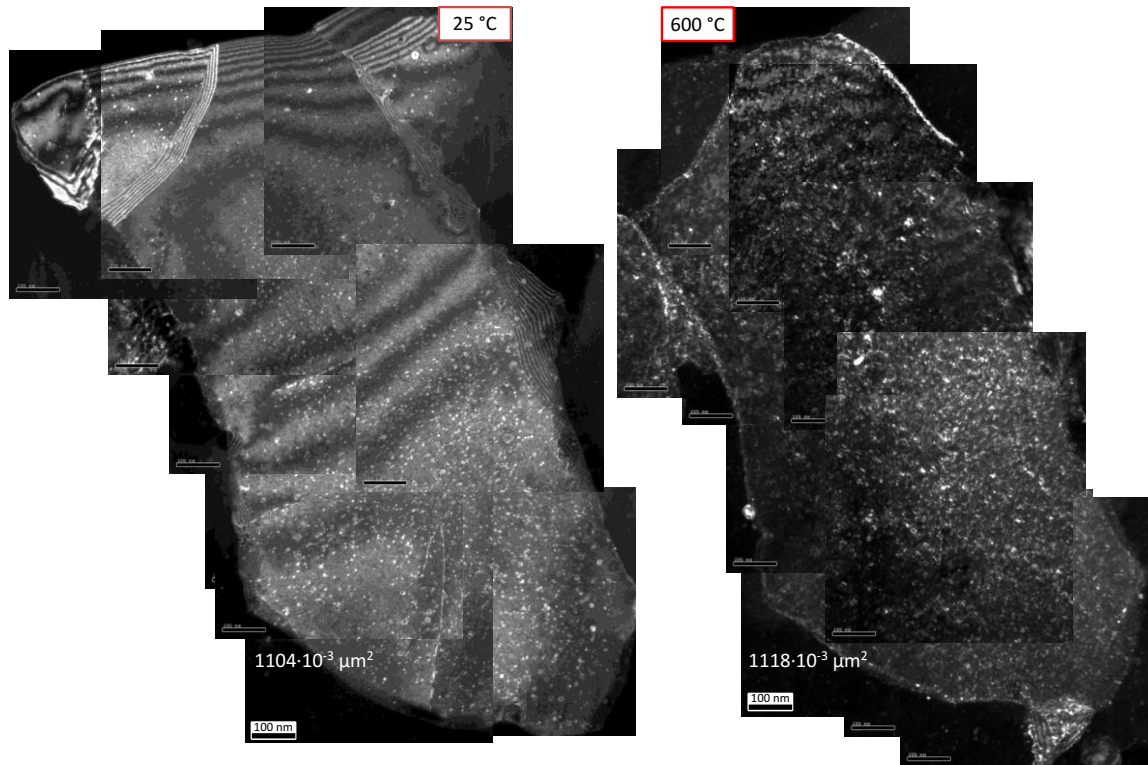


Fig 6.12. Micrograin evolution during the thermal treatment.

The oxide size distribution does not experiment a noticeable variation, and the attained mean value is preserved at 600 °C (Fig 6.13). Consequently, the microstructure of micro grain area analysed is stable by the applied thermal annealing [1].

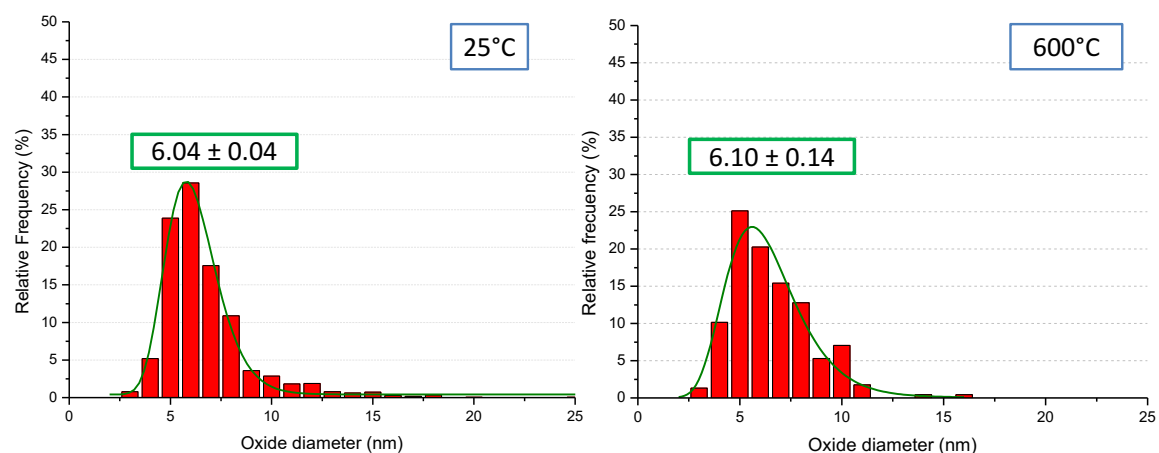


Fig 6.13. Oxide size distribution for the micrometric grain study at RT (left) and 600 °C (right).

6.4. Microstructural features after the annealing

To have general information of the annealed F-ODS-I, based on a large area, a lamella was carved on the material after the thermal annealing (Fig 6.14) where it is possible to see that the bimodal grain size distribution remains after the in-situ test. Over this sample, it will be measured more than 50 grains to characterize the ferritic grain size evolution and more than 100 oxides to study the precipitates types.

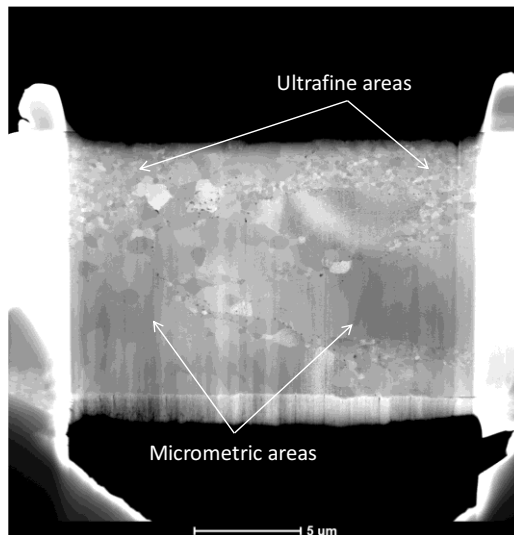


Fig 6.14. Obtained Lamella after the thermal aging at 600 °C on Zr600.

The Fig 6.15 confirms the stability of the UF colonies. In this case, by measuring the complete area it has been drawn the evolution with the temperature of the grain size distribution and the mean value. Although the distribution has slightly changed with the temperature, the mean value of UF grains is equivalent.

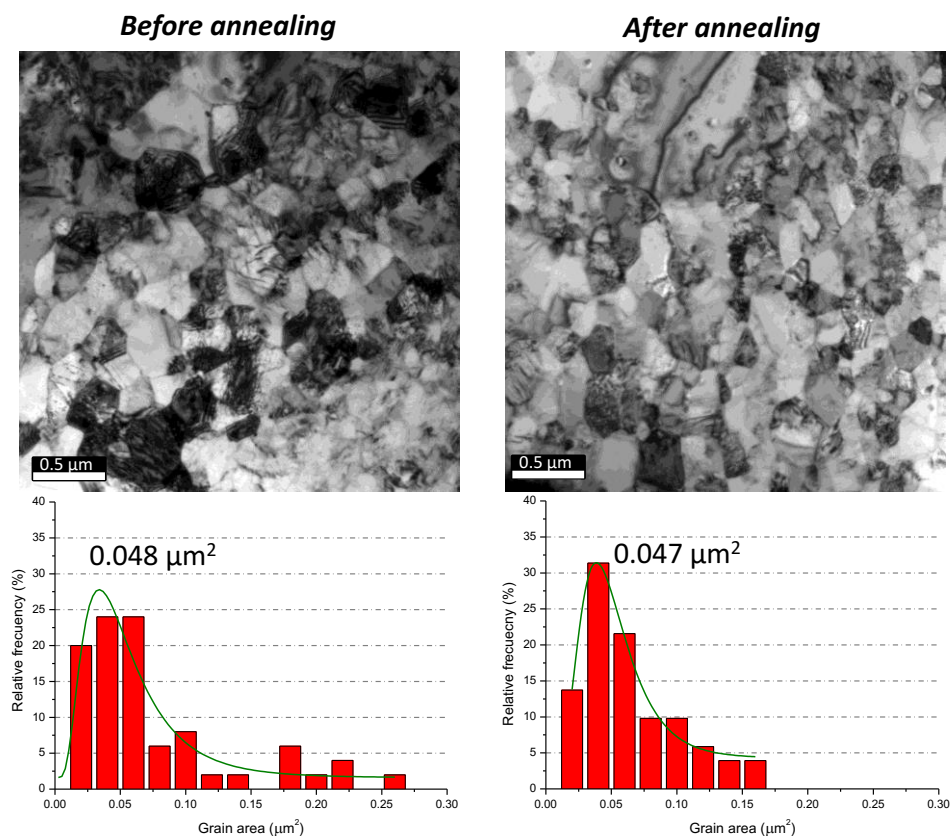


Fig 6.15. Ultrafine regions before and after the in-situ annealing.

No clear changes were observed in the final oxides composition. The five types of oxides studied in Chapter 5 (which are summed up in Fig 6.16), are recorded in the final microstructure after the annealing.

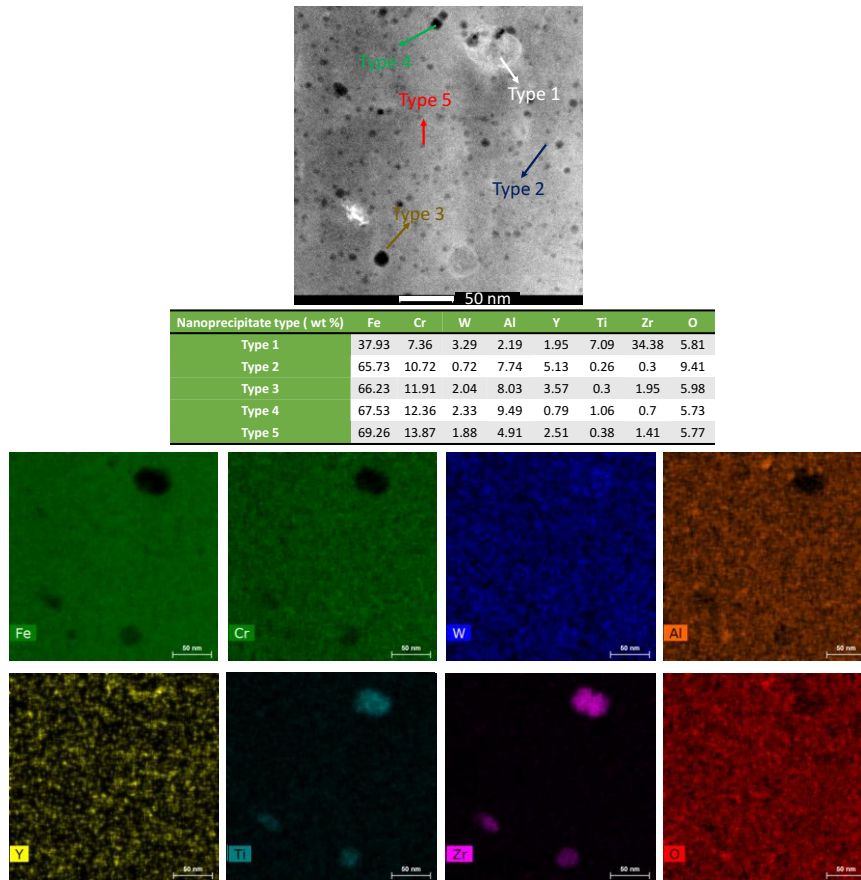


Fig 6.16. Ultrafine regions before and after the in-situ annealing.

Regarding to the evolution of oxides, it was not detected any precipitation coarsening, the mean precipitate size does not increase and it is not detected that the larger ones have grown at the cost of the smaller (Fig 6.17).

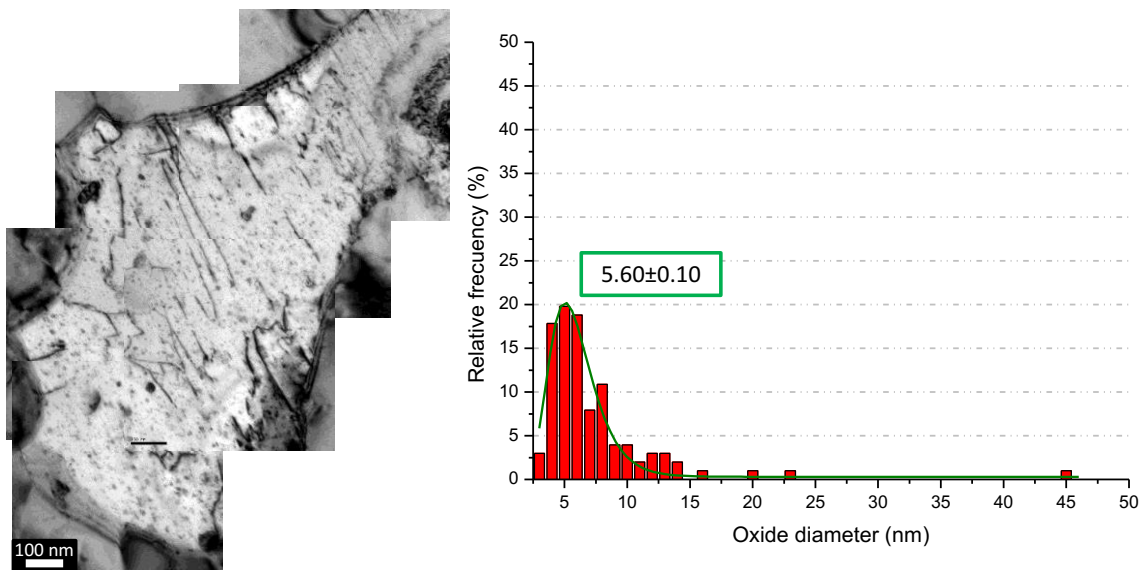


Fig 6.17. Precipitates diameter distribution measured in the carved lamella after the in situ TEM annealing.

The morphology of the precipitated oxides was also checked after performing the lamella, proving that, at least on first instance no change on morphology was observed (Fig 6.18). These maintain their rounded shape after the annealing. The nano-precipitates coherency is determined by the size and inevitably by the final shape. No agglomeration was notified; almost rounded shape is maintained after the test. A. Ramar et al [2] speaks about the dissolution of some nano-oxides at 600 °C, but this effect is not observed in this research. This finding is directly related to the stability of the oxide depending on its coherency [3,4].

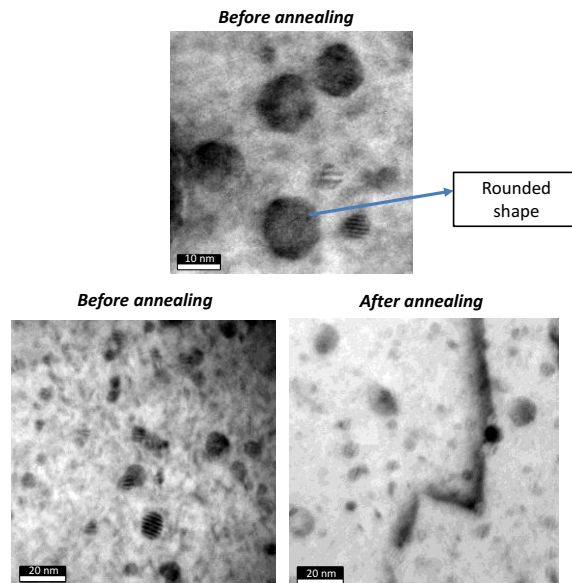


Fig 6.18. Morphology of the nano precipitates in the lamella obtained after the thermal aging at 600 °C.

Finally, the dislocation density was studied in the micrometric grain of Fig 6.16. The dislocation density attained is $8.5 \cdot 10^{13} \text{m}^{-2}$ which matches with the one attained by the in-situ TEM.

6.5. Partial discussion

6.5.1. Effect of temperature on microstructure

In high Cr ODS ferritic steels, two main microstructural features will determine the performance of the material, ferritic grain size and precipitated oxides. One of research areas of interest is the study of the stability of the nano-oxides under different annealing temperatures and atmospheres [5–14]. When a certain temperature is achieved the coarsening of oxides will occur decreasing the mechanical response of the steel. This phenomenon is explained through the Ostwald ripening theory, based on the dissolution of smaller precipitates and growth of the large ones [13,15]. This theory explains the stability of the nano-precipitates through the curvature. As smaller precipitates present higher curvature their stability would be reduced respect to the large ones [13]. However, other authors have defended the stability of smaller nano-oxides based on the coherency due to the lower interfacial energy compared to semi coherent or incoherent precipitates (see Chapter 1 section 1.3.1) [6,16–18].

In this research, Ti or Zr are used to rise the coherency and to improve the thermal stability of the nanoprecipitates [8,19]. As it was discussed in Chapter 5, in Al containing ODS steels, the formation of Y-Al-O is favoured [20,21]. Depending on their size, these precipitates use to be incoherent with the matrix and consequently less stable than Y-Ti-O or Y-Zr-O [22–25].

Thanks to the in-situ TEM on the F-ODS-I Zr 600, it has been stated that no dissolution or growth occur when the annealing is done at 600 °C. The nano-oxides are stable and their size is maintained around 5.5 nm in the UF region (only a 4% of variation between RT and 600 °C) and 6 nm on the micrometric region (1% of variation between RT and 600 °C). Consequently, Zr is

definitely determining the stability of the nano-precipitate. Even if the coherency of the nano-precipitates is not studied in this experiment, this might be one of the reasons why there is no change in oxide size during in-situ TEM annealing tests. Some studies support also this hypothesis, in Al containing ODS steels. P. Yang et al [26] compared two ferritic steels with and without Hf (Fe-16Cr-3Al-1.5W-0.5Hf-0.35Y₂O₃), the coherency promoted by Hf led into stable nano-precipitates with small changes on the precipitates diameter even after 100 h at 1150 °C (from 6.80 to 14.40 nm with Hf addition respect to 9.66 to 38.73 nm without it). Moreover, S. F. Li et al [5] tested a ferritic ODS steel (Fe-16Cr-2W-0.4Ti) at 700 °C (from 10 h to 5000 h), highlighting the outstanding thermal stability of their nano-oxides at this temperature.

However, if thermal activation is higher, the precipitates will evolve despite of the coherency level. Precipitates do not coarsen until a temperature of ~ 0,8 T_m is reached [27]. Z. Oksiuta et al [28] analysed the thermal stability of a ferritic ODS steel (Fe-14Cr-2W-0.3Ti-0.3Y₂O₃) up to 1100 °C, moment in which the microstructure changes, due to the coarsening of the precipitates. Furthermore, X. Mao et al [12] observed differences on the nano-precipitates after annealing the material (Fe-12Cr-1.1-W-0.2V-0.14Ta-0.24Y) up to 1250 °C for 500 h, even if they are coherent. J. Shen et al [18] studied the microstructural stability of Fe-12Cr-2W-0.3Ti-0.25Y₂O₃, in this case the steel loses their stability only when 1400 °C was attained.

Ferritic grain stability could be explained through precipitate stability. On the one side, Zr could form, apart from Y-Zr-O, intermetallics at grain boundaries (see type 1 precipitate on Chapter 5), that lowers the excess of free energy and will reduce the driving force for the grain growth at low temperatures [29].

On the other side, formed nano-oxides will prevent also the migration of grain boundaries at higher temperatures, since more energy is required to overcome these obstacles [16,30,31]. This phenomenon has retained the grain growth during SPS consolidation as well.

After in-situ TEM annealing it has been confirmed the microstructure steadiness (Fig 6.17) also reported by others authors [32]. To corroborate this, it was considered the Zener and Rios approximation (eq. 6.1 and 6.2) showing up the stability of grain size. Zener proposed an expression that considered the pressure that tends to move the grain boundary and the opposite force produced by the precipitates considering the number of intersected precipitates by the boundary [33]. On its behalf, the pinning pressure exerted on the grain boundaries by oxides is directly dependant on oxide size, r_p , and inversely proportional to their volumetric fraction, f_p . Rios et al [34] proposed equation 6.2 giving as a results values eight times smaller than Zener.

$$R_c^{Zener} = \frac{4r_p}{3f_p} \quad (\text{eq.6.1})$$

$$R_c^{Rios} = \frac{r_p}{6f_p} \quad (\text{eq.6.2})$$

Using those theories, and considering the experimental results, it was calculated the critical ferritic grain size (Fig 6.19), in this case, the experimental results fits better with Rios equation. Y. Li et al [1] demonstrated similar results to the one reported in here. In their case the stability of the microstructure is maintained until 5000 h at 700 °C.

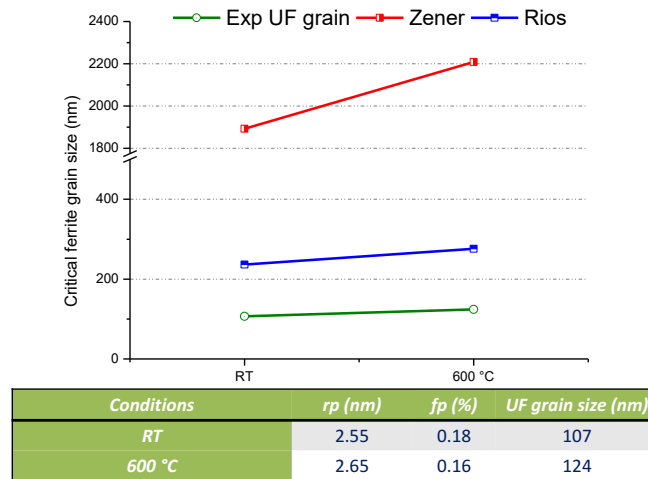


Fig 6.19. Critical ferritic grain size approximation, by using different theories, at room temperature and 600 °C.

6.5.2. Effect of temperature on mechanical properties

In ODS ferritic steels it has been shown how the dislocation lines do not move since a high thermal activation is applied. Alinger et al have proved a stable distribution until 400 °C [35,36], from that point, Z. Oksiuta [28] and M.Dadé [30] have reported the annihilation of dislocation when temperature raises up to 500 °C. The results of this Thesis have shown the dislocation movement when T achieved 600 °C, which is in accordance from previous studies.

Besides, in Chapter 4 and 5 (pp. 84 and 107), SP test show how F-ODS-I materials reduced their performance (F_{max}) at 500 °C. As it was stated on the discussion, the main players for strengthening this type of steels are the density of precipitated oxides and density of dislocations. Precipitated oxides preserve their strengthening contribution as their amount and their sizes remain stable with temperature. Taking into account and the evolution of density of dislocations on the studied UF grains (Fig 6.2) and using the formulas (eq 5.5 and 5.6) it is possible to study the evolution with the temperature for the Yield Strength contribution just considering hardening due to the defects term² (Fig 6.20). Consequently, the mechanical properties decrease will be connected to the modification of dislocations.

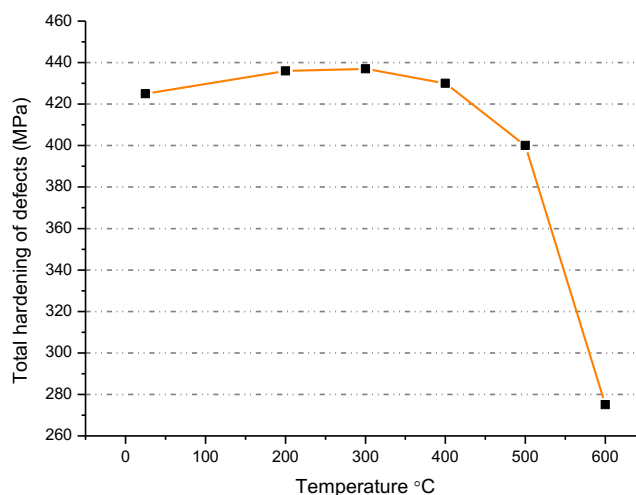


Fig 6.20. Contribution of dislocation and precipitates to the strengthening of the material (MPa) as a function of Temperature (°C).

$$^2 \sigma_{def} = \sqrt{\sigma_{dis}^2 + \sigma_p^2}$$

Besides, if dislocations are blocked until 600 °C an improvement on the stability of the material is achieved and microstructural changes could be delayed. If oxides maintain their size, a stronger pinning effect is produced, avoiding or retarding dislocation movement [5,11,28,37–39].

To conclude with, as it is stated in Chapter 1, ODS ferritic steels use to operate in a range of temperatures between 600-850 °C so these results are promising for future application in service.

6.6. Partial remarks

In-situ TEM annealing is an attractive tool to verify the material response at high temperature, since it opens a new way to analyse and to understand the microstructural evolution under high temperature conditions. The viability of using this method to comprehend ODS steels behaviour has been positively valued. It has been noticed the following aspects:

- The precipitated oxides on Zr600 are stable up to 600 °C and under high vacuum conditions. After the in-situ test, the five oxides types reported in Chapter 5 have been identified as well.
- The precipitation density does not report any significant variation during the whole process.
- Since there is no change on dimensions in both ultrafine and micro grains, the ferritic grain size is stable up to 600 °C. The stability on the nano-oxides has provided a strong pinning effect preventing the grain growth.
- As temperature increases, the dislocation density is reduced (in almost one order of magnitude at 600 °C), indicating the point where the strengthening contribution decreases. This finding matches with results provided by small punch test (in Chapter 4 and 5) where F_m has dropped at 500 °C.

Bibliography

- [1] Y. Li, H. Abe, F. Li, Y. Satoh, Y. Matsukawa, T. Matsunaga, T. Muroga, Grain structural characterization of 9Cr-ODS steel aged at 973 K up to 10,000 h by electron backscatter diffraction, *J. Nucl. Mater.* 455 (2014) 568–572. doi:10.1016/j.jnucmat.2014.08.047.
- [2] A. Ramar, R. Schäublin, Analysis of hardening limits of oxide dispersion strengthened steel, *J. Nucl. Mater.* 432 (2013) 323–333. doi:10.1016/j.jnucmat.2012.07.024.
- [3] K.D. Zilnyk, K.G. Pradeep, P. Choi, H.R.Z. Sandim, D. Raabe, Long-term thermal stability of nanoclusters in ODS-Eurofer steel: An atom probe tomography study, *J. Nucl. Mater.* 492 (2017) 142–147. doi:10.1016/j.jnucmat.2017.05.027.
- [4] K.D. Zilnyk, H.R.Z. Sandim, R.E. Bolmaro, R. Lindau, A. Möslang, A. Kostka, D. Raabe, Long-term microstructural stability of oxide-dispersion strengthened Eurofer steel annealed at 800 °C, *J. Nucl. Mater.* 448 (2014) 33–42. doi:10.1016/j.jnucmat.2014.01.032.
- [5] S.F. Li, Z.J. Zhou, P.H. Wang, H.Y. Sun, M. Wang, G.M. Zhang, Long-term thermal-aging stability of a 16Cr-oxide dispersion strengthened ferritic steel at 973K, *Mater. Des.* 90 (2016) 318–329. doi:10.1016/j.matdes.2015.10.138.
- [6] D.T. Hoelzer, J. Bentley, M.A. Sokolov, M.K. Miller, G.R. Odette, M.J. Alinger, Influence of particle dispersions on the high-temperature strength of ferritic alloys, *J. Nucl. Mater.* 367 (2007) 166–172. doi:10.1016/j.jnucmat.2007.03.151.
- [7] H. Tang, X. Chen, Y.W. Niu, X. Luo, Z. Wang, M. Chen, G. Shi, Thermal stability characteristics of in situ nano-particles formed in metal melt, *Mater. Lett.* 162 (2016) 261–264. doi:10.1016/j.matlet.2015.09.052.
- [8] D. Murali, B.K. Panigrahi, M.C. Valsakumar, S. Chandra, C.S. Sundar, B. Raj, The role of minor alloying elements on the stability and dispersion of yttria nanoclusters in nanostructured ferritic alloys: An ab initio study, *J. Nucl. Mater.* 403 (2010) 113–116. doi:10.1016/j.jnucmat.2010.06.008.
- [9] H.L. Ding, R. Gao, T. Zhang, X.P. Wang, Q.F. Fang, C.S. Liu, Annealing effect on the microstructure and magnetic properties of 14%Cr-ODS ferritic steel, *Fusion Eng. Des.* 100 (2015) 371–377. doi:10.1016/j.fusengdes.2015.06.149.
- [10] E. Aydogan, O. El-Atwani, S. Takajo, S.C. Vogel, S.A. Maloy, High temperature microstructural stability and recrystallization mechanisms in 14YWT alloys, *Acta Mater.* 148 (2018) 467–481. doi:10.1016/j.actamat.2018.02.006.
- [11] M.C. Brandes, L. Kovarik, M.K. Miller, G.S. Daehn, M.J. Mills, Creep behavior and deformation mechanisms in a nanocluster strengthened ferritic steel, *Acta Mater.* 60 (2012) 1827–1839. doi:10.1016/j.actamat.2011.11.057.
- [12] X. Mao, T.K. Kim, S.S. Kim, K.H. Oh, J. Jang, Thermal stability of oxide particles in 12Cr ODS steel, *J. Nucl. Mater.* 428 (2012) 82–89. doi:10.1016/j.jnucmat.2011.09.011.
- [13] F. Siska, L. Stratil, H. Hadraba, S. Fintova, I. Kubena, V. Hornik, R. Husak, D. Bartkova, T. Zalezak, Strengthening mechanisms of different oxide particles in 9Cr ODS steel at high temperatures, *Mater. Sci. Eng. A.* 732 (2018) 112–119. doi:10.1016/j.msea.2018.06.109.
- [14] Y. Sawazaki, S. Ukai, Y. Sugino, S. Hayashi, N. Oono, K. Hamajima, A. Niwa, Development of 15CrODS ferritic steels for over 1273 K service, *J. Nucl. Mater.* 442 (2013) S169–S172. doi:10.1016/j.jnucmat.2013.04.084.
- [15] H. Sakasegawa, F. Legendre, L. Boulanger, M. Brocq, L. Chaffron, T. Cozzika, J. Malaplate, J. Henry, Y. De Carlan, Stability of non-stoichiometric clusters in the MA957 ODS ferritic

- alloy, *J. Nucl. Mater.* 417 (2011) 229–232. doi:10.1016/j.jnucmat.2010.12.056.
- [16] Y.S. Choi, D.H. Kim, S.H. Kim, S.H. Kang, J. Jang, H.N. Han, K.H. Oh, In situ microstructure evolution of oxide dispersion strengthened ferritic steel under uniaxial deformation, *J. Nucl. Mater.* 428 (2012) 98–102. doi:10.1016/j.jnucmat.2011.10.045.
- [17] M.K. Miller, D.T. Hoelzer, E.A. Kenik, K.F. Russell, Stability of ferritic MA/ODS alloys at high temperatures, *Intermetallics*. 13 (2005) 387–392. doi:10.1016/j.intermet.2004.07.036.
- [18] J. Shen, H. Yang, Y. Li, S. Kano, Y. Matsukawa, Y. Satoh, H. Abe, Microstructural stability of an as-fabricated 12Cr-ODS steel under elevated-temperature annealing, *J. Alloys Compd.* 695 (2017) 1946–1955. doi:10.1016/j.jallcom.2016.11.029.
- [19] H. Xu, Z. Lu, S. Ukai, N. Oono, C. Liu, Effects of annealing temperature on nanoscale particles in oxide dispersion strengthened Fe-15Cr alloy powders with Ti and Zr additions, *J. Alloys Compd.* 693 (2017) 177–187. doi:10.1016/j.jallcom.2016.09.133.
- [20] A. Kimura, R. Kasada, N. Iwata, H. Kishimoto, C.H. Zhang, J. Isselin, P. Dou, J.H. Lee, N. Muthukumar, T. Okuda, M. Inoue, S. Ukai, S. Ohnuki, T. Fujisawa, T.F. Abe, Development of Al added high-Cr ODS steels for fuel cladding of next generation nuclear systems, *J. Nucl. Mater.* 417 (2011) 176–179. doi:10.1016/j.jnucmat.2010.12.300.
- [21] C.H. Zhang, A. Kimura, R. Kasada, J. Jang, H. Kishimoto, Y.T. Yang, Characterization of the oxide particles in Al-added high-Cr ODS ferritic steels, *J. Nucl. Mater.* 417 (2011) 221–224. doi:10.1016/j.jnucmat.2010.12.063.
- [22] Y.P. Xia, X.P. Wang, Z. Zhuang, Q.X. Sun, T. Zhang, Q.F. Fang, T. Hao, C.S. Liu, Microstructure and oxidation properties of 16Cr-5Al-ODS steel prepared by sol-gel and spark plasma sintering methods, *J. Nucl. Mater.* 432 (2013) 198–204. doi:10.1016/j.jnucmat.2012.07.039.
- [23] T. Liu, L. Wang, C. Wang, H. Shen, H. Zhang, Feasibility of using Y₂Ti₂O₇ nanoparticles to fabricate high strength oxide dispersion strengthened Fe-Cr-Al steels, *Mater. Des.* 88 (2015) 862–870. doi:10.1016/j.matdes.2015.08.118.
- [24] P. Dou, A. Kimura, R. Kasada, T. Okuda, M. Inoue, S. Ukai, S. Ohnuki, T. Fujisawa, F. Abe, TEM and HRTEM study of oxide particles in an Al-alloyed high-Cr oxide dispersion strengthened steel with Zr addition, *J. Nucl. Mater.* 444 (2014) 441–453. doi:10.1016/j.jnucmat.2013.10.028.
- [25] P. Dou, A. Kimura, T. Okuda, M. Inoue, S. Ukai, S. Ohnuki, T. Fujisawa, F. Abe, Polymorphic and coherency transition of Y–Al complex oxide particles with extrusion temperature in an Al-alloyed high-Cr oxide dispersion strengthened ferritic steel, *Acta Mater.* 59 (2011) 992–1002. doi:10.1016/j.actamat.2010.10.026.
- [26] P. Yan, L. Yu, Y. Liu, C. Liu, H. Li, J. Wu, Effects of Hf addition on the thermal stability of 16Cr-ODS steels at elevated aging temperatures, *J. Alloys Compd.* 739 (2018) 368–379. doi:10.1016/j.jallcom.2017.12.245.
- [27] X. Boulnat, M. Perez, D. Fabregue, T. Douillard, M.H. Mathon, Y. De Carlan, Microstructure evolution in nano-reinforced ferritic steel processed by mechanical alloying and spark plasma sintering, *Metall. Mater. Trans. A Phys. Metall. Mater. Sci.* 45 (2014) 1485–1497. doi:10.1007/s11661-013-2107-y.
- [28] Z. Oksiuta, M. Lewandowska, K.J. Kurzydłowski, Mechanical properties and thermal stability of nanostructured ODS RAF steels, *Mech. Mater.* 67 (2013) 15–24. doi:10.1016/j.mechmat.2013.07.006.

- [29] H. Kotan, Thermal stability, phase transformation and hardness of mechanically alloyed nanocrystalline Fe-18Cr-8Ni stainless steel with Zr and Y₂O₃ additions, *J. Alloys Compd.* 749 (2018) 948–954. doi:10.1016/j.jallcom.2018.03.324.
- [30] M. Dadé, J. Malaplate, J. Garnier, F. De Geuser, F. Barcelo, P. Wident, A. Deschamps, Influence of microstructural parameters on the mechanical properties of oxide dispersion strengthened Fe-14Cr steels, *Acta Mater.* 127 (2017) 165–177. doi:10.1016/j.actamat.2017.01.026.
- [31] X. Boulnat, N. Sallez, M. Dadé, A. Borbély, J. Béchade, Y. De Carlan, J. Malaplate, Y. Brechet, F. de Geuser, A. Deschamps, P. Donnadieu, D. Fabregue, M. Perez, Influence of oxide volume fraction on abnormal growth of nanostructured ferritic steels during non-isothermal treatments: An in situ study, *Acta Mater.* 97 (2015) 124–130. doi:10.1016/j.actamat.2015.07.005.
- [32] P. Susila, D. Sturm, M. Heilmaier, B.S. Murty, V. Subramanya Sarma, Effect of yttria particle size on the microstructure and compression creep properties of nanostructured oxide dispersion strengthened ferritic (Fe-12Cr-2W-0.5Y₂O₃) alloy, *Mater. Sci. Eng. A.* 528 (2011) 4579–4584. doi:10.1016/j.msea.2011.02.078.
- [33] T. Gladman, On the theory of the effect of precipitate particles on grain growth in metals, *Proc. R. Soc. London. Ser. A. Math. Phys. Sci.* 294 (1966) 298–309. doi:10.1098/rspa.1966.0208.
- [34] P.R. Rios, Overview no. 62: A theory for grain boundary pinning by particles, *Acta Metall.* 35 (1987) 2805–2814. doi:10.1016/0001-6160(87)90280-X.
- [35] J.H. Kim, T.S. Byun, D.T. Hoelzer, S.-W. Kim, B.H. Lee, Temperature dependence of strengthening mechanisms in the nanostructured ferritic alloy 14YWT: Part I—Mechanical and microstructural observations, *Mater. Sci. Eng. A.* 559 (2013) 101–110. doi:10.1016/j.msea.2012.08.042.
- [36] J.H. Kim, T.S. Byun, D.T. Hoelzer, C.H. Park, J.T. Yeom, J.K. Hong, Temperature dependence of strengthening mechanisms in the nanostructured ferritic alloy 14YWT: Part II—Mechanistic models and predictions, *Mater. Sci. Eng. A.* 559 (2013) 111–118. doi:10.1016/j.msea.2012.08.041.
- [37] P. Miao, G.R. Odette, T. Yamamoto, M. Alinger, D. Klingensmith, Thermal stability of nano-structured ferritic alloy, *J. Nucl. Mater.* 377 (2008) 59–64. doi:10.1016/j.jnucmat.2008.02.042.
- [38] J.H. Schneibel, M. Heilmaier, W. Blum, G. Hasemann, T. Shanmugasundaram, Temperature dependence of the strength of fine- and ultrafine-grained materials, *Acta Mater.* 59 (2011) 1300–1308. doi:10.1016/j.actamat.2010.10.062.
- [39] M.A. Auger, T. Leguey, A. Muñoz, M.A. Monge, V. De Castro, P. Fernández, G. Garcés, R. Pareja, Microstructure and mechanical properties of ultrafine-grained Fe-14Cr and ODS Fe-14Cr model alloys, *J. Nucl. Mater.* 417 (2011) 213–216. doi:10.1016/j.jnucmat.2010.12.060.

7

*Processing ODS ferritic steels:
New nano-oxides precursors for
14 Cr ODS steels*

Contents

7. Preamble to this chapter	149
7.1. Synthetized nano-precipitates	150
7.2. Characterization of F-ODS-II mechanically alloyed powders	152
7.3. F-ODS-II: Optimization of SPS consolidation	153
7.3.1. Distribution of precipitates in the F-ODS-II	156
7.4. Mechanical response on F-ODS-II materials	160
7.4.1. Room temperature behaviour.....	160
7.4.2. High temperature evaluation	162
7.5. Partial discussion	163
7.5.1. Influence of complex oxide addition on the composition of nano-precipitates	163
7.5.2. Heating rate effect on the final consolidation of material.....	164
7.5.3. Bimodal grain size microstructure.....	164
7.5.4. F-ODS-II mechanical behaviour: Room temperature conditions	165
7.5.5. F-ODS-II mechanical behaviour: High temperature conditions.....	167
7.6. Partial Remarks	167
Bibliography	169

7. Preamble to this chapter

Currently, as it was reported in the previous chapters, one of the biggest challenges for developing an ODS alloy is the competition established between the different oxide formers. During the oxides precipitation, in the presence of various precursors, usually, the one with the highest oxygen affinity determines the formation of oxides with a specific composition and the absence of the other species.

In this chapter, a new process to equilibrate the local concentration of species and to decrease the competition among them is reported. A unique compound, containing the diverse oxide precursors (as complex oxide), is introduced in the prealloyed 14Cr steel powder grade via mechanical alloying (named F-ODS-II). Thus, during milling, local environments enriched in Y, Ti and Zr will promote the presence of Zr in the oxide composition which finally improves the thermal stability of the alloy. SPS was used as consolidation technique to guarantee shorter sintering times and to maintain the obtained nanostructure. Mechanical properties were tested by tensile tests and Vickers microhardness at room temperature and small punch test at high temperatures. In the end, partial conclusions were established trying to estimate the different contribution of the strengthening mechanisms in the final consolidated samples.

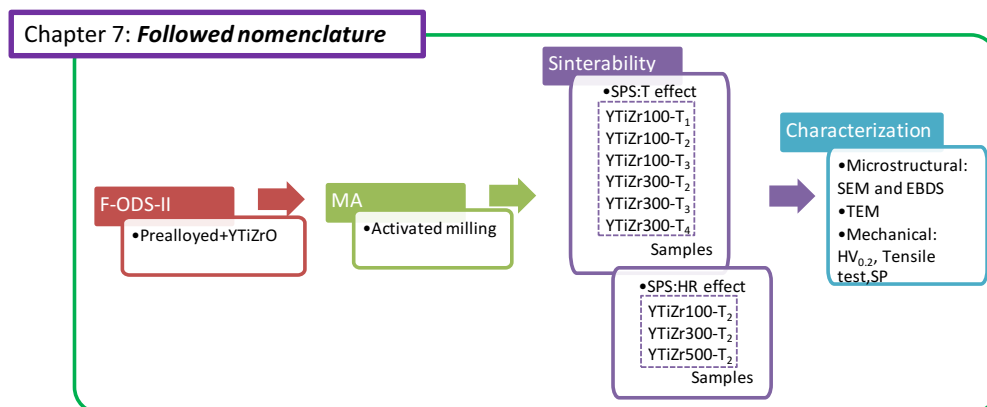


Fig 7.1. Followed nomenclature in Chapter 7 where T is the final temperature attained on SPS consolidation and T₁ represents 1100 °C, T₂ 1150 °C, T₃ 1180 °C and T₄ 1200 °C.

7.1. Synthetized nano-precipitates

Following the synthesis method described in Chapter 3 (Section 3.2.1), the complex nano-oxides Y-Ti-Zr-O were obtained. The synthetized nano-oxides show remarkable small sizes in the range of several nanometers (approx. 20 nm) as shown in Fig 7.2.

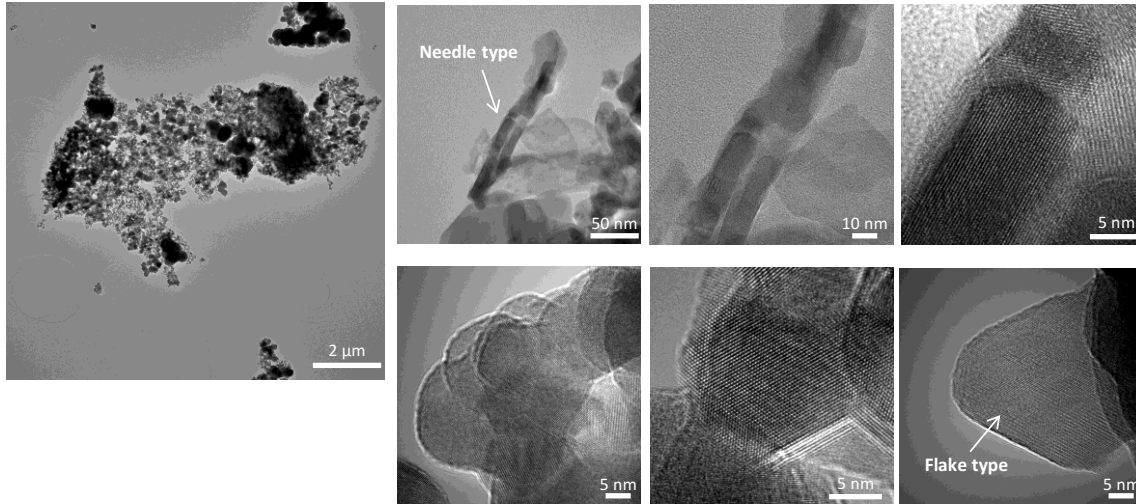


Fig 7.2. Generic morphology of nano-precipitates synthetized of Y-Ti-Zr-O.

The obtained nano-precipitates display a generic morphology composed by needles and flake nano-oxides.

Mapping analysis gives evidences of an homogeneous distribution of the oxide formers (Y-Ti-Zr). Fig 7.3 gathers the TEM images and EDS mapping performed on precipitated powders. Hence, a complex oxide was successfully produced which is confirmed in Fig 7.4, where the EDS results are collected.

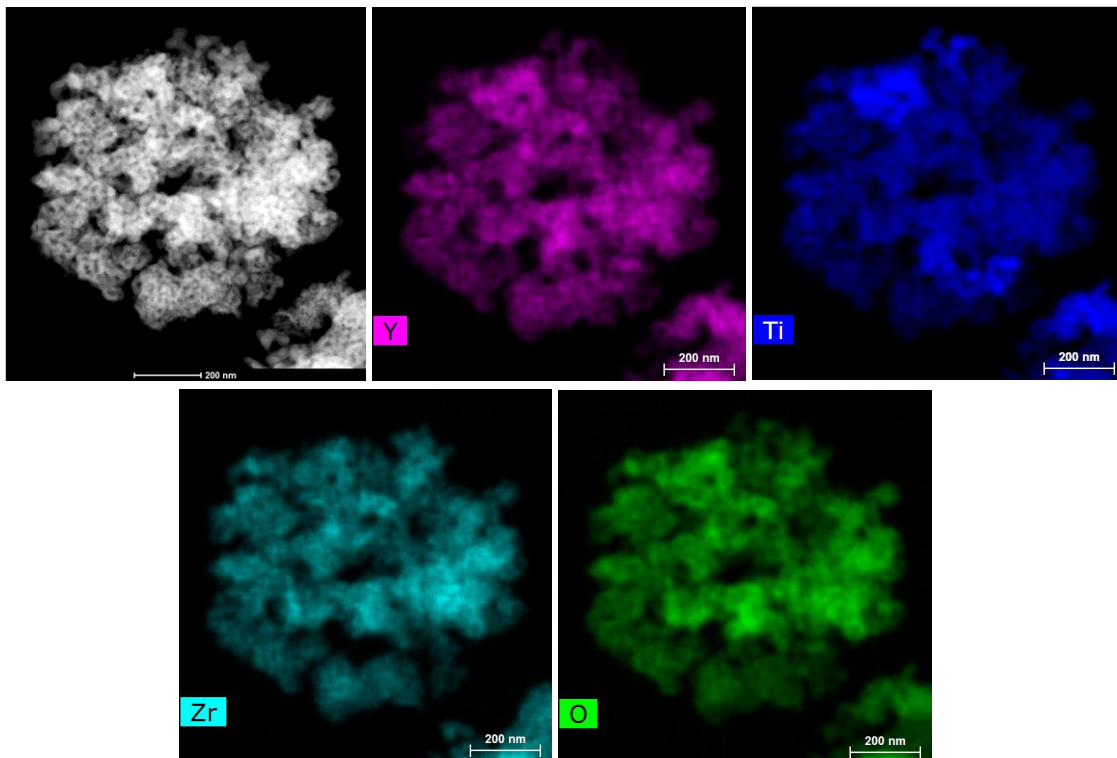


Fig 7.3. STEM images on Y-Ti-Zr-O nano powders, high-angle annular dark-field imaging (HAADF) and EDS mapping analysis.

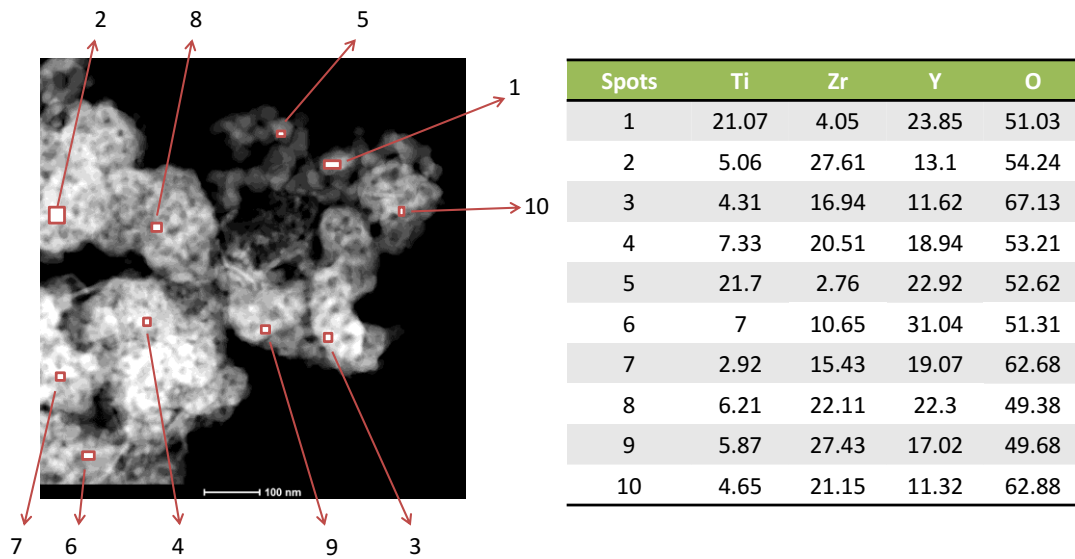


Fig 7.4. STEM and EDS analysis (at%) of the complex nano-oxide obtained by co-precipitation.

After co-precipitation, the powders were pyrolysed at 700°C for one hour in air and with the aim of increasing the crystallinity a thermal treatment was performed at 850 °C for 30 min (Chapter 3, section 3.2.1). The X-Ray characterization after heat treatments, has showed that the powder mainly fulfil a fluorite structure (Fig. 7.5) in accordance with the literature [1]. In addition, it is possible to detect some minority phases such as bixbyite and pyrochlore, ordered version of fluorite. All phases are favourable to produce an ODS steel since normally these are the kind of oxides obtained in the material by using traditional methods. A generic composition was defined as $Y_{0.9}Ti_{0.7}Zr_{2.2}O_{7.1}$ by using EDS in SEM. Nano precipitates with a higher Ti content have associated lower Zr values and vice versa. During the co-precipitation there is a competition between Zr^{4+} and Ti^{4+} as stated on the discussion section of Chapter 5.

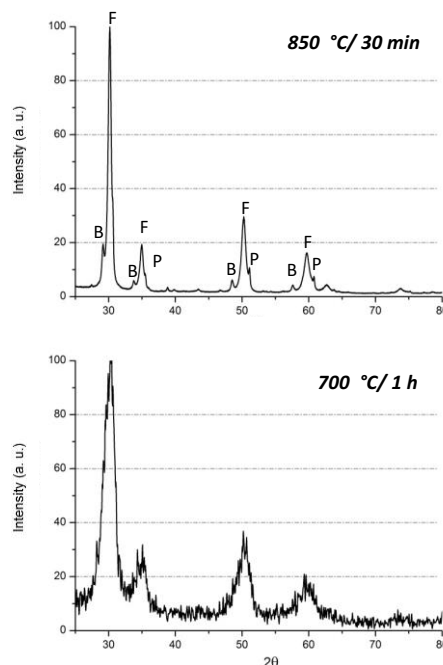


Fig 7.5. XRD of Y-Ti-Zr-O synthesised. Bixbyite (B) and Pyrochlore (P) are ordered version of Fluorite (F) structure (target phase of the precipitated complex oxide) after the thermal treatments reported on chapter 3 [8].

By using HRTEM it is possible to measure the interplanar distance (Fig 7.6) to obtain the lattice parameter. Interplanar distances between 2.9 and 3.2 Å were obtained, nevertheless, it is not possible to ensure the proper formation of a solid solution.

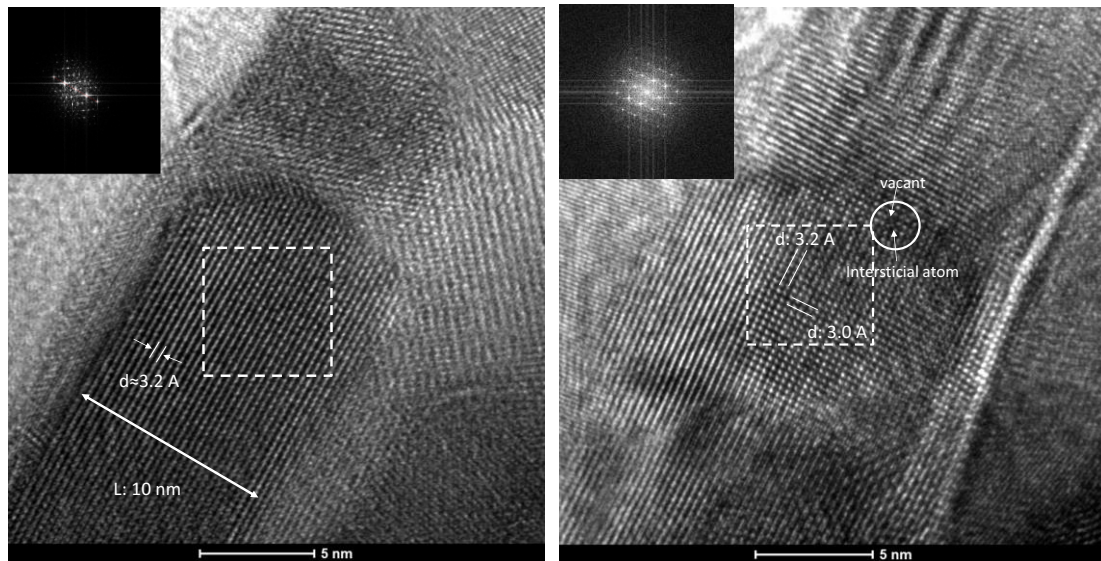


Fig 7.6. Analysis of Y-Ti-Zr-O nano-oxides by HRTEM.

7.2. Characterization of F-ODS-II mechanically alloyed powders

Prealloyed ferritic powder and synthesized Y-Ti-Zr-O nano-oxides were mechanically alloyed (MA) by using M_{act} parameters (see Chapter 3). The MA step is necessary to distribute the oxide formers among the prealloyed powder; besides a bimodal grain size microstructure is ensured after consolidation. As it was stated in Chapter 4, to guarantee a dual grain size distribution is necessary to achieve a high microstrain level and low crystallite size. Milling procedure was stopped once L parameter has reached the same value than in the milling of F-ODS-I ferritic steel i.e 12 nm, considered as a reference, see table 7.1, F-ODS-I- M_{act} . Afterwards, the SEM study of MA powders has shown an irregular particle morphology whose d_{50} is around $93\mu m$ (Fig 7.7, right).

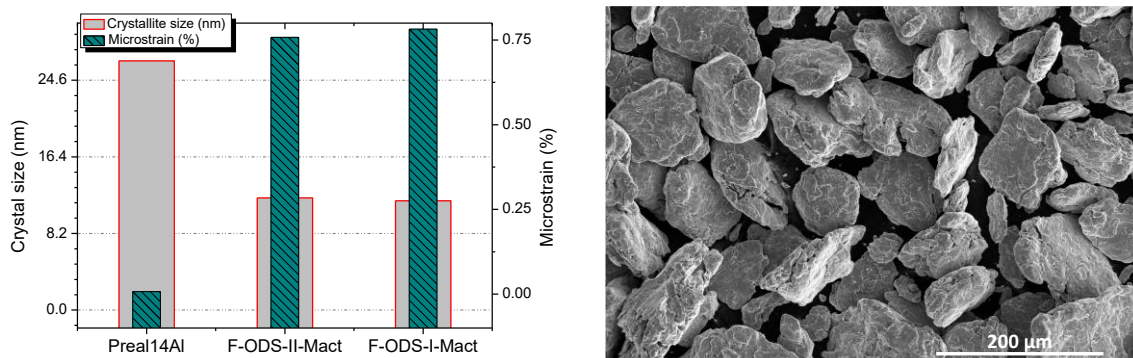


Fig 7.7. Left: structural parameters of prealloyed vs. MA powders, right: MA powder after introducing Y-Ti-Zr-O nano-oxides (F-ODS-II).

Besides, the dislocation density of F-ODS-II powder was calculated to study the dislocation hardening using equation 4.1 and comparing the results with F-ODS-I powders (see table 7.1). Similar values are attained for both powders.

Table 7.1. Particle size and crystallographic parameters for prealloyed and MA powders using M_{act} parameters.

	d_{10} (μm)	d_{50} (μm)	d_{90} (μm)	L (nm)	ϵ (%)	$\rho_{density}$ (m^{-2})	σ_p (MPa)
Preal.14Al	12	30	62	43.1	0.217	$1.07 \cdot 10^{15}$	713
F-ODS-I	40	77	151	11.7	0.782	$1.39 \cdot 10^{16}$	2570
F-ODS-II	49	93	182	12	0.758	$1.30 \cdot 10^{16}$	2491

Furthermore, the control of the interstitial elements was accomplished to grant the quality of the mill performed as it is reported in Table 7.2.

Table 7.2. Particle size and crystallographic parameters for prealloyed and MA powders.

	%C	%N	%O	%Ex.O'
Preal.14Al	0.012	0.007	0.029	-
F-ODS-I	0.149	0.059	0.160	0.11
F-ODS-II	0.094	0.051	0.316	0.06

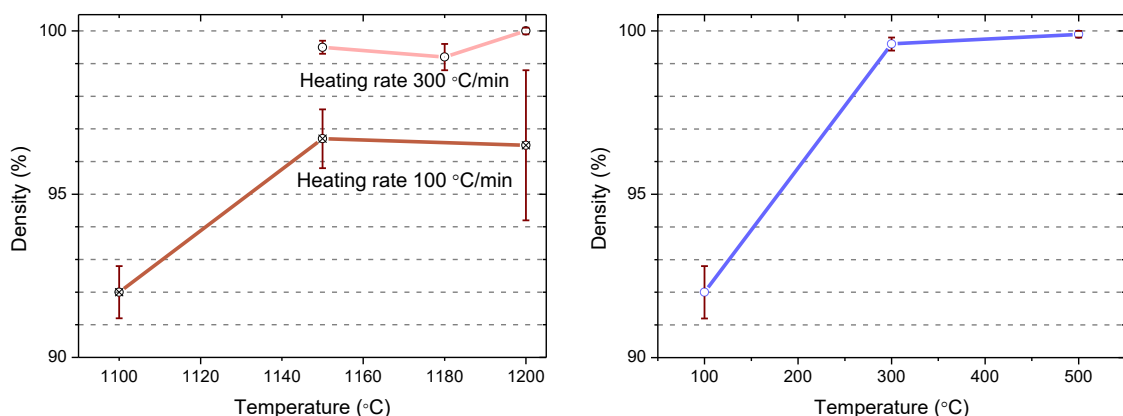
The ExO has to be limited to 0.1% to guarantee the right percentage of oxygen to induce the formation of the different nano-oxides. High value of EX.O could reduce the final precipitation reached (Chapter 4) [2].

7.3. F-ODS-II: Optimization of SPS consolidation

The different parameters used in SPS, such as maximum temperature or heating rate, will determine the final microstructure and the attained densification.

An issue of concern is to determine the effect of the maximum SPS temperature on the density, when the others main parameters remain constant, i.e. pressure, holding time and heating rate (Fig.7.8.left). It is clear, that once a minimum thermal activation is reached, the final density level will depend on the heating rate [3].

By increasing it from 100 to 300 °C/min, the densification level moves approximately from 96% to the fully dense level, 99%. Therefore, there is a clear consequence of the heating rate. To analyse this effect, a constant T of 1150 °C was selected and the heating rate was changed from 100, 300 to 500 °C/min by modifying the amperage introduced into the equipment (fig 7.8. right). Consequently, the Joule effect released a higher level of energy, promoting a local T increase, especially at the particles surfaces [4].

**Fig 7.8.** F-ODS-II performed consolidation: (Left) Density vs temperature and heating rate. (Right) Density vs heating rate when SPS is performed at 1150 °C.

The effect on the final densification is also clear considering the microstructure of consolidated samples (see Fig 7.9). Definitely, a dense steel was achieved when it is consolidated at the highest heating rates (500 °C).

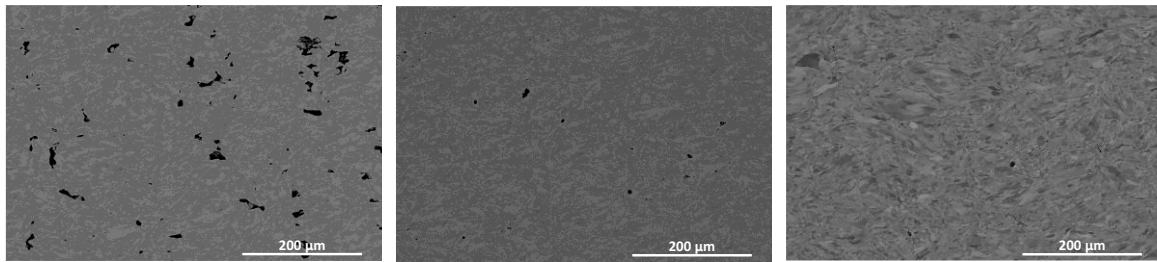


Fig. 7.9. F-ODS-II density evolution by changing the heating rate from 100, 300 and 500 °C/min (from left to right) when the maximum T is 1150 °C.

Differences between samples can be reported on the reached crystallite size, which varies slightly as soon as the temperature rises, independently on the attained heating rate (Fig 7.10). The temperature increase raises the crystallite size reducing the final obtained microstrain. This phenomenon could lead into modifications on the final microstructure and as a consequence determining directly the reached properties.

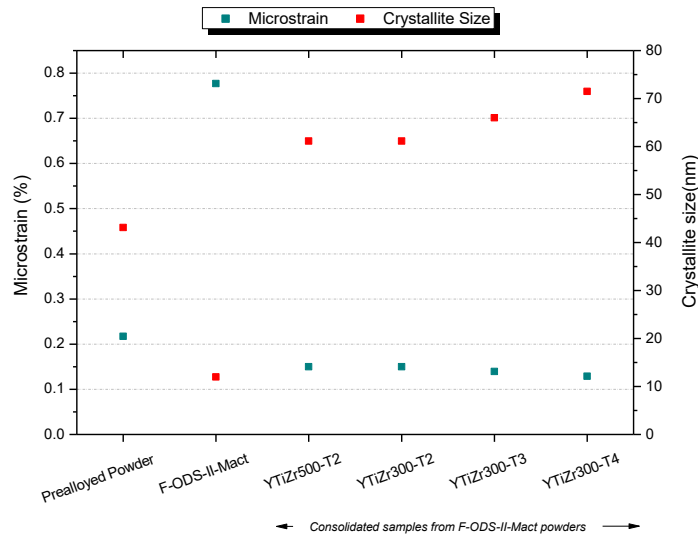


Fig 7.10. F-ODS-II evolution of crystallite size and microstrain of the consolidated materials attained.

Regardless of the used SPS conditions, a bimodal microstructure is also achieved as in F-ODS-I steel. Fig 7.11 shows large micrometric grains with ultrafine (UF) grains colonies. The addition of the co-precipitated nano powders (Y-Ti-Zr-O) is probably determining the further precipitation stage (size, place and composition), and as a result how the nano-oxides will retain the grain growth and the stability of the fine microstructure.

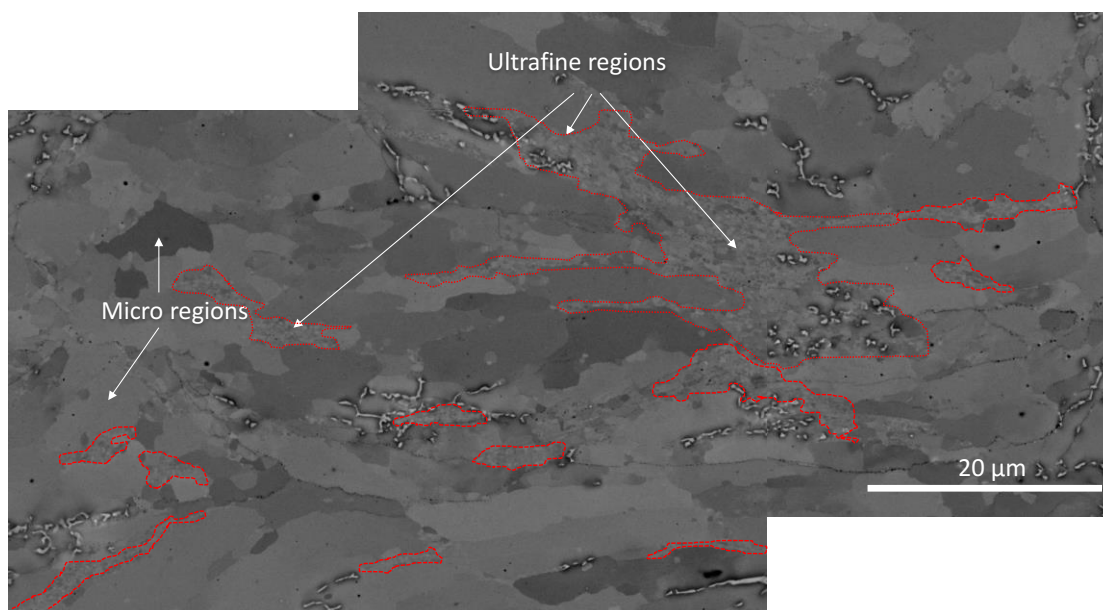


Fig 7.11. Microstructure obtained on F-ODS-II processed at 1150 °C and a H.R. of 300 °/s (YTizr300-T₂).

Besides, using different conditions in the SPS parameters has also an effect on the grain growth (Fig 7.12), especially in the area that ultrafine grains colonies covers [5,6]. For this purpose, an area of approx. $1.4 \cdot 10^4 \mu\text{m}^2$ was assessed by SEM to measure the grain size features. As it is reported on Chapter 3, Fig 7.12 shows on one side the effect of the Heating rate (varied from 300 to 500 °C/min) maintaining the same final temperature (YTizr500-T₂ and YTizr-T₂) and ,on the other side, the effect of the final temperature on the samples maintaining constant the Heating rate (YTizr300-T₃ and YTizr300-T₄).

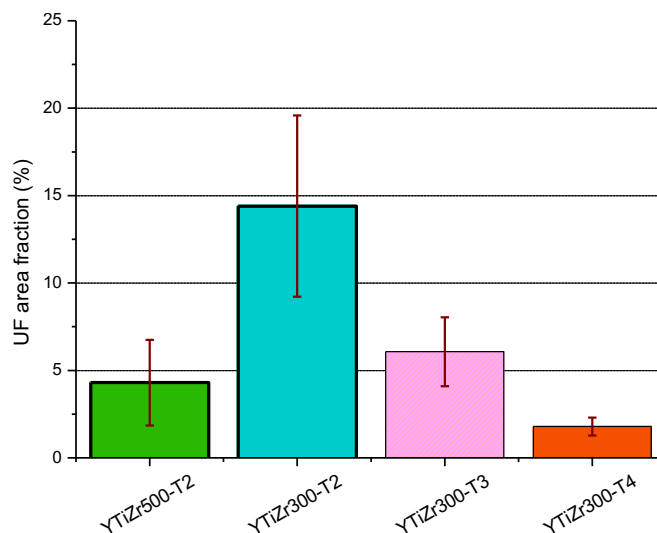


Fig 7.12. Ultrafine regions reported on F-ODS-II alloy, T₂= 1150 °C, T₃=1180 °C, 1200 °C.

Thanks to the EBSD study, it is possible to highlight how the size of ultrafine colonies depends on the thermal activation (Fig. 7.13). In this case the heating rate seems not to determine the final microstructure having higher Uf regions when the material is heated at 300 °C/min. Besides, taking into the account the final temperature attained specimens processed up to 1180 °C (T₃) 300 °C/min can notice a decreased amount of ultrafine grain colonies (See Fig 7.12 and Fig 7.13). No texture was reported on the samples consolidated as it was expected by using SPS.

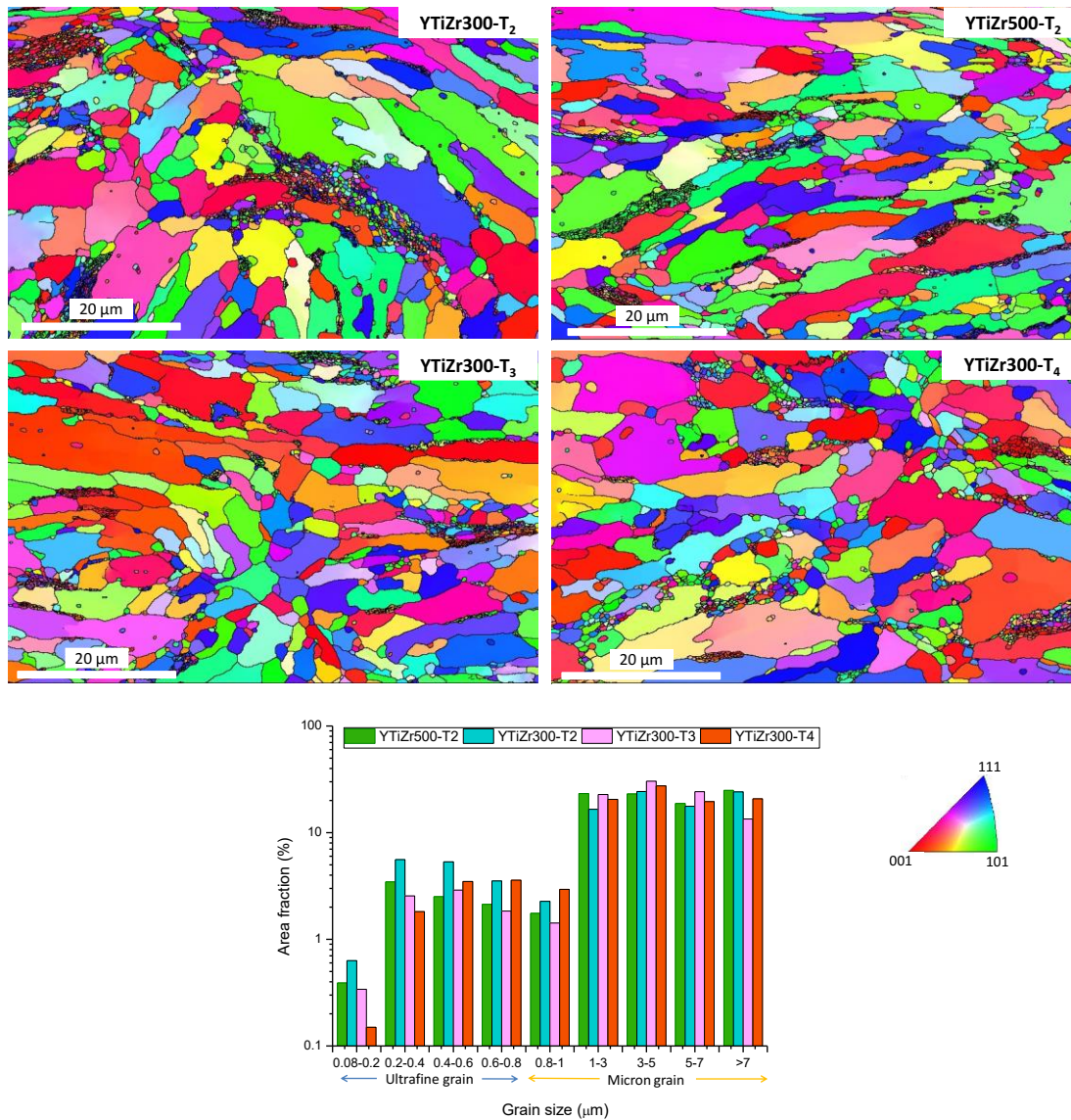


Fig 7.13. Inverse pole Figure maps (Y direction) and grain area fraction distribution on F-ODS-II materials.

In terms of microstructure, the material F-ODS-II could be compared to the one previously processed F-ODS-I [7]. However, a clear drop on the attained ultrafine regions can be observed if F-ODS-II is compared to F-ODS-I (Table 7.3).

Table 7.3. F-ODS-II Average grain size and UF area.

	F-ODS-II				F-ODS-I
	YTiZr500-T ₂	YTiZr300-T ₂	YTiZr300-T ₃	YTiZr300-T ₄	Zr600
UF area fraction (%)	4.3±2.3	14.4±5.1	6.1±1.9	1.8±0.5	32±13
UF grain size (μm)	0.31	0.31	0.32	0.40	0.30
Micrograin size (μm)	2.36	2.17	2.40	2.10	1.51

7.3.1. Distribution of precipitates in the F-ODS-II

TEM characterization was performed on YTiZr500-T₂ samples to determine the nature, size, morphology and distribution of the oxides. Considering the different used SPS conditions, it is supposed that there is no difference on precipitation state since the results studied in Chapter 5 (pp. 102-103) demonstrated that the precipitation state and composition do not depend on the the SPS conditions.

STEM and TEM black field images show an almost homogeneous rounded shape oxide distribution (see fig 7.14, 7.15, 7.16). A total amount of 2000 nano-oxides were measured in order to obtain the final size distribution suggested, where the mean oxide diameter varies from 8 to 11.2 nm. The density of nano-precipitates (Np) , $10^{21} \text{ oxd}/\text{m}^3$, has achieved the same order of magnitude than others ODS steels processed by SPS without Zr [8,9] and there is on the same range of ODS ferritic steel with Zr developed by R.Gao et al by using Sol Gel method [10].

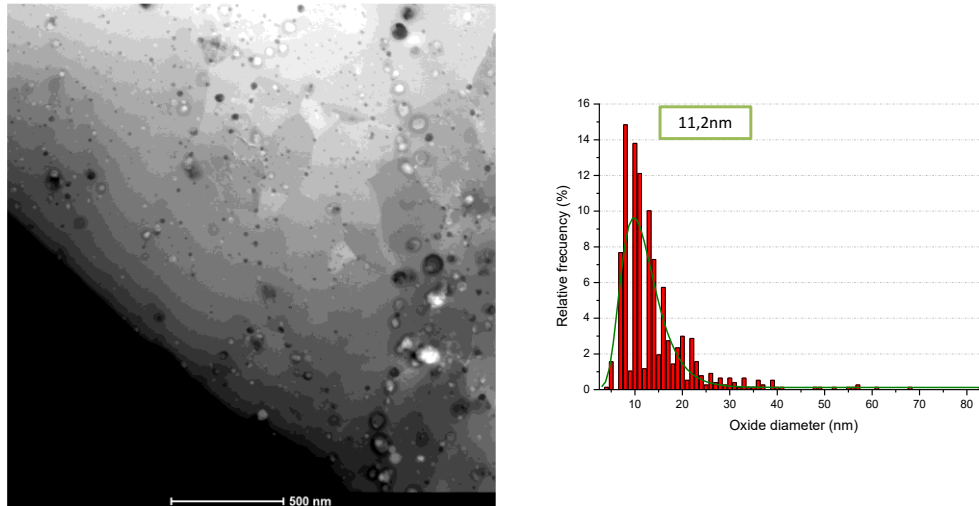


Fig 7.14. STEM characterization on YTiZr500-T₂: (left) STEM Images, (right) oxide diameter distribution obtained by analysing 793 precipitates

To deeply study the micrometrics and ultrafine regions, it was considered a complete grain for both sizes to analyse the precipitation, size distribution and morphology. The micrometric region chose is shown on Fig 7.15.

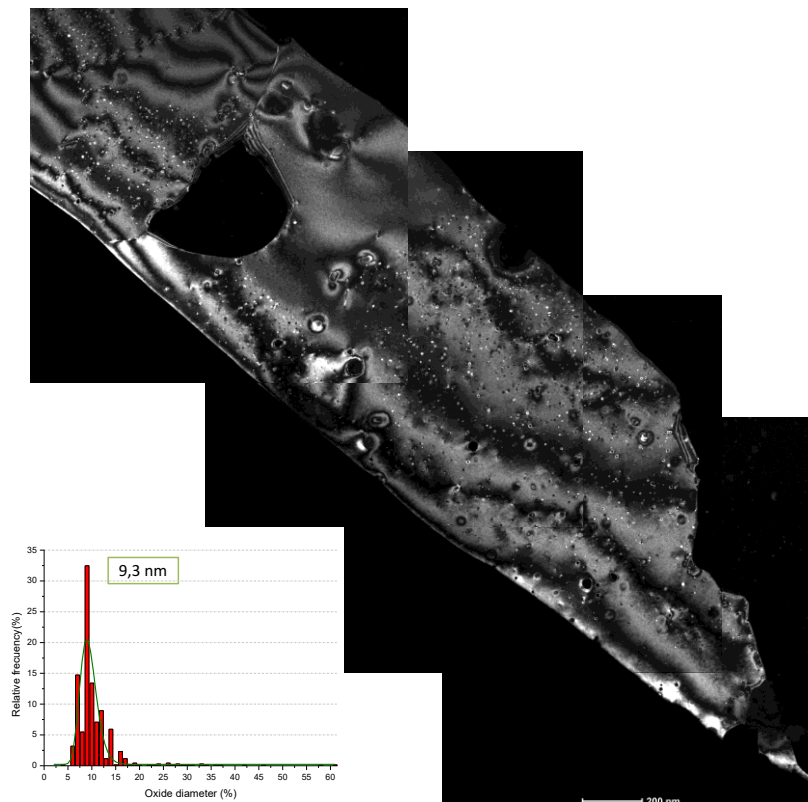


Fig 7.15. Micrometric grain analysis on YTiZr500-T₂ (DF) and oxide diameter distribution.

Considering the micrometric grain, a total area of $2 \cdot 10^6 \text{ nm}^2$ that contain 693 oxides is analysed. The precipitates size distribution is centred at 9.3 nm, and the total density of precipitates measured is $3.45 \cdot 10^{21} \text{ oxd}/\text{m}^3$ which provides a volumetric fraction of 0.14%.

Ultrafine regions were also analysed in order to observe if composition or the density of oxides have changed. A total area of $3.2 \cdot 10^5 \text{ nm}^2$ was analysed in which the oxide size distribution is focused at 8.4 nm (Fig 7.16).

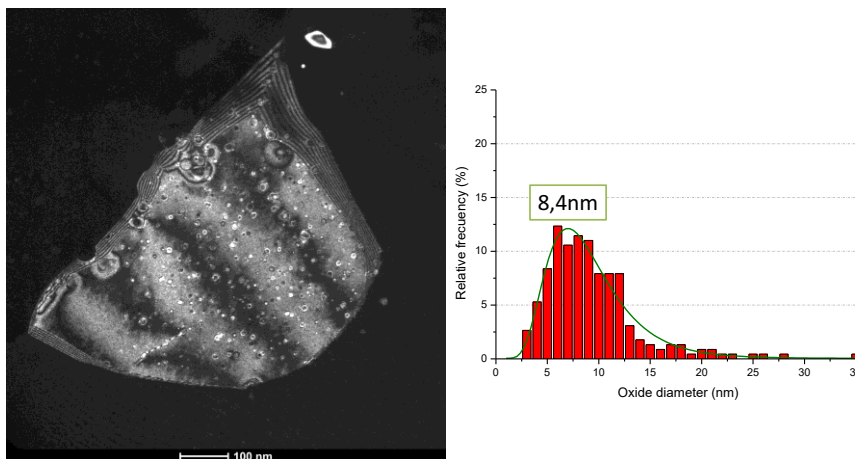


Fig 7.16. Selected ultrafine grain on YTiZr500-T₂ (DF) (right side) and oxide size distribution (left side).

Moreover, in these regions the density of precipitates increases to $7.14 \cdot 10^{21} \text{ oxd}/\text{m}^3$ (that means a frequency of 0.221 %) which can explain the lower local grain growth in contrast to the micrometric area.

Certainly, EDX by TEM shows a clear evidence of the presence of the elements synthetized during the co-precipitation on the nano-oxides obtained. Four types of precipitates are detected (summed up on Fig 7.17), namely:

- 1 **Type 1:** The EDX analysis reveals the presence of Y-Ti-Zr-O. These precipitates exhibit sizes on the range of 10 to 80 nm even if the biggest population is covered by oxides sizes between 10 to 30 nm (which usually display white contrast). From 30 to 80 nm, precipitates presented a black colour contrast even if the composition does not change. Their main localization is inside the grain and at grain boundaries.
- 2 **Type 2:** These oxides are composed by Y-Zr-Al-O. The contrast is white and the analysed sizes are between 9-30 nm. More frequently located inside the grain.
- 3 **Type 3:** These oxides contain Y-Al-O. Their sizes are in the range of 15-30 nm. They are located inside the grain and at the grain boundaries.
- 4 **Type 4:** These precipitates are formed by Y-Zr-O. Their sizes are between 8 and 20 nm, and frequently located inside the grain, just a few on grain boundaries.

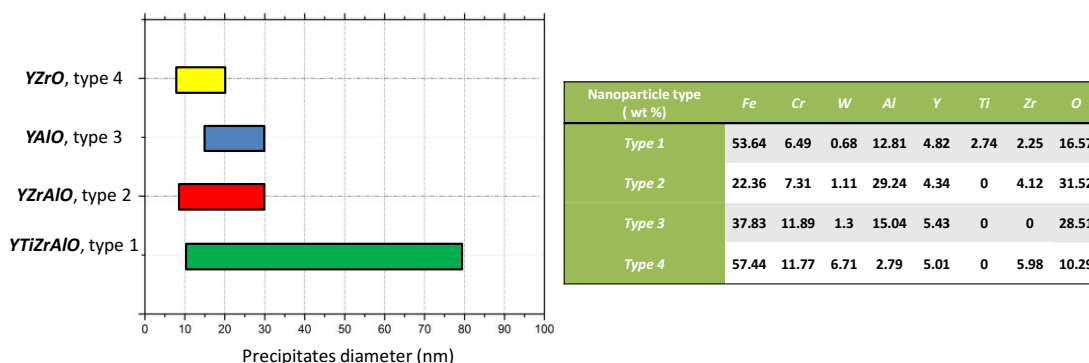


Fig 7.17. Oxides detected on YTiZr500-T₂: (Left) Precipitates diameter depending on composition. (Right) Composition (wt%) of the different precipitates.

These oxides are clearly shown on Fig 7.18, where the mapping of the elements is in accordance with the previous classification.

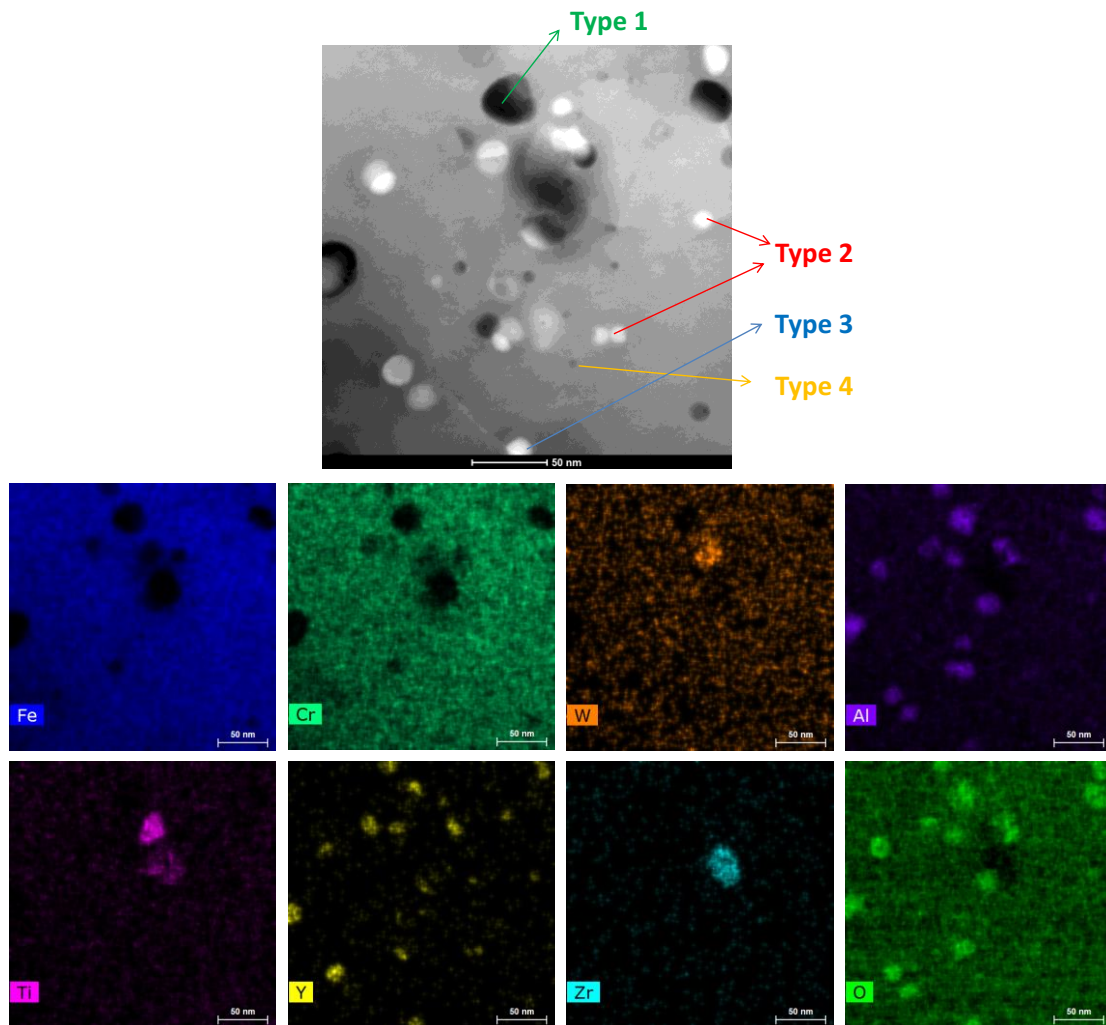


Fig 7.18. EDS Mapping of YTiZr500-T₂.

Although, elements with higher oxygen affinity were introduced to minimise the Y-Al-O formation, the higher Al content of the base prealloyed powder, prevents the total disappearance of these oxides. Nevertheless, it was noticed the formation of complex solid solution such as Y-Ti-Zr-Al-O (type 1 oxide) which represents the highest volume of precipitated oxides. Moreover, from the whole analysed oxides, the 80% has Zr as it is shown in table 7.4. By adding Y-Ti-Zr-O compound, it was increased the oxide formers type 1 rising the possibilities to have Zr on the compound.

Table 7.4. Total number of analysed nano-oxides and fraction of Zr, Y, Ti or Al containing nano-precipitates.

(total n ^o of precipitates)	Y	Zr	Ti	Al
108	99 (91.6%)	86 (79.6%)	62 (57.40%)	78 (72.22%)

If YTiZr500-T₂ and Zr600 are compared, a clear reduction of the density of precipitated oxides is detected (10^{21} vs 10^{22} oxd/m³) meanwhile, the mean oxide diameter is raised (8-11.2 vs 5-6 nm). Also if this material is compared with F-ODS-I, it is important to highlight the absence of TiZr, TiWZr, ZrW or ZrW whose dimension were around 80 nm (see Fig 5.7 on p. 99)

7.4. Mechanical response on F-ODS-II materials

To examine the obtained materials and to evaluate the effect of Zr addition, F-ODS-II will be compared to the consolidated plain prealloyed powder and to previous 14Al-ODS-Tiⁱ without oxides formers [11].

To deeply understand the effect of the complex nano-oxides addition, F-ODS-I-Zr600 will be used as a referenceⁱⁱ.

Finally, to analyse the behaviour of the material at high temperature on SP test, the results will be compared to those obtained from the ODS steel obtained in GETMAT project (high performance ODS steel obtained by HE) [12,13] as in Chapter 4 and 5.

7.4.1. Room temperature behaviour

First, the capability of the material to plastic deformation was evaluated by microhardness testing. The results are sum up in Fig 7.19.

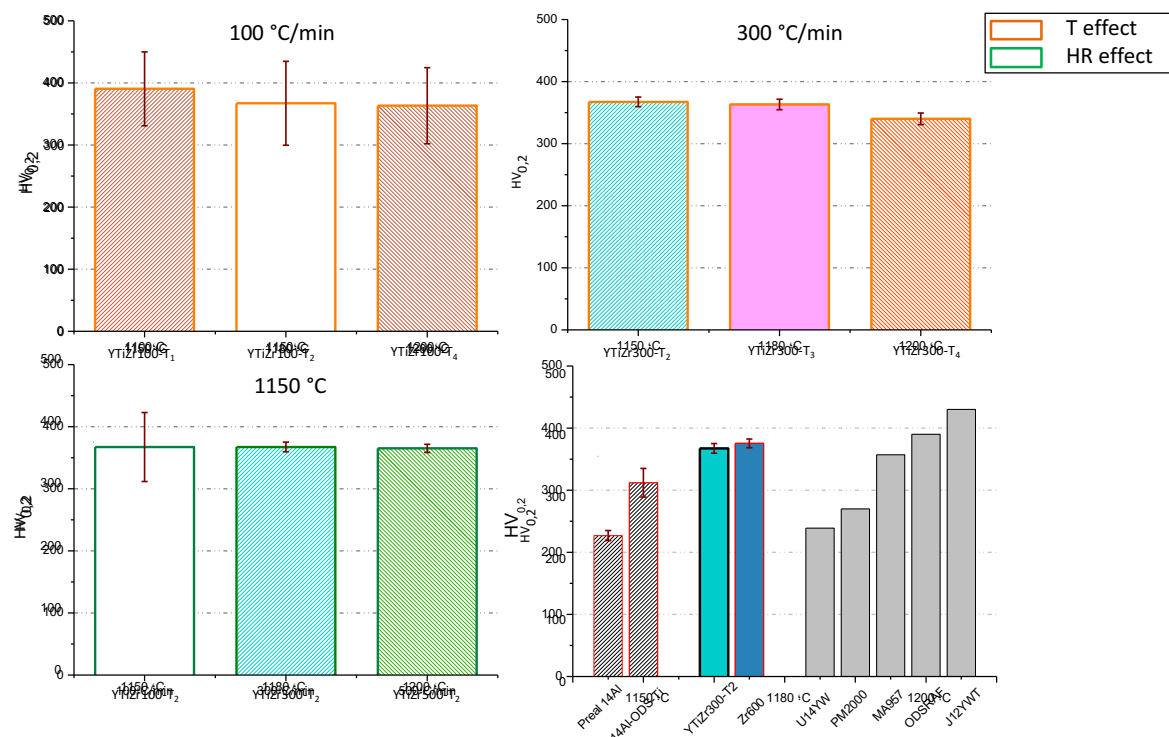


Fig 7.19. F-ODS-II microhardness evaluation depending on different SPS parameters and comparison with F-ODS-I (Zr600), free Zr ODS (14Al-ODS-Ti), free ODS ferritic steel (Prealloyed 14Al) and ODS steels from the literature.

Because of the lower densification of samples consolidated at 100 °C/min (relative density of 96%) the microhardness values have the highest standard deviation, but the value remains comparable to that obtained for higher H.R. (300 and 500 °/min). Indeed, the UF regions could explain why these materials attain these values of microhardness (Fig 7.20).

Improving the density (see section 7.3), promotes stable and repeatable values (Fig 7.19, 300 °C/min and 500°C/min).

ⁱ Y₂O₃ and pure Ti were added

ⁱⁱ Y₂O₃ and pure Ti and Zr were added

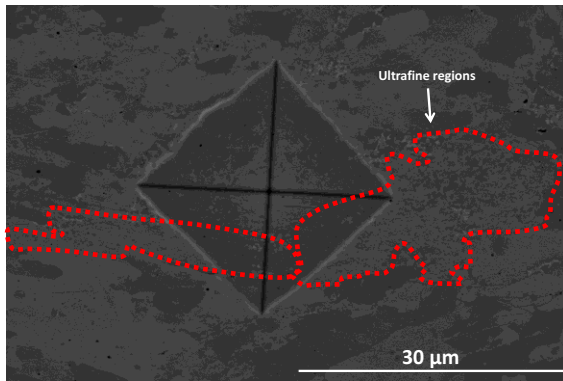
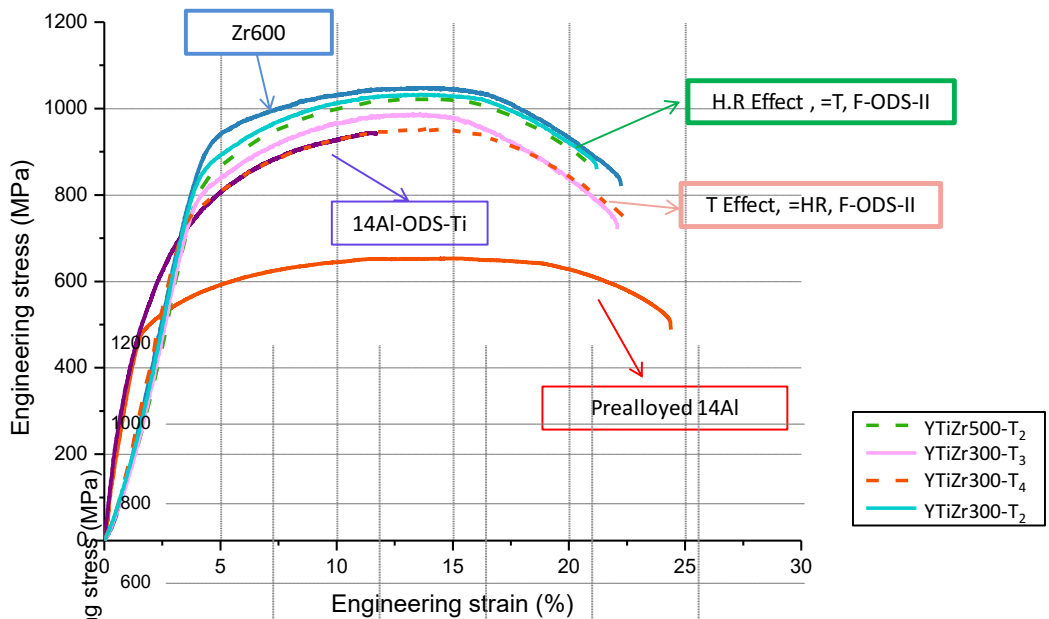


Fig 7.20. Hardness measured on YTiZr100-T₁ reported in the literature [14,15].

It should be noted that YTiZr300-T₂ has achieved a comparable value to Zr600, even if the microstructural features are quite different. When the synthesized oxides are used, the density of precipitated oxides and the ultrafine colonies are smaller.

Therefore, F-ODS-II must be promoting a more effective oxide than the one produced in F-ODS-I. Besides, this new material improves its properties respect to the one developed without Zr, attaining good values of microhardness compared to the one

Additionally, microtensile tests were performed to F-ODS-II alloys whose obtained final density is superior to 98 % (Fig 7.21). Regardless on the SPS conditions, all the materials present an extraordinary UTS values combined with good toughness. The effect of the heating rate is not clear on the final UTS and YS as both alloys (YTiZr500-T₂, YTiZr300-T₂) have achieved similar values.



	UTS (MPa)	YS (MPa)	Toughness (MPa)	Total Deformation (%)
YTiZr500-T ₂	1001 ± 21	815 ± 18	177 ± 12	21.51 ± 1.38
YTiZr300-T ₂	1021 ± 23	841 ± 16	174 ± 29	21.04 ± 3.86
YTiZr300-T ₃	969 ± 20	793 ± 20	183 ± 25	22.73 ± 0.48
YTiZr300-T ₄	935 ± 14	735 ± 25	190 ± 11	24.23 ± 1.79

Fig 7.21. Comparison of engineering tensile stress-strain curves for the F-ODS-II ODS steels, ODS Zr free (14Al-ODS-Ti) and free ODS ferritic steel (prealloyed powder).

As a result of the bimodal grain size, the processed ferritic ODS can be considered as an heterogeneous material with notable differences in ductility or strength for one micrograin area to the ultrafine colonies. Thus, during the tensile test, both areas will behave in a different way. Once the ductile area overcomes the elastic deformation, the harder one (ultrafine colonies)

remain elastic, limiting the further, plastic deformation of the ductile areas. Therefore, an increase of the macroscopic Y.S of the material is measured. On the other hand, for higher stress level, the softer micrograins area will sustain much harder strain, and therefore the toughness of the material is improved. The formed nano-oxides effectively block the dislocation movement which result in this high UTS value.

The amount of ultrafine grain colonies decreases when SPS is performed at 1200 °C and 300 °C/min (YTIZr300-T₄), which explains the reduction in the UTS.

Once again, F-ODS-II has achieved properties comparable to F-ODS-I (Zr600) [7].

7.4.2. High temperature evaluation

The results obtained by Small Punch tests are represented through the load-deflection curves (Fig 7.22). The microstructures promoted by the nano complex oxides together with the dual grain size achieved make the difference respect 14Al-ODS-Ti.

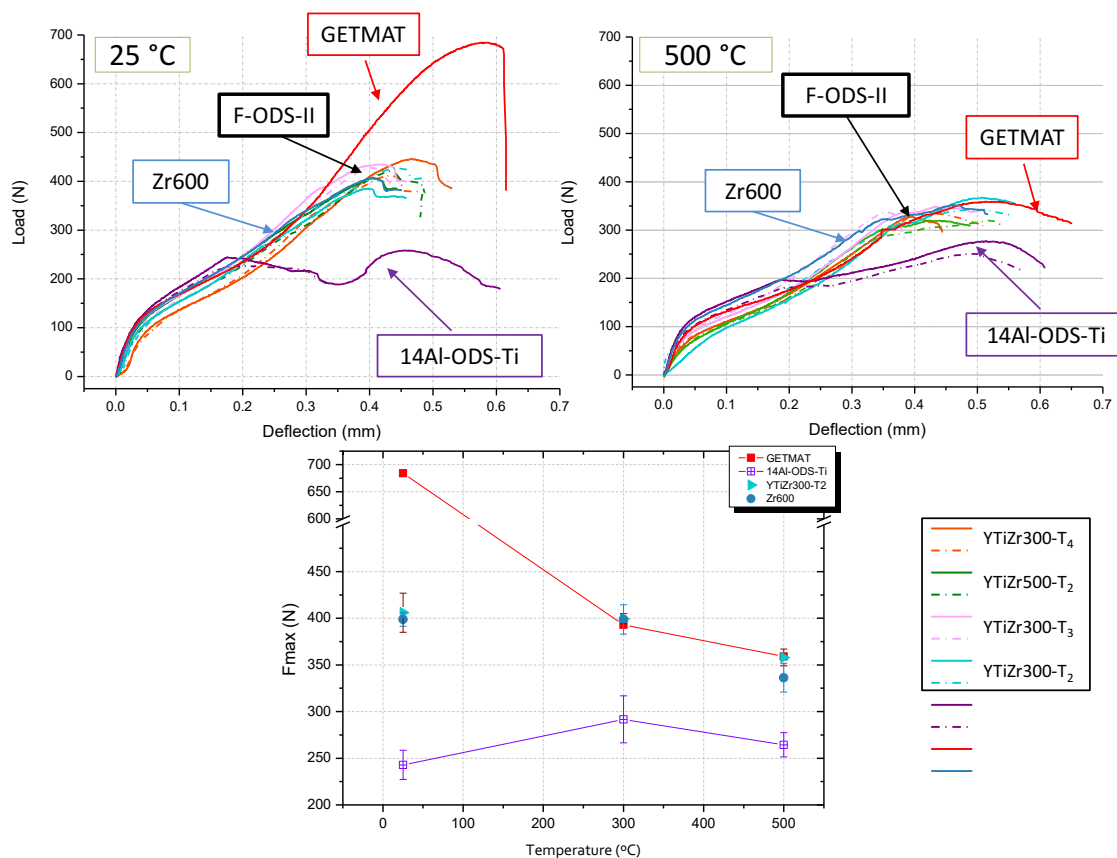


Fig 7.22. Small punch test at RT and 500 °C and maximum load values achieved at different temperatures. Graphs show the comparison between F-ODS-II alloys, Zr600 (F-ODS-I) and GETMAT steel (processed by HE [12,13]).

As it was observed in tensile tests at room temperature no difference was noticed between F-ODS-I-Zr600 and F-ODS-II. Regardless to the addition method to introduced Zr, this element presence seems to be the key factor in the improvement on mechanical properties. F-ODS-II can be compared to GETMAT in terms of maximum load at high temperature (300 and 500 °C). At 300 °C the alloyed developed maintains the maximum load attained at room temperature and only at 500 °C there is small drop.

Fractography of tested samples can describe the failure processes (Fig 7.23). F-ODS-II presents ductile fragile fracture mode with cracks open and circumferentially oriented (similar to F-ODS-I), meanwhile fragile fracture mode with radial cracks are detected in the case of Zr-free ODS steel -14Al-ODS-Ti.

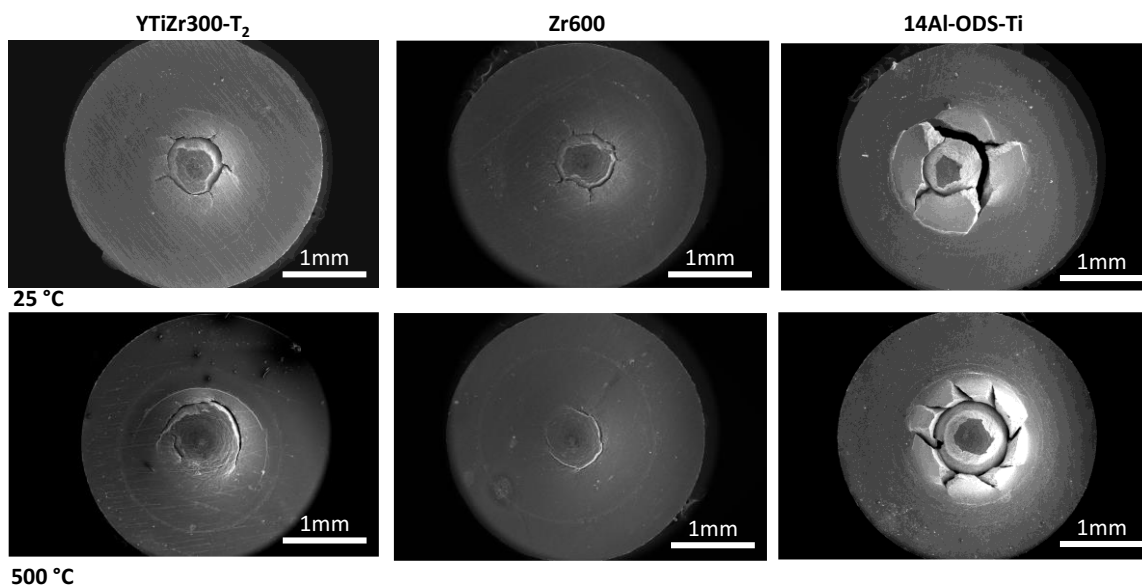


Fig 7.23. Small Punch fracture specimens of F-ODS-II steels.

7.5. Partial discussion

7.5.1. Influence of complex oxide addition on the composition of nano-precipitates

The composition of precipitates in free Al ferritic ODS steels have been studied and it has been demonstrated that with the Zr, Ti and Y_2O_3 addition, the precipitated nano-oxide could achieve the target composition of Y-Ti-Zr-O [16,17]. The presence of this compound should favour the stability of the precipitates on the final microstructure attained. Indeed these nano-oxides have a similar nature to the one used as an oxide precursor in this chapter (see section 7.1).

However, after consolidation, the highest population of precipitates is composed by Y-Zr-Ti-Al-O (type 1) complex oxides, some by Y-Zr-Al-O oxides (type 2) and few by Y-Zr-O (type 4). Therefore, as in chapter 5, the effectivity of Zr on the precipitation of YZrO is limited. Indeed, the Al content of the prealloyed base powder, has definitely changed the results attained (see type 1 and type 2 oxides, section 7.3.1). As stated on the discussions section of chapter 5 in the presence of 5 wt% of Al, it was not possible to avoid the formation of Y-Al-O (type 3 oxides). It should be noted that the content of Y, Ti and Zr (0.2, 0.08, and 0.4 –wt %- respectively) is quite smaller regarding to the 5% of Al content, therefore, the higher Al concentration facilitates a shorter diffusion distance to react with O as K.A.Unocic reported [18].

Ti is analysed on type 1 precipitates (Y-Ti-Zr-Al-O) even if a clear competence with type 2 particles (Y-Zr-Al-O) is observed especially on these particles comprise between 10 and 30 nm. The lower efficiency of Ti to replace or to reduce the formation of Y-Al-O was widely reported in the past [19–21]. However, at least a solid solution with Ti is granted by adding Y-Ti-Zr-O nanoparticles. At the same time, Ti and Zr have a direct competence on forming solid solution with Y and O where the Zr has shifted the Ti presence (explained on the discussion section of Chapter 5) [22]. Besides, the lower diffusion rate of Ti on the BCC matrix respect Zr may explain this result [23]. Therefore, the presence of Y-Zr-Al-O is favoured which explains the presence of type 2 precipitates.

It should be noted that others Zr ODS steels have achieved a bigger precipitates densities than the F-ODS-II developed in this Thesis when Zr was added as elemental powder [24,25]. Indeed, if YTizr-500-T₁ (F-ODS-II) is compared to Zr600 steel (F-ODS-I) it can be observed how the F-ODS-I has reached a higher density of precipitated oxides (10^{22} vs 10^{21} oxd/m³) with a lower mean size (5-6 nm vs 9-11 nm).

It is necessary to keep in mind that the added amount of Zr is different for both ODS families. In F-ODS-II the Zr addition is 0.4 wt% and in F-ODS-I is 0.6 wt%, this fact has a direct effect on the oxides refinement.

Moreover, the short thermal activation of SPS consolidation could reduce the precipitation of the nano oxides when the steel is compared to those processed by HP or HE which should explain the higher value of density of precipitated oxides for ODS steels with Zr addition, 10^{23} oxd/m³ [26].

7.5.2. Heating rate effect on the final consolidation of material

The heating rate is a parameter studied to improve the density on the SPS samples [3,5,6,27]. From the literature mentioned and based on result attained on chapter 5 , it is highlighted how the heating rate effect on densification is marked when the pressure applied is under 60 MPa. Besides, the explanation of this improvement on densification follows two main theories which have been handled during the last few years.

On one side, some authors defend that the differences promoted by changing this parameter on the Joule effect, could produce a temperature gradient since the heating released is dependent on the intensity of current introduced [28]. Upper shell particles have higher probability to form the sintering necks whose phenomenon could be increased by the local heating promoted [29,30]. The surface of particles reached higher T but the high density of lattice defects (that decrease the conductivity of the initial powder) limited the penetration depth of the Joule effect. Therefore, there is a shell/core distribution of T, higher at the outer part of the particles with a marked gradient moving to the centre of them. Achieving these conditions, allowed to reduce the porosity between particles and finally consolidate better the material.

On the other side , there are some studies that reject the possibility of this local heating [28,31], limiting the temperature gradient between the powder surface and the core just to the beginning of sintering process (effective during short times only) which , consequently, leads into a small effect on the final density [32,33]. The improvement on the densification is explained by an overall heating produced in all the powder (up to 100 °C) [28]. Therefore, this phenomenon could explain why up to 1200 °C by using the same heating rate, the submicron regions were reduced.

Both theories could give an explanation to the improved densification studied in this Chapter.

7.5.3. Bimodal grain size microstructure

As it is reported in Chapter 4 and 5, three parameters lead to the heterogeneous recrystallization, namely: the unequal deformation of powders after the MA step, the heterogeneous oxide-formers distribution on milled powders and the SPS consolidation process. Again, the F-ODS-II steels have achieved a bimodal microstructure (see Fig7.13). However, the area fraction that covers the ultrafine grains colonies is smaller than F-ODS-I regardless of the selected heating rate.

If after MA the same dislocation density was reached (F-ODS I vs F-ODS II, table 7.1), the recrystallization stage must be closely connected to the nano-oxides formed. Using the equations proposed in Chapter 6 (p.138) it is possible to connect the grain size with the precipitate size [34]. Table 7.5 reports the critical ferritic grain size calculated on YTiZr500-T₂ with the mean size value of nano-oxides measured by TEM on each region.

Table 7.5. Critical ferritic radius attained by particles pinning.

		Zenner equation (nm)	Rios equation (nm)	Experimental grain size (nm)
F-ODS-II	Micrometric region	4404	550	1050
	Ultrafine region	2545	318	200
F-ODS-I	Micrometric region	2535	316	755
	Ultrafine region	1889	237	150

Due to the oxide mean size (5-6 vs 9-11 nm) the smallest ferritic grain size are reached for Zr600, which also presents the higher precipitates density (10^{22} vs 10^{21} oxd/m³) a smaller Rc is reached. If this phenomenon is connected with the experimental result this should be an explanation on the reduction of the areas covered by Uf. On the other side this can explain why the micrometric has attained a higher average size respect F-ODS-I, since the critical radius attained is far larger than the one presented in F-ODS-I.

Besides, F-ODS-II steels after SPS consolidation have a slightly smaller dislocation density (Table 7.6) which could be connected to the smaller precipitates' densities obtained.

Table 7.6. Hardening promote by dislocation density on the final powder achieved on F-ODS-II.

		$\rho_{\text{dislocation}} \text{ (m}^{-2}\text{)}$
F-ODS-II	YTiZr500-T ₂	$5.10 \cdot 10^{14}$
	YTiZr300-T ₂	$5.09 \cdot 10^{14}$
	YTiZr300-T ₃	$4.40 \cdot 10^{14}$
	YTiZr300-T ₄	$3.82 \cdot 10^{14}$
F-ODS-I	Zr600	$9.07 \cdot 10^{14}$

To conclude with, F-ODS-I family has smaller oxides and higher volumetric fraction that promote higher pinning pressure, which leads to the ferritic grain growth reduction. As a dual grain size distribution is achieved in all the materials consolidated (F-ODS-II), the nano-complex oxides synthetises are influencing directly on the grain growth attained, meanwhile the reduction on the precipitation state (density and size) explains the differences with F-ODS-I and determining the final microstructure as well as the reduced dislocation density.

7.5.4. F-ODS-II mechanical behaviour: Room temperature conditions

It is clear that the Zr addition (independently on the alloying method) determines the mechanical properties since improvements are observed with respect to free Zr ODS ferritic steel (14Al-ODS-Ti, see Fig. 7.19, 7.21, 7.22). ODS steels are hardened by different mechanisms' as it was reported in chapter 4 and 5. The contribution of the different strengthening terms can give an explanation to the differences reported between F-ODS-II materials Table 7.8. (Following the equations on pp. 111-112).

Table 7.8. Yield Strength values for F-ODS-II calculated theoretical approximations vs. YS experimentally obtained (in MPa).

		YTiZr500-T ₂	YTiZr300-T ₂	YTiZr300-T ₃	YTiZr300-T ₄
Strengthening mechanisms	σ_{gb}	189	226	193	191
	σ_{dislo}	493	492	458	427
	σ_p	122	122	122	122
Calculated YS	$\sigma_{y,calc}$	891	927	861	829
	$\sigma'_{y,calc}$	697	733	667	635
Experimental YS	$\sigma_{y,experimental}$	815	841	793	735

The input provided by dislocation density strengthening and oxide strengthening are sharing the biggest contribution to the calculated YS [35–37]. The final grain size obtained in this case could explain the different behaviour obtained in the YS for F-ODS-II, which are highly reduced as soon as the final consolidation temperature is increased.

Moreover, on Fig 7.24, both ODS families are compared (YTIZr300-T2 vs Zr 600) in terms of YS since similar properties were attained during mechanical tests (See section 7.4).

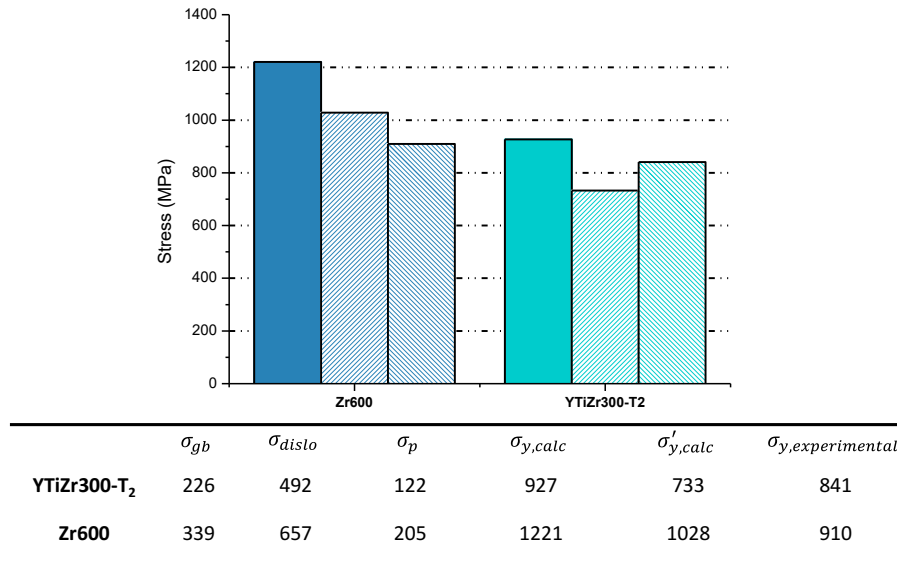


Fig 7.24. Comparison of theoretical contribution to YS (in MPa) considering two approaches vs experimental results comparing YTIZrO300-T₂ and Zr600 where $\sigma'_{y,calc} = f(\sigma_{gb}, \sigma_{dis}, \sigma_p)$ and $\sigma_{y,calc} = f(\sigma_0, \sigma_{ss}, \sigma_{gb}, \sigma_{dis}, \sigma_p)$, explained on chapter 5.

The higher dislocation density along with the precipitation density of Zr600 gives an explanation on the higher theoretical YS attained. However, the experimental YS is similar between both material (841 vs 910 MPa). Indeed, equation 5.Y, ($\sigma_p = \alpha_p M G b \sqrt{N_p d_p}$) depends directly on the misfit between the particle and the matrix (the term α_p) which is determined by the nature of the different precipitates. Certainly, the difference reports between the real YS value and the one calculated in the approximation of fig 7.24 could be related to this factor. In fig 7.24 the constant taken for α_p is 0.33 is the one used by A.Chauhan et al [38]. However, if the constant used is the one from A.Ramar et al ($\alpha_p = 1$) [39] the contribution established by the particles is quite higher. Consequently, if all the constant are taken into the account the strengthening value reported by particles are different (see Fig 7.25). It is well mentioning that as soon as the α_p term increases the particles becomes unshearable, therefore, increasing the contribution to YS (see chapter 1)

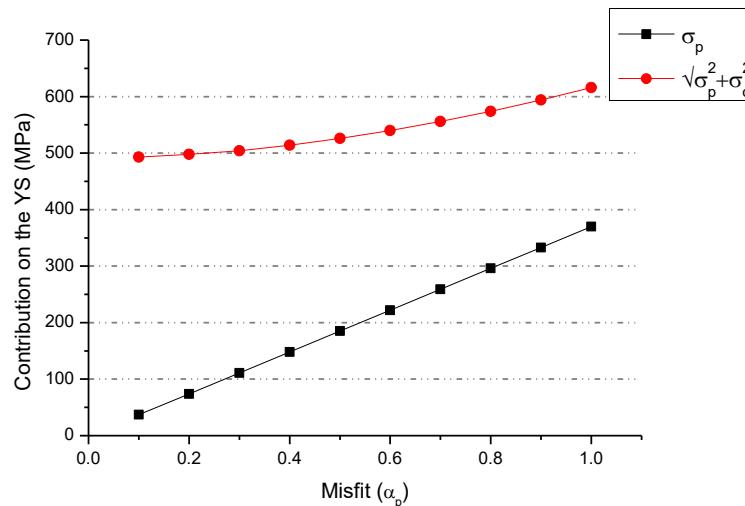


Fig 7.25. Influence of misfit and consequently of the nature of the particle on the final strengthening for the YTiZr300-T₂ steel.

7.5.5. F-ODS-II mechanical behaviour: High temperature conditions

As it could be analysed by SP tests, the maximum load of the material is kept until 300 °C. The drop in the response is shown at 500 °C. Based on previous studies on that field [36], the contribution of dislocation to the final hardening starts to change when 400 °C is reached. From that point, the strengthening provided by s.s and oxide precipitation become the major players and keep properties until approx. 600 °C [36].

The thermal stability of oxides is defined considering the coherency and the coarsening evolution [40–43]. If oxides remain coherent with the matrix, the mechanical behaviour is stable up to 500 °C. Several studies have shown that Zr addition contribute to keep coherency with the BCC structure [16,24–26,44–47]. As it is stated in chapter 6, usually, precipitated nano-oxides present high thermal stability avoiding coarsening until the temperature is close to 0.8 T_m, as it was reported in previous chapters [6].

In this case, for F-ODS-II as the volume fraction of precipitates is reduced, the mechanical behaviour at high T must be defined by the composition of the nano-oxides which allow keeping the coherency with the ferritic matrix.

Even if the nano-complex oxides inserted in this way (Y-Ti-Zr-O) are still not study in terms of stability and coherency to the matrix, the results are really promising for future studies and application under high temperature achieving similar value to Zr600.

7.6. Partial Remarks

A new method to accomplish the addition of oxide formers in the production of a ferritic ODS has been developed. Thanks to the co-precipitation technique is possible to design a complex nano-oxide with a proper composition that will be added by MA; milled powders will be successfully consolidated by SPS. It was demonstrated that:

- Co-precipitation could be an effective method to obtain nano-powders with a tailored composition. By adding a unique compound of oxide formers, it is allowed to produce rich local environments in Y, Ti and Zr on the ferritic grade by high energy milling that should conditioned the later oxide precipitation.
- SPS conditions can be optimized to obtain a fully dense material. The heating rate is the key factor that enables a full densification of the material when the pressure applied is around 50 MPa.

- A bimodal grain size distribution was obtained for all the consolidated samples. The oxides produced, are effective on retaining the grain growth. Ultrafine colonies sizes depend on maximum temperature achieved on SPS.
- The evaluated mechanical properties have shown the good behaviour of the produced ODS steel by this new method. SP at high T shows a really promising results at 300 °C and 500 °C where the material has achieved optimum values, similar to the ones obtained by traditional method of production.

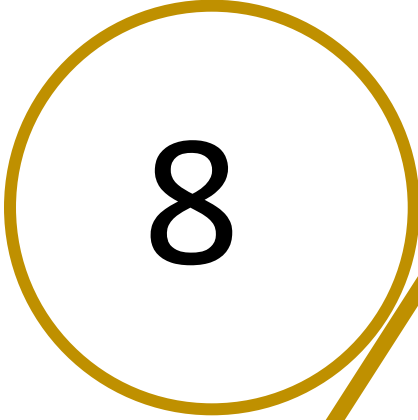
Bibliography

- [1] T.A. Schaedler, W. Francillon, A.S. Gandhi, C.P. Grey, S. Sampath, C.G. Levi, Phase evolution in the YO_{1.5}-TiO₂-ZrO₂ system around the pyrochlore region, *Acta Mater.* 53 (2005) 2957–2968. doi:10.1016/j.actamat.2005.03.010.
- [2] S. Ohtsuka, S. Ukai, M. Fujiwara, T. Kaito, T. Narita, Nano-structure control in ODS martensitic steels by means of selecting titanium and oxygen contents, *J. Phys. Chem. Solids.* 66 (2005) 571–575. doi:10.1016/j.jpcs.2004.06.033.
- [3] X. Boulnat, D. Fabrègue, M. Perez, S. Urvoy, D. Hamon, Y. de Carlan, Assessment of consolidation of oxide dispersion strengthened ferritic steels by spark plasma sintering: from laboratory scale to industrial products, *Powder Metall.* 57 (2014) 204–211. doi:10.1179/1743290114Y.0000000091.
- [4] M.S. Staltsov, I.I. Chernov, I.A. Bogachev, B.A. Kalin, E.A. Olevsky, L.J. Lebedeva, A.A. Nikitina, Optimization of mechanical alloying and spark-plasma sintering regimes to obtain ferrite–martensitic ODS steel, *Nucl. Mater. Energy.* 9 (2016) 360–366. doi:10.1016/j.nme.2016.08.020.
- [5] I. Hilger, X. Boulnat, J. Hoffmann, C. Testani, F. Bergner, Y. De Carlan, F. Ferraro, A. Ulbricht, Fabrication and characterization of oxide dispersion strengthened (ODS) 14Cr steels consolidated by means of hot isostatic pressing, hot extrusion and spark plasma sintering, *J. Nucl. Mater.* 472 (2015) 206–214. doi:10.1016/j.jnucmat.2015.09.036.
- [6] X. Boulnat, M. Perez, D. Fabregue, T. Douillard, M.H. Mathon, Y. De Carlan, Microstructure evolution in nano-reinforced ferritic steel processed by mechanical alloying and spark plasma sintering, *Metall. Mater. Trans. A Phys. Metall. Mater. Sci.* 45 (2014) 1485–1497. doi:10.1007/s11661-013-2107-y.
- [7] E. Macía, A. García-Junceda, M. Serrano, M. Hernández-Mayoral, L.A. Diaz, M. Campos, Effect of the heating rate on the microstructure of a ferritic ODS steel with four oxide formers (Y-Ti-Al-Zr) consolidated by spark plasma sintering (SPS), *J. Nucl. Mater.* 518 (2019) 190–201. doi:10.1016/j.jnucmat.2019.02.043.
- [8] C. Heintze, M. Hernández-Mayoral, A. Ulbricht, F. Bergner, A. Shariq, T. Weissgärber, H. Frielinghaus, Nanoscale characterization of ODS Fe-9%Cr model alloys compacted by spark plasma sintering, *J. Nucl. Mater.* 428 (2012) 139–146. doi:10.1016/j.jnucmat.2011.08.053.
- [9] C.H. Zhang, A. Kimura, R. Kasada, J. Jang, H. Kishimoto, Y.T. Yang, Characterization of the oxide particles in Al-added high-Cr ODS ferritic steels, *J. Nucl. Mater.* 417 (2011) 221–224. doi:10.1016/j.jnucmat.2010.12.063.
- [10] R. Gao, T. Zhang, X.P. Wang, Q.F. Fang, C.S. Liu, Effect of zirconium addition on the microstructure and mechanical properties of ODS ferritic steels containing aluminum, *J. Nucl. Mater.* 444 (2014) 462–468. doi:10.1016/j.jnucmat.2013.10.038.
- [11] N. García-Rodríguez, M. Campos, J.M. Torralba, M.H. Berger, Y. Bienvenu, Capability of mechanical alloying and SPS technique to develop nanostructured high Cr, Al alloyed ODS steels, *Mater. Sci. Technol.* 30 (2014) 1676–1684. doi:10.1179/1743284714Y.0000000595.
- [12] M. Serrano, M. Hernández-Mayoral, A. García-Junceda, Microstructural anisotropy effect on the mechanical properties of a 14Cr ODS steel, *J. Nucl. Mater.* 428 (2012) 103–109. doi:10.1016/j.jnucmat.2011.08.016.
- [13] M. Serrano, A. García-Junceda, R. Hernández, M.H. Mayoral, On anisotropy of ferritic ODS alloys, *Mater. Sci. Technol.* 30 (2014) 1664–1668.

- doi:10.1179/1743284714Y.0000000552.
- [14] Z. Oksiuta, N. Baluc, Effect of mechanical alloying atmosphere on the microstructure and Charpy impact properties of an ODS ferritic steel, *J. Nucl. Mater.* 386–388 (2009) 426–429. doi:10.1016/j.jnucmat.2008.12.148.
- [15] M.J. Alinger, G.R. Odette, D.T. Hoelzer, On the role of alloy composition and processing parameters in nanocluster formation and dispersion strengthening in nanostructured ferritic alloys, *Acta Mater.* 57 (2009) 392–406. doi:10.1016/j.actamat.2008.09.025.
- [16] R. Rahmanifard, H. Farhangi, A.J. Novinrooz, Effect of zirconium and tantalum on the microstructural characteristics of 12YWT ODS steel nanocomposite, *J. Alloys Compd.* 622 (2015) 948–952. doi:10.1016/j.jallcom.2014.11.018.
- [17] H. Xu, Z. Lu, S. Ukai, N. Oono, C. Liu, Effects of annealing temperature on nanoscale particles in oxide dispersion strengthened Fe-15Cr alloy powders with Ti and Zr additions, *J. Alloys Compd.* 693 (2017) 177–187. doi:10.1016/j.jallcom.2016.09.133.
- [18] K.A. Unocic, B.A. Pint, D.T. Hoelzer, Advanced TEM characterization of oxide nanoparticles in ODS Fe–12Cr–5Al alloys, *J. Mater. Sci.* 51 (2016) 9190–9206. doi:10.1007/s10853-016-0111-5.
- [19] P. Dou, A. Kimura, T. Okuda, M. Inoue, S. Ukai, S. Ohnuki, T. Fujisawa, F. Abe, Polymorphic and coherency transition of Y–Al complex oxide particles with extrusion temperature in an Al-alloyed high-Cr oxide dispersion strengthened ferritic steel, *Acta Mater.* 59 (2011) 992–1002. doi:10.1016/j.actamat.2010.10.026.
- [20] P. Dou, A. Kimura, T. Okuda, M. Inoue, S. Ukai, S. Ohnuki, T. Fujisawa, F. Abe, Effects of extrusion temperature on the nano-mesoscopic structure and mechanical properties of an Al-alloyed high-Cr ODS ferritic steel, *J. Nucl. Mater.* 417 (2011) 166–170. doi:10.1016/j.jnucmat.2011.01.061.
- [21] P. Dou, A. Kimura, R. Kasada, T. Okuda, M. Inoue, S. Ukai, S. Ohnuki, T. Fujisawa, F. Abe, S. Jiang, Z. Yang, TEM and HRTEM study of oxide particles in an Al-alloyed high-Cr oxide dispersion strengthened ferritic steel with Hf addition, *J. Nucl. Mater.* 485 (2017) 189–201. doi:10.1016/J.JNUCMAT.2016.12.001.
- [22] D. Murali, B.K. Panigrahi, M.C. Valsakumar, S. Chandra, C.S. Sundar, B. Raj, The role of minor alloying elements on the stability and dispersion of yttria nanoclusters in nanostructured ferritic alloys: An ab initio study, *J. Nucl. Mater.* 403 (2010) 113–116. doi:10.1016/j.jnucmat.2010.06.008.
- [23] D. Murali, B.K. Panigrahi, M.C. Valsakumar, C.S. Sundar, Diffusion of γ and Ti/Zr in bcc iron: A first principles study, *J. Nucl. Mater.* 419 (2011) 208–212. doi:10.1016/j.jnucmat.2011.05.018.
- [24] H. Dong, L. Yu, Y. Liu, C. Liu, H. Li, J. Wu, Enhancement of tensile properties due to microstructure optimization in ODS steels by zirconium addition, *Fusion Eng. Des.* 125 (2017) 402–406. doi:10.1016/J.FUSENGDES.2017.03.170.
- [25] H. Xu, Z. Lu, D. Wang, C. Liu, Effect of zirconium addition on the microstructure and mechanical properties of 15Cr-ODS ferritic Steels consolidated by hot isostatic pressing, *Fusion Eng. Des.* 114 (2017) 33–39. doi:10.1016/J.FUSENGDES.2016.11.011.
- [26] P. Dou, A. Kimura, R. Kasada, T. Okuda, M. Inoue, S. Ukai, S. Ohnuki, T. Fujisawa, F. Abe, TEM and HRTEM study of oxide particles in an Al-alloyed high-Cr oxide dispersion strengthened steel with Zr addition, *J. Nucl. Mater.* 444 (2014) 441–453. doi:10.1016/j.jnucmat.2013.10.028.

- [27] I. Bogachev, E. Grigoryev, O.L. Khasanov, E. Olevsky, Fabrication of 13Cr-2Mo ferritic/martensitic oxide-dispersion-strengthened steel components by mechanical alloying and spark-plasma sintering, *Jom*. 66 (2014) 1020–1026. doi:10.1007/s11837-014-0972-5.
- [28] J. Trapp, B. Kieback, Temperature Distribution in Metallic Powder Particles during Initial Stage of Field-Activated Sintering, *J. Am. Ceram. Soc.* 98 (2015) 3547–3552. doi:10.1111/jace.13757.
- [29] X. Song, X. Liu, J. Zhang, Neck formation and self-adjusting mechanism of neck growth of conducting powders in spark plasma sintering, *J. Am. Ceram. Soc.* 89 (2006) 494–500. doi:10.1111/j.1551-2916.2005.00777.x.
- [30] S. Diouf, A. Molinari, Densification mechanisms in spark plasma sintering: Effect of particle size and pressure, *Powder Technol.* 221 (2012) 220–227. doi:10.1016/j.powtec.2012.01.005.
- [31] U. Anselmi-Tamburini, J.R. Groza, Critical assessment: electrical field/current application—a revolution in materials processing/sintering?, *Mater. Sci. Technol. (United Kingdom)*. 33 (2017) 1855–1862. doi:10.1080/02670836.2017.1341692.
- [32] A.S. Semenov, J. Trapp, M. Nöthe, O. Eberhardt, T. Wallmersperger, B. Kieback, Experimental and numerical analysis of the initial stage of field-assisted sintering of metals, *J. Mater. Sci.* 52 (2017) 1486–1500. doi:10.1007/s10853-016-0444-0.
- [33] P. Franke, C. Heintze, F. Bergner, T. Weißgärber, Mechanical Properties of Spark Plasma Sintered Fe-Cr Compacts Strengthened by Nanodispersed Yttria Particles, *Mater. Test.* 52 (2010) 133–138. doi:10.3139/120.110115.
- [34] X. Boulnat, N. Sallez, M. Dadé, A. Borbély, J. Béchade, Y. De Carlan, J. Malaplate, Y. Brechet, F. de Geuser, A. Deschamps, P. Donnadiou, D. Fabregue, M. Perez, Influence of oxide volume fraction on abnormal growth of nanostructured ferritic steels during non-isothermal treatments: An in situ study, *Acta Mater.* 97 (2015) 124–130. doi:10.1016/j.actamat.2015.07.005.
- [35] J. Shen, Y. Li, F. Li, H. Yang, Z. Zhao, S. Kano, Y. Matsukawa, Y. Satoh, H. Abe, Microstructural characterization and strengthening mechanisms of a 12Cr-ODS steel, *Mater. Sci. Eng. A.* 673 (2016) 624–632. doi:10.1016/j.msea.2016.07.030.
- [36] M. Dadé, J. Malaplate, J. Garnier, F. De Geuser, F. Barcelo, P. Wident, A. Deschamps, Influence of microstructural parameters on the mechanical properties of oxide dispersion strengthened Fe-14Cr steels, *Acta Mater.* 127 (2017) 165–177. doi:10.1016/j.actamat.2017.01.026.
- [37] X. Zhou, Y. Liu, L. Yu, Z. Ma, Q. Guo, Y. Huang, H. Li, Microstructure characteristic and mechanical property of transformable 9Cr-ODS steel fabricated by spark plasma sintering, *Mater. Des.* 132 (2017) 158–169. doi:10.1016/j.matdes.2017.06.063.
- [38] A. Chauhan, F. Bergner, A. Etienne, J. Aktaa, Y. De Carlan, C. Heintze, D. Litvinov, M. Hernandez-Mayoral, E. Oñorbe, B. Radiguet, A. Ulbricht, Microstructure characterization and strengthening mechanisms of oxide dispersion strengthened (ODS) Fe-9 % Cr and Fe-14 % Cr extruded bars, *J. Nucl. Mater.* 495 (2017) 6–19. doi:10.1016/j.jnucmat.2017.07.060.
- [39] A. Ramar, R. Schäublin, Analysis of hardening limits of oxide dispersion strengthened steel, *J. Nucl. Mater.* 432 (2013) 323–333. doi:10.1016/j.jnucmat.2012.07.024.
- [40] X. Mao, T.K. Kim, S.S. Kim, K.H. Oh, J. Jang, Thermal stability of oxide particles in 12Cr ODS steel, *J. Nucl. Mater.* 428 (2012) 82–89. doi:10.1016/j.jnucmat.2011.09.011.

- [41] M.J.R. Sandim, I.R. Souza Filho, E.H. Bredda, A. Kostka, D. Raabe, H.R.Z. Sandim, Coarsening of Y-rich oxide particles in 9%Cr-ODS Eurofer steel annealed at 1350 °C, *J. Nucl. Mater.* 484 (2017) 283–287. doi:10.1016/j.jnucmat.2016.12.025.
- [42] S.F. Li, Z.J. Zhou, P.H. Wang, H.Y. Sun, M. Wang, G.M. Zhang, Long-term thermal-aging stability of a 16Cr-oxide dispersion strengthened ferritic steel at 973K, *Mater. Des.* 90 (2016) 318–329. doi:10.1016/j.matdes.2015.10.138.
- [43] J. Simeg Veternikova, J. Degmova, M. Pekarcikova, F. Simko, M. Petriska, M. Skarba, P. Mikula, M. Pupala, Thermal stability study for candidate stainless steels of GEN IV reactors, *Appl. Surf. Sci.* 387 (2016) 965–970. doi:10.1016/j.apsusc.2016.06.151.
- [44] S. Mohan, G. Kaur, B.K. Panigrahi, C. David, G. Amarendra, Effect of Zr and Al addition on nanocluster formation in oxide dispersion strengthened steel - An ab initio study, *J. Alloys Compd.* 767 (2018) 122–130. doi:10.1016/j.jallcom.2018.07.047.
- [45] M.K. Dash, R. Mythili, R. Ravi, T. Sakthivel, A. Dasgupta, S. Saroja, S.R. Bakshi, Microstructure and Mechanical Properties of Oxide Dispersion Strengthened 18Cr-Ferritic Steel Consolidated by Spark Plasma Sintering, *Mater. Sci. Eng. A.* (2018). doi:10.1016/j.msea.2018.08.093.
- [46] W. Li, T. Hao, R. Gao, X. Wang, T. Zhang, Q. Fang, C. Liu, The effect of Zr, Ti addition on the particle size and microstructure evolution of yttria nanoparticle in ODS steel, *Powder Technol.* 319 (2017) 172–182. doi:10.1016/J.POWTEC.2017.06.041.
- [47] L. Zhang, L. Yu, Y. Liu, C. Liu, H. Li, J. Wu, Influence of Zr addition on the microstructures and mechanical properties of 14Cr ODS steels, *Mater. Sci. Eng. A.* 695 (2017) 66–73. doi:10.1016/J.MSEA.2017.04.020.



Final Remarks

8. Final Remarks

Along this manuscript the different objectives established in Chapter 2 have been fulfilled with the main motivation of understanding and controlling the production of ferritic ODS steels. The main objective of this work was to develop a ferritic ODS steel whose behaviour was compatible with the high requirements demanded on the new GenIV reactors. Starting from the processing route (MA+SPS) until the final evaluation of the material under high temperature conditions, F-ODS-I and F-ODS-II alloys are postulated as an interesting candidate to continue with their study for their application under irradiation conditions.

In Chapter 2 the objectives are divided into different parts, therefore the same procedure will be used for the conclusions.

Starting with the processing route the main conclusions are (Chapter 4, 5, 7):

- During the optimization of milling conditions, it has been observed how M_{act} parameters promoted a bimodal microstructure (micrograin+Uf grain) composed by a higher area covered by Uf regions. Nevertheless, M_{std} favoured a microstructure almost entirely composed by micrograin regions. The difference between M_{act} or M_{std} is based on the way in which the plastic deformation is stored on the alloy as well as the distribution of the attained particle size. Undoubtedly, milling conditions are defining the grain growth and consequently the final reached microstructure.
- The heating rate is determining the reached UF area on the final microstructure. Using the highest HR favours a total area of UF 32% (Zr600) respect the 25% achieved when 100 °C/min are handled (Zr100). Therefore, HR is also decisive on the final grain growth.
- Facing densification, when the maximum pressure applied is around 80 MPa the final densification of the material is not highly influenced by the HR (Chapter 5). However, this phenomenon changes when the pressure used is under 60 MPa (Chapter 7). Increasing the HR from 100 to 300 and 500 rises the density from 96% to 98-99%. Under 60 MPa at 100 °C/min the final density does not change even by increasing the temperature (Until 1200 °C, see Chapter 7). Consequently, the use of HR is higher favourable when SPS consolidation are faced.

Continuing with the Zr addition (Chapter 4,5 and 7):

- When Zr is added as a pure element (F-ODS-I, Chapter 5), the different species formation are reported, from ZrW, ZrTi, ZrWTi (Between 60 and 80 nm), to Y-Zr-Al-O and Y-Al-O (both under 20 nm) and finally Y-Zr-O (under 8nm). The attained oxide diameter distribution is around 5.5 nm and their density is on the range of 10^{22} oxd/m³. Undoubtedly, the amount of Al (5%) governs the final precipitate composition.
- When Zr is added as a complex nano-oxide (F-ODS-II, Chapter 7) the formation of species changed. ZrW, ZrTi and ZrWTi are not analysed. Instead of solid solution composed by Y-Zr-Ti-Al-O is the widest observed species (diameter around 10-80 nm). In a smaller range size (under 30 nm) particles composed by Y-Zr-Al-O are also detected as well as Y-Zr-O. Besides Y-Al-O compound are not avoided even by adding the nano-oxide composed by YTiZrO. The reactive behaviour together with the amount of Al inserted produce the formation of these compound. Using YTiZrO complex particles allows to favour the presence of Ti on the final nano-precipitates. The oxide size varies from 9 to 11 nm and the density is on the range of 10^{21} oxd/m³.
- Comparing F-ODS-I with 14Al-ODS-Ti (Without Zr) shows how Zr reduces the size of precipitates an increase its density (From 12 to 5.5 and 10^{21} to 10^{22}). Undoubtedly, Zr is refining the nano-precipitates attained. However, if F-ODS-II is compared to 14Al-ODS-Ti, values are on the same range. This behaviour is probably related to the amount of Zr inserted as a complex nano-oxide respect the one used on F-ODS-I (0.4 vs 0.6 wt%).

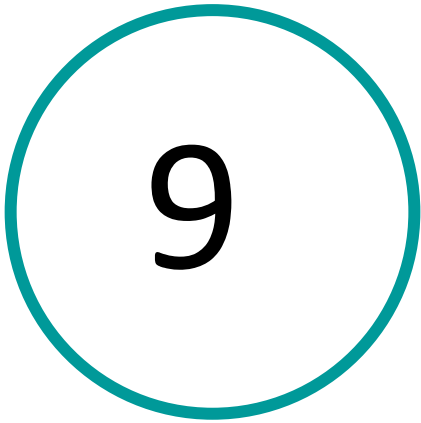
- Nano-precipitates are certainly demarcating the final attained microstructure (being the third parameter after MA, SPS on the control of the grain growth). The precipitation density alone with the diameter of the oxide is determining the final grain size (U_f used to recollect the higher precipitation densities) reached and the mechanical properties at room and high temperatures.

Moreover, facing mechanical properties (Chapter 4,5,7):

- Zr is influencing the mechanical properties of the ODS ferritic alloys. Both F-ODS-I and F-ODS II obtained competitive mechanical properties, reaching higher UTS and toughness than 14Al-ODS-Ti (without Zr addition). Besides, SP test shows how F-ODS-I and F-ODS-II got similar properties at 500 °C (in terms of F_{max}) than GETMAT project material consolidated by HE (See Chapter 4, 5 and 7).
- Ferritic ODS steels mechanical behaviour is caused by different strengthening mechanism namely: Solid solution hardening, Grain size hardening, particles strengthening and dislocation density strengthening. Both in Chapter 5 and 7 it has been demonstrated that particles and dislocation density strengthening are the highest contribution terms to mechanical properties. This factor promotes that refining the grain size has not a strong effect on the final attained properties
- The small drop on the F_{max} when the material is heated at 500 °C is due to the annihilation of dislocation which directly reduces the strengthening promoted by this term on the material. Besides, particle, solid solution and grain strengthening maintain the material properties under 500 °C.

Eventually, considering the thermal stability of the material (Chapter 6), the main conclusions are:

- F-ODS-I-Zr600 presents stables nano-precipitates. After heating the material at 600 °C the precipitation density has slightly decreased, and the diameter has not varied.
- There is no variation on grain dimension after heating the material at 600 °C which means that both micrometric and ultrafine regions, grain are stable under the evaluated temperature.
- When the Zr600 material is heated at 600 °C the dislocation density is modified, observing clearly how some dislocations moves during the time when the alloy is submitted through this temperature. This phenomenon should explain the reduction on F_{max} when the material attains 500 °C during SP in Chapter 4, 5 and 7.
- In-situ TEM annealing tests open a new way to understand the behaviour of ferritic ODS steels when they are submitted through temperature.



Future research lines

9. Future research lines

As it is stated in Chapter 8 many are the conclusion performed on this manuscript. Therefore, based on the results obtained, some are the studies that can be performed in order to continue with the development of 14 Cr ODS ferritic steels.

Starting with the powder production:

- To produce YTiZrO nanoparticles by using spray pyrolysis method, avoiding different solvent which can contaminate the starting nanoparticles.
- Using the M_{act} conditions to mill the powder, reducing the time for milling and increasing the amount of powder produced.
- Increasing the amount of YTiZrO nanoparticles inserted in the matrix equalizing by the Zr amount inserted (0.6%), instead of introducing the same amount of Y (Chapter 7). Promoting in this way a higher density and smaller oxides.
- To develop atomized powders with the oxide formers inserted in the prealloyed powder trying to avoid steps such as MA.

Continuing with the consolidation process:

- Facing fast technologies, the utilization of fast method should be interesting to study and understand the effect of different currents on the material and to evaluate their viability for future development of ODS steels.
- Performing studies of recrystallization by using SPS, analysing the effect of the current on the recovery, recrystallization and further grain growth of the material.
- Scaling the material to industrial scales (bigger samples than 20 mm in diameter) and studying the effects on the microstructure and mechanical properties of the material.
- Improving the sintering effect on FAHP (presented in Chapter 4) by using different heating rates.

Dealing with the composition of the material:

- Using different B percentage should increase the creep behaviour as well as block the grain motion. Consequently, playing with different percentage until a maximum of 0.1% could be interesting.

Following mechanical properties evaluation:

- To perform In-situ TEM tensile tests to understand the effect of oxides grain and dislocation on the final YS of the material.
- To perform In-situ SEM test by heating the sample and evaluate its capability under high temperatures conditions.
- To evaluate the real deformation of the material in micro tensile dog bone samples, by using Au coatings or DIC systems.
- To perform small punch creep tests on the attained samples.

In the end, facing thermal evaluation:

- To increase the temperature on the In-situ TEM annealing systems (near to 1000 °C).
- To compare traditional results (annealing the material in a furnace) with the one attained by the In-situ TEM annealing, obtaining a correlation between both methods.
- To evaluate the material after heating with Pb and PbBi.
- To realize long oxidation test evaluation (up to 10000 hours).
- To irradiate the material and analyse the effect with temperature.

